Extracellular vesicle trafficking enforces microenvironmental dysregulation in Acute Myeloid Leukemia

By

John T. Butler

A DISSERTATION

Presented to the Department of Biomedical Engineering
and the Oregon Health & Science University
School of Medicine
in partial fulfillment of
the requirements for the degree of
Doctor of Philosophy

July 2020

School of Medicine

Oregon Health & Science University

CERTIFICATE OF APPROVAL

This is to certify that the PhD dissertation of

John T. Butler

has been approved

Mentor/Advisor: Daniel Marks, MD, PhD

Mentor/Advisor: Peter Kurre, MD

Chair: Xiaolin Nan, PhD

Member: Evan Lind, PhD

Additional Member: Monica Hinds, PhD

Acknowledgments

The research described within this thesis would not have been possible without the contribution and support of many people. First and foremost, I would like to thank my parents, Kathleen Smith and James Butler, and all of my friends from Burrillville and MED19 for their support and tolerance over the years. I especially would like to thank Chris Latendresse, for help regarding academic advancement, and taking the time out of his day to teach me algebra after I got a 34 on my first college exam. I have two very non-traditional teachers, Timothy Durigan and Charles Boucher to thank for turning me towards a career in science and medicine. Throughout my academic trajectory, no one has been more influential than Jeanne B. Lawrence. Her generosity and mentorship exposed me to research science and granted me the dream of attending college. For that I am deeply grateful. I would also like thank the members of the Lawrence Lab, Laurie Lizotte, Kelly Smith, Lisa Hall, John McNeil, Meg and Kevin Byron and Gayle Pouliot for taking the time to teach me scientific technique, and how to function in a professional environment. From University of Rhode Island, I am indebted to Richard Koske, David Mello and Gregory Paquette for outstanding mentorship and a wonderful undergraduate experience.

At Oregon Health & Science University, I would like to thank all those involved in the MD/PhD training program, especially, David Jacoby for his infectious optimism ~~and for providing us with lunch at Journal Club~~, as well as Alexis Young, Johanna Colgrove, Daniel Marks and Shiuh-Wen Luoh for keeping the ship afloat. I would also like to thank Zip Feng, Jim Goodman, Katy Michaelis and Mollie Marr for helping me navigate the excessively long training program and its near-infinite requirements. Additionally, I would like to thank the Biomedical Engineering program, specifically Monica Hinds for her support and guidance over the years, as well as Erica Hankins Regalo for tolerating my tardiness in submitting paperwork.

This thesis would not be possible without the mentorship and scientific training provided by Peter Kurre and Daniel Marks. I am indebted to you both for opening up your

labs to me, and taking the time to help me improve my writing, grantsmanship, scientific reasoning and presentation skills. I would also like to apologize to Dan Marks for any passive-voice contained within the following pages. Thanks to the current and former members of the Kurre and Marks Lab for your continued support and contributions to this work: Sherif Abdelhamed, Ben Doron, Young-Me Yoon, Noah Hornick, Santhosh Verghese, Lotte Tholen, Amber Halse, Stephanie Krasnow, Peter Levasseur, Kevin Burfiend, Katy Michaelis, Brennan Olsen, Mason Norgard, Abby Buenafe, Christian Huisman, and Xinxia Zhu.

Much thanks to the Department of Pediatrics and Papé Pediatric Research Institute, especially Kirsten Groener and Marika Fugate for always helping me with administrative questions, and Devorah Goldman, Qianyue Yang, Jianya Huan and John Michaels for providing reagents, protocols and helping me solve last minute problems. I would also like to thank Pam Canaday formerly of the Flow Cytometry Core for teaching me the structural dynamics of flow. I am grateful for the microscopy expertise of Xiaolin Nan, Aurelie Snyder and Stefanie Kaech-Petrie who have taught me so much since I arrived at OHSU. Also as the director of the Advanced Light Miscopy Core, Stefanie Kaech-Petrie has amassed and maintained an amazing collection of microscopes that has made much of this work possible. Furthermore, a special thanks to the following funding sources that have made this work possible: Friends of Doernbecher Foundation, Hyundai Hope on Wheels Foundation, The Tartar Trust, the National Cancer Institute NRSA F30 program, NIH MSTP training grant, and the great state of Oregon.

The work described in this thesis would not have been possible without the scientific contributions of Peter Kurre, Sherif Abdelhamed and Ben Doron. Their words, ideas and data are contained throughout multiple sections of this dissertation (denoted at the beginning of each chapter). They are chiefly responsible for much of the work described in chapters 2 and 3. I have contributed considerably to shaping both projects, yet do not intend to take credit for their work. In the respective sections that contain multiple authors, I default to the use of “we” in the description of these studies. For continuity and

completeness, individual studies have been included in original manuscript format, with extended discussion on my own contributions in Chapter 5 and 6.

Furthermore, I would especially like to thank Sherif Abdelhamed for years of encouragement, training, generosity, and laughs throughout my research experience. I would also like to thank Bill Chang and the Beat AML initiative for providing access to primary samples used in Chapter 4. I would like to acknowledge the contributions of Santosh Verghese for creating the myrisotylated GFP constructs used throughout these studies; Peter Levasseur who performed numerous western blots; and Abby Buenafe for helping me with high resolution flow cytometry assays and providing related data (Appx 4.6.1A). And finally I would like to thank the members of my dissertation advisory committee, Dan Marks, Peter Kurre, Xiaolin Nan, Bill Chang, Evan Lind and Monica Hinds for shaping the work described in this thesis, and for actually reading the next 200+ pages.

List of Abbreviation

AML	Acute Myelogenous (myeloid) leukemia
ApB	Apoptotic body
BM	Bone marrow
BMP2	*Bone morphogenic protein*-2
BMPR	*Bone morphogenic protein receptor*
Chop	*C/EBP homologous protein*; UPR response pathway (proapoptotic)
CTL	*Cytotoxic T-lymphocyte*
EC	Endothelial cell
ESCRT	Endosomal complex required for transport
ER	Endoplasmic reticulum
EV	Extracellular vesicle
EX	*Exosomes*
FACS	*Fluoresence activated cell sorting*
G-CSF	*Granulocyte colony stimulating factor*
Grp78	*Glucose-related protein 78* (BiP; *immunoglobulin binding protein*)
GVL	Graft versus leukemia
HL-60	Human acute promyelocytic leukemia cell line
HSC	Hematopoietic stem cell
Hsp70	*Heat shock protein 70*
IF	Immunofluoresence
***IF*-injection**	Intrafemoral injection
IFNɣ	Interferon-gamma
IL-2	Interleukin-2
ILV	Intra-luminal vesicle
LEV	Large extracellular vesicle
LT-HSC	Long term-hematopoietic stem cell
Mk	Megakaryocyte
MDS	Myelodysplastic Syndrome
mGFP	Myristoylated-green fluorescent protein
MoIm-14	Human FLT3-Internal tandem duplication positive AML cell line
MSC	Mesenchymal stem cell
mTOR	Mammalian target of rapamycin
MV	Microvesicle

MVB	Multi-vesicular body
OPC	Osteoprogenitor cell
PBMC	Peripheral blood mononuclear cell
PD-1	Programmed Death Receptor 1
PD-L1	Programmed Death Receptor-ligand 1
pmGFP	Palmitoylated-green fluorescent Protein
qRT-PCR	Quantitative real-time polymerase chain reaction
Smad1/5/8	*Small mothers against decapentaplegic-1/5/8* transcription factor
SMLM	Single Molecule Localization Microscopy
SRM	Super resolution microscopy
ST-HSC	Short term-Hematopoietic stem cell
sXbp1	(spliced) *X-box binding protein transcript*; UPR response pathway
TCR	T-cell receptor
TG	Thapsigargin: ER-Calcium channel inhibitor (SERCA); UPR agonist
Tsg101	*Tumor susceptibility gene 101*
TSPN	Tetraspannin
U937	Human monocytic leukemia/lymphoma cell line
VPS33P	Vacuolar sorting protein -33P

Table of Contents

List of Tables

List of Figures

Abstract

Acute Myelogenous Leukemia (AML) is an aggressive cancer of the bone marrow that affects both adults and children alike. While many patients achieve remission following induction of chemotherapy, the cancer eventually returns in 40% with increased resistance to cancer drugs. Due to high rates of relapse and drug resistance, the 5-year survival remains less than 25%. AML originates from abnormal hematopoietic stem cells (HSCs) that rapidly proliferate in the bone marrow—the principal site of blood-cell production. There is no unifying genetic lesion that underlies AML, however regardless of subtype, the progression of cancer and effects on the bone marrow microenvironment are strikingly similar. As AML cells expand in an uncontrolled manner they successively impair the growth of normal blood cells and cause life threatening cytopenias. The complex interplay of AML and the surrounding microenvironment creates a sanctuary that disrupts hematopoiesis and protects occult myeloblasts from therapy, yet the mechanisms underlying these pro-leukemic changes are not fully explained by traditional models of cell-to-cell crosstalk or physical displacement. It is now understood that AML cells enforce pro-leukemic changes in part by releasing copious membrane-bound packages of cargo, called extracellular vesicles (EVs). Following release, AML-EVs are broadcast throughout the medullary compartment and enter systemic circulation—where they bind and enter recipient cells—delivering tumor-derived factors directly to non-malignant cells.

Despite mounting evidence implicating EVs in bone marrow dysfunction, more research is needed to fully map the directional transfer of AML-EVs to recipient cells, and determine how their respective cargos enforce pro-leukemic alterations to the bone marrow and extramedullary tissues. A better understanding of EV-mediated crosstalk within the AML microenvironment is critical to unraveling the mechanisms that underlie relapse and drug resistance, which have remained elusive for so long. In this thesis, I investigate the fate and function of AML-EV in altering the leukemic microenvironment through direct interactions with HSPCs, supportive stroma and cytotoxic T-lymphocytes.

In chapter 1, I introduce the bone marrow microenvironment, and describe the transformation of normal hematopoiesis to malignant AML. This chapter also focuses on EV-related biology, and synthesizes existing research pertaining to the role of EVs in shaping both homeostatic and pathophysiologic bone marrow function. In chapter 2, I describe the transmission of endoplasmic reticulum stress to bone marrow stromal cells in immunodeficient NSG xenograft recipients through the uptake of AML-EVs. In the leukemic marrow, AML-EVs accumulate in mesenchymal stem cells and osteoprogenitors, activating the unfolded protein response—a pathway linked to chemoresistance in other cancers. Conversely, the uptake of AML-EVs by HSCs does not transmit ER-stress, but rather halts protein synthesis and induces DNA damage, potentially predisposing residual HSPCs for transformation. In Chapter 3, I demonstrate that EV-associated miRNAs directly enforce quiescence on residual hematopoietic stem cells by inhibiting the mTOR pathway (mammalian target of rapamycin). Furthermore, AML-EVs are not restricted to the bone marrow compartment, they able to enter systemic circulation and reach distant tissues. In chapter 4, I show that AML-EVs interact with the immune system outside of the medullary space, and suppress the activation CD8+ T cells to dampen the immune system's anti-tumor response. In order to facilitate these studies, multiple methods were developed to improve the detection of nanoscale EVs and track their fate in experimental models. In Chapter 5, I introduce the limitations of using fluorescence imaging and flow cytometry to study nanoscale EVs, and include methodology for techniques I developed to accomplish the research described throughout this thesis. Finally, in chapter 6, with mounting evidence implicating AML-EVs in enforcing pro-leukemic changes in the bone marrow, I discuss their significance in the progression of AML, and offer future directions aimed at clarifying the role of EVs play in relapse and drug resistance. The work described *herein* was conducted with the goal of preventing EV-enforced dysregulation of the leukemic microenvironment, with the hope of identifying new therapeutic targets to improve outcomes for patients suffering with AML.

Chapter 1: Introduction

Adapted in part from:

1. *Butler JT, Abdelhamed S, Kurre P. Extracellular vesicles in the hematopoietic microenvironment. Haematologica. 2018 Mar;103(3):382-394. doi: 10.3324/haematol.2017.183335. Epub 2018 Feb 8. PMID: 29439185.*

2. *Nehrbas J, Butler JT, Chen DW, Kurre P. Extracellular Vesicles and Chemotherapy Resistance in the AML Microenvironment. Front Oncol. 2020 Feb 14;10:90. doi: 10.3389/fonc.2020.00090. PMID: 32117744*

Abstract

Self-renewal and differentiation are defining characteristics of hematopoietic stem and progenitor cells. Their balanced regulation within the bone marrow is central to lifelong function of both blood and immune systems. In addition to cell-intrinsic programs, hematopoietic stem and progenitor cell fate decisions are subject to extrinsic cues from within the bone marrow microenvironment and systemically. Yet, many of the paracrine and endocrine mediators that shape hematopoietic function remain to be discovered. Extracellular vesicles serve as evolutionarily conserved, constitutive regulators of cell and tissue homeostasis, with several recent reports supporting a role for extracellular vesicles in the physiologic regulation of hematopoiesis. There is also mounting evidence that extracellular vesicles are involved in shaping hematological diseases, such as Acute Myelogenous Leukemia (AML). Here, I introduce AML, and describe the pathophysiological effects EVs have on bone marrow compartment function. I also summarize progress in understanding vesicle biogenesis, cargo incorporation, differential uptake, and downstream effects of vesicle internalization in both health and disease.

Hematopoiesis and the bone marrow microenvironment

The bone marrow—the principal site of hematopoiesis—forms distinct microenvironmental niches that support hematopoietic stem cells (HSC) to maintain a homeostatic balance of quiescence, proliferation and differentiation. Through cell intrinsic and extrinsic regulation, HSCs give rise to all the formed cellular units of the blood, facilitating hemostasis, oxygen delivery, acid-base balance, and both innate and adaptive immunity [1]. At the top of the hematopoietic hierarchy, HSCs contain the greatest pluripotent capacity, and exist in at least two forms. Long-term HSCs (LT-HSC), that maintain the stem cell pool over the life time of the organism via asymmetrical division in a unique process termed self-renewal [2, 3]. Through changes in the epigenetic landscape LT-HSCs give rise to short-term HSC (ST-HSCs), which produce progenitors restricted to one of two lineages—myeloid or lymphoid—and have a comparatively limited capacity to maintain the stem cell pool [1, 3]. Differentiation of hematopoietic stem and progenitor cells (HSPCs) occurs through multiple successive generations, each with decreasing proliferative capacity to produce functionally specialized cells [2, 3]. Myeloid differentiation gives rise to a wide range of related cell types with diverse functions: erythrocytes, megakaryocytes/platelets, monocytes/macrophages/osteoclasts, and neutrophils/eosinophils/basophils. Lymphoid differentiation, on the other hand produces a vast population of distinct B, T, natural killer and dendritic cells that make up the adaptive and cell mediated immune systems. In the bone marrow, many non-hematopoietic stromal elements are critical to regulating hematopoiesis, these cells include mesenchymal stem cells, osteoprogenitor cells, osteoblasts, adipocytes, endothelial cells and neurons [1, 4]. The complex cell-to-cell crosstalk involved in maintaining homeostatic control of hematopoiesis and its response to injury are not fully understood. Nor is the pathophysiological dysregulation that leads to hematological disease, such as the dysplastic transformation of hematopoietic cells to produce tumors of the bone marrow, collectively referred to as leukemias. However, there are numerous studies that describe the importance of the bone marrow microenvironment—specifically stromal population—in dysregulating hematopoiesis and supporting hematological diseases [4-10]. It is important to note that much of what is known about physiological and pathophysiological regulation of hematopoiesis

has been extrapolated from murine models [11]. Though the process of hematopoiesis is thought to be well conserved across mammals, there are clear differences in blood cell development between species, and many of the observations described in mouse models are not substantiated in humans.

To fulfill its critical systemic functions in oxygen delivery, hemostasis and immune defense, hematopoiesis is regulated via integration of cell-intrinsic programs with extrinsic cues from the surrounding bone marrow (BM) microenvironment. Recent studies from infectious diseases, cardiovascular, and cancer fields demonstrate the existence of systemic crosstalk with BM cells that adds to the complexity of compartmental signaling, especially during injury response [1, 8, 12] Cytokines, chemokines and other growth factors act as important mediators in a reasonably well-understood system by which the extrinsic ligands act on cells expressing the cognate receptor **(Fig 1.1A)**. These in turn transmit signals to a network of cellular signaling pathways regulating hematopoiesis, including Wnt, Notch, *Transforming Growth Factor beta* (TGF-β), Phosphatidylinositol-3 Kinase (PI3K), and the *mammalian Target of Rapamycin* (mTOR) [13-15]. Signaling by extrinsic mediators through any one of these pathways triggers activation of quiescent LT-HSCs. More recent studies of the leukemic microenvironment revealed that tumor-derived paracrine factors also act on mesenchymal stromal cells, osteoprogenitors and endothelial cells within the BM, indirectly suppressing hematopoietic stem and progenitor cells (HSPC) [1, 8, 16]. Thus, dynamic compartmental interactions shape physiologic and pathophysiologic regulation of BM function.

Extracellular vesicles in the hematopoietic microenvironment

Extracellular vesicle (EV) biogenesis is a constitutive cellular process, broadly conserved across evolution, with a role in development, homeostatic organismal function and tissue regeneration [17-19]. EVs of various shapes and sizes have been demonstrated in every biofluid tested to date, with substantial variation in structure, content and function [20]. Protein, lipid and nucleic acid (DNA/RNA) components contribute to cell-cell crosstalk at a short distance, or in a paracrine or endocrine manner via the bloodstream (**Fig**

1.1B) [18, 21]. However, owing to their complex cargo and poorly understood selectivity for cellular uptake, many phenotypic outcomes are not easily explained by conventional models of cell-cell crosstalk. The consequences of simultaneously transferring an unknown number of non-randomly assembled proteins and RNA to another cell defy the clear predictions that apply to more conventional receptor-ligand signaling. Thus, while an understanding of the molecular basis for EV crosstalk is in its infancy, the key principles of how EVs shape tissue function are beginning to emerge [20]. Several groups recently demonstrated that EVs contribute to the compartmental regulation of hematopoiesis in the BM [21, 22]. Here, we present current evidence for the role of EVs in both the homeostatic and pathogenic hematopoietic niche with emphasis on regulatory mechanisms, experimental outcomes and the critical open questions in the field.

Figure 1.1: Schematic representation of EV biogenesis and unique aspects of EV trafficking

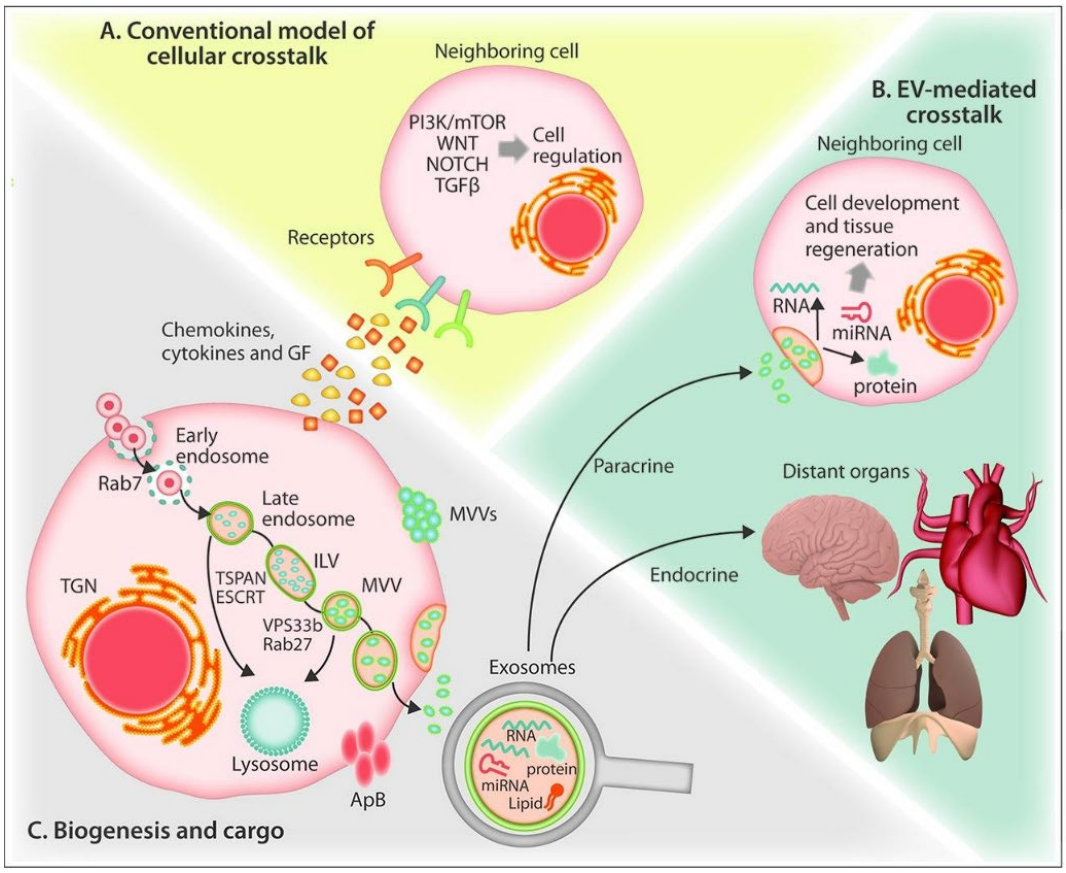

A) The conventional model of cellular crosstalk involves receptor-ligand interactions between secreted chemokines, cytokines and growth factors and cellular surface receptors. **B)** EV-mediated crosstalk occurs through the trafficking of vesicle-associated protein, lipid and RNA/DNA components to proximal cells or to distal organs via the bloodstream in an "paracrine" or "endocrine" manner respectively. **C)** Exosomes are formed from the maturation of early endosomes into Rab7-containing late endosomes leading to the generation of ILVs via the action of TSPNs and ESCRT proteins which sort the endosomal constituents into distinct MVBs. Through the action of Rab27 and VPS33b, MVBs evade lysosome degradation and fuse with the plasma membrane to release 30-125nm exosomes. Cells also release 50-1000nm microvesicles that form through the calcium mediated budding of the plasma membrane, and during programmed cell death, large (>1000nm) apoptotic bodies. *ApB: apoptotic bodies ESCRT: endosomal-sorting complex required for transport; GF: growth factors; ILV: intra-luminal vesicle; MV: microvesicle; MVB: multivesiclular bodies;* mTOR: *Mammalian Target of Rapamycin; PI3K;* phosphatidylinositol-3 Kinase; *TGF-β: Transforming Growth Factor beta*; *TGN: trans-golgi network; TSPN: tetraspanin; VPS33B: Vacuolar protein sorting-associated protein 33B. Figure presented from Butler et al., 2018* [23]

Extracellular vesicles

EVs are membrane-enclosed structures of varying size (30-10,000nm) released from cells to mediate both local and distant intercellular communication. Platelet-derived vesicles were first identified by electron microscopy over 50 years ago [24], yet the full spectrum of subtypes and activities have only become a major focus of interest in recent years. In the early 1980s, it was reported that sheep reticulocytes selectively release transferrin receptor within EVs during programmed enucleation of the maturing red cell, and generally considered as a means to export cellular waste [25]. Recent studies of EVs in the BM demonstrate that EVs serve to regulate hematopoiesis, participate in immune cells activation, and act as mediators of hemostatic functions [19, 26, 27]. Hematological diseases such as leukemia, multiple myeloma or viral infections can coopt EV trafficking mechanisms, upend these homeostatic processes and use EVs to reinforce tumor growth, chemotherapeutic resistance, invasion, metastasis and relapse [28-30].

EVs can be broadly classified into four subtypes (**Table 1.1**) based upon vesicle size and method of cellular release: exosomes (30-150nm), microvesicles (MVs, 50-1000nm), large vesicles (>1000nm) and apoptotic bodies (>1000nm) [31]. It is technically challenging to separate vesicle types, and no standardized method exists to date. Techniques utilized for EV purification often rely on size or density [20]. However, there is overlap between exosomes and MVs in size and composition, and neither size-exclusion chromatography or ultracentrifugation in density gradients yield pure populations [31]. Moreover, due to overlap between these vesicles—in size and miRNA carrier function—with plasma abundant chylomicrons and lipoproteins, EV dimension should be considered an arbitrary surrogate metric, and a more biologically informed classification would likely enhance reproducibility in the field, advance their detection and inform treatment strategies.

Exosomes

The biogenesis of exosomes, the smallest type of EV, begins with the inward cleavage of the plasma membrane to form an endosome containing selectively enclosed cytoplasmic components within the lumen. As demonstrated in **Fig 1.1C**, early endosomes, characterized by the presence of Rab5 protein, undergo maturation into Rab7 containing late endosomes which generate multiple intraluminal vesicles (ILVs) through the action of tetraspanins (TSPNs) and *endosomal sorting complex required for transport* (ESCRT) proteins [32]. Together these proteins function to facilitate further inward cleavage and sorting of endosomal constituents into discrete ILVs. These multivesicular bodies (MVBs), through RAB27- and VPS33b-dependent mechanisms, evade lysosome degradation and fuse with the plasma membrane to release intraluminal vesicles as exosomes [33, 34]. Through this highly regulated endosomal process of formation, exosome size is relatively constant as compared to the larger vesicle types. In addition to TSPNs, proteins *ALG-2 interacting-protein X* and *tumor susceptibility gene 101* (ALIX and TSG101, respectively) are reported to be involved in the endosomal process, and are frequently used as markers for exosomes [20, 31]. Different cell types can release discrete heterogeneous subpopulations of exosomes, each with different proteomic properties and RNA cargo, and divergent membrane protein composition [32, 35].

Microvesicles

Intermediate sized EVs are most frequently referred to as microvesicles (MVs), ectosomes, or if tumor-derived, oncosomes, that arise *via* direct outward budding and cleavage of the plasma membrane. MVs are spherical in shape, spanning a broad range of sizes between 50nm to 1000nm in diameter. They are distinguished based on their formation and release, and do not utilize the endosomal/multivesicular body pathway [36]. Instead MVs are formed through a process that involves calcium influx and remodeling of the cortical cytoskeleton to release the membrane-enclosed cytosolic cargo [20]. Viewed broadly, MVs do not appear to be formed in a consistent manner like exosomes. However, when restricted to a specific cell type, MVs may form in a uniform manner, as illustrated

in one recent study of neutrophils that consistently shed two distinct narrowly defined vesicle populations of ~100nm and ~500nm, both budding at the limiting membrane [37].

Large Vesicles

Large vesicles (LEVs), also referred to as large oncosomes when tumor-derived, are a class of EVs that can reach up to 10 microns in size and contain intact organelles and an ordered cytoskeletal structure [38]. LEVs are similar to apoptotic bodies in size and composition, however unlike apoptotic bodies, LEVs are formed from cleavage of cytoplasmic extensions from intact living cells. LEVs have been described in B-cell acute lymphoblastic leukemia and prostate cancer, and demonstrated within patient samples and in culture of cancer cell lines [38, 39].

Apoptotic bodies

Apoptotic bodies (ApBs) emerge during the course of programmed cell-death, as nuclear karyorrhexis (terminal fragmentation) occurs coincident with the fragmentation of the cytoplasm and surrounding plasma membrane [40]. ApBs consist of an intact plasma membrane enclosing cytosolic components and can contain both organelles and nuclear fragments. These bodies are subsequently eliminated through phagocytosis by surrounding cells and degraded in phagolysosomes [40] It was reported that ApBs can horizontally transfer DNA to phagocytic recipient cells. As an example of this, one study showed that Epstein Barr virus (EBV) infected B-lymphocytes, generate ApBs that carry viral DNA and aid in the viral transfer of EBV to uninfected cells [41]

Table 1.1: Types of extracellular vesicles

EV type (abbreviation) *Pseudonym*	**Size** (nm)	**Biogenesis**	**Constituents**	**Selection**	**Detection**	**Ref**
Exosome (EX) Nanovesicles Nanoparticles	30-150	Early endosomes mature into late endosomes, then through the action of ESCRT, multivesicular bodies are formed containing intraluminal vesicles that fuse with the plasma membrane for release	Lipid membrane Nucleic acids Proteins TSPNs ALIX TSG101	UC DG AC SEC	NTA Cryo-EM TEM SEM	[20, 31-35],
Microvesicle (MV) *Microparticles* *Ectosomes* *Oncosomes*	50-1000	Direct budding and cleavage of plasma membrane mediated by Calcium influx, and remodeling of the cortical cytoskeleton	Lipid membrane Nucleic acids Proteins TSPNS	UC AC SEC	NTA Cryo-EM TEM SEM	[20, 36, 37]
Large vesicle *(LEV)* *Large oncosomes*	>1000	Cleavage of large cytoplasmic extensions from cell body	Lipid membrane Nucleic acids Proteins Organelles Organized cytoskeleton	CF FT FACS	FM FC	[38, 39]
Apoptotic body (ApB)	>1000	Cytoplasmic fragmentation during programmed cell death	Lipid membrane Nucleic acids Proteins Organelles Nuclear fragments Apoptotic markers	CF FT FACS	FM FC	[40, 41]

AC: affinity chromatography; CF: centrifugation; Cryo-EM: cryo-electron microscopy; DG: density gradient; ESCRT: endosomal-sorting complex required for transport; FACS: fluorescence activated cell sorting; FC: flow cytometry; FM: fluorescence microscopy; FT: filtration; NTA: nanoparticle tracking analysis; SEC: size-exclusion chromatography; SEM: scanning electron microscopy; TEM: transmission electron microscopy; UC: ultracentrifugation

Vesicle Fate

Once released from the parent cell, EVs can follow multiple routes. Some cancer cells generate EVs that rupture soon after release from their parent cells, distributing enzymes like *vascular endothelial growth factor* and *matrix metalloproteases* into the surrounding interstitial space in order to promote angiogenesis, and support cancer invasion through metastatic dissemination [42, 43]. EVs released into the blood appear to have a short half-life in circulation. In one representative study of B16-BL6 melanoma-

derived EVs packaged with luciferase and lactadherin, luciferase activity was lost within minutes of intravenous injection with an observed serum half-life of approximately two minutes followed by rapid redistribution into tissues, [44].

A broad range of mechanisms for cellular uptake have been identified for EVs, including membrane fusion, phagocytosis or receptor mediated caveolin-, clathrin- or lipid raft-mediated endocytosis, all culminating with transport of the EV cargo directly into the intracellular compartment [45]. The differences from study to study suggest that EV uptake is a variable process and likely dependent on the type of EV and the parent and recipient cells involved. Experiments showed that uptake is prevented at lower temperatures, suggesting that internalization is energy dependent and does not occur as passive process [46]. The uptake of EVs can be partially blocked by treating vesicles with either heparan sulfate and proteinase K, indicating a role for proteoglycans and surface proteins respectively in gaining entry into the cell [46, 47]. Also, pre-treatment of cells with actin depolymerizing drug cytochalasin D, prior to EV exposure, prevents cytoskeletal remodeling and reduces EV internalization [48]. The use of dynamin 2 inhibitor dynasore, which abrogates caveolin/clathrin-mediated endocytosis also blocks uptake of reticulocyte derived exosomes by macrophages [49]. These data taken together are suggestive of an endocytic process mediating vesicle internalization. Within the hematopoietic niche little is known about specific mechanisms of uptake, though one study reports that megakaryocyte-derived EVs gain entry into hematopoeitic progenitors cells via lipid raft mediated endocytosis, macropinocytosis and membrane fusion [50]. Further study is warranted in order to understand the cellular events by which HSPC and supportive cells of the bone marrow differentially regulate the process of EV entry.

How EVs are specifically targeted to different cell types within the hematopoietic niche in order to regulate hematopoiesis remains largely unknown. Among the most abundant membrane-associated proteins found on EVs are TSPNs, a large cell-surface protein superfamily that interacts with transmembrane proteins and cytosolic signaling molecules to facilitate the organization of these structures into microdomains [50]. TSPNs have been linked to many functions; intracellular signaling through *G-protein coupled*

receptors and *protein kinase* C (PKC); migration and metastasis by interacting with integrins and VCAM; cell morphogenesis by direct binding of alpha-actinin and the induction of actin polymerization [51, 52]. TSPNs are parent cell-type dependent, however CD9, CD63, CD81, CD82, and CD151 are enriched in EVs derived from a range of sources [31]. CD9, a common TSPN used to identify EVs was previously described in association with c-kit/CD117, a tyrosine kinase receptor that is found highly expressed on HSPCs [53]. Tetraspanins such as CD37, CD53 and TSSC6 were found exclusively on hematopoietic cells. It is known that these TSPNs interact with hematopoietic-specific targets likes SHP1, PRR dectin-1, MHC-I/II, integrin α4β1, T-cell/NK-cell co-stimulatory CD2, as well as common signal transducers like PI3K and PKC [54]. Hematopoietic-specific TSPNs and integrins on the EV surface remain strong candidates in targeting vesicles to specific cell types within the hematopoietic niche.

Once inside of the target cell, a recent study demonstrated that EVs are sorted into the endosomal pathway, move quickly through the cytoplasm and then stall at the endoplasmic reticulum (ER), before eventually fusing with lysosomes for degradation [55]. The process of cargo release by internalized EVs remains to be clarified. As the principal compartment for translation within the cell, the ER is a likely site for the deposition of mRNA and miRNA cargo. This and the assembly of the RNA interference-silencing complex in the ER may potentially explain how EVs alter protein synthesis and change cellular behavior. The half-life of internalized EVs is not well defined. In the same study, 293T-derived EVs remain intact for hours to days once inside primary fibroblasts, with 50-60% merging with lysosomes by 48 hours [55]. Though the kinetics of intracellular processing is likely cell-specific and highly dependent on the metabolic state of the recipient cell.

Physiological regulation of Hematopoiesis by EVs

The BM is comprised of hematopoietic and non-hematopoietic cells organized into specialized microenvironments that provide the dynamic regulation of hematopoiesis to assure the adequate formation and function of mature blood cells from HSCs [1]. MSCs, their osteoprogenitor cell (OPC) progeny, as well as endothelial cells (ECs) and adipocytes

coordinately maintain hematopoiesis by regulating proliferation, quiescence, differentiation, and apoptosis of HSPCs through juxtacrine and paracrine activity (**Fig 1.2A**) [12]. As noted, changes in compartmental oxygen concentration, hemorrhage, chemotherapy and irradiation can all prompt the emergence of HSC from quiescence [56, 57], and several lines of evidence suggest that EVs are involved regulating HSC self-renewal (**Fig 1.2B**), and BM function during homeostasis and in response to injury (**Fig 1.2C-F; Table 1.2**,).

Some of the earliest descriptions of EVs revealed their role as platelet derived anti-hemophilic particles and in transferrin receptor release from sheep reticulocytes [17]. Additionally, more recent evidence points to EVs as important physiological mediators of signaling across the immunological synapse [19, 58]. Yet, much less is known about how vesicles might contribute to steady state hematopoietic function or during a regenerative BM response. EV release is very clearly subject to a range of cellular stimuli, including cytokine activation, ionizing radiation, and differences in tissue oxygen tension [59, 60]. Granulocyte-colony stimulating factor (G-CSF) mobilization is one such stimulus that appears to increase vesicle release from hematopoietic progenitors (**Fig 1.2C**) [61]. Following injury, EV release may promote the selective delivery of miRNAs and other cargo, and may explain the enhanced angiogenic and regenerative activity after hypo-perfusion injury in distant tissues [62].

Several groups have studied the release and function of EVs by BM stroma, such as endothelia cells (ECs) and mesenchymal stem cells (MSC). ECs have been shown to generate EVs with pro-angiogenic effects through the actions of miR-126 [63], and are linked to age-related down regulation of osteogenic differentiation within the BM [64, 65]. More literature exists for the release and function of EVs from BM-derived MSCs. Our group recently demonstrated the trafficking of EVs from bone marrow-derived MSCs to hematopoietic cells influencing progenitor commitment (**Fig 1.2D**) [26]. While other groups showed that MSC-derived EVs selectively promoted tumor growth in patients with multiple myeloma [30]. Additionally, MSC-derived EVs regulate angiogenic activity in

endothelial cells, supporting the notion that BM MSC-derived EVs can regulate specific cell populations both in and out of the hematopoietic compartment [66].

In a recent study, the Kurre/Marks Labs showed that murine HSPC (KSL: c-kit+/sca-1+/lineage-depleted) exposed to bone marrow MSC-derived EVs *in vitro* prompted activation with myeloid progenitor biased expansion and a skewed hematopoietic repopulation potential (**Fig 1.2D**) [26]. Remarkably, this process seemed to be dependent on TLR signaling and could be specifically abrogated in HSPCs from TLR4 knockout or MyD88 knockout animals. EVs of all classes are also rich in lipid components, especially products of the arachidonic acid metabolism, including PGE2 [67]. Considering the potent activity of PGE2 in regulating HSC expansion and engraftment [68], it is tempting to speculate that EV bound PGE2 released by MSC contributes to this activity [69].

The EV-mediated influence on hematopoiesis is not limited to supportive stromal cells alone. Megakaryocytes (Mks) also impart regulatory control on HSPCs by releasing MVs to orchestrate specific cell-type commitment (**Fig 1.2E**). Mk-derived MVs are among the most abundant MVs in circulation, and attach to HSPCs by interacting with ICAM-1, CD43, CD18 and CD11b epitopes. Upon cell surface contact, these MVs become internalized where Mk-RNA appears to serve as the mediator of biological effects, which is evidenced by a loss of function of Mk-MVs following RNAase treatment. Functionally, the internalization of these Mk-MVs was found to redirect the differentiation of HSPCs toward functional Mks with limited effects on the phenotype of endothelial or stromal cells [70].

Several studies speak to the importance of EV miRNA in regulating erythropoietic differentiation of HSPCs in both mouse and human models [71]. One recent report showed that erythroleukemia cells respond to hypoxia by rapidly releasing exosomes containing miR-486, a known regulator of erythroid differentiation, that targets Sirt1 in $CD34^+$ HSPCs (**Fig 1.2F**)[72]. This confirmed and extended previous studies that had implicated the increased expression of miR-486-5p in supporting erythroid differentiation of $CD34^+$ cells *in vitro* [73]. Conversely, the inhibition of miR-486-5p has been found to suppress $CD34^+$

cell growth *in vitro* and *in vivo*, and decrease erythroid differentiation and survival of erythroid cells. It is tempting to speculate that a similar physiological mechanism might exist to regulating hypoxia-responsive erythropoiesis to increase the delivery of oxygen to starved tissues.

EVs within the BM microenvironment modulate the behavior of HSCs in other ways. For example, treatment with pharmacologic concentrations of G-CSF used to mobilize stem and progenitor cells for collection and subsequent transplantation causes an increase in EVs containing high levels of miR-126 within the BM. These EVs are internalized by stroma, HSPCs and endothelial cells, delivering miR-126 into the cell, where it acts to translationally suppress vascular cell adhesion molecule 1 (VCAM-1). This decrease in VCAM-1, along with other signaling events, results in reduced HSPC adhesion and a shift into the peripheral blood, for collection by leukapheresis (**Fig 1.2C**) [61] Experimentally, EV-contained miR-126 released from mobilized human CD34 cells confers proangiogenic activity and promotes hindlimb ischemia repair [62]. Another recent study has found that aging and oxidative stress alter the miRNA content of EVs in the BM microenvironment leading to age-related stem cell dysfunction. The investigators showed that BM-derived EVs from aged mice contain abundant miR-183-5p, that when endocytosed by primary BM stromal cells from young mice, decrease proliferation and inhibit osteogenic differentiation by reducing heme oxygenase 1, an enzyme essential in heme catabolism [74]. MVs derived from mouse embryonic stem cell (mESC) were found to contain high levels of transcripts associated with pluripotency (Wnt-3 and Oct-4), and when exposed to hematopoietic progenitors led to their expansion [75]. Additionally, hematopoietic progenitors exposed to mESC-MVs were found to upregulate the expression of early HSC markers (SCL, HoxB4 and GATA2) and led to phosphorylation of MAPK p24/44 and serine-threonine kinase AKT [75].

Finally, HSCs may contribute to their own stemness in part through secretory signaling and autocrine loops, involving VPS33B (*Vacuolar Protein Sorting Protein 33b*) mediated release of exosomes as carriers of thrombopoietin and *angiopoietin-like protein 2 and 3*, wherein the loss of VPS33B compromised HSC potential and reduced

leukemogenicity in cancer models (**Fig 1.2B**) [54] This and other studies discussed in this section support the view that within the physiologic BM microenvironment, HSPCs release and internalize EVs, and are broadly responsive to regulation by vesicle trafficking in order to maintain hematopoiesis.

Figure 1.2: Current evidence for EV crosstalk in the homeostatic bone marrow

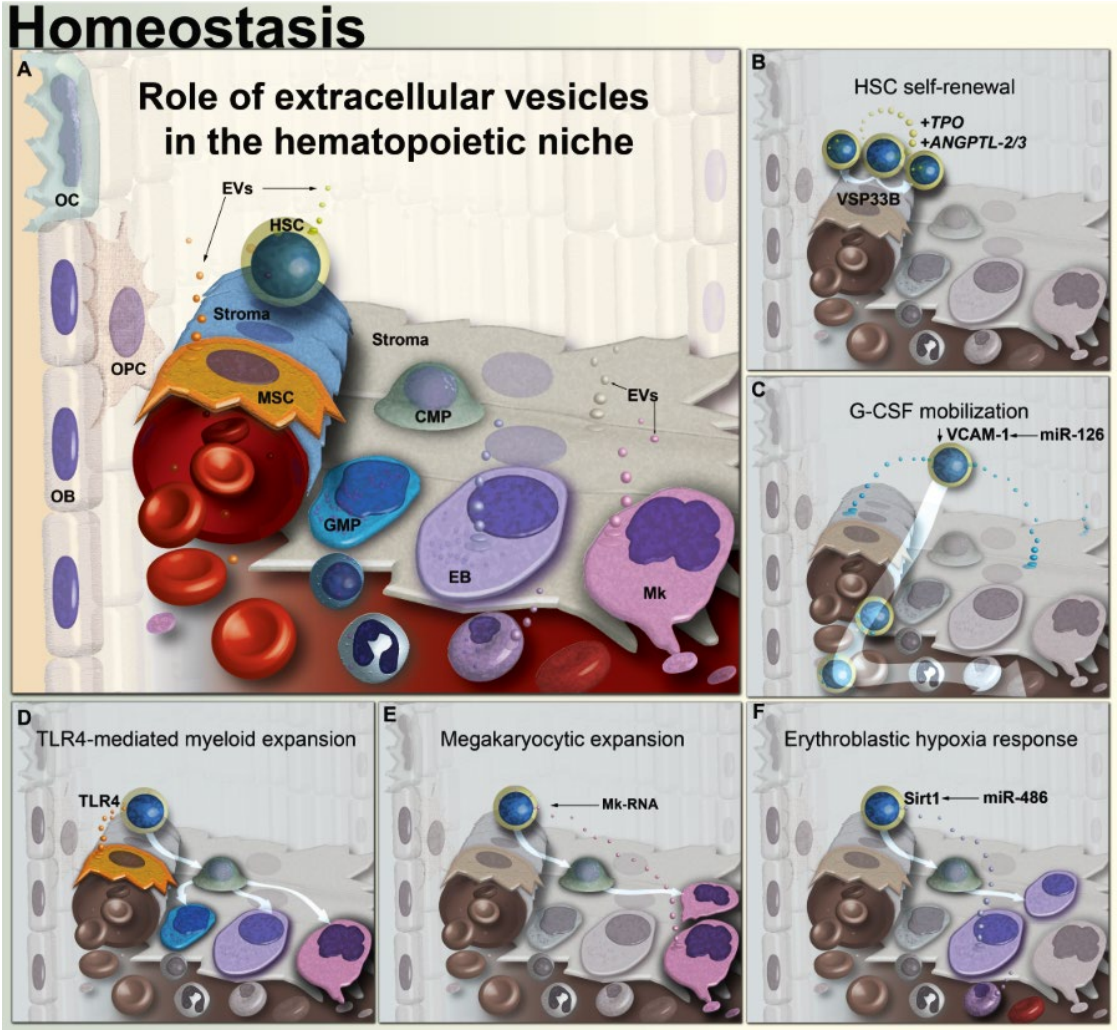

A) In the homeostatic BM microenvironment, stromal elements and EV-mediated signaling, maintain HSCs and support differentiation. **B)** HSPCs autoregulation stemness by releasing critical proteins through the exosomal pathway via the action of VPS33B. **C)** G-CSF infusion stimulates release of EVs containing miR-126 that down-regulate VCAM-1, resulting in HSPC mobilization. **D)** MSC-derived EVs signal to HSPCs through the TLR-4 pathway, resulting in myeloid-biased expansion. **E**) Mk-derived MVs increase differentiation of new Mk cells through RNA-mediated signaling. **F)** Hypoxia induces erythroleukemia cells to release EVs containing miR-486 increasing erythroblastic differentiation. *ANGPTL-2/3; angiopoietin-like protein 2 and 3; CMP: common myeloid progenitor; EB: erythroblast; EVs: extracellular vesicles; G-CSF: granulocyte-colony stimulating factor; GMP; granulocyte monocyte progenitor; HSPC: hematopoietic stem and progenitor cell; Mk: megakaryocytes; MSC: mesenchymal stem cell; miR: microRNA; MV: microvesicles; TLR-4: Toll-like receptor 4; TPO: thrombopoietin; VCAM-1: vascular cell adhesion molecule; VPS33B: Vacuolar protein sorting-associated protein 33B.*

Table 1.2: Physiological regulation of hematopoiesis by EVs

EV origin	Recipient cell	Cargo	Molecular target and effect	Functional event	Ref
Reticulocytes	Macrophage	Transferrin receptor		Release and recycling of transferrin receptor during enucleation and maturation of erythrocytes	[17]
MSCs	HSPCs		TLR4: binding/activation	TLR4 signaling results in myeloid biased expansion and skewed hematopoietic repopulation potential of HSPCs	[26]
Megakaryocytes	HSPCs	Mk-RNA	ICAM-1: binding/entry CD63: binding/entry CD18: binding/entry CD11b: binding/entry	Selective differentiation of progenitors into functional megakaryocytes	[70]
Erythro-leukemia cells	HSPCs	miR-486-5p	Sirt1: downregulation	Promotes erythroid differentiation in response to hypoxia	[72, 73]
G-CSF stimulated BM stroma	Stroma ECs HSPCs	miR-126	VCAM-1: downregulation	Down regulation of VCAM1 leads to mobilization of HSPCs out of the niche and into peripheral blood	[61]
Aged mouse BM cells	Young mouse BM stromal cells	miR-183-5p	HMOX1: downregulation	Reduced proliferative ability of stromal cells and decreased osteogenic differentiation	[74]
Mouse embryonic stem cells	HSPCs	Wnt3, Oct4,	SCL: upregulation, HoxB4: upregulation GATA2: upregulation MAPK p24/44: phosphorylation	Expansion of HSPCs and expression of markers associated with early HSC states	[75]
HSPCs	HSCPs	TPO, ANGPTL2, ANGPTL3	Autocrine signaling loop: maintains stemness	VPS33B mediated release of exosomes is required for maturation of secretory growth factors and maintaining cell stemness	[54]

ANGPT1: angiopoietin 1; ANGPTL2/3: angiopoietin-like protein 2/3; BM: bone marrow; G-CSF: granulocyte colony stimulating factor; HMOX: heme-oxygenase molecule 1; HSC: hematopoietic stem cells; HSPCs: hematopoietic stem and progenitor cells; ICAM1: intercellular adhesion molecule 1; IGF1: insulin-like growth factor 1; IL8: interleukin 8; MDS: myelodysplastic syndrome; miR: micro-ribonucleic acid; Mk: megakaryocyte; MSC: mesenchymal stem cell; MMP9: matrix metalloprotease 9; SCF: stem cell factor; TLR4: Toll-like receptor 4; TPO: thrombopoietin; VCAM1: vascular cell adhesion molecule 1; VPS33B: vacuolar protein sorting 33B.

Acute Myelogenous Leukemia

Aside from their role in the cellular crosstalk in the BM under physiological conditions, EV trafficking also plays a distinct role in dysregulating hematopoiesis in Acute Myelogenous Luekemia (AML), as well as other hematological malignancies and extramedullary cancers (**Fig 1.3A-C**; **Table 1.3**) [21, 22, 57]. AML is a genetically heterogeneous disease caused by accrued molecular instability in hematopoietic stem and progenitor cells (HSPCs) that leads to differentiation arrest concomitant with unchecked gains in proliferative capacity [76]. First described in 1845, in a patient that presented with an enlarged spleen and liver; Rudolf Virchow named the disease Leukemia, meaning "white blood" to describe the expansion of white blood cells in the vascular space of the enlarged organs [77]. Leukemia was eventually determined to be a disease of failed hematopoiesis, and is now characterized—as acute or chronic—based on rate of progression, and by the lineage of hematopoietic commitment—as myeloid or lymphoid. Importantly, the malignant leukemic cells, unlike solid tumors, uniquely reside within an expansive microenvironment encompassing the bone marrow, spleen/lymphoid tissue, liver and vasculature. The systemic localization of leukemic cells has greatly complicated the understanding of intrinsic and extrinsic mechanisms of initiation, progression and therapeutic resistance for AML and other leukemias [78-80].

Acute myeloid leukemia is the most common acute leukemia in adults, and second most common in children, with an annual incidence rate of 4.3 per 100,000 persons [81]. Patients typically present with symptoms associated with anemia, shortness of breath, weakness and fatigue, or more severe pancytopenia, with excessive bruising, bleeding and infection due to loss of platelets and functional leukocytes [79]. At diagnosis, peripheral blood analysis reveals normocytic, normochromic anemia, with highly variable leukocyte counts that range from very low (<5000/μl) to excessively high (>100,000/μl). The majority of patients (~95%) have evidence of primitive myeloid cells—colloquially referred to as 'blasts"—in peripheral blood smears that contain high nuclear to cytoplasmic ratios, prominent nucleoli, and often contain improperly fused primary granules (Auer Rods/Bodies) [82]. These blasts often stain positively for myeloperoxidase, the chief

component of primary granules formed early in the development of myeloid-derived cells. Presumptive diagnosis is often made by manual differential of peripheral blood cells, however a definitive diagnosis requires evaluation of bone marrow through aspiration and biopsy typically at the posterior superior iliac crest. Bone marrow is further characterized through morphological analysis, flow cytometric immunophenotyping, and molecular and cytogenetic analysis [82, 83]. The presence of >20% abnormal myeloblasts in the bone marrow or peripheral blood, or the presence of certain characteristic cytogenetic abnormalities with associated hematological dysplasia are both diagnostic for AML [76].

At the molecular levels, the genetic alterations that underline AML vary considerably. AML is associated with numerous characteristic cytogenetic abnormalities, including 15;17 (*PML-retinoic acid receptor*), 8;21 (*RUNX1-RUNX1T1*), and 9;11 (*MLLT3-KMT2A*) chromosome translocations, and inversions or intrachromosomal translocations of Chromosome 16 [84]. Commonly AML is driven by oncogenic mutations in fms-like tyrosine kinase 3 (FLT-3), WNT, MYC, and the RAS family of proteins [84, 85], or disruption of major tumor–suppressor/tumor-suppressor-related genes, such as p53 and NMP1. Together these mutations drive unchecked proliferation in primitive myeloid cells. While mutations in differentiation-related transcription factors such as RUNX1 and CEBPA are often involved in arresting differentiation of primitive cells. These molecular features can be found both individually or in combination, complicating the classification and treatment of AML. Some of these common mutations are associated with response to treatment. Tandem internal duplication of oncogene FLT-3 (FLT-3-IDT) —present in roughly 25% of cases—is considered to have an unfavorable prognosis [82, 86], while NMP1 mutations—occurring in roughly 30% of cases—is favorable [87].

Currently AML is classified by the World Health Organization system based on morphology, immunophenotype, genetics and associated clinical features into six classifications [81]:

- **AML with recurrent genetic abnormalities**
- **AML with myelodysplasia-related features**
- **Therapy-related AML and MDS**
- **Myeloid sarcoma (extramedullary peripheral mass)**
- **Myeloid proliferations related to down syndrome**
- **AML not otherwise specified (FAB subclassification)**
  - **AML with minimal differentiation (M0)**
  - **AML without maturation (M1)**
  - **AML with maturation (M2)**
  - **Acute myelomonocytic leukemia (M4)**
  - **Acute monoblastic and monocytic leukemia (M5)**
  - **Pure erythroid leukemia (M6)**
  - **Acute megakaryoblastic leukemia (M7)**

The longstanding standard of treatment for AML in adult patients includes an induction phase of 7-days of cytarabine followed by 3-days of an anthracycline (i.e. doxorubicin, danurubacin). This 7+3 combination therapy is now augmented with the addition of hypomethylating agents for patients over the age of 65 or tyrosine kinase inhibitor midostaurin for patients with FLT-3 mutations [88, 89]. Bone marrow cellularity and leukemic burden are reanalyzed 14 days after initiation of treatment to assess response to chemotherapy and determine if additional induction and dose-escalation is necessary. Complete remission is commonly achieved following induction phase in 60-80% of patients, however that majority of these patients will quickly relapse without post-induction maintenance therapy and/or hematopoietic cell transplant (HCT) [88, 90]. Despite these efforts, the overall five-year survival has remained low—around 25%—as the majority of patients' experience relapse and develop refractory disease [91].

Murine models of AML

The use of cytarabine for the treatment of leukemia was initially tested in an early mouse model by engrafting a transformed cell line (L12110) that was isolated from DBA/2 mice following exposure to potent carcinogen 3-methylcholantrene. These transformed cells were capable of inducing secondary leukemias following transplant and were used to test efficacy of chemotherapeutic agents throughout the 1960s [11, 92, 93]. Like many spontaneous, chemical-, or radiation-induced murine leukemia cells, the disease tended to by lymphoid in nature and did not adequately phenocopy AML. Unlike humans, mice peripheral blood mononuclear cells are lymphoid predominant, and typically present with lymphoid-derived cancer with distinct phenotypes from human myeloid leukemias [11].

Numerous transgenic approaches have been used to induce myeloid-derived leukemias in mice, and study the genetic basis of malignant transformation. Most well-known are conventional PML-RARA models used to identify the driving mutation in Acute Promyelocytic Leukemia (APL) and to develop targeted all-*trans*-retinoic acid (ATRA) target therapy [11, 94]. Likewise, knock in or conditional expression models incorporating Tet or Cre-inducible fusion genes within the MLL locus also demonstrated strong initiation of AML. Fusion within the MLL locus are found in 70% of childhood AML and 10 % of adult. One of the more common fusion partners is AF9 through t(9;11)(p22;q23) translocation. The resulting fusion gene is able to initiate AML without secondary mutations in both constitutive knock in and inducible models [11, 95, 96]. In these models the extent of disease severity was dependent on the cellular target expressing the transgene. MLL-AF9 expression was able to initiate a more severe disease in HSCs (KSL), with milder phenotypes resulting from targeting committed progenitors such as CMP or GMPs, with expectantly reduced proliferative capacity [11, 96]. Conversely, recapitulating the common RUNX1-ETO fusion found in 20-30% of patients through translocation t(8;21)(q21;q22), provoked abnormal hematopoiesis but failed to initiate AML without addition of mutagenic agents. Similarly inducing conditional NPM1 mutations or FLT3 internal tandem duplication common to AML were not sufficient to induce AML, and required additional oncogenic-driver mutations to precipitate overt transformation [11].

Collectively, transgenic models were critical to mapping genetic associations involved in AML development. However, despite major successes in developing models to study genetic initiation, many of these models still fail to phenocopy human disease, perhaps due to genetic/epigenetic differences in associated regulatory elements, lack of clonal evolution, or fundamental difference between human and murine hematopoiesis. Furthermore, many of these models depend on long latency periods, and function independent of non-cell autonomous microenvironmental factors that may prime the bone marrow for leukemic transformation and chemotherapeutic resistance, creating limitations to modeling therapeutic response.

Due to the highly heterogeneous nature of the genetic/epigenetic aberrations that underlie AML, an experimental system studying patient-derived leukemic blasts was essential to understanding sub-type specific differences and test drug response within the native context of the bone marrow [97]. Patient-derived blasts span from technically challenging to impossible to maintain and expand in *ex vivo* culture, as AML blasts are often reliant on the cell-extrinsic and contact-dependent signaling of the bone marrow to proliferate. In attempt to provide surrogate microenvironmental conditions required for cell maintenance, patient-derived blasts were transplanted into immunocompromised athymic mice [11, 97]. Unfortunately, engraftment remained poor due to the presence of a functional B and NK cells. This was overcome by developing more severely immune deficient mouse models by breeding Non-Obese Diabetic (NOD) mice bearing mutations in genes necessary for IL-2 production (involved in lymphocyte development and activation), with Severe Combined Immunodeficiency Disease (SCID) mice that have dysfunctional V-D-J recombination (critical to developing T and B cell receptor repertoires) due to mutations in the protein DNA-activated catalytic peptide gene (Prkdc) [98]. Engraftment was further improved by introducing a null mutation of the IL-2 receptor gamma chain (IL-2r). The resulting NOD-SCID--IL2rγ^{null} (NSG) background has allowed for reliable maintenance and expansion of patient-derived blasts, and has been a powerful platform to test drug response [11, 97].

Despite major success in maintaining patient-specific leukemias in xenograft models, it is increasingly understood that the immune system plays a critical role in AML prognosis. Lymphocytes are involved in cytotoxic elimination of tumor cells, and their function is critical to enhancing chemotherapeutic response in AML [99]. Therefore, xenografts models are of limited use for studying the fate and function of immune cells in the context of leukemia and how they contribute to remission. To study leukemia in the context of a functional immune system, multiple syngeneic models were established to study the immune landscape and immune-based therapies in AML. One of the oldest is the TIB-49 (C1498) model, which is an aggressive myeloid-like leukemia that spontaneously arose in a C57BL/6 mouse [100, 101]. Blasts from this animal were established into a cell line that does not require specialized culture conditions and can be engrafted into wild-type C57BL/6 mice without irradiation or drug-induced immune suppression. Additionally, transgenic animals are also useful for modeling the immune landscape in AML. One such model was developed by crossing FLT3-ITD/Tet2 floxed C57BL/6 mice with CRE recombinase expressing mice under the myeloid LysM promoter, which targets the loss of Tet2 to the myeloid lineage, leaving lymphoid cells functionally intact [102]. Despite the restriction of available genotypes, and lack genetic/epigenetic complexity and microenvironmental dysregulation that underlies human AML, syngenetic leukemia models have proven to be instrumental to studying the role of the immune system in AML. Due to the heterogeneous nature of AML and complexity of the bone marrow microenvironment, no murine model fully replicates human disease pathology and phenotypic outcomes, yet murine models have been fundamental to understanding myeloid leukemia, and allowed for the exploration of new therapeutic avenues to improve survival for patients with AML [11].

AML and the bone marrow microenvironment

The dysfunction of the supportive stromal elements of the bone marrow—with clear roles in regulating hematopoiesis—have become an important aspect of leukemogenesis, promoting transformation of HSPCs, and enabling unchecked expansion. For example, studies demonstrated that disrupting Dicer1 and Notch signaling in bone marrow

osteoprogenitors alone, induced hematopoietic dysfunction, producing myelodysplasia and eventual leukemic transformation [10, 103]. Thus, dysregulation of the bone marrow microenvironment remains a constitutive aspect of leukemic initiation and clonal evolution that facilitates disease relapse and chemoresistance. EVs have emerged as key mediators of bone marrow dysregulation; their widespread release effectively alters the stromal compartment, residual HSCs and even immune cells in the leukemic niche.

The complex interplay of AML and the surrounding microenvironment creates a sanctuary that protects occult myeloblasts from therapy, disrupts normal hematopoiesis and primes the bone marrow for eventual relapse and acquisition of resistance-related modifications [104-107]. Clearly, a better understanding of cellular crosstalk within the AML microenvironment is of critical importance to improving survival and quality of life for patients with AML. Research specifically pertaining the role EVs play in dysregulating hematopoiesis, remodeling the bone marrow microenvironment, and promoting relapse and resistance will be investigated *herein*.

EV-mediated dysregulation of the bone marrow in AML

Through previous studies using a xenografted NSG mouse model, The Kurre lab showed that AML blasts release EVs that transfer miRNAs -150 and -155, which target cMyb, a highly expressed transcription factor in progenitor cells resulting in the reduction of HSPC clonogenicity (**Fig 1.3A**). In those studies, the coincident downregulation of the niche retention factor CXCL12 led to HSPCs mobilization from the bone marrow into the peripheral blood (**Fig 1.3B**) [21, 108]. These observations were extended more recently by others showing that AML-EVs not only downregulate the HSC-supporting factors (CXCL12, Stem Cell Factor, and Insulin-like Growth Factor 1), but simultaneously suppress hematopoiesis and osteolineage development by upregulating Dkk1 expression in BM stromal cells (**Fig 1.3B**) [22]. On the other hand, one study showed AML-EVs increase the number of HSPCs by enhancing their survival while retaining their clonogenicity and stemness with no change in the hematopoietic CD34+, CD34+, CD38−, CD90+, and CD117+ phenotypes [109]. Illustrating one of the key challenges in understanding HSPC

regulation by EVs, neither of the two latter studies identified the specific EV component responsible. Our group previously showed that EVs released by steady state or reprogrammed malignant stroma carry cytokines [26, 106, 110]. Because most analyses of secreted cytokines do not separate vesicle-bound and vesicle-free forms, it is entirely possible that some of the known cytokine activities that regulate HSPC in the leukemic niche reflect EV mediated trafficking.

Other hematological disorders impact hematopoiesis indirectly by altering the function of the supportive stroma. Both AML and Myelodysplastic Syndrome (MDS) cells were shown to reduce the hematopoiesis-supportive capacity of MSCs by delivering miR-7977 via EVs. After uptake by MSCs, the EV trafficked miR-7797 suppress the hematopoietic growth factors (Jagged-1, Stem Cell Factor and Angiopoietin-1) by targeting the poly (rC) binding protein 1 (PCBP1) post-transcriptional regulator (**Fig 1.3C**) [111]. MSCs from patients with MDS also were shown to release EVs which traffic miR-10a and miR-15a to CD34+ progenitor cells, causing the transcriptional regulation of MDM2 and P53 genes, altering HSPC viability and clonogenicity [112]. EVs released from chronic myelogenous leukemia (CML) have also been implicated in altering the bone marrow microenvironment by activating epithelial growth factor receptor (EGFR) signaling in stromal cells. CML exosomes were shown to contain amphiregulin, an EGFR activating ligand that leads to the downstream expression of MMP9 and IL-8, giving leukemia cells adhesive and proliferative advantage within the hematopoietic niche [113].

Extramedullary cancers, such as melanoma, also use EVs for the endocrine regulation of BM progenitors. For example, one study showed that melanoma EVs mobilize BM progenitors by targeting the receptor tyrosine kinase, c-MET, in turn upregulating pro-inflammatory molecules at sites of macrophage trafficking to promote their invasion and metastasis in distant organs [114].

Figure 1.3: Current evidence for EV crosstalk in the leukemic microenvironment

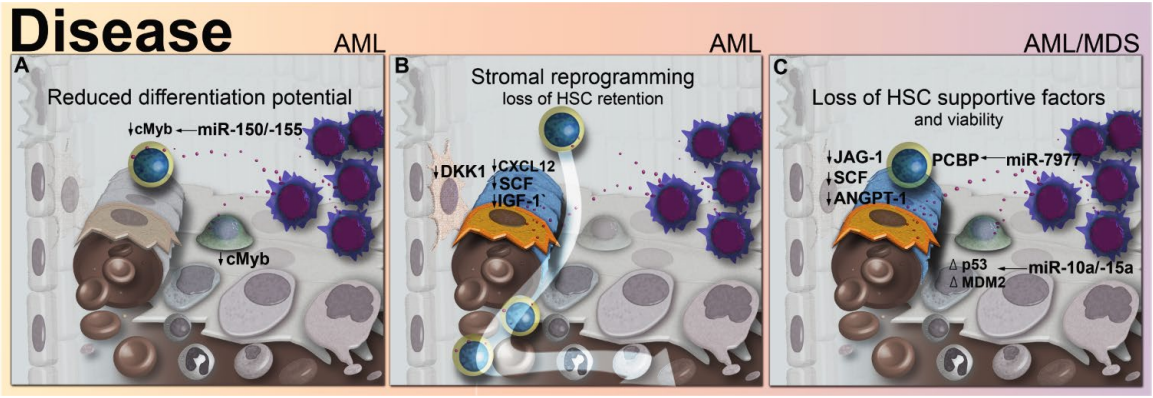

A) EVs from AML blasts traffic miR-155 to HSPCs and down-regulate critical transcription factor, c-MYB, resulting in reduced differentiation potential. **B)** AML-EVs reprogram MSCs and stromal cells, and downregulate niche retention factor CXCL12 and supportive factors SCF and IGF-1 resulting in mobilization of HSPCs from the BM. **C)** AML and MDS EVs promote the loss HSPC supportive factors JAG-1, SCF, ANGPT-1 through the trafficking of miR-7797 to supportive stroma blocking PCBP1, leading to reduced HSPC viability and hematopoietic potential. *AML: acute myelogenous leukemia; ANGPT-1: angiopoietin 1; BM: bone marrow; CXCL12: C-X-C motif chemokine 12; EVs: extracellular vesicles; HSPCs: hematopoietic stem and progenitor cells; IGF-1: insulin-like growth factor 1; MDS: myelodysplastic syndrome; miR: microRNA; MSC: mesenchymal stem cells; PCBP1: poly-rc binding protein 1; SCF: stem cell factor.*

Table 1.3: Pathophysiological regulation of hematopoiesis by EVs

EV origin	Recipient cell	Cargo	Molecular target and effect	Functional event	Ref
AML blasts	HSCPs	miR-150/155	cMYB; downregulation	Suppression of cMYB in HSPC reduces clonogenicity and leads to down regulation of niche retention factor CXCL12 and mobilization of HSPCs to peripheral blood	[21, 108]
AML blasts	BM Stroma		CXCL12: downregulation SCF: downregulation IGF1: downregulation DKK1: upregulation	Down regulation of HSC-supportive factors and suppression of hematopoiesis and osteolineage development by upregulating Dkk1 expression in BM stroma	[22]
AML and MDS cells	MSCs	miR-7977	PCBP1: downregulation Jagged1: downregulation SCF: downregulation ANGPT1: downregulation	Reduced HSC-supportive growth factors and hematopoiesis-supportive capacity of MSCs	[111]
MDS patient MSCs	CD34+ progenitor cells	miR-10a/15a	P53: transcriptional dysregulation MDM2: transcriptional dysregulation	Alteration of HSCPs viability and clonogenicity	[112]
CML cells	BM stroma	Amphiregulin (EGFR-ligand)	EGFR: activation MMP9: upregulation IL8: upregulation	Alteration of BM microenvironment leading to increase attachment and proliferative advantage of CML cells	[113]
Melanoma cells	BM progenitors		c-MET	Mobilization of BM progenitors and upregulation of proinflammatory molecules at sites of macrophage trafficking lead to promotion of invasion and metastasis	[114]

AML: acute myeloid leukemia; ANGPT1: angiopoietin 1; BM: bone marrow; CML: chronic myelogenous leukemia; EGFR: epithelial growth factor receptor; HSC: hematopoietic stem cells; HSPCs: hematopoietic stem and progenitor cells; ICAM1: intercellular adhesion molecule 1; IGF1: insulin-like growth factor 1; IL8: interleukin 8; MDS: myelodysplastic syndrome; miR: micro-ribonucleic acid; MSC: mesenchymal stem cell; MMP9: matrix metalloprotease 9; SCF: stem cell factor; TLR4: Toll-like receptor 4;

EVs and therapeutic resistance in the leukemic microenvironment

For AML, the five-year survival remains low due to the frequency of relapse and acquired therapeutic resistance [84]. Clonal adaptation in response to therapy can occur as a result of intrinsic genetic features, or as an acquired process following selective pressure [115]. However, there are many studies that indicate cell-extrinsic processes function to protect occult blasts from destruction, and are increasingly recognized in driving resistance to therapy. These extrinsic processes include miRNA induced silencing, drug efflux pump expression and upregulation of immune inhibitory ligands that block the function of lymphocytes [116-119]. Increasing reports indicate that EV trafficking promotes the development of resistance to both chemo- and immune therapy in AML, and other cancers. Malignant cells appear to have an inherently higher rate of EV release, and collectively their secretomes contain molecules that promote cancer proliferation, metastasis, and drug resistance [120]. In AML, EV mediated signaling directly transfers chemoresistant properties between individual AML cells (**Fig 1.4A-C**). EVs harvested from a chemoresistant clones of AML were able to upregulate anti-apoptotic protein BCL2 in formerly chemo-sensitive AML, protecting cells from chemotherapy induced apoptosis [107]. Similarly, EVs from multi-drug resistant AML cells were able to promote the expression of drug efflux pump protein MRP-1 (multidrug resistant protein 1), lowering their sensitivity to danorubicin [121]. Furthermore, the transfer of EVs between AML cells and stromal elements have also been described to increase chemoresistance in multiple studies [22, 106, 122].

Figure 1.4: EV mediated transfer of chemoresistance between leukemia cells in the BM microenvironment.

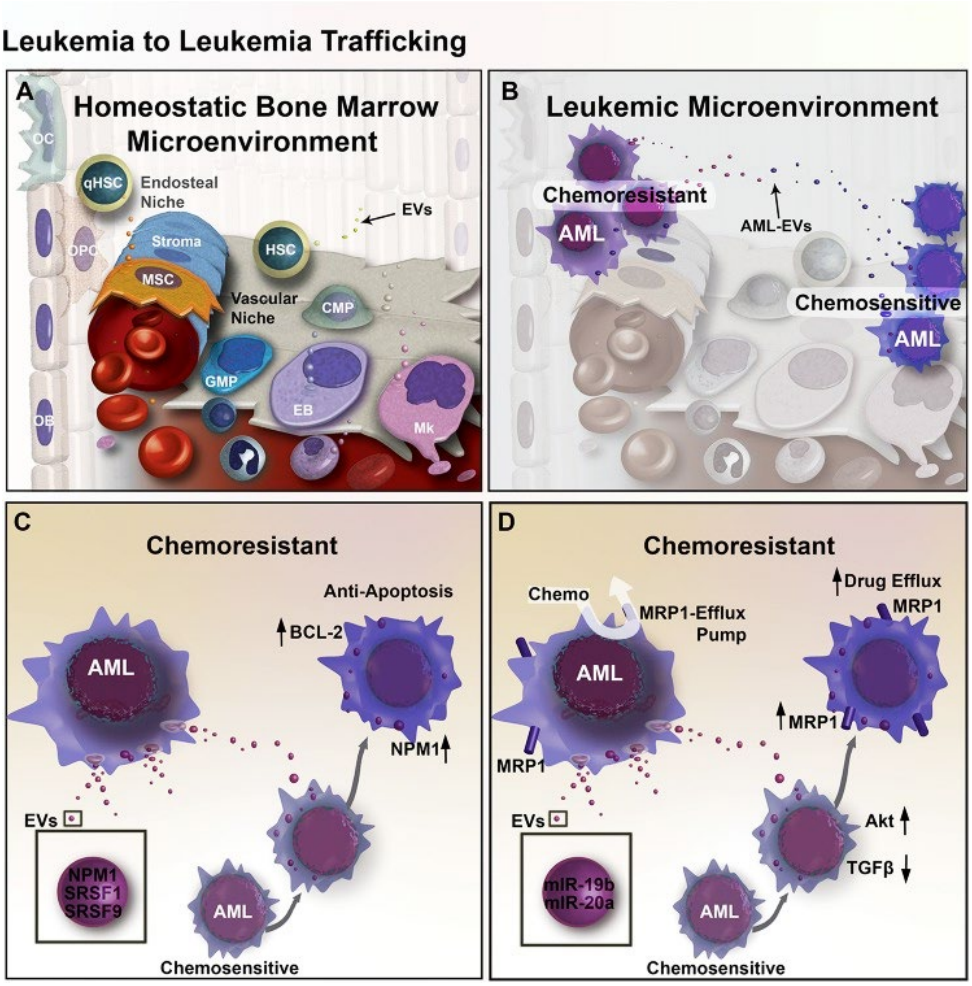

A) Diagram of the BM microenvironment, composed of the hematopoietic niche (right) stromal compartment (left). Hematopoietic Stem and Progenitor Cell (HSPC) give rise to Common Myeloid Progenitors (CMP), Granulo-Monocytic Progenitor Cells (GMP), Erythroblasts (EB), Megakaryocytes (Mk), and many other cell types that populate the cells of the blood. In the stromal compartment, Mesenchymal Stromal Cells (MSC) give rise to Osteoprogenitor Cells (OPC) and Osteoblasts (OB), together these cells function to form bone and regulate hematopoiesis in part through EV-mediated signaling. **B)** Expansion of leukemic cells results in microenvironmental dysregulation. EV trafficking between AML cells transfers regulatory factors that induce resistance to chemotherapy. **C)** Chemo-experienced AML cells shed EVs containing NMP1, SRSF1, and SRSF9, which increase apoptosis resistance through upregulation of BCL-2 and NPM1 in unexperienced recipient AML cells. **D)** EVs from chemo-experienced AML cells also contain miR-19b and−20a, which reduce TGF-β signaling and increase Akt signaling and the expression of MRP1 chemo-efflux pump in recipient AML cells. Figure presented from Nehrbas, Butler *et al.*, 2020 [123]

AML and the cell mediated immune system

A primary role of the cell-mediated immune system is to identify and destroy tumor cells. It is now becoming understood that AML blasts, like other solid tumors, utilize numerous adaptive processes to prevent detection and destruction by cytotoxic T-cells [124-128]. Cytotoxic T-cells (CTL) are fundamental to the elimination of virally infected and neoplastic cells. CTL—from the adaptive arm of the immune system—express CD8 and recognize abnormal autologous cells that present “foreign” proteins on MHC class I molecules. Upon recognition by the T-cell receptor (TCR), CTL release enzymes (perforin and granulysin) capable of permeating the cell membrane and activating the caspase cascade to induce apoptosis in target cells bearing intracellular infections or malignant transformations [129].

CTL also refers to effector CD8+T-cells, which are at the terminal end of a highly regulated developmental process [129]. These cells first develop in the bone marrow as immature lymphocytes, and travel to subcapsular region of the thymus to begin VDJ rearrangement of TCR gene locus. This process is mediated by recombination-activating

genes (RAG1/2) and allows for the creation of vast repertoire of thymocytes (T-cells) with greater than 10^{11} unique TCRs [130]. Following successful recombination, cells begin to express both CD4 and CD8 co-receptors within the TCR complex. These double positive thymocytes move through the thymus to undergo a two phase selection process: First in the thymic cortex, double positive thymocytes expressing TCRs able to bind MHC molecules on cortical epithelial cells are induced to mature, while those that do not die[130]. Maturation results in restriction of co-receptor expression, creating single positive CD4+ cells capable of interacting with MHC class II (Helper or Regulatory T-cells) or CD8+ cells capable of interacting with MHC I (cytotoxic T-cells). Single positive thymocytes (CD4+ or CD8+T-cells) move to the corticomedullary junction where they interact with dendritic cells and macrophages that highly express self-peptides through an autoimmune regulator protein (AIRE)-dependent mechanism. High affinity binding of single positive T-cells to self-antigens results in strong negative selection, thus preventing the production of auto-reactive T-cells. The CD4+ or CD8+ T cells that remain leave the thymus as mature Naïve T-cells [130].

Naive CD8+T-cells circulate through the blood into secondary lymphoid tissue, and can remain in circulation for years [130]. Upon recognition of a dendritic cell displaying both a complementary peptide on MHC I and a secondary signal—co-stimulatory CD80/86 molecule —T cells become “primed”. Following this two-signal stimulus, primed CD8+ T cells proliferate and differentiate into effector and memory T-cells, which enter circulation to surveil peripheral tissues for abnormal tumor cells displaying their complementary peptide. Importantly, primed T-cells require only one signal for activation, expansion and cytotoxic effector function [129, 130].

Both the priming of naive CD8+T-cells and the activation of memory/effector T cells are modulated by the expression of inhibitory or stimulatory signals by antigen presenting or target cells [131, 132]. The expression of inhibitory signals within the immune synapse can inhibit T-cell proliferation, differentiation, and block cytolytic function. The most studied inhibitory pathways include programmed death receptor-1 (PD-1/CD274) and cytotoxic T-lymphocyte-associated protein-4 (CTLA-4/CD152), and are expressed on the

surface of activated effector T-cells as additional "checkpoints" to dampen autoimmunity [131, 132]. However, ligands specific for these pathways are often adaptively upregulated by tumor cells, giving them a selective advantage in tumor formation and progression by suppressing immune responses [133]. Monoclonal antibodies that block checkpoint inhibitor receptors and their ligands are in clinical use and clinical trials to improve immune response in multiple solid tumors, and are beginning to be examined in multiple clinical trials for use in AML [124, 134-136]

For many years leukemias, unlike many solid tumors, were considered non-immunogenic due to comparatively low mutational burdens and the assumption that leukemia cells do not present adequate neo-epitopes for lymphocyte recognition. However, mounting evidence has eroded this false assumption [124, 137]. Immunosurveillance was first demonstrated in the Graft-vs-Leukemic (GVL) effect mediated by HCT [124]. The durable remission sometimes achieved by HCT are now known to be induced by adoptive transfer of functional lymphocytes, chiefly CTL and natural killer cells [119]. This GVL occurs under alloreactive conditions, however autoreactive clearance of AML precursors by patients' own lymphocytes is strongly demonstrated by the high frequency of leukemia development in chronically immunosuppressed individuals following solid organ transplantation [119, 138]. Additionally, AML cells are able to both down regulate MHC class I expression while upregulating inhibitory checkpoint proteins to interfere with the formation of the immune synapse, and reduce T-cell effector function [119, 138]. Furthermore, AML cells can secrete soluble factors like indoleamine 2-3 dioxygenase, arginase, and nitric oxide which also inhibit T-cell activation and proliferation [124].

EVs protect leukemia cells against immune detection and clearance

While several chemoresistance mechanisms in leukemia involve direct delivery of critical molecules via EVs, resistance to elimination can also arise through immune dysregulation (**Fig 1.5A-C**). AML cells release exosomes that contain potent

immunosuppressive proteins, such as programmed death-receptor ligand 1 (PD-L1) [139]. PD-L1 binding to its cognate receptor, programed death-receptor 1 (PD-1), in solid tumors is able to suppress effector T cell activation in response to T cell receptor stimulation [140, 141]. Expression of PD-L1 by tumor cells prevents T cell-mediated immune recognition and clearance, which increases the number of T cells with an "exhausted" and unreactive phenotype. Others have shown in models of both prostate cancer and melanoma that exosome-bound PD-L1 contributes to T cell suppression *in vitro* and *in vivo*. Additionally, exosomal PD-L1 can act as a decoy, sequestering anti-PD-L1 checkpoint inhibitors and outcompeting the anti-PD-1 checkpoint blockade for binding sites on cytotoxic CD8+ T cells [142, 143]. For AML, it remains unknown whether EV-associated PD-L1 is able to suppress cytotoxic T cells, and contribute to immune evasion. Additional research is needed to determine the role EVs play in modulating the immune response in AML. Circulating AML-EVs bearing inhibitory immune ligands may have profound implications for promoting resistance to both adoptive T cell and immune checkpoint inhibitor therapies (**Fig 1.5C**).

Additionally, AML-EVs can reduce the efficacy of adoptive natural killer (NK) cell therapy in AML patients through interaction with adoptively transferred NK-92 cells [110, 139]. Natural Killer cells are a component of the innate immune system, which are not dependent on MHC class I expression. Through the action of multiple receptors, NK cells directly recognize abnormal cells presenting viral associated ligands, tumor related peptides, or surface bound antibodies, and in response release cytolytic granules to induce apoptosis. AML-EVs reduce the efficacy of activated NK by trafficking inhibitory ligands to NK receptors. Incubating NK-92 cells with EVs derived from AML patients resulted in a 40% reduction of NKG2D receptor expression, which is critical to mounting a cytotoxic response against abnormal cells. EV-mediated inhibition of NKG2D reduced cytotoxicity against AML blasts by 37% (**Fig 1.5A**). Exosome delivery of TGF-β to NK-92 cells is believed to be in part responsible for the decrease in NKG2D through TGFβRI/II pathway activation [139].

In CLL, exosomes may lower the bioavailability of rituximab, a common immunomodulatory antibody that targets the CD20 epitope on B-cells. Similar to solid tumor studies that suggest that EVs act as decoys, exosomal binding of anti-CD20 reduces circulating levels of rituximab, protecting lymphocytic leukemia cells from anti-CD20 mediated opsonization **(Fig 1.5B)**. This may explain why a number of CLL patients develop resistance to rituximab treatment [144].

Figure 1.5: EV-mediated resistance to immunotherapy.

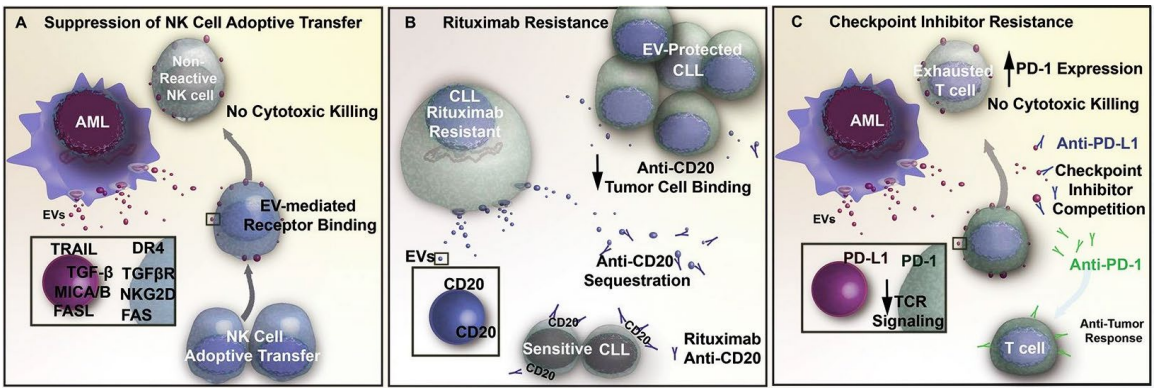

A) AML-EVs contain numerous immunosuppressive ligands (TRAIL, FASL, MICA/B) that reduce natural killer (NK) cell reactivity through receptor mediated binding. This EV-mediated signaling interferes with cell-based therapy, diminishing cytotoxic killing of tumor cells following adoptive transfer of NK cells. **B**) EVs in CLL contain surface CD20, which acts as a decoy by sequestering Rituximab (anti-CD20) and preventing therapeutic antibodies from binding and opsonizing the tumor cells. **C**) AML cells release EVs that contain immunosuppressive ligand PD-L1. The transfer of PD-L1 via EVs reduces T cell activation in response to TCR stimulus. PD-L1 also acts as a decoy that competes with checkpoint inhibitor binding and prevents therapeutic antibodies from reaching their intended target. Figure presented from Nehrbas, Butler *et al.*, 2020 [123]

General Hypotheses

Our long-term goal is to better understand how EVs contribute to AML progression, drug resistance, and relapse, and create new therapeutic options aimed at improving drug response and survival for patients suffering from AML. Over the last two decades EVs emerged as powerful means to package and transport bioactive cargos in a paracrine and endocrine fashion. These membrane-derived vesicles have the potential to simultaneously traffic a multitude of regulatory molecules in concentrations not achievable by secreting

soluble factors alone. Packing into membranes also enhances stability of regulatory cargo and facilitates transfer to specific-recipient cells using specialized cell adhesion and/or receptor ligand interactions. In AML, EVs are broadcast within the tumor microenvironment, but they also enter the systemic circulation, where they likely influence the function of extramedullary tissues. AML, unlike solid tumors, exists largely within the vascular spaces. As a result, these liquid tumors likely have an inherently greater capacity to increase circulating EV concentrations, and systemically dysregulate sites of hematopoiesis, and lymphoid tissues to facilitate disease progression and resistance to therapy. Determining the underlying mechanisms, and directional transfer of EV-mediated signaling is imperative to realizing new therapeutic options to improve survival and quality of life for patients with AML. To elucidate the fate and function of AML-EVs, we propose the *following* aims, which focus on EV-mediated dysregulation of the bone marrow stroma, hematopoietic stem cells, and cytotoxic T lymphocytes.

Specific Aims

1. Define the role of EV trafficking in altering the bone marrow stroma

In AML, the bone marrow transforms into a self-reinforcing microenvironment that protects leukemia cells from elimination. The cellular composition of a hematopoiesis-supporting stromal compartment is found to be drastically altered in AML. However, the underlying biology of these alterations are not well understood. Due to evidence of stromal alterations in murine models bearing low tumor burdens with limited cell to cell contact between the AML and stroma, we hypothesize that AML-EVs transfer regulatory cargo to stromal cells to alter their cellular fate. Here we focus on the interaction of AML-EVs with hematopoiesis supporting mesenchymal stem cells and osteoprogenitors using both in vitro and in vivo models. We found that EVs alone are able to transmit endoplasmic reticulum stress to key stromal elements and activate the unfolded protein response pathway. Activation of the unfolded protein response—a known mechanism of chemoresistance in other cancers—induces apoptosis in osteoprogenitors resulting in their loss from the

stromal compartment.

2. Identify the mechanism underlying the enforcement of quiescence on long-lived HSCs in the AML microenvironment

AML represses normal hematopoiesis to produce lethal anemias and pancytopenias. Paradoxically, progenitor cells are lost from the hematopoietic niche in AML, while long-term HSC—bearing the greatest pluripotent capacity—increase in frequency within the bone marrow. These primitive cells remain in a quiescence state, yet regain repopulation capacity upon transplantation. Due to the reversibility of the phenotype and prior observation of EV accumulation in these cells, we hypothesize that EV trafficking effectively limits LT-HSCs fitness to reduce cellular competition in the leukemic niche. We found that EVs transmit distinct miRNAs that target the mTOR pathway to suppress protein synthesis in LT-HSC. EV exposure results in the retention of residual quiescent cells that demonstrate enhanced repopulation capacity following removal of EV-mediated suppression, but contain lasting DNA damage that may prime HSCs for transformation.

3. Characterize the immunosuppressive effects of AML-EVs on cytotoxic T lymphocytes

Mounting evidence indicates that initiation, progression and relapse of AML occurs while evading destruction by the cell-mediated immune system. Due to the presence of immunosuppressive ligand PD-L1 on AML-EVs, I hypothesized that EVs effectively inhibit T-cell activation in response to T-cell receptor stimulation. I found that AML blasts shed PD-L1 via EVs in an IFNy-dependent manner. Binding of AML-EVs to CD8+T-cells reduces their capacity to express cytokines involved in expansion and effector function, an effect which can be partially rescued using checkpoint inhibitors to block PD-1 engagement on cytotoxic T lymphocytes. The presence of circulating EVs bearing immuno-inhibitory ligands has strong implications for both adoptive T cell and checkpoint inhibitor-based therapies.

4. Generate new methods to improve the study of AML-extracellular vesicles

Understanding the structure, function, and fate of extracellular vesicles is complicated by their nanoscale size, and by their heterogeneous nature. Exosomes and small microvesicles are typically 50-200nm in size, and fall beneath the diffraction limit of standard light microscopy. To date, EVs released from cell and tissues were largely characterized by molecular methods that fail to resolve distinct subpopulations that are differentially enriched for specific surface markers and cargos. Using high resolution imaging and flow cytometry systems, I set out to develop new methods of EV quantification that allow for the detection of EVs on an individual basis. Through these techniques I am able to identify surface markers and resolve differences in the composition of EVs

Chapter 2: Transmissible ER stress reconfigures the AML bone marrow compartment

Compiled from: *Doron B, Abdelhamed S, Butler JT, Hashmi SK, Horton TM, Kurre P. Transmissible ER stress reconfigures the AML bone marrow compartment. Leukemia. 2019 Apr;33(4):918-930. doi: 10.1038/s41375-018-0254-2. Epub 2018 Sep 11. PMID: 30206307*

Abstract

Successive adaptation of the bone marrow (BM) from homeostatic hematopoietic microenvironment to a self-reinforcing niche is an integral aspect of leukemogenesis. Yet, the cellular mechanisms underlying these functional alterations remain to be defined. Here, we found that AML incursion precipitates compartmental endoplasmic reticulum (ER) stress and an unfolded protein response (UPR) in both leukemia and stromal cells. We observed that extracellular vesicles (EV) transmit ER stress in vivo from the AML xenograft to BM stroma, whereby the upregulation of core UPR components drives subsequent osteolineage differentiation of mesenchymal stem cells (MSC). Finally, we show that the underlying mechanism involves quantitative incorporation and cell-cell transfer of Bone Morphogenic Protein 2 (BMP2), a potent osteogenic signal, by AML-EVs. Corroborative studies in AML patient samples support the translational relevance of AML-EVs as a platform for BMP trafficking and source of compartmental crosstalk. Transmissible ER stress was previously identified as a source of chemoresistance in solid tumor models, and this work reveals a role in remodeling the BM niche in AML.

Introduction

Hematopoiesis occurs in operationally defined niches in the bone marrow (BM) and is regulated through reciprocal signaling between hematopoietic and stromal tissue

components [1, 4, 145-148]. Leukemia cells, including Acute Myeloid Leukemia (AML), actively compete with hematopoietic stem cells (HSC) for niche occupancy. The successive tumor growth in turn affects stromal cell function, and results in reduced chemotherapeutic efficacy as well as impaired blood formation [16, 149-151]. These observations do not appear to be AML subtype-specific, and in fact similar defects have been described in murine models of CML [9, 152]. Evidence from several groups indicates that remodeling and secretory conversion of the microenvironment accounts for the role of the BM as a sanctuary site for residual, drug-resistant disease and relapse [104, 153]. This notion is further consistent with observations that AML patient-derived mesenchymal stem cells (MSCs) exhibit an altered secretion of cytokines with reduced hematopoietic support and a more chemoprotective phenotype [154-156]. While inherently translational, snapshot analysis of patient samples at diagnosis limits our ability to model the dynamic crosstalk that reconfigures the BM microenvironment, and risks artifacts due to propagation in tissue culture. Murine xenograft studies have been widely used for the study of leukemia-stroma cell interactions, providing an opportunity for prospective in vivo modeling while benefitting from validated strategies for immunophenotypic isolation of distinct stromal populations for study [9, 145, 149, 157, 158].

To better understand how leukemia induces changes in the composition of the BM compartment, we focused on the two mesenchymal populations central to AML leukemogenesis: MSCs, which maintain the potential to differentiate along adipo-, chondro-, and osteolineages; and Osteoblastic Progenitor Cells (OPCs), a population of osteolineage committed progeny that will mature into osteoblasts [9]. Both populations contribute to hematopoietic homeostasis or, conversely, their functional disruption can lead to myelodysplastic growth and clonal evolution [10]. We were particularly interested in understanding the reciprocal crosstalk in the AML niche that would spur osteogenic differentiation bias, previously implicated during AML expansion [9, 152, 159, 160], and known to alter the release of soluble factors that regulate growth and niche adhesion [161].

The studies herein identify significant compositional changes in the niche of AML xenograft animals associated with osteogenic MSC differentiation. We show that the

underlying mechanism relies on transmissible ER stress (TERS) [162, 163], and identify AML derived extracellular vesicles (EVs) as a contributory factor in promoting the unfolded protein response (UPR) in stromal cells, a known stimulus for altering secretion and inducing osteogenic MSC differentiation [164-166]. We show that EVs accomplish these changes by trafficking BMP2, a known regulator of osteogenesis and inflammation.

Results

AML remodels the bone marrow

To examine BM niche composition and function *in vivo* we used NOD-scid IL2Rγ null (NSG) xenografts [149-151] with tail-vein grafting, but without conditioning irradiation to ascertain undisturbed BM niche function [21, 108]. To avoid expansion artifacts during *in vitro* cell culture of MSCs and OPCs, we isolated endosteal MSC and OPC populations directly from mice using fluorescence activated cell sorting (FACS) [5] (**Fig2.1A**). Specifically, we excluded hematopoietic and endothelial cells (CD45 and TER119, and CD31, respectively) to sort two immunophenotypically distinct mesenchymal populations: SCA-1+/CD51+ MSCs and SCA-1-/CD51+ OPCs [9, 167] (**Fig 2.1B**). We analyzed cells sorted from long bones for morphological differences, clonogenic growth, and extracted RNA to transcriptionally validate differential expression of genes characteristically expressed in either population (**Fig 2.1C**). With this strategy in place, we generated several xenograft cohorts via intravenous, tail-vein injection of three human AML cell lines: Molm-14, U937, and HL-60. Chimerism was tracked by the percentage of human CD45+ cells over time in the peripheral blood and at time of harvest in the bone marrow. We included xenografts with a marrow chimerism > 60% in this study to simulate niche remodeling effects during advanced disease, reflective of AML patients at diagnosis [168]. Functionally, we observed reduced fibroblastic colony forming (CFU-F) potential in both MSCs and OPCs from all three AML xenograft cohorts (**Fig 2.1D**). Strikingly, we also observed a significant shift in the proportion of the two populations (Figure 1e), with increased MSC/OPC ratios, signifying a compositional change within the BM niche.

Figure 2.1: AML negatively impacts the endosteal niche.

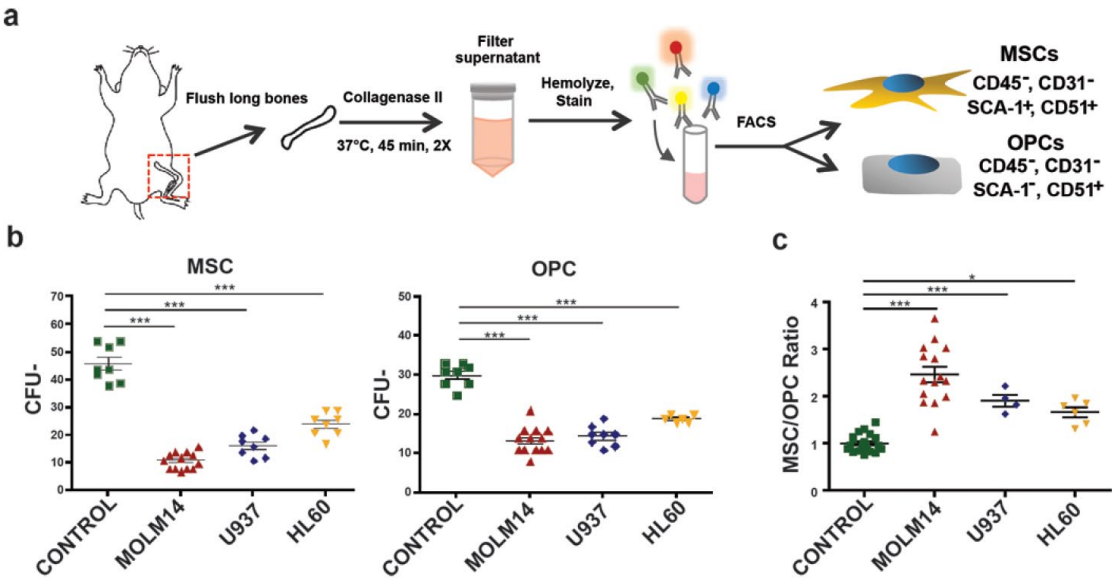

AML negatively impacts the endosteal niche. **A)** MSC and OPC harvest workflow. Long bones from control and xenografted mice are removed, flushed, crushed, and incubated in Collagenase II. Disadhered cells are then filtered, stained with antibodies, and sorted via FACS. **B)** CFU-F assay of MSCs and OPCs derived control and AML xenografted animals. Error bars are standard error of the mean ($n = 8, 13, 8, 8$ animals per condition). **C)** The ratio of MSCs/OPCs in control and AML xenograft animals. Error bars are standard error of the mean ($n = 22, 14, 4, 6$ animals per condition). Significance in **b** and **c** was determined using ANOVA and Bonferroni correction. *$p < 0.05$, ***$p < 0.001$.

MSCs and OPCs exhibit differential fates in the AML bone marrow

As Osterix-expressing progenitor cells have been previously shown to be sensitive to AML-induced apoptosis [158, 169], we hypothesized that the altered ratio of MSCs over OPCs may be due to increased apoptotic turnover of OPCs. Indeed, isolated OPCs exhibited increased apoptosis within xenografts as measured by increases in Annexin V positivity and Ser-15 phosphorylated p53, but not overall p53 (**Fig 2.2A**). These OPC differences were significant in Molm-14 and U937 xenografts, and did not reach statistical significance for HL-60 xenografts. Xenograft- derived MSCs on the other hand did not show evidence of apoptosis or p53 engagement under these conditions (**Fig 2.2B**). Rather,

we observed significant induction of osteolineage differentiation in MSCs from AML xenografts. Specifically, MSCs in all three xenograft models showed increased expression of Runx2, Osterix, and Dkk3, whereas markers of late osteoblastic development, Col1α1 and Spp1, were significantly reduced when compared to MSCs from control animals (**Fig 2.2C**). This was further consistent with increased in vitro osteogenic- and reduced adipolineage differentiation of Molm-14 xenograft-derived MSCs, using Alizarin Red S (binds to calcium) and Oil Red O (lipophilic) stains, respectively (not shown). Together, the data suggest that leukemia cells provide extrinsic cues that promote osteogenic MSC differentiation and increased apoptosis in OPCs, resulting in aggregate changes in the overall composition of the BM compartment in vivo.

Figure 2.2: MSCs and OPCs exhibit differential fates in the leukemic bone marrow.

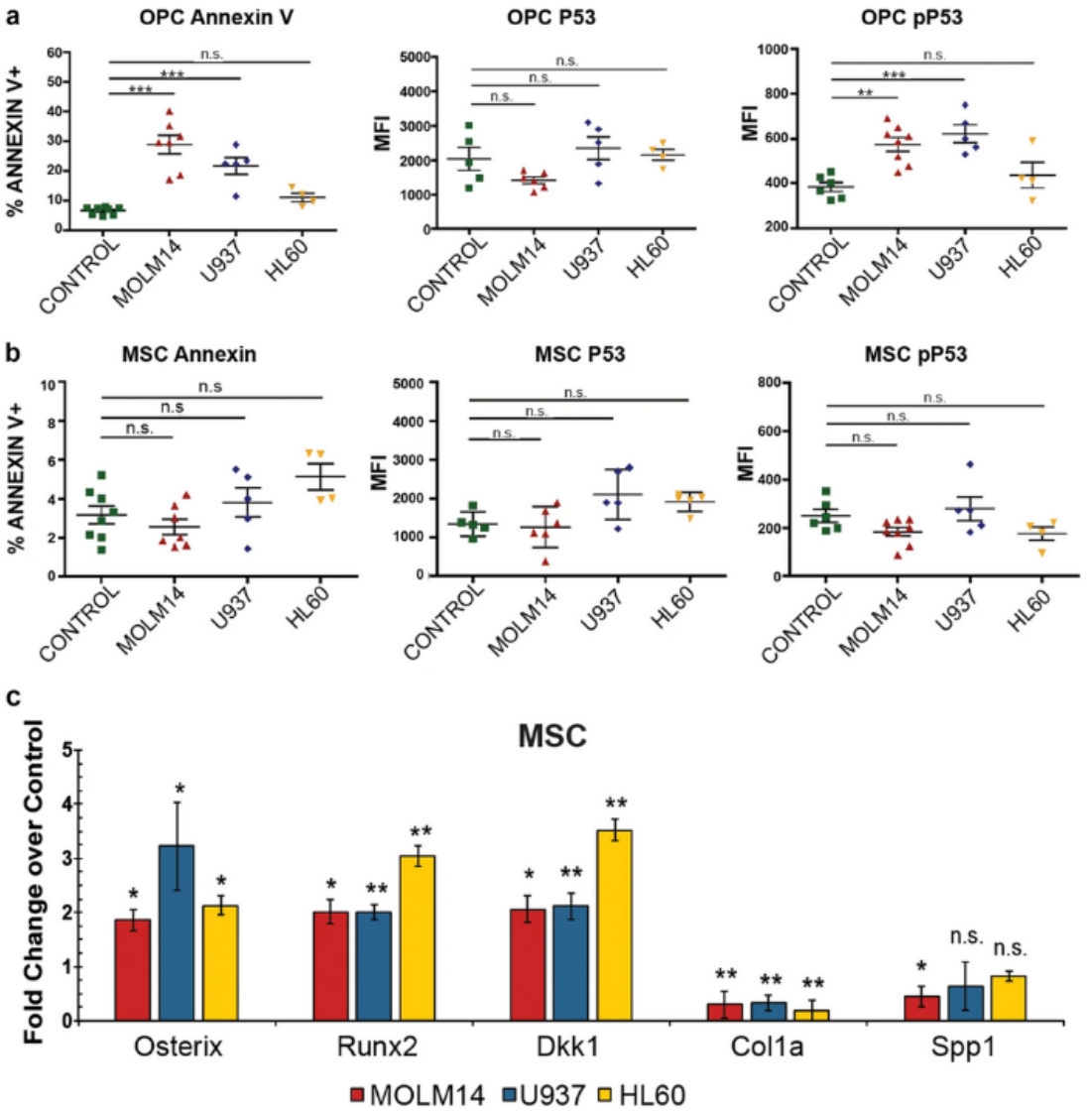

MSCs and OPCs exhibit differential fates in the leukemic bone marrow. **A-B**) Analysis of apoptosis in stromal populations. The percentage of Annexin V^+ cells, and the MFI of P53 and Ser-15 phosphorylated P53 in control and xenografted animals within OPC (**A**) and MSC (**B**) gates. Error bars are standard error of the mean from ($n = 8, 7, 5, 4$) animals for Annexin V dataset and ($n = 5, 6, 5, 4$) for the pP53 and P53 experiments. Significance in **A** and **B** was determined using ANOVA and Bonferroni correction. $^{**}p < 0.01$, $^{***}p < 0.001$. **C)** Expression analysis of genes involved in early and late osteogenesis of xenograft-derived MSCs compared to control MSCs. Fold change determined by $2^{-\Delta\Delta Ct}$ in pairwise analysis against control MSCs. Error bars are standard error of the mean from four animals per condition. Significance was determined by ANOVA and Student's *t*-test. $^{*}p < 0.05$, $^{**}p < 0.01$, $^{***}p < 0.001$

Stromal UPR induction in AML xenografts

Both the increasing translational burden within the ER during osteogenic differentiation [170] and reports of the XBP1 dependent upregulation of Osterix, a master regulator of osteogenesis [164], led us to consider the involvement of the UPR in inducing AML-mediated MSC differentiation. We therefore assembled a RT-PCR survey panel to screen for UPR induction, observing broad engagement in xenograft-derived MSC and OPC populations compared to those from control mice (**Fig 2.3A-B**). With Molm-14 xenografts, both populations exhibited 2-30 -fold upregulation of Grp78, a core regulatory component of the UPR and spliced Xpb1, a chaperone inducer. There were more subtle increases in the unspliced isoform of Xbp1 and upregulation of Chop. Promotion of osteogenesis by the UPR [171] under these ER stress conditions was supported by increased Runx2 and Osterix gene expression after exposure of MSCs to the UPR inducer thapsigargin (**Fig 2.3C**). By contrast, hematopoietic progenitor cells, identified by the expression of c-Kit, Sca-1, and the absence of lineage markers (i.e. KSL) did not exhibit induction of the UPR, suggesting a stroma-restricted response (**Fig 2.3D**). To further implicate the UPR in the increase in apoptosis within the OPC population, we sorted for annexin V+ OPCs and Annexin- populations from both Molm-14 xenografts and controls (**Fig 2.3E**). Specifically, we reasoned that the UPR should preferentially be induced in annexin V+ cells, and indeed we observed significant upregulation of Grp78, Chop, XBP1 and sXBP1 genes in Molm14 xenograft derived annexin V+ cells compared with those from controls (**Fig 2.3F**). Altogether, the data suggest that ER stress in the AML niche contributes to the adaptive changes in BM stromal fate and composition.

Figure 2.3: MSCs and OPCs exhibit increased ER stress.

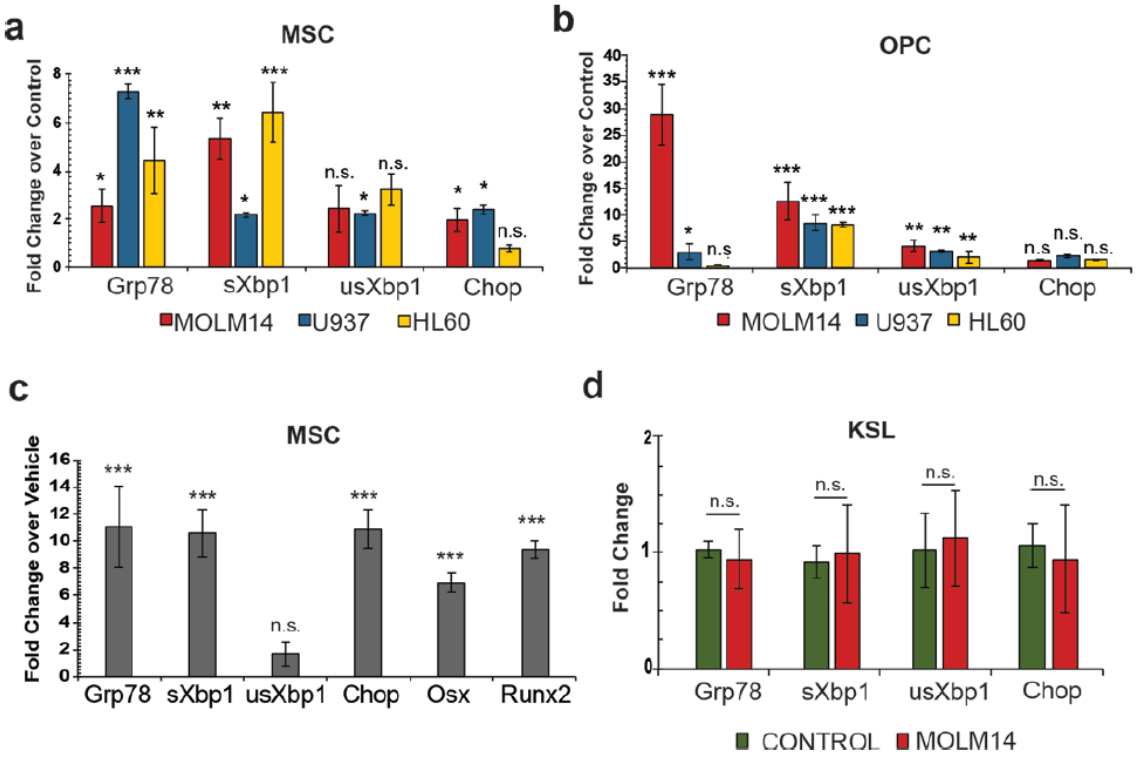

MSCs and OPCs exhibit increased ER stress. **A-B)** Expression analysis of genes involved in the UPR from xenograft-derived MSCs (**A**) and OPCs (**B**). Fold change determined by $2^{-\Delta\Delta Ct}$ in pairwise analysis against control MSC and OPCs, respectively. Error bars are standard error of the mean from four animals per condition. Significance was determined by ANOVA and Student's *t*-test. $*p < 0.05$, $**p < 0.01$, $***p < 0.001$. **C)** Expression analysis of genes involved in the UPR and osteogenesis in MSCs cultured in 1 ng/mL thapsigargin compared to vehicle-treated MSCs. Fold change determined by $2^{-\Delta\Delta Ct}$ against control cells. Error bars are standard error of the mean from three biological replicates. Significance was determined by Student's *t*-test. $***p < 0.001$. **D)** Expression analysis of UPR genes in hematopoietic stem cells (c-KIT$^+$, SCA-1$^+$, lin$^-$; KSL) from Molm-14 xenografts. Fold change determined by $2^{-\Delta\Delta Ct}$ against KSL from control animals. Error bars are standard error of the mean from three animals per condition. Significance was determined by Student's *t*-test. $*p < 0.05$, $**p < 0.01$, $***p < 0.001$

Uptake of AML-derived EV into endosteal cells *in vivo* and *in vitro*

We and others previously demonstrated that AML-derived EVs enter into stromal cells (CD45- / plastic-adherent) *in vitro* [108, 150]. To more specifically visualize MSC and OPC uptake of AML-derived EVs *in vivo* we generated Molm-14 cells stably expressing a myristoylated GFP transgene (Molm-14-mGFP), which functions as a continuously produced lipid membrane label [21]. The Molm-14-mGFP cells release brightly labeled EVs into the extracellular space tissue culture and enable us to detect EV dissemination in the BM and within the peripheral blood for the lifespan of the xenograft animals (**Fig 2.4A**). Here, we used this approach to map the cellular uptake of xenograft-derived EVs *in vivo* and performed live-cell microscopy of FACS-purified MSC and OPC. At animal sacrifice, the sorted cells are transferred to culture dishes and labeled with Hoechst nuclear stain and Cellmask, a lipophilic dye used to mark the cytoplasm. Results reveal that both MSCs and OPCs from Molm-14-mGFPfp xenografts, but not control animals, contained discrete mGFP+ vesicles (**Fig 2.4B**). For quantification of mGFP+ vesicle uptake, we next scored mGFP+ foci in both cell types. The MSCs and OPCs from xenografted animals (day 21 sacrifice) were found to contain GFP+ vesicles in 55% and 34% of cells respectively (**Fig 2.4C**). In both cell types the total number of internalized foci ranged from one to thirty EVs with no difference between mean the number of EVs in MSC vs. OPC (**Fig 2.4D**). We further confirmed vesicle uptake using confocal live-cell microscopy of MSCs and OPCs exposed to Molm-14-mGFP EVs *in vitro* (**Fig 2.4E**). Next, in determining the spatial distribution inside recipient cells, we found that most EVs released *in vivo* from the Molm14 xenograft traffic to the ER in both MSCs and OPCs, as shown by ER Tracker co-staining (**Fig 2.4E-F**). This intracellular localization at the ER is consistent with previous observations of EV fate [55]. Finally, because UPR induction generally leads to an increase in the size of the ER compartment [172, 173], we visualized ER size and morphology of MSCs and OPCs exposed to Molm-14-mGFP-derived EVs in vitro using ER-Tracker [174]. Results confirmed that EV-treated cells display a dilated ER, similar to cells treated with thapsigargin, a known inducer of ER stress and UPR, when qualitatively compared to vehicle-treated cells [173] (**Fig 2.4G**).

Figure 2.4: AML-EVs traffic to the ER of MSCs and OPCs

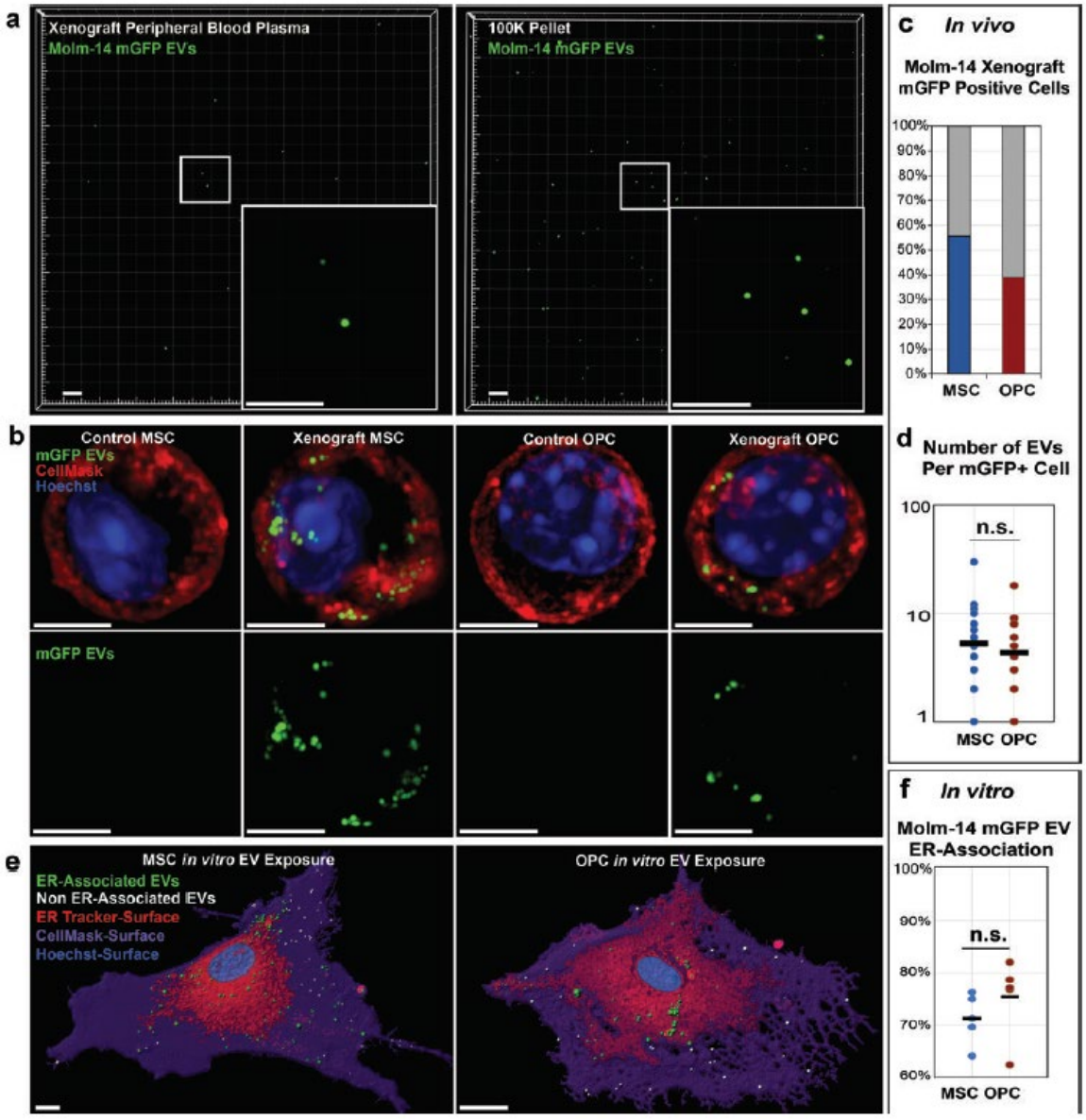

A) Solid capture imaging of mGFP+ EVs from peripheral blood of Molm-14- mGFP xenografts (left) and from in vitro Molm-14-mGfp mGFP cells (right). Scale bars are 5μm. B) Live-cell imaging of MSCs and OPCs derived from control and Molm-14-mGFPfp xenografts. mGFP: green, Cellmask: red, Hoechst: blue. Scale bars are 5μm. C) Quantification of Molm-14-mGFPfp xenograft-derived MSCs and OPCs containing mGFP+ vesicles. 50 cells per cell type analyzed from 2 animals. D) Quantification of mGFP+ vesicles per positive MSC and OPC derived from Molm-14-mGFP xenografts. 50 cells per cell type analyzed from 2 animals, significance determined by Student's t-test *P<.05. E) Representative images of live-cell, confocal microscopy of in vitro expanded MSCs (left) and OPCs (right) exposed to EVs harvested from Molm-14-mGFP cells. Green: ER-localized mGFP+ vesicles, white: cytosol-localized mGFP+ vesicles, red: ER surface, purple: plasma membrane surface, blue: Hoechst. Scale bars = 5μm. F) Quantification of ER-localization of internalized mGFP+ vesicles in in vitro expanded MSCs and OPCs. 5 cells per cell type analyzed, significance determined by student's T-test *P<.05 G) Representative images of live-cell, confocal microscopy of in vitro expanded OPCs exposed to vehicle (left), Molm-14-mGFP-derived EVs (center), or 1.0ng/mL thapsigargin. Red: ER surface, green: mGFP+ EVs, purple: plasma membrane surface, blue: Hoechst.

AML-EVs induce the UPR in MSCs and OPC *in vivo*

The observation that EVs traffic to the ER in MSC and OPC prompted us to systematically test the possibility that EVs transmit ER stress, and may account for UPR activation and altered MSC and OPC fates [29, 45, 175]. To test this hypothesis, we performed intrafemoral injections, delivering dose-matched, purified EVs from *in vitro* cultured healthy human bone marrow-derived CD34+ cells versus either vehicle or Molm-14-mGFP cells (**Fig 2.5A**), an approach we validated previously [21]. Animals were sacrificed 48 hours later, and MSCs and OPCs were sorted directly into RNA extraction buffer for subsequent examination of UPR induction by qRT-PCR. Molm-14-mGFP-derived EVs induced a UPR in OPCs when compared to femurs receiving CD34+ derived EV (**Fig 2.5B**). Furthermore, EVs derived from the CD34+ cell cultures did not promote a UPR in MSC and OPC cells when compared to vehicle-treated femurs, indicating that the observed ER-stress is not a cross-species artifact (**Fig 2.5C**). Consistent with their apoptotic fate, OPCs exhibited a more substantial increase in Grp78 and spliced Xbp1 expression than MSCs when exposed to AML-derived, but not healthy CD34+ cell-derived, EVs (**Fig**

2.5D). For further confirmation of EV-mediated UPR induction we expanded MSCs and OPCs in vitro and again observed a persistent, but more modest increase of the UPR in both cell types 48 hours post EV-exposure, where CD34+-derived EVs had no effect. Recent reports also indicate TERS crosstalk between cancer and bystander cells in pancreatic and breast tumor microenvironments [162, 163]. To test the possibility of TERS from AML cells to stroma, we first measured UPR induction in FACS-purified Molm-14 cells explanted from xenografts at sacrifice and at 48 and 96 hours during subsequent in vitro propagation. Remarkably, when compared against Molm-14 cells grown in vitro, we found sharply increased, but rapidly diminishing transcriptional activity of several key UPR components over time in cell culture (**Fig 2.5E**). Next, we had the opportunity to test blasts enriched from AML patients at diagnosis and compared their UPR status to healthy controls. In a set of 38 AML samples we found that a subset of 8 exhibited a robust UPR, illustrated by the upregulation of GRP78 and phosphorylated eIF2α protein. We had access to available material from five of those patients and confirmed both GRP78 and elevated phosphorylated eIF2α protein levels (**Fig 2.5F**). To better correlate the magnitude of UPR induction in patients with our xenograft results, we also performed an additional transcriptional analysis of GRP78, s/usXBP1, and CHOP expression in these patient samples and found highly significant differences from healthy control bone marrows (**Fig 2.5G**). Similarly, we observe induction of total phospho-IRE1 at the protein level in the U937 leukemia cells, with rapid kinetics that peak at 6 hours, consistent with the subsequent transcriptional upregulation of Grp78. Consistent with the UPR induction in three AML cell lines representing different subtypes in our xenograft studies, UPR activity in AML patient samples did not segregate by AML subtype or cytogenetic lesion. With the availability of peripheral blood plasma from the UPR+ AML patients, we purified plasma-derived EVs by serial ultracentrifugation and performed intrafemoral injections into recipient mice [21], with contralateral vehicle controls and harvested of MSCs and OPCs 48hrs later. Even though modest, and likely suffering from both dilution effects and single dosing, serum EVs from AML patients appeared to induce UPR in bone marrow MSC and OPC, whereas serum-EVs from healthy donors failed to do so. Our experiments suggest that ER stress in the AML niche is transmitted by a leukemia-derived, transmissible, EV-bound factor.

Figure 2.5: AML cells exhibit an UPR *in vivo*.

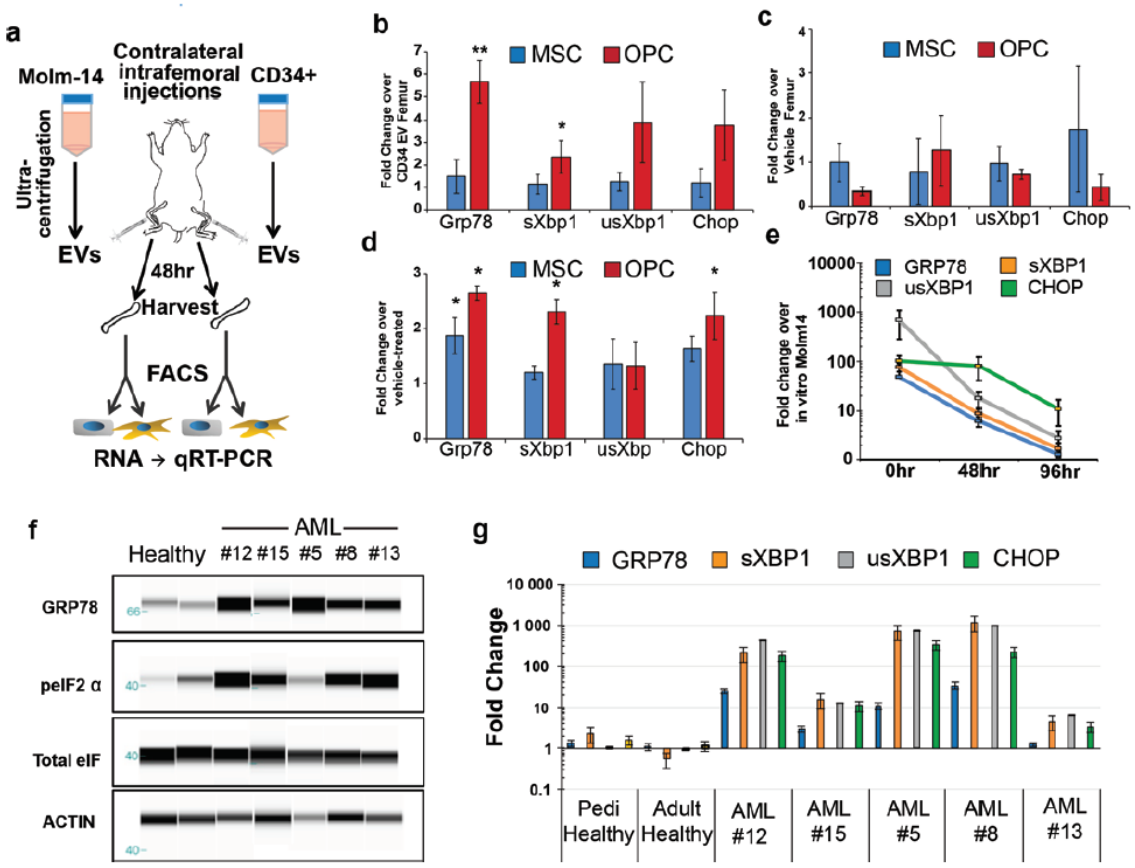

A) Experimental outline for intrafemoral injections. EVs from Molm-14-mGFP cells and healthy CD34+ cells were injected contralaterally into femurs of recipient mice. Femurs were harvested 48hrs later, MSCs and OPCs were sorted into RNA extraction buffer for gene expression analysis. **B)** Expression analysis of UPR genes from MSCs and OPCs from Molm-14-mGFPfp EV injected femurs. Fold change was determined by 2-ΔΔCt against respective cells from CD34+ EV injected femurs. Error bars are standard error of the mean from three animals per condition. **C)** Expression analysis of UPR genes from MSCs and OPCs from CD34+-derived EV injected femurs. Fold change was determined by 2-ΔΔCt against respective cells from vehicle injected femurs. Error bars are standard error of the mean from three animals per condition. **D)** Expression analysis of UPR genes from in vitro cultured MSCs and OPCs exposed to Molm-14-mGFPfp EVs. Fold change determined by 2-ΔΔCt against vehicle-treated cells. Error bars are standard error of the mean from three separate experiments. Significance in **B** and **C** was determined by Student's t-test, *P<.05, **P<.01. D-E) Timecourse of UPR gene expression in explanted Molm-14-mGFPfp. Molm-14-mGFPfp cells were sorted out of xenograft bone marrow based on human CD45 expression and cultured ex vivo. RNA was extracted from cells directly from the sort (0hr) or 48 and 72hrs in normal culture media in vitro. Fold change determined by 2-ΔΔCt against in vitro cultured Molm-14-mGFPfp cells. Error bars are standard error of the mean from three separate experiments. **E-F)** UPR status was determined by protein levels of GRP78, and phosphorylated eIF2α in AML-patient samples and healthy pediatric and adult controls**. F-G)** Expression analysis of UPR genes from blasts from AML patient samples. Fold change determined by 2-ΔΔCt in pairwise analysis against control samples. Error bars are standard error of the mean.

UPR induction enhances EV release and cargo

To further test the observation that AML cells experiencing UPR, transfer ER stress and induce UPR in stromal cells, we harvested and quantified EVs from thapsigargin-treated Molm-14-mGFP cells. Consistent with prior observations [176], we found that Molm-14-mGFP also produce more EVs when experiencing ER stress, without compromise to cell viability or proliferation (**Fig 2.6A**). The dose-matched EVs derived from thapsigargin-treated Molm-14-mGFP in turn strongly induced a UPR in MSCs and OPCs when compared to the cells exposed to dose-matched, vehicle-treated Molm-14-mGFP EVs (**Fig 2.6B**). To understand the EV component responsible for UPR induction

we turned to a recent study of AML patients and murine models that revealed an osteogenic differentiation bias in BM MSCs elicited through BMP signaling [159]. We tested the hypothesis that AML elicits stromal UPR and osteogenic differentiation via BMP cargo trafficked via EV. We observed that ER stress via thapsigargin treatment significantly induced the expression of several BMP family genes in Molm-14 cells (**Fig 2.6C**). In striking similarity to loss of UPR during tissue culture (**Fig 2.5D**), ex vivo analysis of the BMP family gene expression revealed significant upregulation in vivo, and rapid decline during four days propagation in culture (**Fig 2.6D**). This BMP gene set was also upregulated in our patient samples (**Fig 2.6E**). Since AML patients have been previously reported to have elevated circulating BMP2 levels [177], we determined BMP2 levels by ELISA on EVs harvested from Molm-14-mGFP cells and found a significant increase in BMP2 protein associated with EVs obtained from thapsigargin-treated cells compared to vehicle treated cells (**Fig 2.6F**). Intriguingly, there was no detectable change in vesicle free BMP2 (that is, not contained in EVs), suggesting that EV trafficking accounts for increased BMP signaling under these circumstances. Due to the increased EV output of thapsigargin-treated cells, we repeated the BMP2 ELISA following normalization of EV counts, and confirmed that Molm-14-mGFP both increase their EV output, and the amount of BMP2 protein packaged in EVs. Further consistent with a model whereby AML-EV elicit UPR in MSC is the loss of Grp78 response following pharmacological inhibition using a UPR inhibitor (GSK2606414) even as the specific UPR branch requires future clarification. Altogether, these data suggest a model whereby AML blasts utilize the UPR to adapt to metabolic ER stress in the BM niche. In aggregate, we demonstrate that the trafficking of EVs from AML cells to stroma leads to ER stress transmission and promotes the subsequent changes in stromal at least in part through the action of EV-associated BMP2 (**Fig 2.6H**).

Figure 2.6: AML cells alter their EV cargo upon UPR induction.

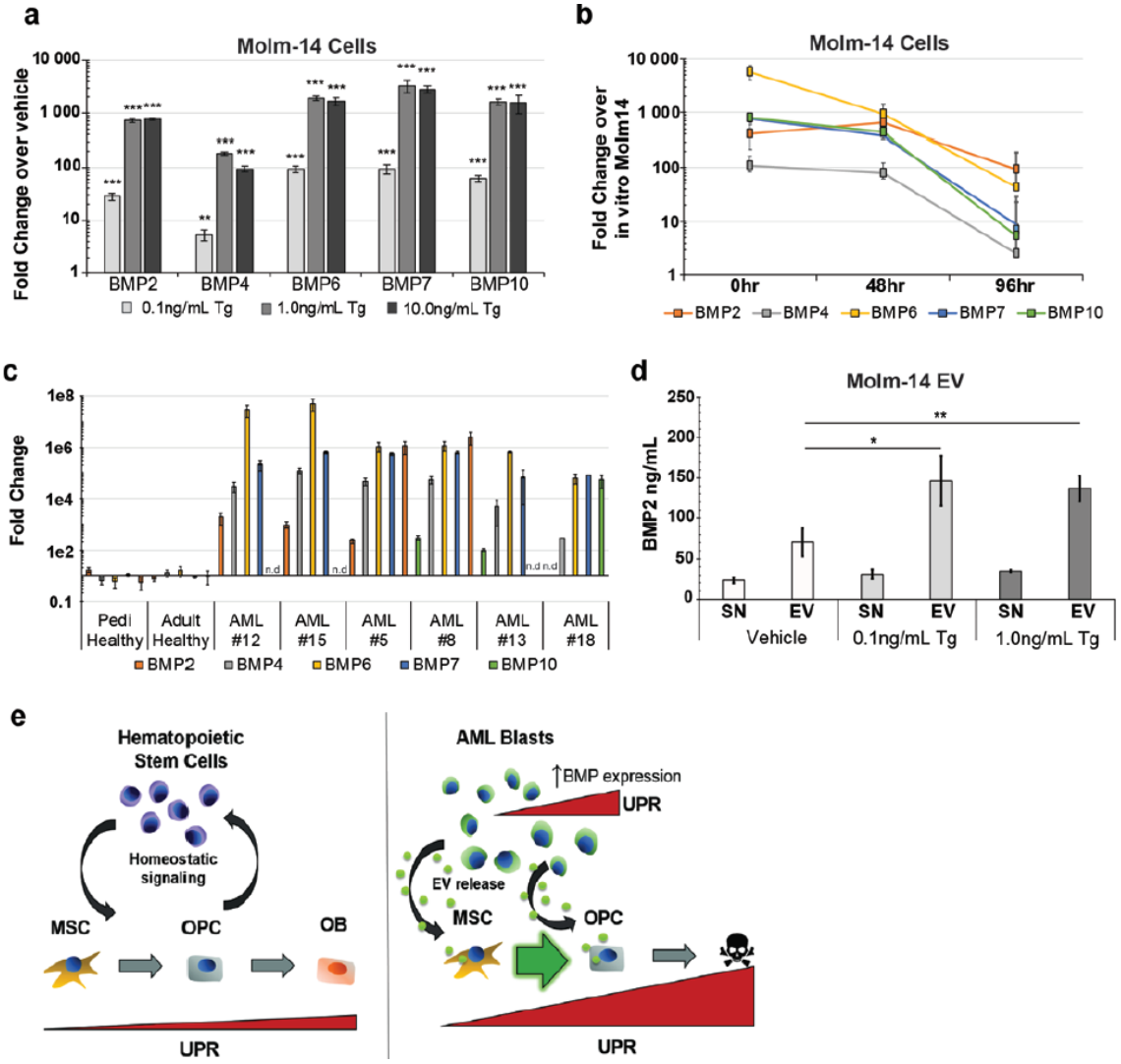

A) Expression analysis of BMP genes in Molm-14-mGFP cells cultured in thapsigargin. Fold change determined by 2−ΔΔCt against vehicle-treated cells. Error bars are standard error of the mean from (n = 4, two separate experiments). Significance was determined using ANOVA and Bonferroni correction. *p < 0.05, **p < 0.01**. B)** Timecourse of BMP gene expression in explanted Molm-14-mGFP. Molm-14-mGFP cells were sorted out of xenograft bone marrow based on human CD45 expression and cultured ex vivo. RNA was extracted from cells directly from the sort (0 h) or 48 and 72 h in normal culture media in vitro. Fold change determined by 2−ΔΔCt against in vitro cultured Molm-14-mGFP cells. Error bars are standard error of the mean from (n = **7**, two separate experiments). **C)** Expression analysis of BMP genes from AML patient samples. Fold change determined by 2−ΔΔCt in pairwise analysis against control samples. Error bars are standard error of the mean. **D)** Concentration of BMP2 protein in the supernatant (SN) and pellet (EV) from EV harvest of Molm-14-mGFP cells cultured in thapsigargin. ELISA was used to determine protein concentration. Error bars are standard error of the mean from three separate experiments. Significance was determined by ANOVA and Student's t-test. *p < 0.05, **p < 0.01. **E)** Model for AML-mediated remodeling of the endosteal niche. Niche homeostasis is maintained by reciprocal crosstalk between stromal and hematopoietic components (left). AML proliferation results in an intrinsic UPR that is transferred to stromal cells in part by increased EV output and BMP2 incorporation into EVs. This signaling axis promotes ER stress in recipient stroma and contribute to the differential fates of MSCs and OPCs (right)

Discussion

While circulating blasts are rapidly eliminated by conventional chemotherapy, at least 40% of AML patients relapse with drug-resistant disease that persists in the BM. The adaptive changes that foster the survival of AML clones in the BM niche not only coincide with disease progression, but may play a causative role in leukemic drug resistance and hematopoietic suppression [104, 178]. Accordingly, the crosstalk between tumor cells and the microenvironment that adapts stroma function represents a critical gap in our understanding of AML leukemogenesis. We and others previously demonstrated the trafficking of AML derived EVs to BM stroma [108, 150, 179, 180], and this work demonstrates EV involvement in the transmission of ER stress, whereby AML cells actively shape the BM composition and alter the MSC phenotype.

To better understand the cell-cell signaling that alters and coopts the BM during AML invasion, we relied on a xenograft model that does not require host irradiation, and we prioritized the direct *ex vivo* analysis of immunophenotypically defined cell populations without tissue culture propagation in an unmanipulated microenvironment. First, we set out to undertake an unbiased survey of stroma composition with emphasis on the two key populations involved in endosteal niche function, where AML preferentially localizes [104, 181]. Using a validated immunophenotyping strategy, we observed a systematic shift in the proportion of MSCs and OPC that proved to be highly reproducible across different AML xenograft cell lines and correlated directly with suppression of clonal fibroblast expansion (CFU-F) and a p53-mediated pro-apoptotic response in OPC. Intriguingly, MSC simultaneously experienced a broad and significant induction of osteogenesis with a reduction in adipogenesis.

The UPR represents a strong stimulus for osteogenic differentiation [165]. Here, we reasoned that MSC differentiation toward a more secretory phenotype might be provoked by ER stress and engage one of three branches of the UPR as an adaptive mechanism to adjust protein folding and secretory load [164, 166, 182]. Others previously showed that AML blasts similarly undergo a UPR to adjust to ER stress [183, 184]. Our observations not only confirm those studies, but demonstrate that AML cells can transfer ER stress to elicit these changes in the BM. The transmission of UPR responses from AML cells to both MSC and OPC is entirely consistent with recent evidence that ER stress can be transferred between cells in a tissue compartment, a known mechanism of drug resistance in pancreatic and breast cancer [162, 163]. Remarkably, some of the key events, namely UPR induction and BMP expression in AML cells rely on conditions encountered in vivo. Tissue culture propagation on the other hand prompted a rapid loss in expression of central UPR components GRP78, spliced XBP1 and BMP. From a clinical perspective, leukemia cell UPR has already been implicated in resistance to standard-of-care agents such as cytarabine [185]. Along with the microenvironmental signaling promoting the UPR in AML blasts, this may provide a target to ameliorate compartmental resistance. Furthermore, the effects of these potential therapeutics on the composition and function of stromal cells

should also be considered, as they could potentially reduce or exacerbate microenvironmental remodeling.

We previously showed that AML cells produce EVs that enter bystander cells in the AML niche and deliver protein and RNA regulatory cargo [21, 150]. While often viewed as effectors of broad phenotypic changes, EV trafficking can be a narrowly specific signaling paradigm, as in the case of suppressed colony formation via EV miRNA targeting of the c-Myb transcription factor that is highly expressed in hematopoietic progenitors, but not in HSC, MSC or OPC [21]. In other words, EVs are multicomponent signaling devices and the outcomes in target cells differs based on target cell identity. The data certainly do not exclude mechanisms other than BMP trafficking in EV-mediated stromal UPR induction [186], and additional EV cargo likely modulates ER stress responses and subsequent phenotypic changes in BM stroma further. It is tempting to speculate that intracellular localization and cargo deposition at ER membranes [55] may also be involved in the translational suppression via miRNA by ER resident components of the miRNA processing machinery [187, 188].

Among reports of osteogenic differentiation in AML patient-derived MSCs [158, 160, 169], one study directly linked BMP2 release by AML blasts with MSC differentiation and leukemia promotion [159]. Our data now indicate that AML-derived EVs are carriers of BMP2, and elicit a UPR response and osteogenic differentiation in MSC. Whether the UPR results directly from BMP signaling, or as a consequence of osteogenic differentiation, remains unclear [166]. Importantly, just like BMP2 expression and UPR responses, upregulated EV production by AML cells requires specific environmental conditions found *in vivo*. Indeed, we demonstrate significant increases in gene expression of several BMPs other than BMP2 under *in vivo* conditions, and it is conceivable that several BMPs contribute to UPR response. Studies in CML revealed a self-reinforcing BMP loop with autocrine and paracrine BMP2/4 signaling as a source of inflammation and chemoresistance, and our observations leave open the possibility that similar events may operate in the AML niche [189].

Reciprocal signaling in the BM microenvironment contributes to AML pathogenesis, and the successive emergence of a more leukemia-permissive microenvironment can be viewed as a part of leukemogenesis [104, 106, 158, 160, 190-192]. Our patient sample numbers are too small to conclusively comment on AML subtype specific differences, or on disease outcome by UPR status (Supplemental Table 2). However, it is worthwhile to note that BM stroma effects in our studies seemed remarkably similar among different AML subtypes, an observation that echoes studies by others [150]. The intensity of the response however, may fluctuate across AML subtypes, evidenced by the reduced propensity for HL-60 to induce apoptosis in OPCs (Figure 2a). This should provide strong motivation to uncover the durability of the observed changes, determine their impact on drug resistance, and develop adjuvant therapies that increase treatment efficacy without further escalating toxicity.

In aggregate, we demonstrate that AML-EVs contribute to changes in BM stromal composition through ER stress transfer. We believe that these studies tie together several disparate observations in patients and murine models to support a model whereby AML-EV trafficking of BMP2, transmits a stromal UPR and induces osteogenic differentiation of MSC.

Materials and Methods

Mice and xenografts

NOD-scid IL2Rγ null mice were purchased from The Jackson Laboratory (Bar Harbor, ME, USA). Male and female animals 6 to 8 weeks old were used in the experiments. Molm-14 cells (1 × 105 per animal), HL-60 cells (5 × 106 per animal), or U937 (2 × 105 per animal) were engrafted into non-irradiated animals by tail vein injection. No randomization process was used. Chimerism was determined by flow cytometry using a human CD45 antibody. We used a chimerism cutoff of >%60 for use in xenograft experiments. Animals were sacrificed at indicated time points and bone marrow from femurs and tibias was collected from each animal. Husbandry and experimental procedures

were performed in accordance with federal guidelines and protocols approved by the Institutional Animal Care and Use Committee at Oregon Health & Sciences University.

MSC and OPC isolation

Long bones were isolated and marrow plugs flushed as previously described [21]. Bones were then broken into small pieces with surgical scissors and incubated in Collagenase II (Sigma Aldrich) buffer (DMEM, 2% FBS, 1% Penicillin/Streptomycin, 2mg/mL Collagenase II) for one hour at 37°C and 200 RPM. The solution was then filtered through a 70μm filter, and then washed with Hemolytic Buffer. Hemolyzed cells were then filtered into Cell-Strainer tubes (Corning, Corning, NY, USA) and resuspended in FACS Wash (DPBS, 2%FBS), stained with antibodies, and then sorted/analyzed using flow cytometry. In vitro cultured cells were propagated in MSC media (MEMα, 15% FBS, 1X penicillin/streptomycin) at 37°C, 5% CO2, and >95% humidity.

Intrafemoral injections of cell line and serum-derived EVs

Animals were anesthetized using isoflurane (1.5-2.0%) and carefully shaved at the injection site using an electric razor. The shaved area was disinfected and sterilized by alternately scrubbing with 1% betadine and 70% ethanol three times. The injected leg was bent at the knee at a 90˚ angle keeping the femur vertical. The injected femur was accessed by gentle twist, using a 25-gauge needle at the patellar groove into the femoral cavity. The coring needle was carefully removed and a 27-gauge injection needle was inserted into the femoral cavity to slowly inject 50 µl of the sample suspended in PBS.

Statistical analysis

All experiments were replicated at least three times with the exception of the intrafemoral injections of patient-derived plasma, where available material was limiting (Figure 5g). Statistical analyses were performed using the PRISM software for Windows produced by Graphpad Software Inc. (La Jolla, CA, USA). Comparisons between two groups were performed with a two-tailed Student's t-test. One-way analysis of variance

(ANOVA) was utilized when comparing more than two groups. T-tests with Bonferroni correction were used to determine p-values. An N of at least three animals or biological replicates was used in all analyses. Error bars represent ± Standard Error of the Mean. For qRT-PCR analyses, a pairwise comparison of fold change (2ˆ-ΔΔCT) between control and xenograft-derived cells, or between vehicle-treated and EV-treated cells was performed. An N of at least three was used in these analyses. For all experiments, statistical significance was set at *= p-val <0.05, **=p-val <0.01, and ***=p-val <0.001 . No statistical test was used a priori to determine the sample size. No randomization was used to allocate animals to particular groups; age and sex-matched recipients were used for transplantation experiments. The investigators were not blinded to experimental groups during analysis.

Vesicle trafficking transfers ER stress in the leukemic microenvironment: Perspective implications for chemo-resistance

Compiled from: Butler JT, Kurre P. Transmissible ER stress shapes the leukemic microenvironment. Oncotarget. 2019 Jun 25;10(41):4080-4082. doi: 10.18632/oncotarget.27012. PMID: 31289607

Acute Myeloid Leukemia (AML) is a genetically heterogeneous disease that arises from clonal expansion of rare hematopoietic stem cells (HSC) that bear acquired somatic mutations. Specific molecular lesions define key subgroups for risk group stratification and current therapy rapidly induces initial remissions in over 80% of patients, but nearly half relapse[193]. While genetic adaptation contributes to persistence and relapse, evidence is now exceedingly strong that the expanding AML clones effect a series of adaptive, and in part inflammatory, niche changes that protect residual AML cells from elimination by chemotherapy [5]. The development of a self-reinforcing leukemic niche in the BM can be considered a constitutive aspect of leukemogenesis and implies an unmet need to more

fully understand how AML subverts the BM stroma toward chemoresistance. Recent work in several hematologic and non-hematologic cancers has revealed endoplasmic reticulum (ER) stress with induction of an unfolded protein response (UPR) as one mechanism by which compartment wide chemotherapy resistance can arise [194]

ER stress, the unfolded protein response and extracellular vesicles.

ER stress results from protein misfolding in conditions of nutrient or oxygen deprivation, and engages an unfolded protein response (UPR) program to enable chaperone production and protein repair. Under excessive proteotoxic stress, the UPR pathway can also activate cell death via caspases and Bcl family members [195]. These context-dependent outcomes are triggered through the central UPR sensor gene GRP78, and differentially regulated via three downstream branches. The PERK-eIF2α branch halts protein translation, allowing protein repair before resuming protein synthesis. IRE-1/XBP1 and ATF6 branches upregulate protein chaperones through stimulation of nuclear ER stress response elements. Interestingly IRE-1/sXbp-1 axis enhances survival in multiple cancer types, and is detectable in 82% of AML cell lines and 71% of AML patient samples, but not in normal CD34+ myeloid stem cells [184]. Silencing of IRE-1 and other UPR components in AML, multiple myeloma (MM) and chronic lymphocytic leukemia (CLL) mediates apoptotic or anti-tumor effects [196]

The recent discovery of transmissible ER stress (TERS) in the solid tumor microenvironment indicated that tumor cells secrete largely unknown factors that transfer UPR responses to bystander cells (e.g. other tumor or myeloid cells) and generate drug resistance in the process [162]. Our recent study not only confirmed the transmission of ER stress to mesenchymal stromal cells (MSC) and osteoprogenitor cells (OPC) in the AML niche, but revealed that the resulting phenotypic changes in MSC resulted from transfer of AML-derived extracellular vesicles (EVs) (**Fig 2.7A**) [6]. That observation extends prior work from our group and others to show the broad impact of AML-EV in the BM niche (reviewed in [23]).

EV biogenesis is a constitutive cellular process resulting in the release of different vesicle subclasses that traffic between cells and signal through their protein and nucleic acid cargo [106] We observed that following ER-stress induction in AML cells, EV release and EV-associated BMP2 levels increased while free-BMP2 in the supernatant remained unchanged. Intriguingly, both ER stress response and BMP expression rapidly subsided when AML cells were propagated in tissue culture. Additionally, super resolution imaging studies revealed that BMP2 increased within the cells and appeared to colocalize with the membrane- and EV-associated tetraspanin CD63 within intracytoplasmic vesicles, indicative of pre-exosomal multivesicular bodies (**Fig 2.7B**). EVs released from these cells also stained with BMP2 (**Fig2.7C**). Altogether, our data for the first time suggested that AML-EVs rich in bone morphogenic protein (BMP) -2 may serve as a mechanism for UPR transfer.

Figure 2.7: Extracellular vesicles traffic BMP2 in the AML microenvironment

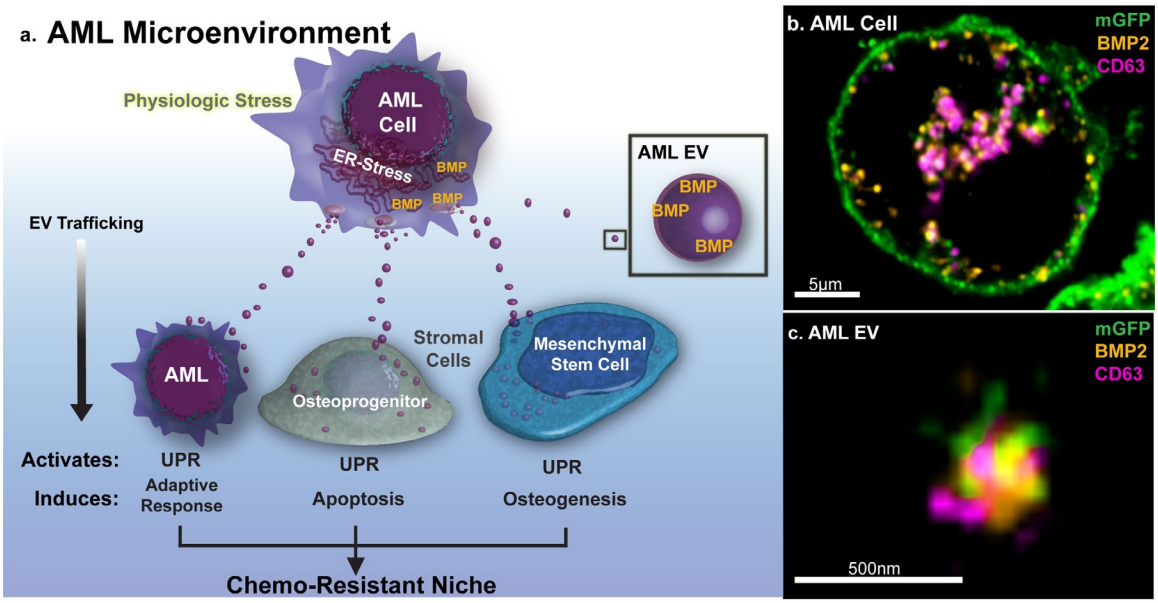

A) Acute Myelogenous Leukemia cells (AML) in the bone marrow microenvironment demonstrate marked ER-stress and high expression of bone morphogenic proteins. Under conditions of ER-stress, AML cells shed copious extracellular vesicles (EVs) that transmit endoplasmic reticulum (ER) stress and bone morphogenic proteins (BMP) to recipient bone marrow cells. This activates the Unfolded Protein Response Pathway (UPR) and leads to adaptive changes among stromal components in the leukemic microenvironment to enforce a chemo-protective niche **B)** BMP (orange) expression is upregulated in AML cells (Molm-14mGFP, modified to express a myristoylated GFP tag), explanted from xenograft animals, and is compartmentalized into intracytoplasmic membranes (mGFP) along with CD63 (magenta) which are indicative of pre-exosomal multivesicular bodies. *Central slice from 3DAiryscan Z-stack, scale bar=5µm.* **C)** EVs isolated from ER-stressed Molm-14 cells co-stain with anti-BMP2 and EV-marker CD63. *Airyscan super resolution technique, scale bar=500nm*

A UPR perspective on compartmental chemotherapy resistance

Published work, including ours, thus suggests a role for ER stress in adapting the leukemic compartment. AML-EVs already serve several known protumorigenic roles in modulating bystander cells, including stromal cells, hematopoietic progenitors, and NK

cells, and contribute to drug resistance in myeloid malignancies, including AML [23, 189]. The notion of BMP as a responsible TERS factor in the AML BM is consistent with its known role in leukemia progression and induction of osteogenic differentiation, respectively [197, 198] Whether EV serve as carriers of UPR inducing protein cargo more broadly awaits independent confirmation, but a link between ER-stress and drug resistance, perhaps via inflammation, is already well supported, even though mechanistic insight into the precise relationship is currently missing. Similarly, whether the UPR signaling pathways activate and sustain chronic inflammation in the AML niche, and the role of EV in reprogramming the microenvironment toward drug resistance remain to be clarified.

The genetic heterogeneity of AML combined with its dynamic clonal succession and adaptive niche remodeling provide a formidable therapeutic challenge [193]. Understanding the sanctuary function of the BM in AML will enable us to develop new adjuvant therapies without further escalating treatment toxicity, and insight into the role of the UPR promises to reveal additional unexplored targets to overcome extrinsic chemoprotection.

Funding

These above studies were funded in part by: Hyundai Hope on Wheels (PK, JTB, TMH), Max Blue Butterfly Campaign (PK), R01-CA164024 (TMH), the St Baldrick's Cancer Research Foundation (PK).

Chapter 3: Extracellular vesicles impose quiescence on residual hematopoietic stem cells in the leukemic niche.

Compiled from: *Abdelhamed, S; Butler, JT; Doron, B, Halse, A, Nemecek, E, Wilmarth, PA, Marks, DL, Chang, BH, Horton, TM and P, Kurre Extracellular vesicles impose quiescence on residual hematopoietic stem cells in the leukemic niche. EMBO Rep. 2019 Jul; 20(7): e47546. doi: 10.15252/embr.201847546 PMC6607014*

Butler JT; Abdelhamed, S; Gao, L; Lim, J; Horton, TM and P Kurre; Leukemic Stress Targets the mTOR Pathway to Suppress Residual HSC in the BM Microenvironment. Blood 2019; 134 (Supplement_1): 3730. doi.org/10.1182/blood-2019-125682 (poster presentation).

Abstract

Progressive remodeling of the bone marrow microenvironment is recognized as an integral aspect of leukemogenesis. Expanding acute myeloid leukemia (AML) clones not only alter stroma composition, but also actively constrain hematopoiesis, representing a significant source of patient morbidity and mortality. Recent studies revealed the surprising resistance of long-term hematopoietic stem cells (LT-HSC) to elimination from the leukemic niche. Here, we examine the fate and function of residual LT-HSC in the BM of murine xenografts with emphasis on the role of AML-derived extracellular vesicles (EV). AML-EV rapidly enter HSC, and their trafficking elicits protein synthesis suppression and LT-HSC quiescence. Mechanistically, AML-EV transfer a panel of miRNA, including miR-1246, that target the mTOR subunit Raptor, causing ribosomal protein S6 hypo-phosphorylation, which in turn impairs protein synthesis in LT-HSC. While HSC functionally recover from quiescence upon transplantation to an AML-naive environment, they maintain relative gains in repopulation capacity. These phenotypic changes are accompanied by DNA double-strand breaks and evidence of a sustained DNA-damage

response. In sum, AML-EV contribute to niche-dependent, reversible quiescence and elicit persisting DNA damage in LT-HSC.

Introduction

Acute myeloid leukemia (AML) is a genetically heterogeneous disease that arises from mutations in hematopoietic stem and progenitor cells (HSPC). The characteristic, and often disproportionate, suppression of native hematopoiesis that develops in the bone marrow (BM) during disease progression and post-treatment relapse accounts for significant morbidity and mortality [80, 83, 193, 199, 200]. Substantial experimental evidence supports the malignant transition of BM function during AML invasion, and its role in disrupting hematopoiesis and sustaining AML [9, 104, 154, 156, 190, 201]. Several prior studies of BM niche-conversion emphasize leukemia-induced alterations in stromal and vascular function [9, 149, 181, 202]. Cell-cell interactions also target the hematopoietic components in the BM, and contribute to the functional suppression and displacement of the hematopoietic progenitors predominantly responsible for steady-state hematopoiesis [3, 21, 149-151, 203].

The fate of residual hematopoietic stem cells (HSC) under leukemic-stress, however, is more elusive. Unlike the depletion of highly-susceptible HSPC, HSC proved to be more resilient during leukemic invasion, and multiple groups reported the relative accumulation of primitive hematopoietic cells in both murine models and xenograft studies [9, 16, 149, 151, 204, 205]. Intriguingly, HSC in the leukemic niche enter quiescence through an unidentified process, yet retain their repopulation capacity upon subsequent re-transplantation [204].

Extracellular vesicles (EV) comprise multiple populations of nano-sized vesicles, which carry protein and nucleic acids, participate in the regulation of BM function [23, 206, 207]. We recently showed that AML-EV, including exosomes, are highly abundant in microRNA (miR)-150 and miR-155, which both target the transcription factor c-Myb to suppress HSPC clonogenicity [21, 105, 106, 108]. Here, we test the hypothesis that EV impact

the fate of residual HSC in the AML niche *via* a distinct mechanism, since HSC function does not rely on c-Myb expression at high levels [208].

Our studies in immunodeficient mice confirm the relative accumulation and quiescence of residual HSC previously observed [150, 151, 204, 205], and reveal that AML-EV suppress protein synthesis in LT-HSC. Mechanistically, AML-EV traffic miR-1246 to LT-HSC to cause the translational suppression of the mTOR subunit Raptor, which in turn facilitates the hypo-phosphorylation of S6RP with ensuing deficits in protein synthesis. Intriguingly, while these changes are resolved upon transfer to a naïve BM niche, we show that AML-EV elicit DNA-damage that persists *in vitro* and *in vivo* through serial progenitor replating and transplantation, respectively.

Results

AML-EV are taken up by hematopoietic cells, including LT-HSC

We previously showed [21, 108, 168, 179] and herein confirmed that AML cells (Molm-14 and U-937) predominantly release nano-sized, lipid bilayer vesicles with a diameter of 50-130nm, as demonstrated by Cryo-TEM imaging (**Fig 3.1A**). To investigate the quantitative uptake of AML-EV in HSC, we relied on a set of AML cell-lines (Molm-14, U-937 and HL-60) that were transduced with a lentiviral vector to constitutively express green fluorescence protein with a myristoyl group (mGFP) (**Fig 3.1B**). The resulting GFP-tag was incorporated into the lipid bilayer of both the cell and the released EV, allowing measurement of uptake *in vivo* and *in vitro,* as previously reported [21]. As modeled in **Fig 3.1C,** we then injected these engineered AML cells into NSG mice for 3-6 weeks to allow the AML cells to reach to 20-40% of the BM. We targeted low levels of chimerism to minimize cell-cell contact driving the AML-HSC crosstalk. GFP^+ EV purified from the peripheral blood plasma of Molm-14 and the U-937-xenografts were visualized by

fluorescence microscopy (**Fig 3.1D**). Live-cell imaging of xenograft-derived KSL and LT-HSC demonstrated the uptake of $mGFP^+$ EV into the intracellular space (**Fig 3.1E**). Next, we measured the kinetics of EV-uptake by exposing KSL and LT-HSC to EV harvested from Molm-14-mGFP or U-937-mGFP cells *in vitro*. By capturing live-cell 3D z-stacks at 0, 30 and 150 minutes, we found that both KSL and LT-HSC bind and internalize numerous $mGFP^+$ EV within 30 minutes of exposure with continued accumulation at 150 minutes (**Fig 3.1F**). We also analyzed KSL from wild-type Molm-14-xenografts to rule out confounding autofluorescence. HSPC harvested from non-transduced Molm-14-xenografts contained no $mGFP^+$ foci and exhibited relative background fluorescence similar to non-xenografted controls (**Fig 3.1G**) confirming that $mGFP^+$ foci were membrane-derived vesicles originating from Molm-14-mGFP and U-937-mGFP cells.

Figure 3.1 *In vivo* and *in vitro* uptake of AML-EV in hematopoietic stem cells

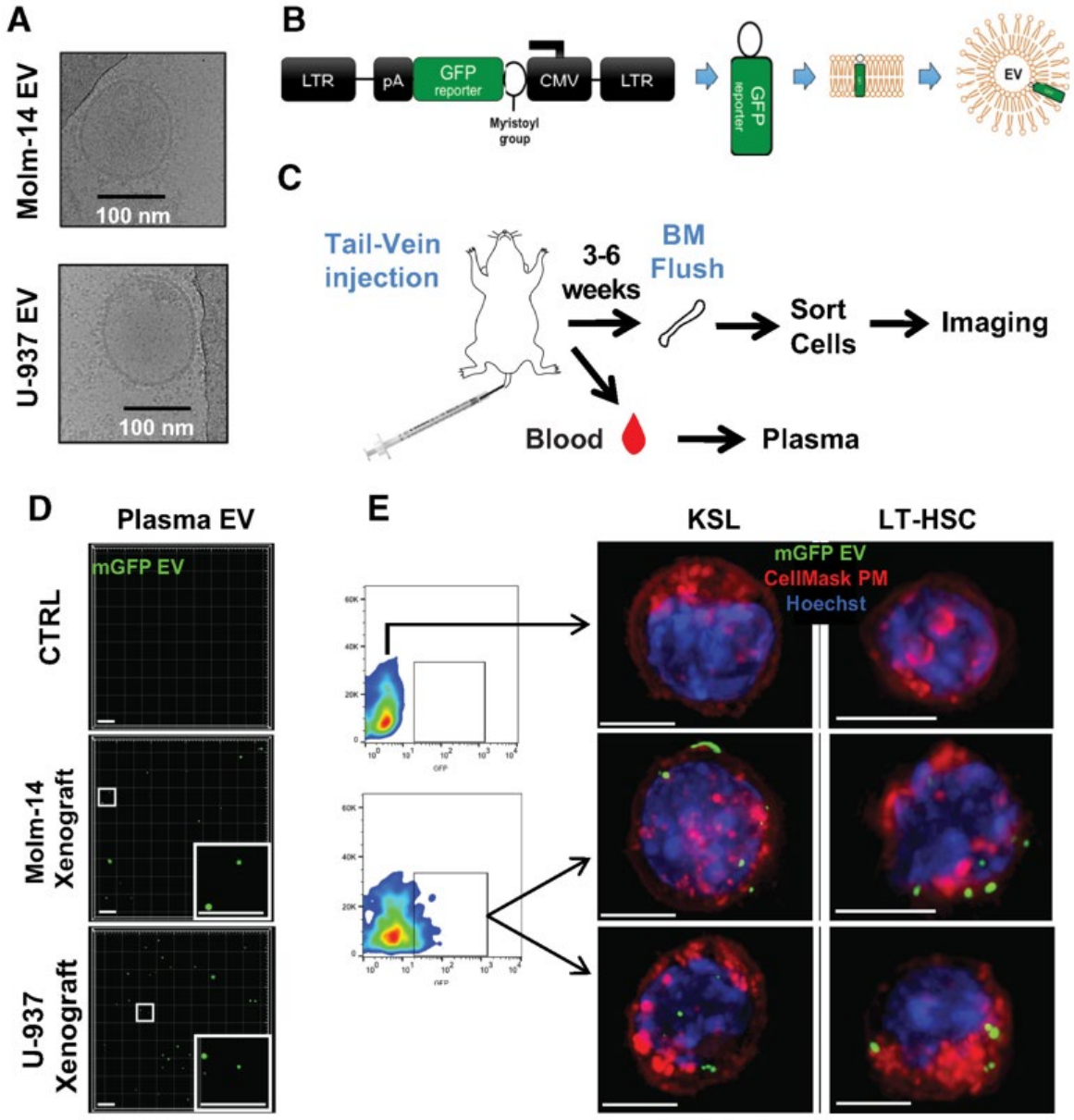

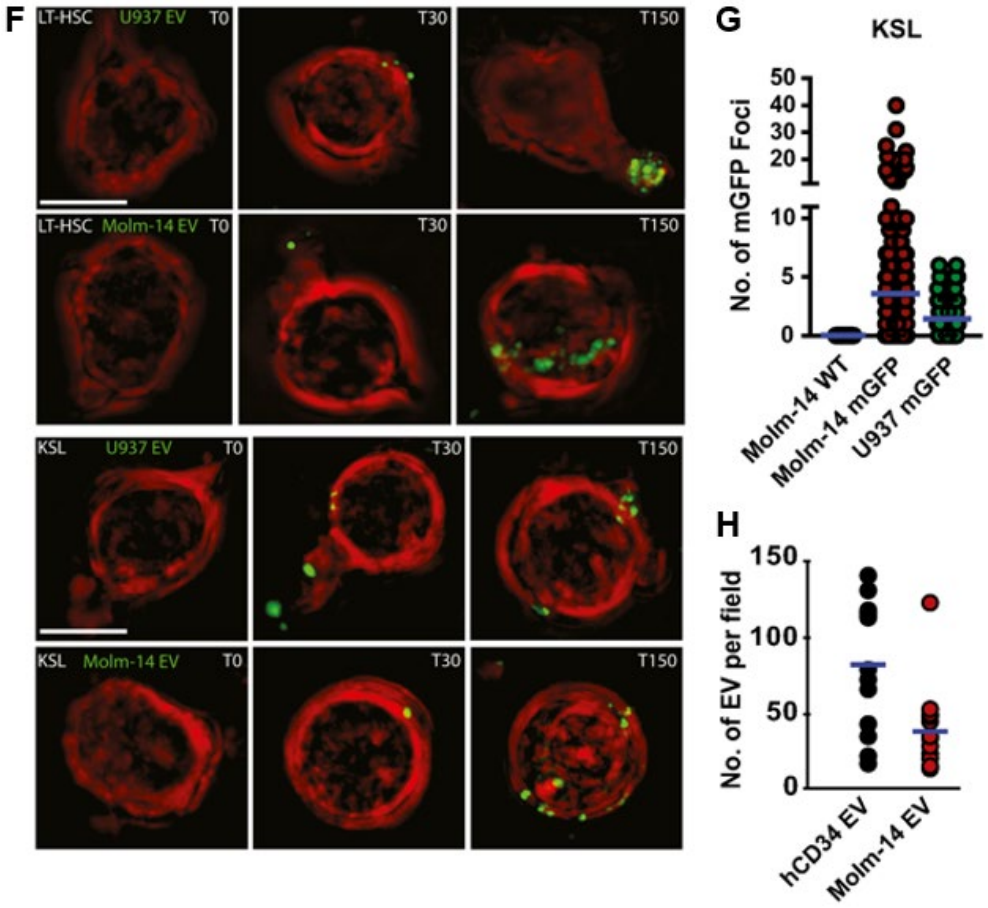

A) Cryo-TEM images demonstrate the lipid bilayer EV purified from Molm-14 and U-937 cells. Scale bars are 100 nm. **B)** A schematic diagram of the myristoylated GFP (mGFP)-expressing lentiviral construct and its incorporation into the cell membrane and EV. Long terminal repeat (LTR), poly-adenylate (pA), cytomegalovirus (CMV). **C)** Schematic diagram of the workflow. Cells were injected via tail-vein injection into NSG mice. After 21 days, bone marrow (BM) cells were flushed to sort GFP+ cells by flow cytometry and perform imaging of sorted HSC. **D)** Peripheral blood (PB) plasma of control animals contains no mGFP+ foci (top); however, Molm-14-mGFP (middle) and U-937-mGFP (bottom) xenografts contain numerous mGFP-labeled EV (green) detectible without vesicle concentration. Scale bars are 5 μm. **E)** Live-cell microscopy of KSL cells (left panel) LT-HSC cells (right panel). Cells were sorted from control mice (top), Molm-14-mGFP (middle), and U-937-mGFP (bottom), stained with Cell Mask (red) and nuclear stain Hoechst (blue), imaged using the GE/API Deltavision (DV) widefield microscope (60× objective) to show the uptake of the GFP+ EV (green). Scale bars are 5 μm.

F) Microscopic images using the CoreDV microscope (60× objective) of live LT-HSC (top rows), or KSL (bottom rows), *in vitro* exposed to EV from Molm-14-mGFP and U-937-mGFP cells for 0, 30, and 150 min. Green: mGFP+ EV, red: plasma membrane surface. Scale bars = 5 µm. **G)** Quantification of mGFP+ EV foci in KSL FACS purified from AML xenografts: wild-type Molm-14 (n = 40), Molm-14-mGFP (n = 247), and U-937-mGFP (n = 107). The background autofluorescence was measured in non-engrafted controls, and this threshold value was then subtracted from xenografted mice. Individual mGFP+ foci were counted in individual KSL from xenografted animals using Imaris software. **H)** Microscopic quantification of EV from hCD34 (3×10^7 cells) or Molm-14 (3×10^7 cells). The purified EV were stained with the lipid dye, FM1-43, imaged using the Yokogawa CSU-W1 spinning disk microscope (100× objective) and quantified using Imaris software.

AML-EV increase the relative frequency of LT-HSC, upregulate P53 and confer quiescence.

To study the effect of AML-EV on residual HSC fate, we relied on the Molm-14-xenograft model complemented with intra-femoral (*IF*) injection of EV from Molm-14, HL-60 and U-937 cell-lines *vs.* EV from expanded healthy donor BM $CD34^+$ cell (hCD34) followed by flow cytometric analysis (**Fig 3.2A**). To ensure a valid comparison of the injected EV, we normalized the numbers of the EV-producing cells (EV from $3x10^7$ cells/femur) and confirmed their EV concentration by microscopic quantification using a lipid dye, FM1-43, finding no significant differences (**Fig 3.1H**).

We first assessed the frequencies of myeloid progenitors LK ($Lineage^-/c\text{-}Kit^+$); the early progenitor/stem pool KSL ($Lin^-/C\text{-}kit^+/Sca\text{-}1^+$); and LT-HSC ($KSL/CD48^-/CD150^+$) (**Fig 3.2A**). While there was no change in KSL frequency or absolute cell number, AML-EV caused a relative reduction of myeloid progenitor LK cells (**Fig 3.2B-C** and **Appx 3.2.1A**). More importantly, we observed a significant increase in LT-HSC frequency and absolute cell number in Molm-14-xenografts and after *IF* injection of Molm-14-EV, but not after control $CD34^+$ EV (**Fig 2B-C** and **Appx 3.2.1A**). In addition to cell line-derived EV, we also tested EV from the plasma of six AML patients (**Table 3.1**). *IF* injection of patient-plasma EV confirmed the observed reduction in LK and a concomitant increase in

LT-HSC (**Fig 3.2C**). Together, the data suggest suppressed progenitor differentiation with proportional accumulation in LT-HSC after exposure to AML-EV.

To further test this hypothesis, we investigated the impact of AML-EV on cell-cycle status in the xenograft model and after direct injection of AML-EV. We found that AML-EV consistently induced quiescence in LT-HSC as shown in the histograms after Hoechst staining (**Fig 3.2D**), as well as the fraction of cells in G_0 cell cycle phase determined by Ki67 staining (**Fig 3.2E)**. AML-EV mediated quiescence was also observed in the bulk KSL population (**Appx 3.2.1B**) and occurred after *IF* injection of AML-EV, but not after injection of EV from healthy hCD34 control cultures. Owing to its crucial role in regulating HSC quiescence [209], we evaluated the P53 activation in residual HSC. We found a significant upregulation of P53 in LT-HSC and KSL from xenografted mice as well as the *IF*-injected mice with EV from AML cells or patient plasma (**Fig 3.2F-G** and **Appx 3.2.1C**). We also observed hyper-phosphorylation of $P53^{Ser15}$ in LT-HSC influenced by AML-EV (**Appx 3.2.1D**). We found a significant hypo-phosphorylation of $MDM2^{ser166}$, a negative regulator of P53, in both KSL and LT-HSC from xenografted mice and after *IF* injection of Molm-14-EV (**Appx 3.2.1E**). In further agreement, we observed transcriptional upregulation of the *Cdkn1a* (p21), a P53-effector, in KSL from Molm-14-xenografts relative to control (**Appx 3.2.1F**). We found no evidence of senescence induction via $P16^{INK4a}$ expression in KSL from Molm-14-xenografts (**Appx 3.2.1F**). Likewise, no evidence of apoptosis was observed in KSL or in LT-HSC from Molm-14-xenografts (**Appx 3.2.1G**). Together, our data thus far demonstrated a proliferative defect in LT-HSC by AML-EV.

Table 3.1: Patient Data

Patient ID	Age at diagnosis (years)	Gender	Treatment	Risk group	Cyto-genetic/ Molecular change	Survival to date (weeks)	Status
1	3	Male	ADE	Low	t(8;21)	221.1	Alive
2	4.8	Female	ADE	High	FLT3-ITD	150	Alive
3	9.9	Male	ADEB	Low	t(11;19)	6.14	Deceased
4	11.1	Male	ADE	Inter-mediate	t(9;11)	182.3	Alive
5	12	Male	ADE	Low	t(6;11)	36.7	Dead
6	15.5	Male	JAK inhibitor (Ruxilitinib)	High	t(19;11)	3.14	Dead

Abbreviations: ADE: cytarabine, daunorubicin, etoposide; JAK: Janus kinase; Inv: inversion; ITD: internal tandem duplication

Figure 3.2: AML-EV increase the relative frequency of LT-HSC, upregulate P53 expression, and confer quiescence

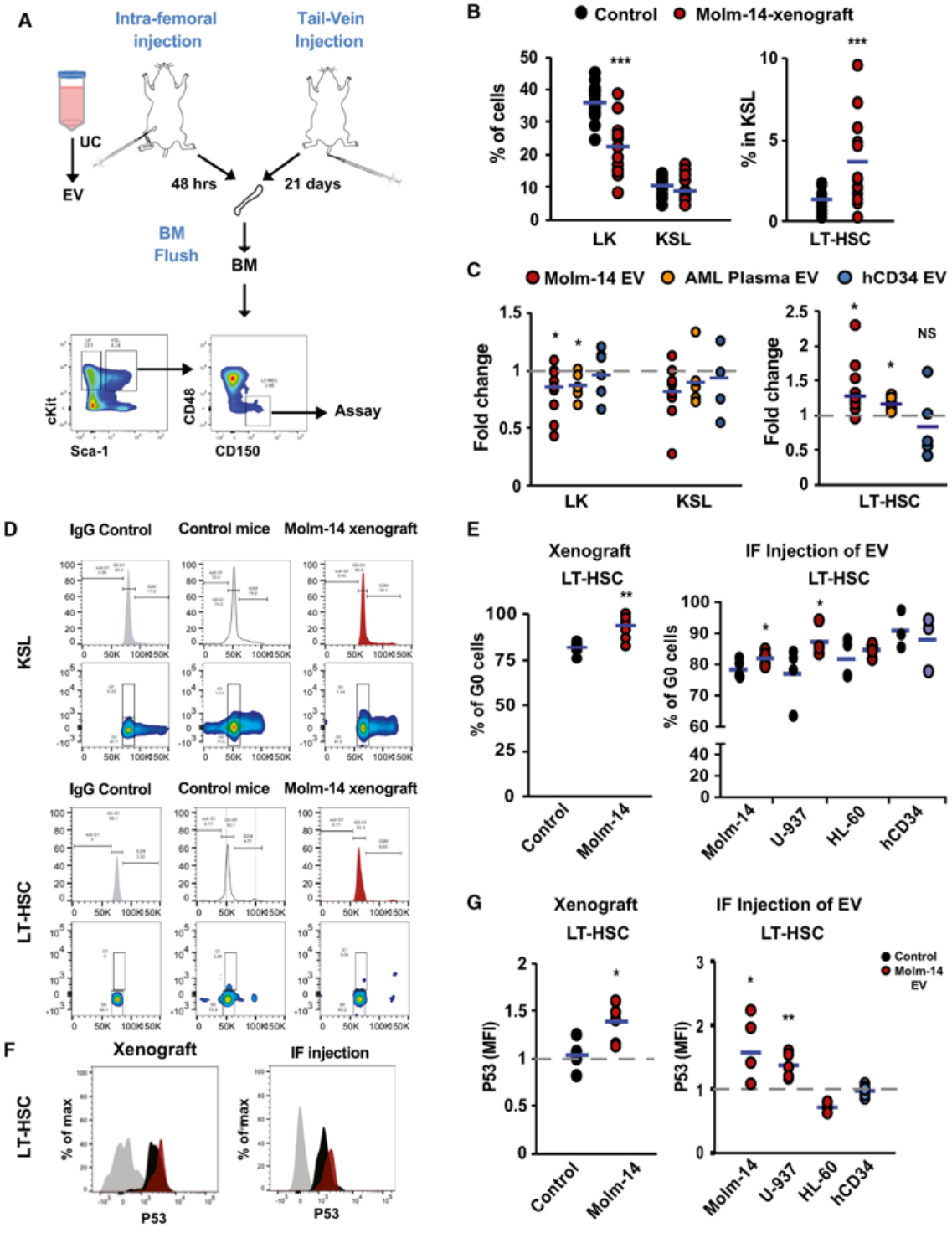

A) A Schematic diagram of methods: the in vivo AML xenografts (tail-vein injection of 105 Molm-14 cells or vehicle per mouse) and the intrafemoral (IF) injection of AML-EV into one femur with a contralateral control vehicle-injected femur of the same mouse. EV were isolated by serial high-speed centrifugation (at 2×, 10×, 100 × 103 g) from AML cell-line culture media or AML patient plasma. Bone marrow was flushed from long bones at the indicated time points, and immunophenotypic analysis was performed by flow cytometry. **B-C)** Flow cytometric analysis showing the frequency of LK and KSL cells in lineage-negative cells (left panel) and LT-HSC in KSL (right panel) in: (**B**) Molm-14 xenograft (red, n = 10) versus control (black, n = 10). Data were obtained from at least two independent experiments. **C)** IF injection of EV from Molm-14 cells (red, n = 8), AML plasma EV (orange, n = 6), and human CD34 EV (blue, n = 4) relative to the vehicle-injected contralateral femurs. Data were obtained from at least two independent experiments. Statistics: Student's t-test (*P < 0.05, ***P < 0.001). **D)** Cell-cycle histograms of KSL (upper panel) and LT-HSC (lower panel) from Molm-14 xenografts or control using Hoechst-33342 staining. **E)** Flow cytometric analysis of the Ki67-ve percentage of LT-HSC representing the G0 phase of cell cycle in: (left panel) Molm-14 xenografts (red, n = 7) versus control (black, n = 9); (right panel) IF injection of Molm-14-EV, U-937 EV, HL-60 EV (red, n = 5,4,4) versus human CD34 EV (blue, n = 3) versus controls (black). Data were obtained from at least two independent experiments Statistics: Student's t-test (*P < 0.05, **P < 0.01). **F- G)** Flow cytometric analysis of intracellular P53 levels shown in histograms (**F**) and MFI (**G**) of LT-HSC in: (left panel) Molm-14 xenograft, n = 6 red versus non-engrafted control, n = 4 black, or (right panel) IF injection of EV from Molm-14, U-937, HL-60 (red, n = 5,5,3) or human CD34 cells (blue, n = 6) normalized to vehicle-injected contralateral femurs. Data were obtained from at least two independent experiments. Statistics: Student's t-test (*P < 0.05, **P < 0.01).

AML-EV induces ribosome biogenesis suppression in hematopoietic cells.

To understand the mechanism by which AML-EV may enforce quiescence, we performed tandem mass tag proteomic profiling of *in vitro* cultured c-Kit$^+$ HSPC (to obtain the minimum required amount of protein lysates) treated with EV from HL-60 or Molm-14 for 48 hours *vs.* vehicle-treated controls. We used the differential expression statistical package EdgeR [210] with multiple testing corrections to calculate the false discovery rate

(FDR) of differentially-expressed proteins between EV- and vehicle-treated. Numbers of quantifiable proteins and biological replicates differed between the Molm-14 experiments (4407 proteins, 2 vehicle replicates, 4 EV replicates) and the HL-60 experiments (4883 proteins, 4 vehicle replicates, 4 EV replicates). We chose FDR cutoffs for each experiment (FDR $<10^{-2}$ for the Molm-14 experiment and FDR $<10^{-9}$ for the HL-60 experiment) to produce lists of differentially abundant candidates that contained ~10% of the quantifiable proteins. There were 394 differentially-regulated proteins in response to the Molm-14-EV (221 upregulated and 173 downregulated), with 491 differentially regulated in response the HL-60-EV (325 upregulated and 166 downregulated). While there were 111 commonly upregulated proteins, 54 proteins were consistently downregulated in HSPC after treatment with both HL-60-EV and Molm-14-EV relative to vehicle-treated controls (**Fig 3.3A**). Functional analysis of these proteins using the *Database for Annotation, Visualization and Integrated Discovery* (DAVID) platform identified ribosomal biogenesis as the most highly-enriched functionally related gene group among downregulated targets in EV-exposed cells (**Fig 3.3B**). This category comprised ribosomal proteins involved in RNA-binding, -splicing, and translation initiation (**Fig 3.3C**).

AML-EV suppress protein synthesis only in LT-HSC

Ribosomal biogenesis is a principal regulatory step for protein homeostasis [211]. This prompted us to test the effect of AML-EV on protein synthesis rates among HSPC populations. We used the recently validated OPP Click-iT assay [212] that relies on the incorporation and labeling of a modified puromycin analogue in newly generated proteins, and thus positively correlates gains in fluorescence intensity with protein synthesis. After animal sacrifice, cells were cultured in RMPI with 10% FBS and treated with OPP for 30 minutes to measure the fluorescently-labeled OPP by flow cytometry. Among the different HSPC populations, only the LT-HSC from Molm-14-xenografts showed significant suppression in their protein synthesis, as represented in the histogram and MFI quantification (**Fig 3.3D** and **Appx 3.3.1A-B**). Protein synthesis was similarly suppressed in LT-HSC and KSL cells from *IF*-injected mice with EV from Molm-14, U-937 and AML patient plasma, but not the hCD34-EV, and more modestly by HL-60-EV (**Fig 3E** and **Appx 3.3.1C**). These data suggest that the global EV-mediated ribosome biogenesis

impairment in all HSPCs most profoundly suppresses protein synthesis in LT-HSC, but not KSL or other progenitors. Together, the data demonstrate protein synthesis suppression and quiescence induction in LT-HSC by AML-EV.

Figure 3.3: AML-EV impair ribosome biogenesis in hematopoietic cells and suppress protein synthesis in LT-HSC

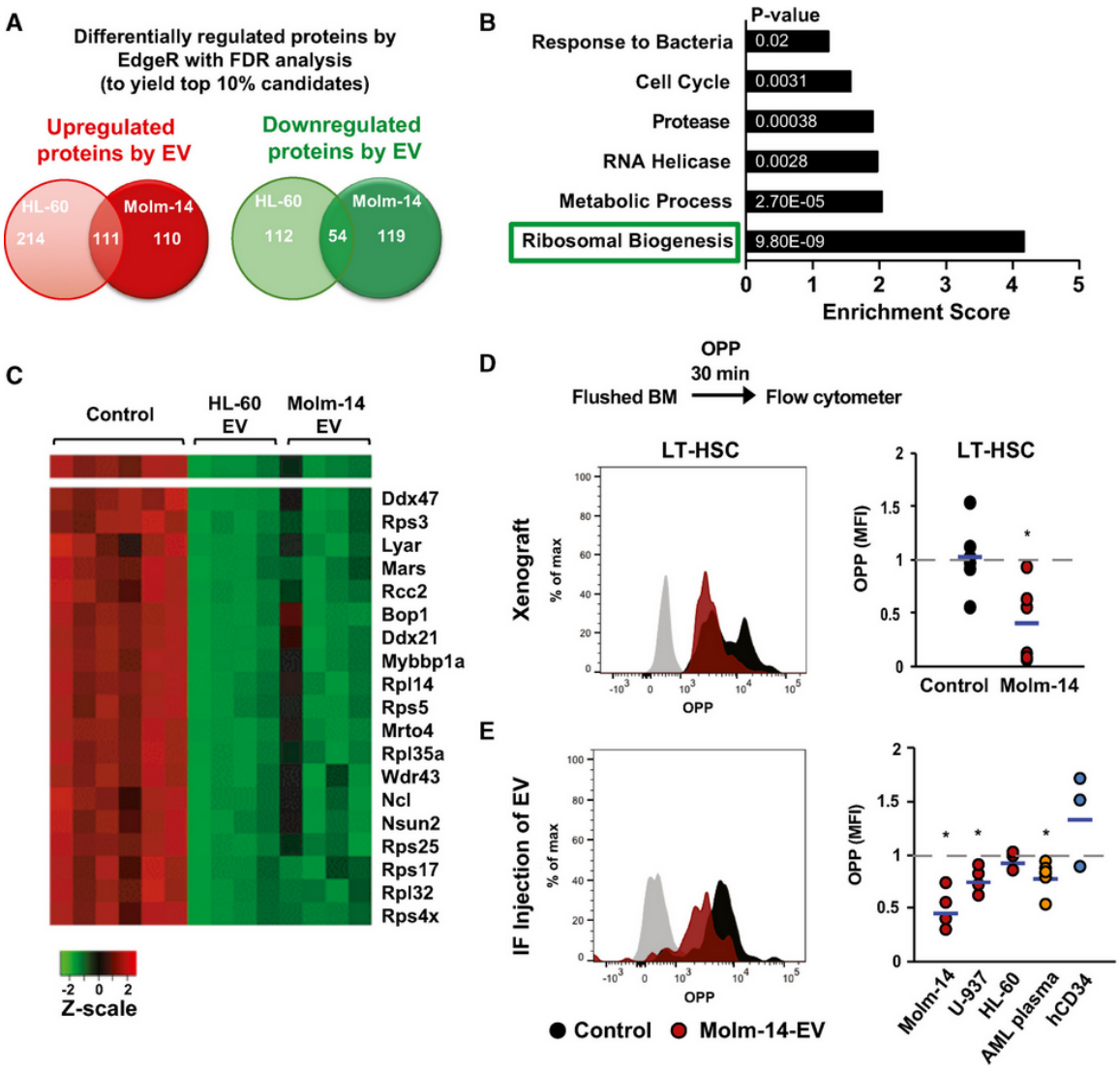

A) A Venn diagram showing the most highly up- and downregulated proteins between Molm-14-EV and HL-60 EV-treated cKit+ HSPC determined by isobaric TMT labeling and edgeR analyses to calculate the false discovery rate (FDR) analysis to obtain ˜10% of the differentially regulated proteins. We obtained 325 and 221 upregulated proteins in the HL-60 dataset and the Molm-14 dataset, respectively. We also obtained 166 and 173 downregulated protein in the HL-60 dataset and the Molm-14 dataset, respectively. Among them, 54 proteins were commonly downregulated. **B)** A bar graph showing the functional annotation enrichment analysis by DAVID biostatistical plate form of the 54 commonly downregulated protein identified the indicated pathways; among them, the ribosomal biogenesis pathway showed the highest enrichment. P-values are indicated in white. Modified Fisher's exact test. **C)** A heatmap showing the highly deregulated ribosomal proteins in AML-EV-exposed cells. **D-E)** Flow cytometric analysis showing the histograms and MFI of O-propargyl-puromycin (OPP) incorporation in LT-HSC in: (D) Molm-14 xenografts, red n = 6 versus non-engrafted controls, black n = 6, or (E) IF injection of EV from Molm-14, U-937, HL-60 (red, n = 5,4,3), AML patient plasma (orange, n = 6) or human CD34+ cells (blue, n = 3) normalized to vehicle-injected contralateral femurs after subtracting the background fluorescence. Data were obtained from at least two independent experiments. Statistics: Student's t-test (*P < 0.05).

AML-EV impair protein synthesis in LT-HSC via the mTOR pathway

The mTOR pathway is critical for translating extrinsic signals into cell-intrinsic events and, among other functions, governs ribosome biogenesis and protein synthesis [213-215]. Because we found a global reduction of ribosome biogenesis in HSPCs (**Fig 3.3**), we evaluated the EV-mediated regulation of the mTOR pathway using the bulk HSPCs, KSL. Our qPCR transcriptional analysis indicated the downregulation of several mTOR associated targets, including the mTORC1 subunit *Raptor*, in KSL from Molm-14-xenografts relative to controls (**Fig 3.4A**). KSL cells from femurs injected with Molm-14-EV confirmed the suppression of *Raptor*, and other mTOR-associated genes, relative to cells from vehicle-injected contralateral femurs (**Fig 3.4B**). To assess mTOR activity, we tested the effect of AML-EV on S6RP phosphorylation, a downstream mTOR effector [215], and found that a consistent reduction of pS6RP in LT-HSC in the xenografts relative to control mice (**Fig 3.4C-D**) and after injection of AML-EV but not hCD34-EV (**Fig 3.4C-**

E). Similarly, AML-EV decreased pS6RP in KSL, suggesting that the AML-EV-mediated mTOR suppression affects the HSPC pool more broadly (**Appx 3.4.1A**). Consistent with the reported role of Raptor in regulating HSC quiescence [213], we found that both siRNA-targeted silencing of Raptor and Rapamycin (a pharmacological Raptor inhibitor) suppressed LT-HSC activation and increased the percentage of cells at G_0 phase (**Appx 3.4.1-C).** Indeed, KSL and LT-HSC from Molm-14 xenografts showed significant suppression of the Raptor protein assessed by flow cytometry (**Appx 3.4.1D**). To test if mTOR suppression requires the continued uptake of AML-EV, we examined mTOR expression after seven days of *ex vivo* culture of HSPC derived from Molm-14 xenografts or control mice. Interestingly, we found a complete reversion of the pS6RP suppression in the xenografts-derived KSL and LT-HSC relative to Day 0 (**Appx 3.4.1E**). We specifically ruled out significant changes in c-Myc levels, another critical protein synthesis regulator, in KSL as well as LT-HSC of AML-xenograft and following *IF*-injection of AML-EV (**Appx 3.4.1F-G**). The data thus far indicate that AML-EV impair mTOR-dependent ribosome biogenesis in the pooled HSPC populations. Important from a functional point of view, LT-HSC reveal an exaggerated sensitivity to protein synthesis suppression consistent with previous reports [212, 216, 217].

EV miRNAs target Raptor and suppress protein synthesis

We recently demonstrated that AML-EV highly incorporate specific cellular miRNAs capable of altering bystander cell function [21, 23, 168]. Those studies identified a panel of miRNAs that were highly abundant in AML cell-line EV and plasma EV from AML patients, but not those from healthy donors. The panel includes miR-27a-5p, miR-155-5p, miR-181b-5p, miR-1246, and miR-1290, some previously reported as potential AML biomarkers [168, 218-220]. We hypothesized that one or more of these candidate AML-EV miRNAs might cooperate in the mTOR-dependent suppression of LT-HSC protein synthesis. To test this, we used synthetic miRNA mimics and functionally screened their ability to suppress protein synthesis in murine NIH-3T3 cells relative to a scramble control miRNA. Several mimics, including miR-1246, showed a significant reduction of OPP fluorescence and pS6RP (**Fig 3.4F-G**). Transcriptional analysis of the mTOR-associated genes showed that among the miRNAs, miR-1246 mimic significantly downregulates

Raptor (**Appx 3.4.1H**). Flow cytometric analysis confirmed that miR-1246 mimic suppressed Raptor protein levels (**Fig 3.4H** and **Appx 3.4.1I**). Notably, experiments with the luciferase reporter system containing the *Raptor* 3`UTR indicated that the miR-1246 mimic most profoundly suppresses the *Raptor* gene (**Figure 3.4I**). We further confirmed that miR-1246 levels were in fact higher in EV from AML patient *vs.* healthy donor plasma, and increased alongside AML disease burden in Molm-14-xenografts. As expected, nucleofection of miR-1246 mimics into LT-HSC *ex vivo* increased their quiescence (**Fig 3.4J**), whereas nucleofection of LT-HSC with Anti-miR-1246 rescued the Molm-14 EVs-mediated quiescence induction (**Fig 3.4K**). Altogether, AML-EV deliver miR-1246 and other miRNAs that downregulate the Raptor/mTOR pathway to suppress protein synthesis and induce quiescence in HSC.

Figure 3.4: AML-EV-contained miR-1246 suppresses protein synthesis in LT-HSC via the mTOR pathway

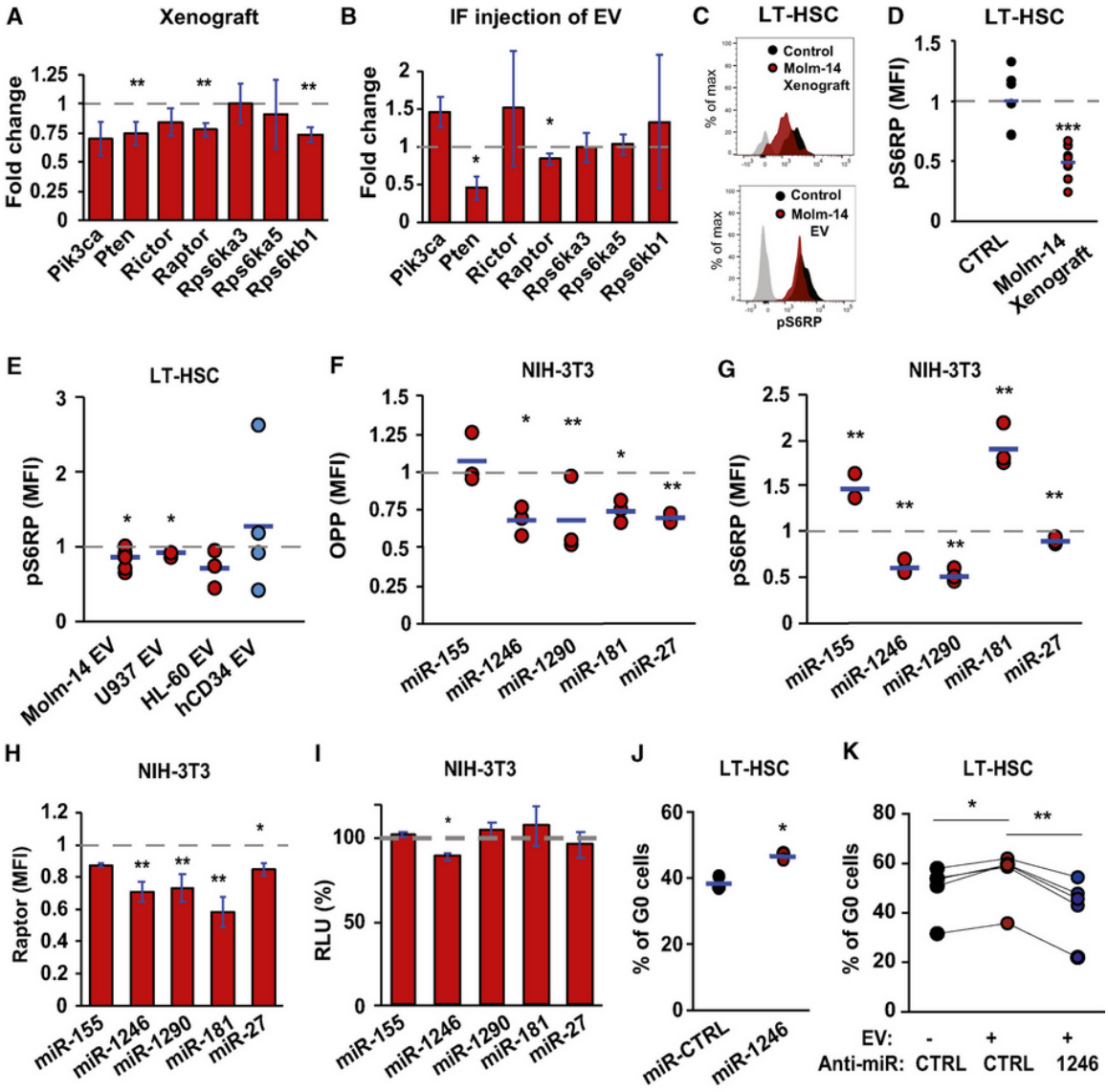

A) qRT–PCR gene expression analysis showing the fold change of PI3K/mTOR-associated gene panel in KSL cells sorted from: (A) Molm-14-xenografted mice or (B) IF-injected mice with Molm-14-EV relative to their controls and normalized to Gapdh endogenous control. Data are expressed as mean ± SEM from at least three independent experiments, performed in technical replicates. Statistics: One-way ANOVA with Bonferroni post hoc correction (*P < 0.05, **P < 0.01). **C–E)** Flow cytometric analysis showing the histograms (C) and MFI of intracellular pS6KRP in LT-HSC in: (D) Molm-14 xenograft (red, n = 9) versus non-engrafted control (black, n = 7), or (E) IF injection of EV from Molm-14, U-937, HL-60 (red, n = 7,3,3), or human CD34 cells (blue, n = 4) normalized to the control contralateral femur with subtraction of background fluorescence. Data were obtained from at least two independent experiments. Statistics: Student's t-test (*P < 0.05, ***P < 0.001). **F-G)** Flow cytometric assessment of protein synthesis showing the MFI of: (F) OPP or (G) pS6RP in NIH-3T3 cells 72 h after transfection with the indicated miRNA mimics. The results were calculated relative to control (miR-scramble) with the background fluorescence subtracted and performed with at least three independent experiments, in technical replicates. Statistics: one-way ANOVA with Bonferroni post hoc correction (*P < 0.05, **P < 0.01). **H)** Flow cytometric analysis showing the MFI of Raptor in NIH-3T3 cells 72 h after transfection with the indicated miRNA mimics. The data were calculated relative to miR-scramble and are presented as mean ± SEM, and the background fluorescence was subtracted. Performed with at least three independent experiments, in technical replicates. Statistics: one-way ANOVA with Bonferroni post hoc correction (*P < 0.05, **P < 0.01). **I)** Dual-luciferase reporter assay. NIH-3T3 was transfected with the miRNA mimics. Three hours later, the cells were transfected with the Raptor 3′UTR cloned into the psiCheck-2 vector for a total of 48 h. Data are presented as %RLU (relative luciferase units) of the miR-scramble control as mean ± SEM from at least three independent experiments, performed in technical replicates. Statistics: one-way ANOVA with Bonferroni post hoc correction (*P < 0.05). **J-K)** Cell-cycle flow cytometric analysis using Ki67/Hoechst-33342 staining of the percentage of LT-HSC in the G0 phase after nucleofection of cKit+ cells using the Amaxa™ P3 Primary Cell 4D-Nucleofector Kit, (J) Cells were nucleofected with miR-scramble (CTRL) or miR-1246 mimic (n = 3) for 72 h, (K) cells were nucleofected with anti-miR-scramble (CTRL) or anti-miR-1246 (n = 5) and 1 h later co-treatment with Molm-14 EV for 72 h. Statistics: Student's t-test (*P < 0.05, **P < 0.01).

LT-HSC restore serial repopulation capacity and protein synthesis rates

Others previously noted the reversibility of quiescence once hematopoietic cells are removed from the leukemic niche [151, 205]. To test this possibility in our model, we first examined the serial colony forming unit assay (CFU-C) as a correlate of potential functional impairment of residual HSPC pool by AML-EV (**Fig 3.5A**). Surprisingly, we observed a consistent increase in colony growth compared with controls (**Fig 3.5B**). Further subtyping of the colonies revealed that the observed increase in overall CFU-C was due to gains in the less-committed bi-potential granulocyte/monocyte progenitors (**Fig 3.5B**). We then tested the reversibility of protein synthesis suppression and quiescence *in vivo*. We transplanted male donor KSL from AML-xenografts or controls into sub-lethally irradiated (150cGy) female recipients (**Fig 3.5A**). Following validation of the sensitivity in defined mixtures of cells from both sexes at different ratios (**Appx 3.5.1A-B**), we evaluated the donor chimerism by qPCR quantification of the sex-determining region Y (SRY) in the recipients' peripheral blood (PB) leukocytes [221]. Twenty-one days after transplantation, the animals were sacrificed and LT-HSC revealed normalized OPP-incorporation, pS6RP and P53 levels (**Fig 3.5C**). These data echoed the pS6RP activity recovery that we observed in xenograft-derived KSL and LT-HSC after *ex vivo* culturing in AML-free media (**Appx 3.4.1E**). Consistent with the CFU-C results, xenograft-derived donor cells showed initial levels of PB chimerism (SRY) that exceeded those from control donors (**Appx 3.5.1C**).

To evaluate the long-term repopulation performance, we transplanted KSL from male Molm-14-xenografts or controls into secondary sub-lethally irradiated female recipients and serially tracked the PB donor chimerism for 12 weeks. This was followed by a second round of transplantation using unfractionated BM from the secondary recipients into tertiary sub-lethally-irradiated females, while tracking the original (male) donor cell chimerism for another 20 weeks. The results showed increased short-term (until week 6 in the secondary recipients, **Fig 3.5D**) and long-term (tertiary recipients, **Fig 3.5E**) repopulation potential of the AML-xenograft-derived groups by *t-test* and regression

analysis, respectively). We also observed an increase in the BM LT-HSC levels after secondary transplantation (**Appx 3.5.1D**).

Figure 3.5: LT-HSC restore protein synthesis and proliferative function upon transplantation to a non-leukemic host

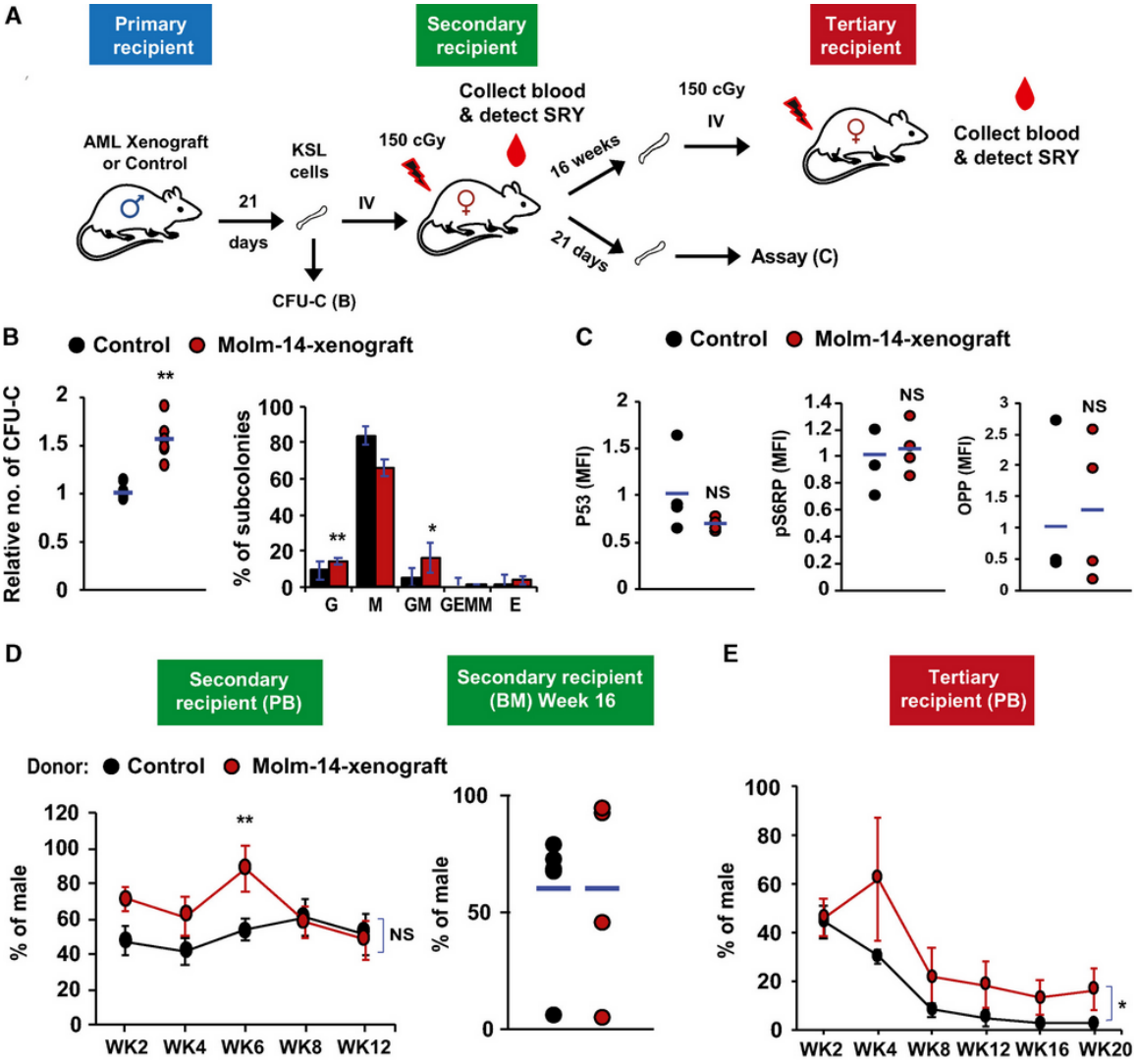

A) A diagram showing the scheme of repopulation experiments on non-leukemic host. KSL cells were purified from Molm-14-xenografted male mice (red) or control males (black) and transplanted into 150 cGy sublethally irradiated female recipients (104 cells per mouse) and used for subsequent repopulation studies described in (D, E). **B)** CFU-C assay showing the relative number of colonies (left panel) and the colony subtypes (right panel) from KSL cells derived from Molm-14-xenografted mice (red, n = 6) versus non-engrafted control mice (black, n = 5) and in vitro-cultured for 7 days in methylcellulose media. Experiments were performed in technical triplicates. "G"—granulocyte, "M"—monocyte, and "E"—erythrocytes. Statistics: Student's t-test (*P < 0.05, **P < 0.01). **C)** LT-HSC assessment after repopulation, recipient female mice (n = 4 per group) were sacrificed after 21 days and their LT-HSC were compared using P53, pS6RP, and OPP flow cytometric assays. Statistics: Student's t-test. **D-E)** Evaluation of the *in vivo* long-term repopulation capacity. (D) For secondary transplantation (n = 6 per group), PB samples were collected twice weekly for 12 weeks (WK), and the donor chimerism was measured by qPCR of sex-determining region Y (SRY) normalized to Gapdh gatekeeper as shown in the left panel. Sixteen weeks later, mice were sacrificed and BM male chimerism percentage was assessed as shown in the right panel. (E) For tertiary transplantation, unfractionated BM cells from the secondary recipients (n = 6 per group, 106 cells per mouse) were injected into tertiary 150 cGy sublethally irradiated female recipients and blood SRY levels were assessed for 20 weeks. Statistics: Student's t-test for two-sample comparison and regression analysis for longitudinal comparison (NS = not significant, *P < 0.05 and **P < 0.01).

Enhanced replating potential and DNA-damage accrual in AML-EV exposed cells

Our sex-mismatched xenograft approach did not permit selective recovery of purified HSC after transplantation. To understand the *in vivo* resistance to LT-HSC depletion and persistent, if modest, repopulation advantage, we therefore performed serial *ex vivo* CFU-C replating and evaluated the clonogenicity of stem and early progenitor subsets from Molm-14-xenografts or control mice (**Fig 3.6A**). To insure a valid comparison, the serially-plated cells were normalized prior to each replating. Our results showed persistently higher CFU-C counts and average number of cells per colony (**Fig 3.6B-C**) as well as relative number of cells (**Appx 3.5.1E**) for all xenograft-derived progenitors relative to the controls. The data also showed that the xenograft-derived cells were more resistant than control-derived cells to exhaustion.

Given the gains in AML-EV mediated quiescence in HSC and gains in replating efficiency, we decided to evaluate their DNA-damage response (DDR) [222-224]. We observed a consistent increase in γH2AX foci (**Fig 3.6D)**, indicating the presence of DNA double-strand breaks, along with the induction of canonical DDR-transcripts (including the non-homologous end joining pathway transcripts) in KSL selected HSPC from AML-xenografts relative to controls (**Fig 3.6E**). Interestingly, the observed DDR (γH2AX foci and DDR-transcripts) in xenograft-derived cells persisted through subsequent replating *vs.* controls (Week 1 in **Fig 6F-G** and Week 2 in **Fig 3.6H-I**). Next we attempted to corroborate this observation *in vivo* and assessed the DDR in HSPC after sex-mismatched serial transplantations (**Fig 3.6J**). Again, we found a consistent increase in γH2AX foci and DDR-transcripts, in both KSL and LT-HSC from xenograft-derived serially-transplanted mice relative to the control ones (**Fig 3.6K-L**). Together, the data indicate the accrual of DNA-damage and a sustained DNA-damage response in residual progenitor and stem cells in the AML niche that, unlike the protein synthesis suppression, is not reversible. Based on the aggregate data, we propose a model whereby AML-EV transfer of miRNA leads to suppression of the mTOR subunit Raptor and promotes quiescence in LT-HSC (**Fig 3.7**). However, while protein synthesis suppression is functionally relieved upon transfer to naïve microenvironment, LT-HSC in the AML niche accrue and retain DNA-damage.

Figure 3.6: AML microenvironment conditioned HSC accrue persistent DDR and gain a proliferative advantage

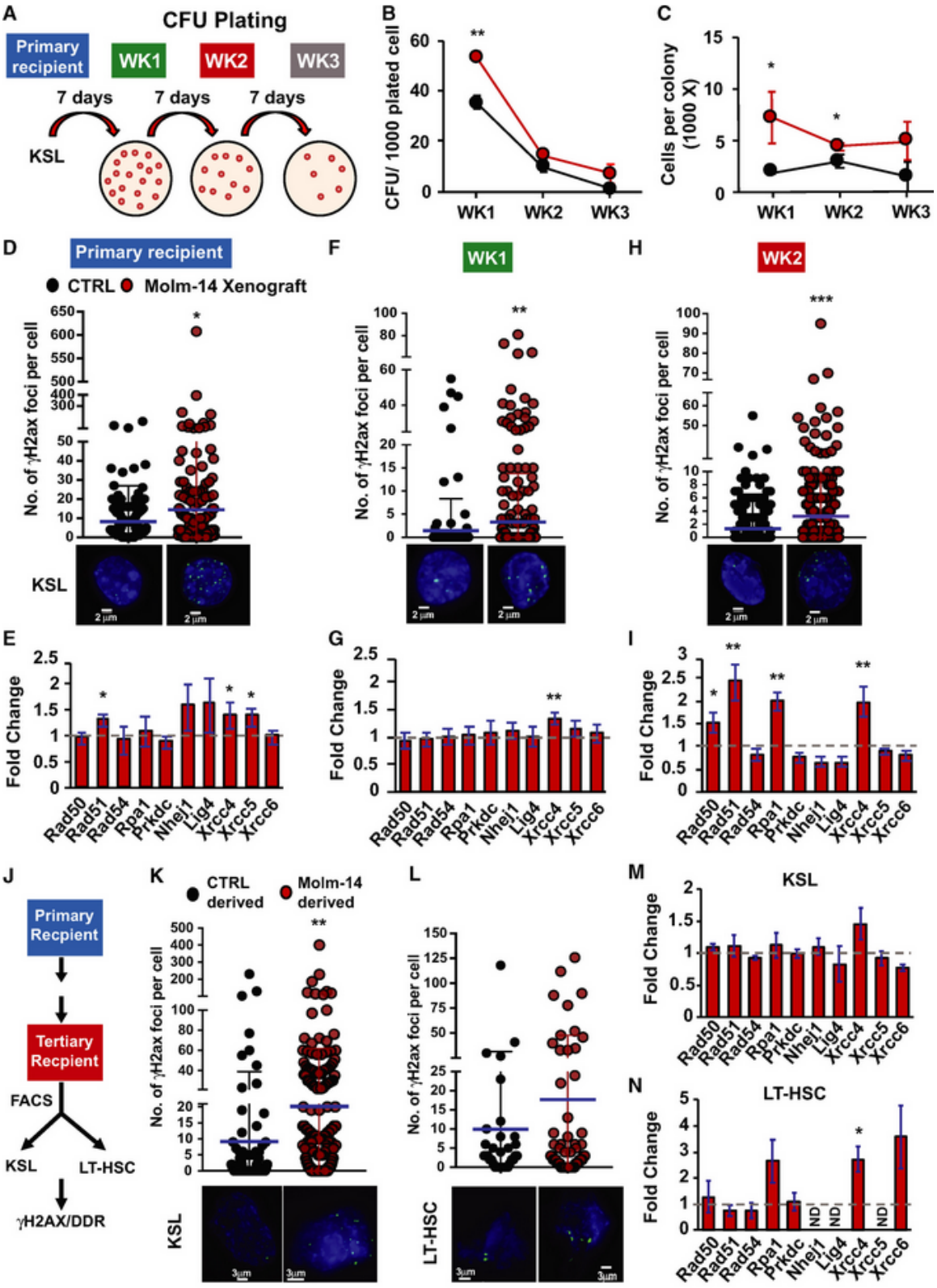

A) A schematic diagram demonstrating the serial replating experiment. KSL cells were sorted from primary recipient control mice (black, n = 4) or Molm-14 xenografts (red, n = 4) and plated in triplicate (500 cells/plate/mouse) in methylcellulose media. Seven days later, colonies were counted and serially replated in triplicate (5,000 cells/plate/mouse). The replating process was repeated twice for a total of three rounds (labeled week "WK" 1, 2, and 3). **B-C)** Serial replating CFU-C analysis presented as mean ± SEM showing (B) the number of colonies per 1,000 plated cells and (C) the number of cells per colony, for each week time point. Statistics: Student's t-test (*P < 0.05, **P < 0.01). **D–I)** DNA-damage assessment in KSL from primary recipients and after two turns of replating. (D, F, H) Number of γH2AX foci in control-derived and Molm-14-xenograft-derived mean ± SD (D) primary recipient KSL, n = 211 and 321, (F) cells from W1 plating, n = 218 and 369, and (H) cells from W2 plating, n = 770 and 853. All cells were stained with phosphoH2axser139 and the nuclear stain Hoechst (blue), imaged using the GE/API DV widefield microscope (60× objective) to show the γH2AX foci (green) and counted using Imaris software. Scale bars are 2 μm. Statistics: Student's t-test (*P < 0.05, **P < 0.01, and ***P < 0.001). (E, G, I) qRT–PCR gene expression analysis showing the fold change of select DNA-damage response-gene panel in Molm-14-xenograft-derived (E) primary recipient KSL, n = 6, (G) cells from W1 plating, n = 4, and (I) cells from W2 plating, n = 4. Data indicated by bars of fold change calculated relative to matching controls were normalized to the endogenous control Gapdh and are presented as mean ± SEM. Statistics: one-way ANOVA with Bonferroni post hoc correction (*P < 0.05, **P < 0.01). **J)** Scheme of DDR assessment in KSL and LT-HSC derived from serial in vivo repopulation. **K-L)** Number of γH2AX foci, respectively, in control- and Molm-14-xenograft-derived (K) KSL, n = 101/204, and (L) LT-HSC, n = 33/53. Images were processed similar to (D–F). Scale bars are 3 μm. Statistics: Student's t-test (**P < 0.01). Mean ± SD. **M-N)** . qRT–PCR analysis of the DNA-damage gene panel in Molm-14-xenograft-derived (M) KSL and (N) LT-HSC, relative to matched controls. Data depicted as fold change relative to matching controls were normalized to the endogenous control Gapdh and are presented as mean ± SEM. Statistics: one-way ANOVA with Bonferroni post hoc correction (*P < 0.05).

Figure 3.7: Synopsis

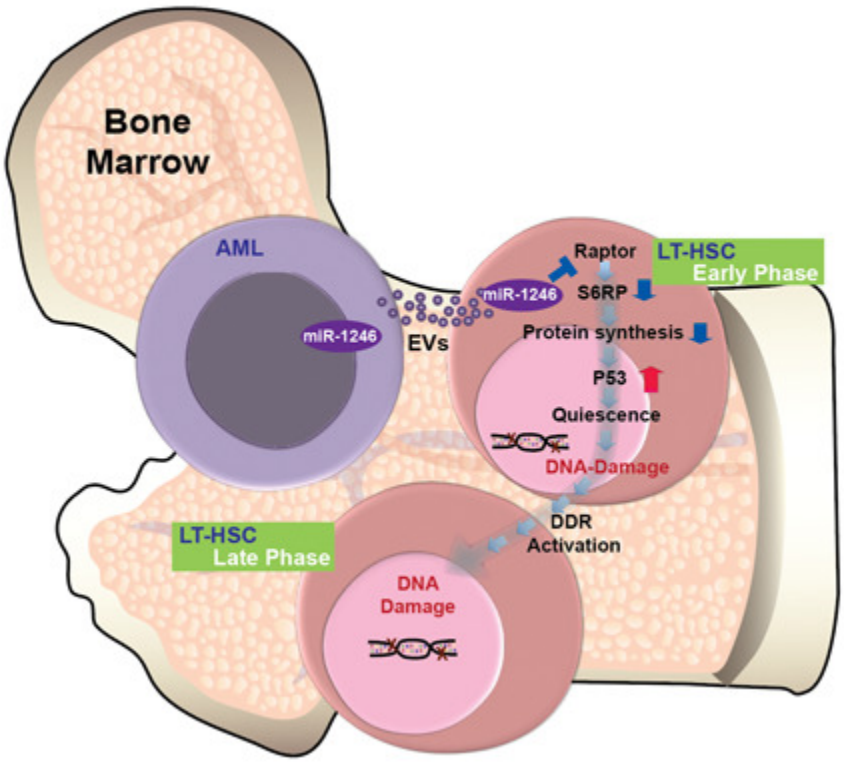

Acute myeloid leukemia (AML) functionally remodels the bone marrow niche. AML cells constitutively release extracellular vesicles (EVs) enriched in miR-1246, that traffic to long-term hematopoietic stem cells (LT-HSC) and induce quiescence and DNA damage.Following EV uptake into LT-HSC, miR-1246 downregulates the Regulatory-associated protein of mTOR (Raptor) leading to the hypo-phosphorylation and deregulation of S6 ribosomal protein (S6RP). Deregulation of the S6RP mediates protein synthesis suppression associated with P53-dependent quiescence. While quiescence and protein synthesis suppression are reversible upon transfer to naïve recipients, cells accrue double-strand DNA-breaks that persist, and generate a long-lasting DNA-damage response (DDR) while conferring gains in proliferative capacity.

Discussion

A series of studies over the past decade has shown that the presence of AML blasts in bone marrow leads to functional alterations in stromal components with emergence of a leukemia-permissive niche [5, 43, 106, 149, 225]. Recently, investigators have also begun to provide detailed analyses of residual hematopoietic cells in the AML-BM, revealing the initially surprising, and seemingly selective, quiescence and preservation of LT-HSC [150, 151, 204, 205, 226]. At the same time, both the mechanisms by which residual HSC function in the AML niche is altered [151] and reports of mutation accrual in phenotypically normal cells of AML patients in remission [227, 228] remain unexplained. Our studies herein suggest a model of cell-cell crosstalk involving AML-derived EV that shape residual HSC function, eliciting reversible quiescence in the short term, but persistent DNA-damage.

EV trafficking serves a broad range of constitutive cellular functions, whereby several subclasses of nano-sized vesicles transfer protein and nucleic acids between cells, including the BM niche [23, 43, 108, 150, 179, 229]. We previously reported the loss of BM progenitors as a result of AML-EV trafficking [21]. Here, we hypothesized that EV also regulate residual HSC and contribute to their relative resistance to elimination, observed by others [151, 204, 205, 226]. To test this hypothesis, we combined *in vivo* modeling in a non-irradiated niche, high-resolution immunophenotyping of the hematopoietic compartment, and an EV-labeling system using myristoylated fluorescence tagging [21, 230]. Differential uptake of EV into hematopoietic cells has not been previously explored, and we began by showing that cells at different levels of hematopoietic differentiation, including immunophenotypically-defined stem cells, were susceptible to AML-EV entry, without significant differences in entry kinetics into HSC compared to progenitors.

In a series of xenografts, we confirmed cell-cycle quiescence and relative enrichment of LT-HSC [149, 150], but also replicated those outcomes using *IF* injection of

AML-EV. EV signaling relies on transfer of protein or nucleic acids, but rather than EV content survey we took an outcome-driven approach to resolve the underlying mechanism. Proteomic screening pointed to the possibility that AML-EV exposure conferred quiescence through deregulation of ribosome biogenesis, consistent with the observed P53-upregulation and cell-cycle arrest [211, 231]. The idea that compromised ribosomal protein synthesis can erode HSC homeostasis is well established in models of myelodysplasia [232] and inherited BM disorders, such as Diamond-Blackfan Anemia [233, 234]. Experimentally, we combined flow cytometric analysis for cell identity (HSPC *vs*. LT-HSC) and OPP-incorporation. Although we observed a consistent ribosomal biogenesis impairment in all the HSPC cells, we found the most profound suppression of protein synthesis in LT-HSC using AML-xenografts, and confirmed by injection of EV from AML cell lines as well as AML patient plasma.

To understand how EV target HSC protein synthesis, we explored dysregulation among key-components of the mTOR pathway, a critical gatekeeper of cellular proliferation and transmission of extracellular signals. Given the role of miRNA in regulating hematopoiesis on the one hand, and miRNA cell-cell transfer via AML-EV on the other [10, 229], we next focused on a specific panel of highly incorporated miRNA as potential regulators of mTOR. We investigated our previously identified candidate panel, including miR-155-5p, miR-1246, and miR-1290 [168], as well as miR-27a-5p and miR-181b-5p as putative AML biomarkers [218-220]. In a succession of experiments, we observed that among these candidates, miR-1246 specifically targeted the mTORC1 subunit *Raptor*, causing a downstream loss in protein synthesis and inducing cell quiescence. The data align well with the loss of known Raptor functions in the mTOR pathway, namely HSC activation, proliferation and ribosome biogenesis [213, 216, 235, 236]. Moreover, Raptor was previously shown to be required for HSC regeneration and its loss led to accumulation of monocytoid cells, pancytopenia, and splenomegaly in mice [237]. Our data was further consistent with observations of reversible HSC quiescence by others [151, 205] and supports the direct action of AML-EV miRNA on mTOR and protein synthesis suppression that is readily reversed in a naïve niche, i.e. following transplantation to a healthy host. Thus, our results fit a model of translational suppression by AML-EV miRNA [238] and find support

in existing reports of miRNAs suppression of protein synthesis [239, 240] and targeting Raptor in hematopoietic cells [241-243]. Although miR-1246 was previously identified as a regulator of cancer progression, drug-resistance [244, 245] and a putative biomarker [168, 246], our data suggest a role in regulating HSC.

While the enforced quiescence of HSC is a plausible protective response to leukemic-stress in the BM, several studies have shown that it renders them susceptible to DNA-damage through reliance on non-homologous end joining for double-strand lesion repair [222, 247]. Unrepaired DNA breaks in HSC in turn pose a significant risk to long-term functional integrity [248]. The increase in cellular susceptibility to DNA-damage sets them up for additional mutations that contribute to the formation of subsequent oncogenes. In AML patients, the acquisition of mutations in residual HSC can promote clonal expansion, malignant transformation, and overt relapse [227, 228, 249]. These studies provide an intriguing context for the double-strand breaks we observed here, and which persisted through serial *in vitro* replating and *in vivo* transplantation, respectively. While the gains we identified in proliferative fitness are consistent across all experiments, and replicate observations by others whereby AML-exposed HSC outcompete controls [151], future studies will have to address the question of specific genomic lesions.

In summary, we propose a model whereby AML use EV-miRNAs to suppress protein synthesis *via* targeting of the mTOR pathway in LT-HSC to elicit their quiescence (**Fig 3.7**). Despite the functional LT-HSC recovery, these cells acquire long-lasting DNA-damage. This model readily accommodates observations by several other groups in the field that indicate the selective preservation of HSC in the AML niche. Whereas HSPC are generally susceptible to EV entry and utilize the mTOR pathway, HSC selectively enter quiescence in this model owing to their unique sensitivity to protein synthesis disruption [212, 216, 217]. It is tempting to speculate that the complex interplay of cells in the AML niche that leads to a selective advantage and subsequent transformation of residual HSC may involve EV. Finally, given the reversibility of BM failure in the context of AML, as noted by others [149, 151, 204, 205], our data reveals potential therapeutic targets to accelerate hematopoietic recovery. We believe that this study deepens our understanding of cell-cell

communication and reveals unexpected collateral damage among hematopoietic stem cells in the AML niche.

Methods

Animals

All animal studies were approved by the OHSU Institutional Animal Care and Use Committee (IACUC). Mice were purchased from the Jackson Lab. For Molm-14-xenografts, cells (0.1×10^6/animal) were engrafted into 6-8 weeks old NOD Cg-Prkdc^{scid} Il2rg^{tm1Wjl}/SzJ (NSG) mice by tail-vein injection. For *Intra-femoral* (*IF*) injections, NSG and C57BL/6J mice of 6-10 weeks old were used and *IF* injection was performed as previous [21, 108]. Animals were anesthetized, the injection site disinfected and the femur was positioned at 90˚ with the tibia. The femur cavity was cored and EV in 50µl PBS (Hyclone) were slowly injected.

Cell culture

Molm-14 and HL-60 cells were provided by Dr. Jeffery Tyner, OHSU. U-937 cells were purchased from ATCC. Cells were cultured in RPMI (Gibco) with 10% fetal bovine serum (FBS, Gibco) and 1x penicillin/streptomycin (Gibco) at 37°C, 5% CO_2, and >95% humidity. Mycoplasma co-precipitate with EV and contamination was excluded using the MycoAlert Plus kit (Lonza). Healthy donor CD34$^+$ were purchased from ATCC. Cells were cultured at 37°C, 5% CO_2, and >95% humidity in the X-vivo media (Lonza) with BIT 9500 Serum Substitute (StemCell Technologies), FMS-like tyrosine kinase 3 ligand (50 ng/ml), G-CSF (10 ng/ml), IL-3 (10 ng/ml), IL-6 (10 ng/ml), stem cell factor (SCF) (50 ng/ml), and thrombopoietin (25 ng/ml) (Peprotech).

EV preparation

EV were purified by serial high-speed centrifugation as previously described [21]. For culture media EV, cells were cultured for 48 hours in RPMI media with vesicle-free

FBS. For plasma EV, peripheral blood was obtained under IRB approved protocols at Texas Children's Cancer and Hematology Center, Baylor College of Medicine, Houston TX. Culture media or plasma were serially spun at 300*g*, 2000*g* and 10,000*g*. The supernatants were then centrifuged at 100,000*g* using the SW32Ti rotor (Beckman-Coulter) to pellet-down the EV.

Flow cytometry sorting and analysis of BM cells

For sorting, BM cells were flushed from long bones as previously reported [21, 108]. Briefly, femur and tibia were isolated, and cells were flushed using RPMI with 2% FBS and spun at 300*g*. Red blood cells (RBC) were hemolyzed and cells were filtered through 35µm nylon mesh cell-strainers followed by suspension in PBS with 2% FBS. BM cells were then stained with the appropriate antibodies at 4°C for 30 minutes before flow cytometric sorting using the Influx™ cell sorter (BD Biosciences). The immunophenotypic classification of HSPC populations were previously reported [250]. For analytical flow cytometry, stained cell were analyzed using CANTOII flow cytometer (BD Biosciences). For intracellular staining, cells were fixed with 2% paraformaldehyde, permeablized with 0.5% Triton-X, intracellularly stained. Protein synthesis quantification was performed using the Click-iT™ Plus o-propargyl-puromycin (OPP) Alexa-Fluor™488 kit (according to manufacturer protocol (Thermo Fisher). Cells were treated with OPP, cultured at 37°C for 30 minutes, and labeled. All data were analyzed using FlowJo software (Tree Star) and presented as mean fluorescence intensities (MFI).

RNA, DNA extraction and RT-PCR

KSL cells were sorted into Buffer RLT (Qiagen) and total RNA was extracted using the RNeasy kit (Qiagen). Total RNA was quantified using the NanoDrop 2000c spectrophotometer (Thermo Fisher). RNA (50 ng) samples were converted into complementary DNA using the SuperScript III First-Strand Synthesis kit (Invitrogen). For SRY male chimerism analysis, blood samples were collected, RBC were hemolyzed and genomic DNA was extracted using the DNeasy kit (Qiagene). All the RT-PCR analyses were performed using the FastStart PCR SYBR Mix and the LightCycler® 480 thermo-

cycler (Roche Diagnostics). Relative quantification was calculated using the ΔΔCT algorithm with *GAPDH* or *ACTB* as endogenous control when appropriate. For miRNA quantification, blood samples were collected from mice, spun at 100*g* and plasma was extracted. EV were purified and their total small RNA was extracted using the miRNeasy kit (Qiagen). The TaqMan miR-1246 assay kit (Applied Biosystems) was used for reverse transcription and qRT-PCR analyses and the U6 snRNA was used as endogenous control.

Dual Luciferase reporter system

The assay was performed as previously described[21]. The 3' untranslated regions (3`UTR) of Raptor was PCR-amplified from freshly isolated murine c-Kit$^+$ genomic DNA and cloned into psiCHECK-2 vector (Promega). NIH-3T3 cells were first transfected with the miRNA mimics (50nM). After 3 hours, the cells were re-transfected with 100ng of the 3'Raptor_psiCHECK-2 construct for additional 45 hours. Cells were then washed in PBS and the dual-luciferase assay was measured according to the manufacturer's protocol (Promega). The *Firefly* and *Renilla* luminescence were quantified using the Synergy H1 Luminometer (Biotek), and the relative luminescence units (RLU) were compared with the miR-Scramble.

CFU-C assay

KSL (500 cells) were cultured in methylcellulose with cytokines (Stem Cell Technologies) into 35-mm dishes (Thermo Fisher). Cells were incubated at 37°C with 5% CO_2 for a week and colonies were counted using a 4x magnification light microscope. For serial replating, methylcellulose was solubilized in PBS. Cells were then pelleted-down at 300*g* and plated (5,000 cells/plate) in methylcellulose for another week. The replating process was repeated for a total of three rounds.

Microscopic imaging

For γH2AX staining, cells were spun into microscope-glass slides (Fisher Scientific) at 300*g*, fixed, permeabilized and stained by anti-phosphoH2ax^{Ser139} (Biolegend) and Hoechst (Thermo Fisher). Images were taken by the GE/API Deltavision

widefield microscope. Live-cell, Cryo-TEM and EV imaging are described in detail in the appendix.

Statistical analysis

Paired and unpaired student′s t-test were used to compare flow cytometric results among two groups for IF and xenograft experiments, respectively. One-way ANOVA with Bonferroni correction was used to compare two or more groups and for qRT-PCR. Statistical significance was set at *P <0.05, **P <0.01, and ***P<0.001.

Funding

This study was supported by a Hyundai Hope on Wheels Scholar Grant, Max Blue Butterfly Campaign (P.K), and the OHSU Medical Research Foundation (S.A). Mass spectrometric analysis was performed by the OHSU Proteomics Shared Resource with partial support from NIH grants P30EY010572, P30CA069533, and S10OD012246.

Chapter 4: Extracellular vesicles traffic PD-L1 to confer CD8+T cell immunosuppression in acute myelogenous leukemia

Compiled from: *Butler, JT; Abdelhamed, S; Levasseur P. Bueafe A; Olsen, B; Chang, BH, P, Kurre and D Marks. Extracellular vesicles traffic PD-L1 to confer CD8+T cell immunosuppression in acute myelogenous leukemia (in preparation)*

Abstract

Acute Myelogenous Leukemia (AML) is an aggressive malignancy arising from abnormal myeloid-derived hematopoietic cells. For patients with AML, the 5-year survival remains a dismal 25% due to high rates of relapse and resistance to cancer drugs. There is mounting evidence that AML cells evade cell mediated immune system's anti-tumor response by upregulating immuno-inhibitory ligands. AML cells express PD-L1, a potent checkpoint ligand which disrupts T cell activation through engagement of PD-1. As a result, multiple clinical trials using checkpoint inhibitors in AML are ongoing, though efficacy has yet to be determined. A better understanding of PD-L1-related biology in the context of AML is critical to interpreting patient outcomes. Here we demonstrate that AML cells dynamically release functional PD-L1 onto extracellular vesicles (EVs), through an IFNγ-dependent mechanism. Using a syngenetic mouse leukemia model, we find that AML-EVs enter systemic circulation and bind splenic T-cells. Similarly, we find that EVs from AML cells lines and patient samples, potently suppress CD8+T-cell activation in response to TCR stimulation, and further show that PD-1/PD-L1 axis checkpoint blockade partially reverses EV-mediated suppression. Our study is the first to report that EV trafficking of PD-L1 contributes to CD8+T-cell dysfunction in AML, demonstrating a previously undiscovered mechanism of immune escape.

Introduction

Cytotoxic CD8+ T-lymphocytes play a vital role in opposing neoplastic cell growth. Through recognition and binding of tumor-specific neoepitopes, CD8+T-cells induce apoptosis in malignant cells, and limit tumor progression [129]. Despite these adaptive processes, cancer cells evade the immune surveillance by aberrantly expressing immunomodulatory proteins that suppress CD8+T-cell activation. Among them, Programed Death-Receptor Ligand 1 (PD-L1) is a well-known transmembrane protein that inhibits T-cell response. First discovered in myeloid cells as mechanism of self-tolerance, PD-L1 expression is widely co-opted across cancer due to the strong selective advantage of inhibiting cell mediated immune destruction [251]. PD-L1 ligation to its receptor, PD-1 found on T-cells, blocks the production of cytokines Interleukin-2 (IL-2) and Interferon -γ (IFN) involved in T-cell proliferation and effector function. This effectively suppresses the activation and clonal expansion of T-cells in response to T-Cell Receptor (TCR) stimulation.

AML is a heterogeneous malignancy arising from myeloid-derived hematopoietic stem and progenitor cells. Like other cancers, there is mounting evidence that AML cells are not immunologically silent [124]. Despite low mutational burden, expression of developmental antigens is common due to broad alterations in the epigenetic landscape [252]. The appearance of the Wilms Tumor-1 (WT-1) antigen is a common example of this, which occurs coincident with the development of reactive T-cell subsets in AML patients [124, 252]. While the high expression of developmental antigens is associated with improved survival, AML blasts can adaptively express immunomodulatory proteins, including PD-L1, to oppose immune destruction [124, 125, 136, 140, 253-259]. Similar to normal myeloid cells, the expression of PD-L1 by blasts and myelodysplastic cells remains dynamic in response to microenvironmental conditions. Several groups showed that lymphocyte-secreted IFNs and TNFα upregulate PD-L1 in AML and MDS, protecting dysplastic cells from T-cell-mediated cytotoxicity, and providing a proliferative advantage [260-262].

Exosomes and microvesicles—collectively referred to as extracellular vesicles (EVs)—have been found to contain surface-bound PD-L1 in the context of melanoma, glioblastoma, prostate and non-small cell lung cancer. Exosomes (EXs; 30-150nm), microvesicles (MVs; 50nm-1μm) are nanosized membrane-derived vesicles, which in the context of cancer, act to concentrate and transport cancer-specific regulatory cargo through the tumor microenvironment and blood to distant recipient cells. Vesicle-bound PD-L1 is functional, and suppresses CD8+Tcell activation and promotes tumor progression in multiple solid tumors [142, 143, 263, 264]. Prior work indicates that AML cells also release EVs that contain PD-L1 [139]. In the bone marrow, EV trafficking is involved in both maintaining homeostatic control of hematopoiesis, and creating a leukemia permissive microenvironment in patients with AML [6, 21, 23, 108, 139, 265]. For AML, there is growing evidence to suggest that AML-EVs potently suppress natural killer cells [139, 253], however research focusing on cytotoxic T-cells is more limited, and the functional nature of EV-associated PD-L1 remains to be determine.

For patients with AML and MDS, there are increasing reports of T-cell dysfunction, which are recapitulated in syngeneic animal models. AML is often accompanied by high expression of PD-1 and other inhibitory receptors on effector CD8+T-cells, with a weak response to CD28/TCR co-stimulation *ex vivo* [124, 125, 266, 267]. As a result of this mounting data, there are numerous ongoing clinical trials utilizing PD-1/PD-L1 checkpoint inhibitors in the treatment of AML [134, 135, 268-270].Thus far data from these trials suggests mixed efficacy, therefore a more comprehensive understanding of immune modulation in AML is critical to effectively harness the immune system to improve patient outcomes. We hypothesized that AML cells respond to microenvironmental IFNs by upregulating the expression and the release of PD-L1 via extracellular vesicles, where it functions to systematically dampen the anti-tumor response of effector T-cells. Herein we demonstrate using a syngeneic mouse model that AML-EVs are released into systemic circulation and bind splenic T-cells, reducing their capacity to expand *ex vivo*. We further show that AML cell lines and primary samples dynamically release EVs containing PD-L1 in response to IFNγ stimulation. These AML-EVs potently antagonize CD28/TCR co-stimulation, suppressing CD8+Tcell activation and expansion. Together these data provide strong

evidence that circulating EVs in AML actuate the PD-1 pathway in effector T-cells to systemically limit the anti-tumor immune response.

Results

AML blasts systemically release EVs that bind splenic T-cells

By creating AML cell lines that express myristoylated or palmitoylated GFP (mGFP or pmGFP) (**Fig 4.1A,C**), membrane-derived vesicles (**Fig 4.1B**) released from these cells retain the GFP reporter allowing for tracking and quantification in both *in vitro* and *in vivo* assays (**Fig 4.1D**) [6, 21, 108, 265]. In a previous study, by xenografting NSG mice with mGFP expressing human AML cells, we found that AML-EVs are shed into the peripheral blood at concentrations correlating with BM tumor burden (*see chapter 5*). To study the effect of AML-EVs in an immunocompetent animal model, we engrafted wild-type C57BL/6 mice with $1x10^5$ pmGFP expressing TIB-49 cells (ATCC: C1498) (**Fig 4.1E**), which are extensively used as murine model of leukemia [100, 101, 140, 271-273]. Animals were sacrificed between 21 and 25 days after inoculation to assess tumor burden. Flow cytometric analysis revealed limited infiltration of TIB-49pmGFP cells into the spleen with a mean value of 1.34% of total CD45+ cells (range 0.01-8.34%). The bone marrow contained a proportionally higher tumor burden (mean 6.5%; range 0.01%-49.2%) with principal sites of tumor growth occurring in the liver. Similar to our human xenograft model, the peripheral blood of TIB-49 engrafted animals contained numerous GFP+EVs (**Fig 4.1E-F**) that were detectable even at low tumor burdens (**Fig 4.1H**).

Figure 4.1: AML-EVs are released systemically and collect in the spleen

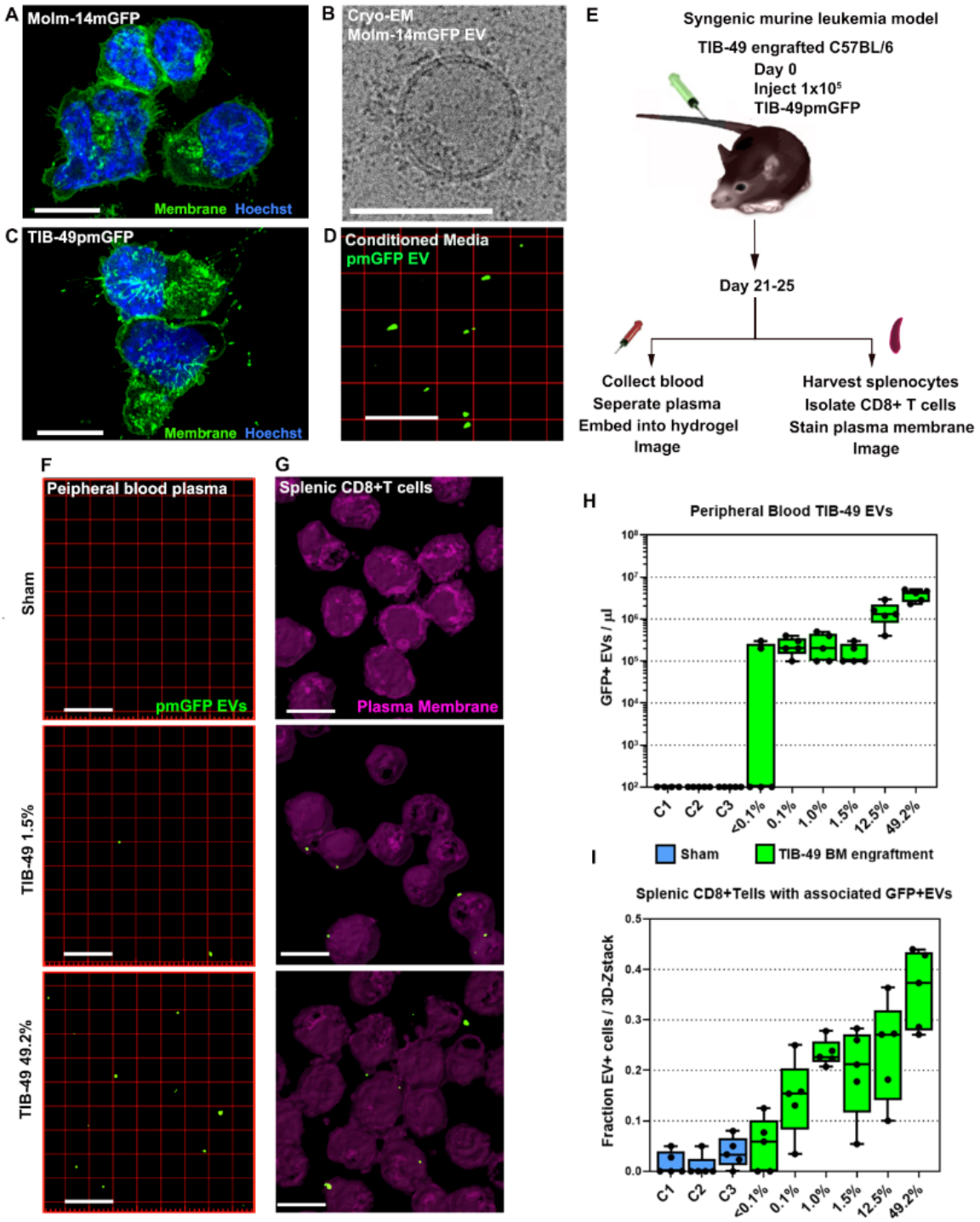

A) Molm-14 AML cells expressing endogenous GFP-tagged lipid membranes (mGFP; green). Scale bars = 5µm. **B)** Cryo-electron micrograph of exosomes harvested from Molm-14 cells. Scale bar = 100nm. **C)** Murine TIB-49 Leukemia cells expressing palmitoylated-GFP (pmGFP). **D)** EVs retain membrane-associated GFP and are detected in the conditioned media of TIB-49 cells. Scale bar = 5µm. **E)** Immunocompetent syngeneic AML model created by engrafting TIB-49pmGFP into C57BL/6 mice. Animals were maintained for 21-25 days before harvesting peripheral blood, bone marrow and spleens. **F)** Hydrogel embedding peripheral blood plasma reveals GFP+ EVs circulating in TIB-49pmGFP engrafted animals. Scale bare = 5µm. **G)** Splenic CD8+T-cells adsorb AML-EVs *in vivo*. **H)** Peripheral blood EV counts per µl increase with bone marrow tumor burden. Concentrations calculated from five 1x10-4 µl volumes per animal by super resolution imaging. **I)** Splenic CD8+T-cells with associated GFP+ EVs. Fraction EV associated T-cells measured with five 3D-Z stacks per animal.

To determine whether AML-EVs accumulate in the spleen and interact with T lymphocytes, we isolated splenic T-cells from both sham-injected and tumor engrafted animals (**Appx 4.1.1**). Flow cytometric analysis revealed that both CD4+ and CD8+T-cells contained detectable GFP+ foci (**Appx 4.2.1A**). To confirm that the GFP signal was due to AML-EVs, we purified CD8+T-cells by magnetic negative selection (Stem Cell) and performed 3-D *ex vivo* live cell imaging, using CellMask to label the plasma membrane (**Fig 4.1G**). We found that splenic CD8+T-cells from tumor animals contained bright localized GFP foci associated with the outer plasma membrane, that were similar in size and intensity to AML-EVs seen in the peripheral blood, as well as in previous *in vitro* imaging studies. In tumor animals, 10-40% of CD8+T-cells contained GFP foci which correlated to overall tumor burden in respective animals. As expected, T-cells isolated from sham-injected animals contained diffuse autofluorescence, but lacked bright localized GFP signal (**Fig 4.1G,I**).

CD8+T-cells from tumor animals have increased PD-1 expression and reduced response to co-stimulation

To assess the functional status of splenic CD8+T-cells from tumor-bearing animals, we used flow cytometry to measure cell counts, baseline PD-1 expression, and expansion

in response to co-stimulation with CD3/CD28 antibodies. We found that spleens from tumor animals had a 2-fold increase in total PD-1+/CD8+T-cells compared to sham animals, and decreased viability ex vivo. In tumor bearing mice, TIB-49 cell infiltration was significantly higher in the bone marrow compared to the spleen, yet the increase in PD-1+ T-cells was proportional at both sites (**Fig 4.2A-C; Appx 4.2.1B-D**). To measure splenic CD8+T-cell response to TCR stimulus, we stained purified CD8+T-cells from tumor and sham animals with CFSE and cultured for 5 days with CD3/CD28 co-stimulation to measure proliferation-dependent dye-dilution. Cells isolated from 6 tumor animals (3 animals per cohort) showed a significantly attenuated response to co-stimulation at day-5 compared to those from sham animals (**Figure 4.2D, Appx 4.2.1E**).

Additionally, we and others found that TIB-49 cells expressed low levels of PD-L1 *in vitro* [101], but significantly upregulated PD-L1 following engraftment, measured *ex vivo* upon harvest (**Fig 4.2E**). This upregulation of PD-L1 can be simulated *in vitro* by culturing the cells in IFNγ [101, 261, 274]. Following a 24-hour pulse with 20ng/ml IFNγ, TIB-49 cells showed a significant elevation of PD-L1, localized within the plasma membrane and endosomal compartment (**Fig 4.2F**).

Figure 4.2: Altered immunologic landscape in leukemic mice is recapitulated *in vitro* through EV-exposure

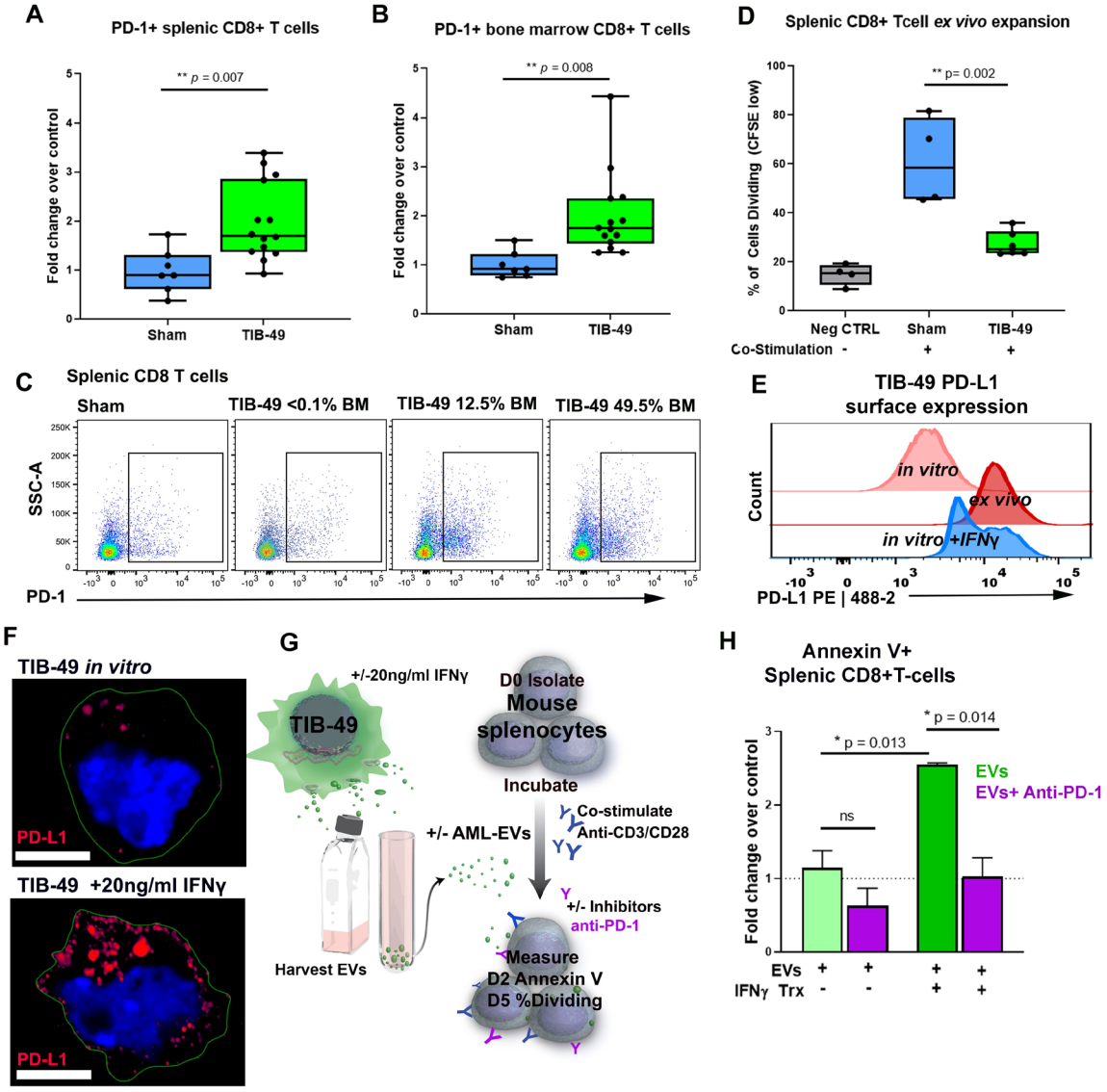

A-B) CD8+T-cells from tumor animals show an increase in PD-1+ expressing cells, in both the spleen and bone marrow that correlates with bone marrow tumor burden. Points represent individual animals. PD-1 expression normalized to sham injected animals **C)** Representative flow plots of PD-1+ CD8+T-cells from sham injected and tumor animals with varying bone marrow tumor burden. **D)** Splenic CD8+T-cells from tumor animals show reduced proliferation in TCR co-stimulation (anti-CD3/anti-CD28) as compared to Sham animals, and non-stimulated controls (Neg CTRL). Division measured by CFSE dye-dilution by gating on low intensity population 5 days after co-stimulation. **E)** Representative histograms of TIB-49 PD-L1 expression in under normal culture conditions (*in vitro)*, following bone marrow engraftment *(ex vivo), and* following culture with 20ng/ml mouse IFNγ for 24–hours (*in vitro+IFNγ*). **F)** Representative images of PD-L1 expression and localization (red) in TIB-49 cells cultured for 24-hours with or without 20ng/ml IFNγ. Scale bars = 5μm. **G)** Workflow for exposing CD8+T cells to EVs harvested from TIB-49 and measuring apoptosis and cell division by flow cytometry. **H)** Annexin V binding in CD8+T-cells exposed to EVs from TIB-49 cells (green) treated with or without IFNγ, and the addition of PD-1 blocking antibodies (magenta). **Graphs represent two technical replicates**. Annexin V binding normalized to non-EV exposed co-stimulated control vales Statistics: Significance determined by Student's two-tailed t-test, bars represent pairwise comparison. * $p<0.05$, ** $p<0.01$, *** $p<0.001$, ns = not significant. ***Additional Mouse in Vitro experiments in process (7/2/20). I) CD8+T cells proliferation (CFSE low-D5) in response co-stimulation and EV exposure. G) Add independent replicate to Annexin-V binding data set above.***

TIB-49-EVs suppress activation and proliferation of CD8+T-cells

With the widespread release of AML-EVs into the leukemic microenvironment, vascular space and lymphoid tissue, we set out to determine if purified AML-EVs alone were able to contribute T-cell dysfunction and reduced viability observed in our mouse model (**Fig 4.2G**). Since previous reports implicated AML-EVs in inducing apoptosis in CD8+T-cells [139, 253], we set out to test if EVs harvested from TIB-49 cells cultured *in vitro* could increase annexin-V binding in CD8+ splenocytes isolated from healthy C57BL/6 mice. Exposing bulk splenocytes ($2.5x10^4$) to EVs purified from *in vitro* cultured TIB-49

cells ($3x10^6$) for 48 hours surprisingly did not increase annexin-V binding in CD8+T-cells. Since PD-L1 expression was significantly upregulated *in vivo*, we set out to test if EVs from IFNγ-stressed TIB-49 cells resulted in an apoptotic response in T-cells. To simulate microenvironmental conditions we pulsed TIB-49 cells in IFNγ (20ng/ml) for 24-hours, washed twice, then cultured cells in EV-depleted media for an additional 24 hours before collecting EVs to prevent carryover of IFNγ to T-cells. EVs from IFNγ-stressed TIB-49 cells induced a 2.5-fold increase in annexin-V binding, compared to non-treated controls. To determine if EV-mediated apoptosis was dependent on PD-L1, we added PD-1 blocking (5ug/ml) antibodies at the time of EV exposure. PD-1 blockade completely rescued CD8+T-cells (**Fig 4.2H**), returning T-cell annexin-V binding to control levels (p= 0.014).

AML-EVs bind human CD8+T-cells and suppress activation

To determine if EVs from human AML cell lines can bind and suppress human CD8+T-cells, we exposed human CD8+T-cells to EVs collected from Molm-14mGFP cells treated with or without human IFNγ (*as described above*). First, to determine if AML-EVs bind CD8+T-cells, we isolated primary human CD8+T-cells by magnetic selection and co-stimulated with tetrameric anti-CD3/CD28 antibodies for 24hours. We then introduced AML-EVs (from 24h culture of $3x10^6$ cells) or vehicle for 24 hours, and analyzed the relative GFP fluorescence intensity in the CD8+T-cell population by flow cytometry (**Appx 4.3.1A**). Low intensity mGFP signal was detected in 3-5% of the T-cells across EV exposed conditions (**Appx 4.3.1C**). To examine EV-binding using a more sensitive approach, we co-stimulated CD8+T-cells for 24-hours, then added EV samples and incubated cells for 1-hour before washing and plating onto Matrigel coated imaging chambers. T-cells exposed to EVs from IFN-stressed AML cells showed a higher EV binding than T-cells from non-IFN-treated AML cells (48% vs 32%, p=0.037). In both EV-exposed conditions CD8+T cells contain mGFP+ foci similar in size and intensity to those previously observed in spleens of engrafted animals (**Fig 4.3A**), while control cells only contained diffuse autofluorescence.

To determine if AML-EVs interfere with T-cell viability and proliferation, we co-stimulated CD8+T-cells for 1-hour then added EVs from Molm-14 cells and healthy PBMCs (treated with and without IFNγ), and measured annexin-V binding (day-2) and CFSE dye dilution (day-5). CD8+T-cells ($2.5x10^4$ cells) were incubated with EVs collected from standardized cultures of $3x10^6$ AML cells or PBMCs cells for 24 hours. Activation of EV-exposed T-cells was compared against controls that were not co-stimulated (C1) or were co-stimulated in vehicle only (C2). We found that EVs from Molm-14 cells significantly increased annexin-V binding roughly 1.5-fold regardless of IFNγ treatment status, while EVs from PBMCs slightly increased annexin-V binding but only following IFNγ treatment (**Fig 4.4B-C**). CFSE dye-dilution analysis revealed that EVs from Molm-14 cells treated with IFNγ significantly reduced 5-day proliferation (CFSE low population) to 86% of non-EV exposed control levels ($p<0.001$), while EVs from non-IFN treated Molm-14 cells and PBMCs had a milder effect (**Fig 4.4D-E)**. To determine if the reduction of proliferating T cells was due to suppression of T-cell activation, we exposed co-stimulated CD8+T-cells to EVs from multiple IFNγ-treated AML cell lines and 293TmGFP (non-hematopoietic mGFP expressing cells), and measured the canonical T-cell cytokine response 24-hours later (**Fig 4.3B).** Activation status was assessed by intracellular staining and flow cytometry to detect the expression of IL-2 and IFNγ involved in early in T-cell activation and expansion [275]. We found that EVs harvested from AML cell lines potently suppress T-cell activation at 24-hours post-co-stimulation (**Fig 4.3F-I; Appx 4.3.1C**), while EVs collected from 293T cells (similarly expressing mGFP) had no effect on T-cell activation.

To test if patient-derived EVs could interfere with T-cell co-stimulation, primary peripheral blood mononuclear cells (PBMCs) were obtained from the five AML patients with >80% circulating blasts (**Table 4.1**). These patients were selected based on RNA-seq data which identified them as PD-L1 high expressers with adverse or intermediate risk (P1, P2, P3) or PD-L1 low expressers with intermediate risk (P4, P5) from the Beat AML collection [258]. To collect EVs, $1x10^7$ patient-derived mononuclear cells were cultured for 48-hours in EV-depleted media (without growth factors to prevent carryover to T-cells) before collecting conditioned media and concentrating EVs by ultracentrifugation. Since

both the potency of EVs and the dynamics of release likely vary between patient-specific blasts, EV dosages were again standardized by concentration of parent cells. Human CD8+T-cells were exposed to patient-derived EVs for 24-hours, before measuring cytokine response (*as previously described)*. T-cells exposed to patient-derived EVs demonstrated markedly reduced IL-2 and IFNγ production compared to T-cells treated with EVs collected from healthy PBMCs (**Fig 4.3J-K**). Four out of five patient-derived EV samples significantly reduced the percent of T-cells expressing IL-2 (P1 p=0.015; P2 p=0.015, P3 p=0.009; P4 p=ns; P5 p=0.024) and IFNγ. Due to limited availability, and lack of proliferation of patient-derived blasts in culture, T-cell suppression assays using primary-AML derived EVs were performed in triplicate in one standalone experiment.

Table 4.1: Patient Data

Alias	Beat AML ID	AML (WHO)	Risk	PD-L1 Expression status (RNAseq)	Sample Type
P1	14-0041	**AML with inv(3)(q21q26.2)**	Adverse	High	PB >80% blasts
P2	16-0479	**AML with myelodysplasia-related changes**	Intermediate	High	PB >80% blasts
P3	15-0539	**Acute monoblastic and monocytic leukemia**	Adverse	High	PB >80% blasts
P4	14-0355	**Acute monoblastic and monocytic leukemia**	Intermediate	Low	PB >80% blasts
P5	16-0077	**Therapy-related myeloid neoplasms**	Intermediate	Low	PB >80% blasts

RNAseq: High expression >1 by normalized RPKM from BEAT AML, low expression <1 [258]

Figure 4.3: AML-EVs bind and suppress human CD8+T-cells

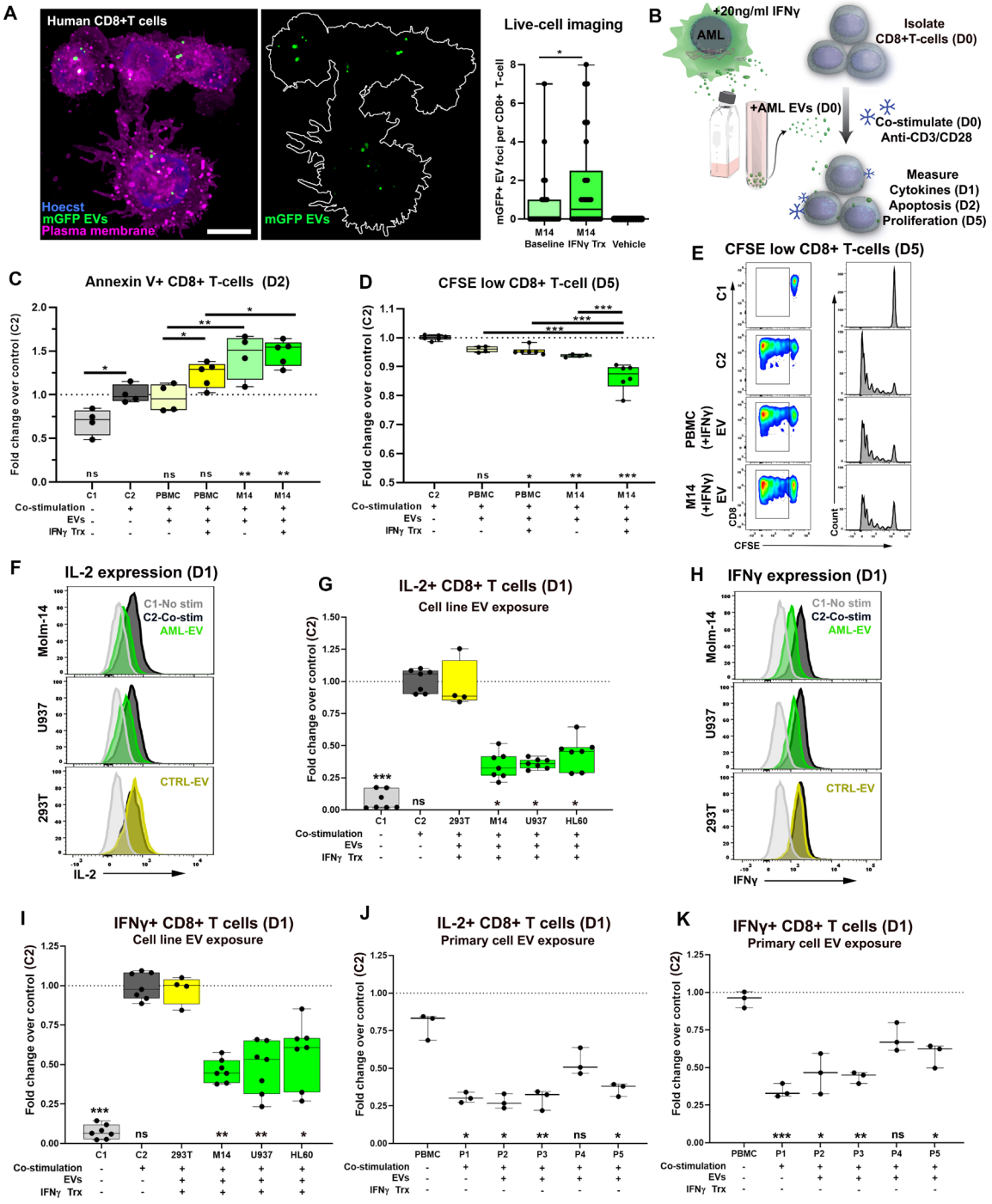

A) Super resolution microscopy confirms that GFP labeled AML-EVs (green) bind CD8+Tcells (magenta) which are detectable on the surface and internally after 1 hour of exposure. (Left) 3D Z-stack displayed as maximum projection. Scale bar = 10μm. (right) Quantification of mGFP+ foci in T-cells exposed to EVs from Molm-14mGFP cells treated with or without IFNγ, points represent individual cells (n=35). Significance determined by Student's two-tailed T test ($p<0.05$). **B)** Workflow for exposing human CD8+T cells to EVs (harvested from AML cell lines, patient samples and healthy PBMCs) and measuring response to co-stimulation. **C)** Annexin-V binding on CD8+Tcells exposed to EVs from AML (green) and healthy PBMCs (yellow) treated with and without IFNγ. Annexin-V binding assessed by flow cytometry at day-2 post co-stimulation. **D-E)** CD8+Tcells proliferation following exposure of EVs from AML (green) and healthy PBMCs (yellow) treated with and without IFNγ. CFSE low population measured 5-days post co-stimulation. (C-D) Significance determined by one-way ANOVA with Dunnett's T3 multiple comparison to C2 control value (lower). Direct comparison between conditions was performed by students two-tailed T test (upper). **F)** Histograms of IL-2+/ CD8+T-cells at baseline (C1), following co-stimulation (C2), or following co-stimulation with AML (green) or 293T CTRL (yellow) EV exposure. **G)** IL-2+/CD8+T-cells at baseline (C1), following co-stimulation (C2), or following co-stimulation with AML (green) or 293T CTRL (yellow) EV exposure. **H)** Histograms of IFNγ+/CD8+T-cells at baseline (C1), following co-stimulation (C2), or following co-stimulation with AML (green) or 293T CTRL (yellow) EV exposure. **I)** IFNγ+/CD8+T-cells, at baseline (C1), following co-stimulation (C2), or following co-stimulation with AML (green) or 293T CTRL (yellow) EV exposure. (C, D, G ,I) Graph represents two independent replicates with 2-4 technical replicates per condition, data normalized to non-EV exposed co-stimulated control (C2) values. **J)** IL-2+/CD8+T-cells following co-stimulation with or with EVs harvested from PBMCs of five AML patients (P1-P5) or healthy controls (PBMC). **K)** IFNγ+/CD8+T-cells following co-stimulation with or without EVs harvested from PBMCs of five AML patients (P1-P5) or healthy control (PBMC). **J-K)** Due to limited sample graph represents a standalone experiment with three technical replicates. Statistics: Significance was determined by one-way ANOVA with Dunnett's T3 multiple comparison test to 293T EVs for cell line experiments, or healthy PBMCs for patient derived samples. (* $p<0.05$, ** $p<0.01$, *** $p<0.001$, n.s.= not significant)

AML cells transiently upregulate PD-L1 in response to IFNγ

To characterize PD-L1 expression across AML subtypes, we stained three AML cell lines and primary peripheral blood mononuclear cells from five AML patients and

measured surface expression by flow cytometry and immunofluorescence. Cell lines and patient samples expressed variable levels of PD-L1 at baseline (**Appx 4.4.1A**). For patient samples, their peak fluoresence intensities were consistent with RNA seq values, however there was significant heterogeneity observed within 3 of the 5 patient samples, suggesting distinct subclones of blasts or myeloid derived suppressor cells expressing higher levels of PD-L1. Imaging of PBMCs from patient P2 confirmed a mixed cellular morphology. The majority of cells had a typical "blast-like" appearance with scant cytoplasm, a large central nucleus, and low expression of PD-L1 (**Appx 4.4.1B;** left panel). Interestingly, a rare subset of myeloid cells demonstrated a larger and more complex cytoplasm, with numerous filopodia and blebbing membrane regions. These cells frequently contained robust PD-L1 expression that localized to filopodial extensions, and more clearly demarcated the outer membrane and clustered within membrane pits (**Appx 4.4.1B**; right panel).

To measure the response to T-cell secreted IFNγ on PD-L1 expression, we treated AML cells lines and patient samples with 20ng/ml IFNγ. This resulted in a significant increase in PD-L1 surface expression by 24 hours across AML samples tested (Molm-14, U937, P3, P4, P5) (**Fig 4.4A**). Myeloid (CD33+) PBMCs taken from a healthy donor (hPBMC), also significantly upregulated PD-L1 in response to IFN. Super resolution imaging confirmed the increase in PD-L1 in Molm-14 cells, and showed that in a rare subset of cells, IFNγ exposure induces a vesiculated appearance, which contained PD-L1 localized within blebbing membrane regions (**Fig 4.4B**). Taken together, these results indicated that at baseline patient derived AML variably express PD-L1 yet significantly upregulate surface-bound PD-L1 in response to IFNγ similar to the TIB-49 cells and healthy CD33+ PBMCs.

PD-L1 is shed on AML-EVs and is enhanced by IFNγ exposure

To determine if PD-L1 is released onto membrane-derived EVs, we performed density gradient purifications to isolate EVs into fractions of sequential density and separate soluble protein. Cell culture supernatant from Molm-14s and U937s (treated with and without IFNγ) were separated into 20 fractions by serial ultracentrifugation in layered solutions of iodixanol (**Fig 4.4C**). Again, Molm14 cells that express myristoylated GFP

were used in this experiment, allowing for fluorescent identification of the fractions containing sedimented mGFP+ EVs (**Fig 4.4D**). The Individual fractions were then transferred onto PVDF membrane and stained with anti-PD-L1 antibody. Staining was found within the fractions that co-sedimented GFP+ EVs, with peak GFP intensity and PD-L1 concentrating in fractions with densities consistent for EXs and small MVs (**Fig 4.4D**; Fraction 13 and 14: 1.090-1.130 g/ml) [142, 276]. EV-associated PD-L1 was detected for Molm-14 but not U937s at baseline (**Appx 4.5.1A**), however EV-associated PD-L1 was detected from both cell types following a 24-hour pulse with IFNγ, and continued to increase 24-hours after washing out IFNγ (**Fig 4.4D**). Interestingly IFNγ exposure also increased the intensity and total fractions positive for mGFP signal (**Fig 4.4D; Appx 4.5.1A-B**), indicative of an increase in total EV release. Of note, mGFP or PD-L1 signal was not detected in lower density fractions containing predominantly soluble protein, or in conditioned media that was depleted of EVs by ultracentrifugation ("100K SPNT") (**Appx 4.4D**).

To further confirm the presence of PD-L1 on AML-EVs, we harvested EVs by differential ultracentrifugation and performed Western blots for PD-L1 using TSG101 as an exosome-specific control [277]. Western blots (with Licor imaging) showed that vesicles collected from Molm-14 and U937 stained for PD-L1, producing a 50kDA band and a faint 30kDa band. Similar to the dot blot array, IFNγ treatment induced an increase in both total EVs (TSG101) and vesicle associated PD-L1. In contrast to the results of the dot blot array, PD-L1 was detected at baseline in U937 EVs by western blot (using higher sample volume), and revealed an additional ~45kDA band following IFNγ exposure in both cell types. (**Fig 4.4E**; **Appx 4.5.1C**). EV-associated PD-L1 was further confirmed by western blot using an alternate PD-L1 antibody and method *as described in Chen et al., 2018* [142] (**Fig 4.4F; Appx 4.5.1D**).

To measure the relative change in PD-L1+EVs in response to IFNγ, EVs were immunocaptured using imaging chambers pre-coated with anti-PD-L1. We found a 1.5-fold increase in anti-PD-L1-bound mGFP+ EVs from 100K pellets of IFNγ-treated Molm-14mGFP cells versus non-treated cells under volume matched conditions (**Appx 4.4D-E**).

In contrast to this finding, analysis by ELISA (Quantikine R&D systems) failed to detect PD-L1 in all purified EV samples (without lysis), yet detected extracellular PD-L1 in the sera of AML patients, and healthy controls, with the highest concentrations found in AML patients (**Appx 4.4F**).

Using high-resolution flow cytometry (HRFC) we characterized EVs directly from conditioned media of AML cell lines [278, 279]. Through this method, we identified that mGFP+ EVs (Molm-14) co-stain with tetraspanins CD63 and CD9, hematopoietic marker CD45, adhesion molecule ICAM1, but not megakaryocyte/platelet marker CD41 (**Appx 4.6.1A**). Pulsing cells with 20ng/ml IFNγ increased the total mGFP+ EVs by 2-fold in conditioned media from 48-hour cultures (p=0.022) (**Fig 4.4G**). At baseline, very few PD-L1+ EVs were detectable in conditioned media from Molm-14, U937 and TIB-49 cells by HRFCs. Interestingly, the PD-L1+ EVs were not highly detected during IFNγ exposure, but increased significantly after IFNγ was removed and cells were returned to fresh media. Across cell lines, we detected an increase in PD-L1+ EVs in conditioned media 24- to 48-hours post-IFNγ pulse, which occurs coincident with the loss of PD-L1 from the cell surface (**Fig 4.4G-J**). At 24- and 48-hours post-IFNγ pulse, we detected a significant 1.8- and 2.8-fold increase in total PD-L1+ EVs released from Molm-14 cell respectively (p=0.036, p=0.026), while U937 increased 1.7- and 4.5-fold, but failed to reach significance (p=0.286, p=0.055). To validate antibody binding to vesicle-associated epitopes, we added detergent Triton X-100 to disrupt lipid-membrane, which resulted in a loss of both mGFP+ and PD-L1+ vesicle populations (**Fig 4.4I; Appx 4.6.1B**).

Figure 4.4: PD-L1 is shed on AML-EVs and is enhanced by IFNγ exposure.

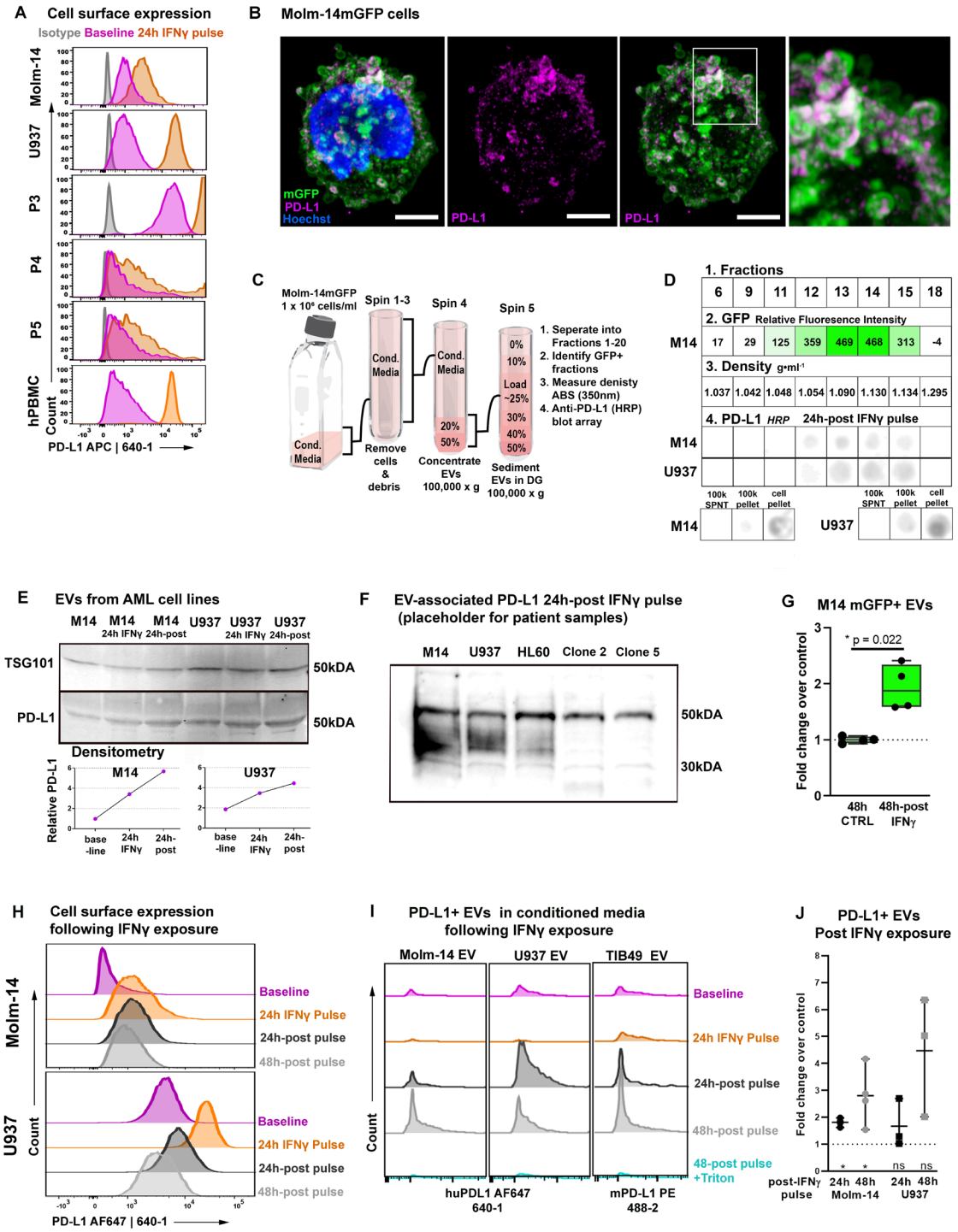

A) Histograms of AML cell line and patient-derived PBMCs PD-L1 expression at baseline (magenta) and following IFNγ exposure (10ng/ml), as measured by flow cytometry. **B)** Molm-14 cells endogenously expressing mGFP were pulsed with IFNy overnight and stained with PD-L1 (magenta) and Hoechst (DNA, blue); Super resolution microscopy demonstrations clusters of PD-L1 (magenta) localizing to membrane-associated vesicles (mGFP, green) that protrude outwards from the plasma membrane. Scale bars = 5 μm. **C)** Diagram showing the workflow for purification of EVs by centrifugation in discontinuous iodixanol density gradients solutions. **D)** Analysis of density gradient fractions with peak membrane-tagged GFP+ EVs and associated PD-L1 residing in fractions 13 and 14 (1.09 – 1.13 g/ml). GFP measured by plate reader (488ex/510em), density measured by iodixanol absorbance at 350nm, and PD-L1 by immunoblot array. **E)** Western blot analysis of EV-associated PD-L1 and exosomal marker TSG101 released from AML cell lines ($3x10^6$ total cell per condition) at baseline, after a 24-hour pulse of IFNγ (10ng/ml), and 24 hours after IFNγ washout. Graphs show relative densitometry normalized to TSG101 for Molm-14 EVs (upper) and U937 EVs (lower). **F)** Western blot confirmation of AML-EV associated PD-L1 from IFNγ pulsed AML cell lines using an additional primary antibody validated by Chen et al., 2018. **G)** mGFP+ EVs increase in conditioned media (48-hour cultures) following IFNy pulse. Significance determine by Student's two tailed t-test. **H)** Baseline cell surface expression of PD-L1 (pink) increases following 24-hour pulse with INFy (orange) and diminishes at 24-hour (black) and 48-hours (light grey) after washing out IFNγ. **I)** Relative change in PD-L1+ EVs from conditioned media of AML cells at baseline (magenta), following a 24-hour pulsed in IFNγ (orange), and 24-hours (black) and 48-hours (light grey) after washing out. EV-associated PD-L1 signal increases after IFNγ wash out across samples but is lost after addition of Triton X-100 detergent (blue). Histograms represent total PD-L1+ events per 60 seconds. **J)** Relative change in PD-L1+ EVs in conditioned media of AML cells at 24-hours and 48-hours post-IFNγ pulse. Fold-change normalized to conditioned media from non-treated cells. Results from two independent experiments with multiple replicates per condition. Significance determined by student's two-tailed t-test in pairwise comparison to non-treated control values. (*$p<0.05$, ns = not significant).

Treating AML cells with GW4869 modulates EV release and resulting T-cell suppression

We set out to determine if treating AML cells with GW4869—an inhibitor of sphingomyelinase and exosomal release—would result in a detectable change in EV

release and alter the suppressive effect on CD8+T-cells. Using HRFC, we found that conditioned media from AML cells treated with GW4869 (10uM) produced approximately 36% fewer GFP+ EVs after 24-hours of treatment (p=0.042), compared to vehicle treated control cells (**Fig 4.5A-B; Appx 4.6.1C-D**). To compare the change in EV-mediated suppression, Molm-14mGFP cells were treated IFNγ for 24 hours, washed then treated with or without the addition of GW4869 for 24 hours. EVs were concentrated from conditioned media by ultracentrifugation (100K x g pellet), and exposed to T-cells in volume matched conditions. EV exposed T-cells were cultured along with co-stimulatory antibodies for 24-hours before measuring IL-2 production as previously described. Treatment of Molm-14 cells with GW4869 reduced the suppressive effect of 100k pellets, increasing the number cells expressing IL-2 from 45% to 61% (p=0.019) of co-stimulated control values (**Fig 4.5A, C**).

Blocking PD-1/PD-L1 rescues AML-EV induced T-cell suppression

To test whether the suppression of CD8+T cells is mediated by AML-EVs in a PD-1 dependent manner, T-cell function assays were performed as previously described with the addition of blocking antibodies (**Fig 4.5A**). Induction of T-cell apoptosis in response to Molm-14 EVs was significantly reduced from 1.48-fold to 0.79-fold compared to control levels following PD-1 blockade (p<0.001). Interestingly anti-PD-1 also decreased annexin V binding in T-cells exposed to EVs from IFNγ treated PBMCs (1.23-fold to 0.65-fold p<0.001), but not EVs from non-IFN treated PBMCs (0.96 to 0.86; non-significant) as compared to controls (**Fig 4.5D**). Incorporating PD-1 blockade also partially restored T-cell proliferation in response to AML-EVs in CFSE dye dilution assays. PD-1 blockade increased the proliferative population from 0.86% to 0.95% of control values (p<0.001), while anti-PD-L1 antibodies failed to produce the same effect (**Fig 4.5E**). Additionally, to determine if checkpoint blockade could restore T-cell activation in response to AML-EVs, we measured IL-2 and IFNγ production following co-stimulation as previously described. In AML-EV exposed conditions, both PD-1 and PD-L1 blockade increased IL-2 production in T-cells from 35% to 72% (p<0.001) and 69% (p<0.01) of non-EV exposed

control values, respectively (**Fig 4.5F; Appx4.7.1A-C**). This effect was also seen EV samples collected from three out of five patients (**Fig 4.5G; Appx 4.7.1A-D**), with anti-PD-1 providing a more robust response across conditions than anti-PD-L1. Importantly, treating co-stimulated T-cells with blocking antibodies in the absence of AML-EVs did not significantly alter annexin-V binding, proliferation or cytokine response in CD8+T-cells. In sum, our data demonstrates a mechanism by which AML blasts export PD-L1 via EVs in response to T-cell secreted IFNγ. AML-EVs impair CD8+ T cell function by suppressing activation and expansion, which can be rescued by blocking PD-1 at the T-cell surface (**Fig 4.6**).

Figure 4.5: Blocking EV release or PD-1 binding rescues AML-EV induced T-cell suppression

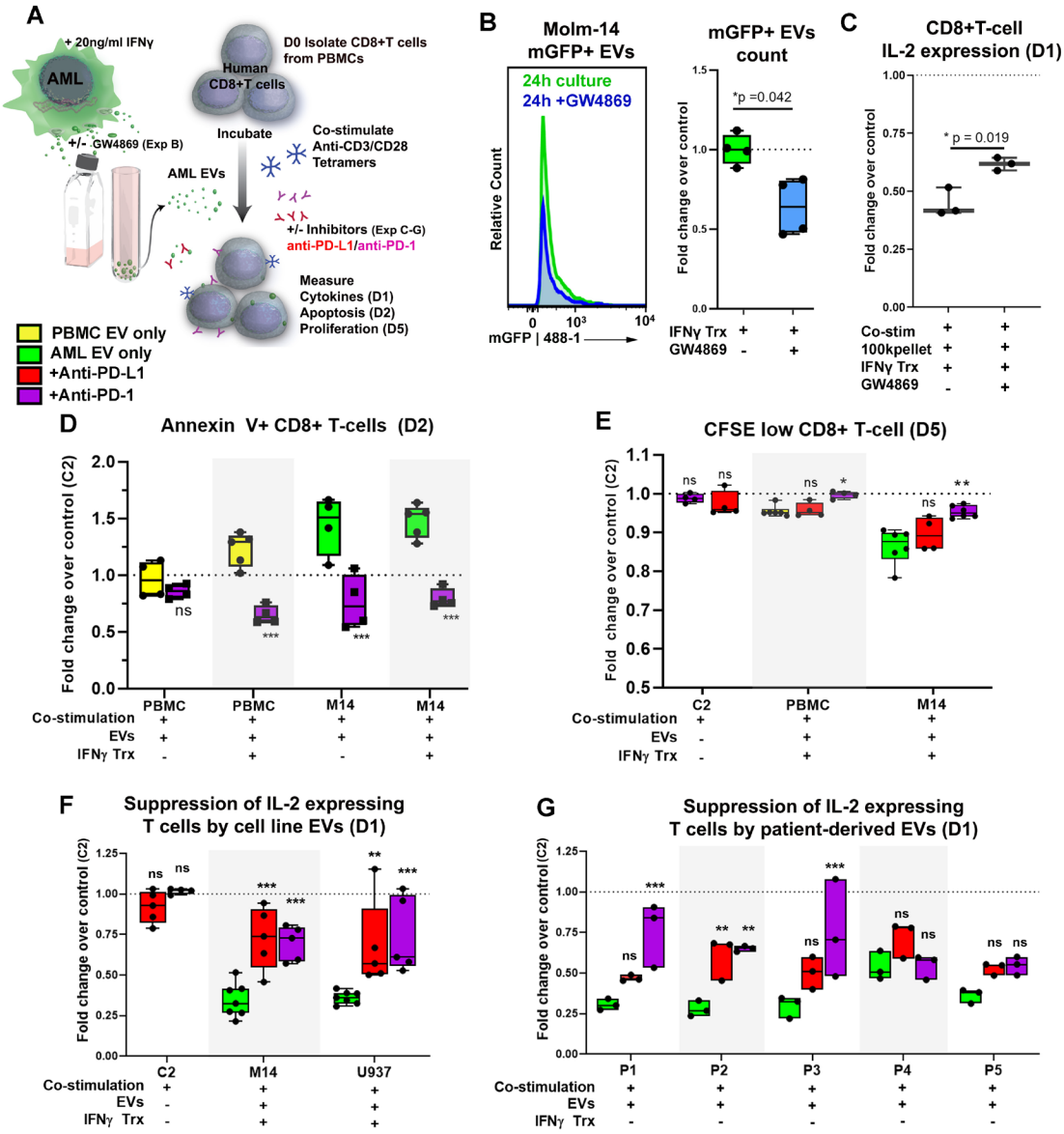

A) Workflow for pretreating AML cells with exosomal release inhibitor GW4869, and preforming T-cell suppression assays with or without immune checkpoint blocking antibodies. **B)** Representative HRFC histograms (left) and fold change (right) in mGFP+ EVs released in a 24-hour culture from Molm-14mGFP treated with GW4869 (blue), normalized to untreated controls (green). **C)** CD8+T-cells exposed to 100K pellets from Molm-14 cells pretreated with GW4869 has significantly less effect on IL-2 expression compared to 100K pellets from untreated Molm-14 cells. Data normalized to non-EV treated co-stimulated control values. B-C) Significance determined by Student's two-tailed t-test. **D)** Annexin-V staining on CD8+T cells following EV exposure with or without PD-1 blocking antibodies. **E)** Proliferating CFSE low CD8+T-cell population following exposure to EVs with or without addition of blocking antibodies (PD-L1, red; PD-1, Purple). **F)** CD8+Tcell production of IL-2 following exposure to cell line AML-EVs alone, or with the addition of blocking antibodies (PD-L1, red; PD-1, Purple). Total cytokine expressing cells in each condition compared to non-EV exposed controls that were co-stimulated (C2) with blocking antibodies, and normalized to co-stimulated controls without blockade. Graphs represent two biological replicates with 2-4 technical replicates per condition. **G)** CD8+Tcell production of IL-2 following exposure to patient-derived PBMC EVs alone, or with the addition of blocking antibodies (PD-L1, red; PD-1, Purple). Total cytokine expressing cells in each condition normalized to co-stimulated controls without blockade. Due to limited sample, graph represents a standalone experiment with three technical replicates. Statistics: **D-G)** Significance determined by two-way ANOVA with Tukey's multiple comparison test to respective EV exposed conditions without antibody blockade. (* $p<0.05$, ** $p<0.01$, *** $p<0.001$, n.s.= not significant).

Figure 6: Synopsis

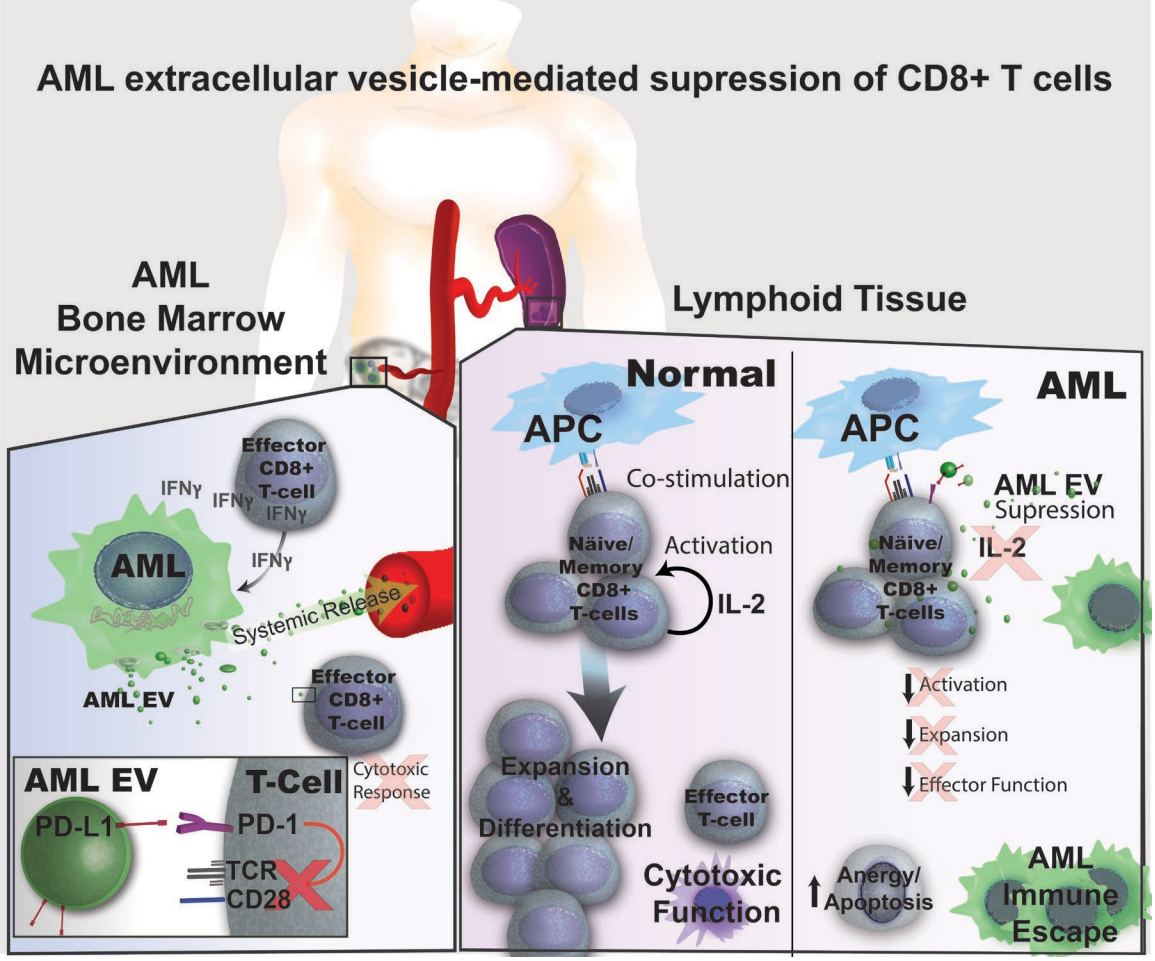

Discussion

Recently, tumor-derived EVs emerged as a powerful mediator of resistance to both chemo and immune based therapies in hematological malignancies [118, 123, 139, 253, 280]. In multiple solid tumors models, the release of PD-L1+ EVs support immunotolerance by suppressing the function of CD8+T-cells in both the tumor microenvironment and distant lymphoid tissue [142, 143, 263, 264]. Our study provides strong evidence for the involvement of PD-L1+ exosomes and microvesicles in dampening the T-cell mediated anti-tumor response in AML. The widespread release of AML-EVs is known to create a leukemia permissive microenvironment by dysregulating recipient cells in the bone marrow. Here we show that EV-mediated dysregulation extends to cytotoxic T cells, both in the bone

marrow and peripherally. It is known that AML-EVs directly inhibit cell mediated immunity by subduing Natural Killer cells, and promoting regulatory T-cells expansion and function [139, 281]. Here we demonstrate that AML-EV similarly impact CD8+T-cell function. We show that multiple AML subtypes shed PD-L1 on EVs, which is enhanced in response to IFNγ stimulation, and likely other inflammatory cytokines produced by immune cells in the tumor microenvironment. Though it was previously reported that AML cells release EVs that contain PD-L1 [139], we are the first to elucidate their biological effect on CD8+T-cells, and demonstrate that AML-EVs directly suppress T-cell activation in response to TCR stimulation. These findings demonstrate another mechanism which allows AML to evade the immune system's anti-tumor response and possibly mediate resistance to immune based therapies.

We demonstrated, using a syngeneic immunocompetent murine leukemia model, that EVs enter the peripheral blood, and bind CD8+T-cells within the spleen. The direct infiltration of TIB-49 cells into the spleen, remained low in this model with a median value of 0.099% of total CD45+ splenic cells across 14 tumor animals (range 0.01-8.3%), making it ideal to study the trafficking of AML-EVs from the tumor microenvironment to distant lymphoid tissue. The splenic CD8+T-cells harvested from tumor animals showed a reduced capacity for expansion and expressed higher levels of PD-1, rendering them more susceptible to ligation by PD-L1. *In vitro*, leukemia-derived EVs also directly induced T-cell apoptosis, and blocked expression of cytokines IL-2 and IFNγ, limiting expansion in both murine and human models.

It is not surprising that myeloid-derived leukemia cells—like their differentiated myeloid counterparts involved in self-tolerance—have the ability to dynamically express PD-L1 in response to extrinsic signaling. Unlike many solid tumors that constitutively activate PD-L1 through mutations in IRF1, the expression of PD-L1 on AML blasts is an adaptive response to microenvironmental stress and exposure to cytokines such as IFNγ [260-262]. A recent study found that AML patients with refractory disease displayed higher expression of IFN-related genes in the tumor microenvironment [99], while in other cancers microenvironmental IFNγ signaling is linked to resistance to immune checkpoint blockade

[282]. Therefore, the contribution of the PD-L1/PD-1 interaction in mediating T-cell dysfunction in AML may be underestimated due the heterogeneous and transient expression of PD-L1 on blasts, which is dependent on microenvironmental context and interactions with immune cells. This is demonstrated by engrafting TIB-49 cells into C57BL/6 mice, which express very low levels of PD-L1 in culture [101]. *In vivo* TIB-49 cells adaptively upregulate PD-L1 to dampen immune cell activation and proliferation in response to effector T and NK cell secreted cytokines. This is further supported by the fact that the TIB-49 cells used in our mouse model express a highly abundant "neoantigen", as the cells contain membrane-tagged GFP, spanning both the inner and outer membrane of the cells. Despite this abundant foreign antigen, the cell mediated immune system failed to clear TIB-49 cells, allowing for tumors to establish in immunocompetent C57BL/6 mice, providing further evidence of a dysfunctional anti-tumor response.

In our study, all AML cell lines and patient-derived PBMCs tested responded to IFNγ stimulus by upregulating PD-L1 surface expression, similar to healthy peripheral blood myeloid cells. Intriguingly, release of PD-L1 onto EVs was primarily enhanced following the removal of IFNγ stimulus, whereby protein abundance appeared to shift from the cell surface into released extracellular vesicles. We found that IFNγ exposure increased the release of total mGFP+ EVs from AML cells in response to IFN exposure. This is in contrast to a study of prostate cancer cells which showed that PC3 cells shed more EV-associated PD-L1, but had no effect on total amount of EVs released from the cells [143].

In this model, shedding of EVs enforces immune suppression by trafficking EV-associated PD-L1 throughout the tumor microenvironment and blood to dysregulate CD8+T-cells. When blasts experience high levels of IFN indicative of proximal activated effector T cells, PD-L1 surface expression is favored, however when IFN stimulus is lost, PD-L1 is shed from the surface likely along with other IFN-upregulated proteins such as MHC. We propose that AML-EVs act to concentrate immune checkpoints for targeted delivery to CD8+T-cells over long distances, whereby soluble forms of PD-L1 would diffuse in extracellular space, limiting effective concentrations at sites distant to the secreting cell. Furthermore, myeloid cells from the PBMCs of healthy subjects responded

to IFN by upregulating surface expression of PD-L1, as expected. Interestingly EVs harvested under these conditions induce a minor increase in T-cell apoptosis and suppression of proliferation that was restored following PD-1 blockade. These results may indicate a role of PD-L1+ EVs in modulating immune response under non-malignant conditions, and requires further study.

Once released, it is currently unknown how AML-EV are able to target and bind distant CD8+T cells. One possibility is that PD-L1 itself is involved in docking EVs onto the T-cell surface, and that blocking PD-1 reduced EV binding to T-cells [263]. Although we have seen some evidence of this in our flow cytometry experiments, additional and more sensitive methods are needed to confirm this finding. Additionally, we have preliminary data indicating EVs from AML cell lines contain abundant leukocyte functional antigen (LFA)-associated adhesion molecules, ICAM1 and CD44. We hypothesize that these adhesion molecules act to target AML-EVs to effector T-cells expressing LFA-1 and E-Selectin. The presence of surface-bound ICAM1 on AML cells and EVs—like PD-L1—is also upregulated in response to IFNγ (**Appx 4.4.1C, 4.6.1C-D**). This increase in ICAM1 (in addition to an increase in total EV release) would also help explain why IFNγ exposure escalates AML-EV binding onto CD8+T-cells. It was previously reported that mature dendritic cells release ICAM1+ and MHC-II+ exosomes, which function to enhance priming of naïve T-cells [283]. Together these additional surface proteins may shed light on how AML-EVs target and bind T-cells, and merit further study.

For AML, remission following stem cell transplantation relies on a T-cell mediated graft-versus leukemia effect, highlighting the importance of T-cells in opposing tumor growth [284]. Therapeutic strategies to increase AML antigenicity with hypomethylating agents, or increase reactive T-cells through adoptive transfer, are both promising. Unfortunately, relapse following treatment often occurs with high expression of PD-1, and other exhaustion markers, such as T-cell immunoglobulin and mucin domain-containing protein 3 (TIM-3), B- and T-lymphocyte attenuator (BTLA), and Lymphocyte Activation gene-3 (LAG-3) on autologous and/or allografted T-cells [128, 270, 285-287]. Frequently, chemotherapeutic non-responders also show elevated expression of exhaustion markers on

peripheral blood and bone marrow CD8+T-cells [271, 288]. T cell exhaustion in AML is driven in part by PD-L1 [259], where high expression levels are associated with poor prognosis [289]. Multiple pre-clinical studies demonstrate that this PD-L1 mediated immune suppression is prevented by PD-1/PD-L1 blockade and related MEK inhibitors [102, 259, 261, 262, 274]. As a result of these findings, there are numerous ongoing clinical trials utilizing PD-1/PD-L1 checkpoint inhibitors in the treatment of AML, yet efficacy has yet to be determined [134, 135, 268-270]. Our data indicates that systemic release of EVs which are found extensively throughout the marrow, blood, and spleen [21, 168, 253, 265, 290, 291], contribute to T-cell exhaustion, and may impede response to immunotherapy.

Through our studies, we found that AML cells release EVs into the bone marrow microenvironment and directly into circulation, which are present in high concentration within the peripheral blood. At 12.5% bone marrow engraftment we measured 10^6 AML-EVs/ µl of blood, roughly 10^3 AML-EVs per circulating CD8+T-cell [292]. PD-1 ligation is best known for inhibiting effector T cells in the tumor microenvironment, yet recent evidence from murine viral models shows that it constrains responses across the differentiation spectrum, including naïve T-cell activation, where PD-1 is rapidly upregulated in response to TCR/peptide binding, prior to cell division [293]. Therefore, both the local and systemic release of extracellular PD-L1 (and other inhibitory ligands) via AML-EVs likely provides AML blasts a secondary protection against tumor infiltrating lymphocytes, antagonizing the function of local effector T-cells, while also altering the activation and differentiation of naïve T –cells in distant lymphoid tissues [293].

For AML, enhancing the T-cell response through incorporating checkpoint blockade into chemotherapeutic regiments and post-induction transplantation, may indeed provide a more durable remission. Similar to findings in Melanoma, it is possible that circulating PD-L1+ EVs levels may be a viable biomarker to predict patient response to checkpoint inhibitor therapy [142]. Furthermore, the systemic abundance of AML-EVs may require higher concentrations of checkpoint inhibitors to overcome competitive binding of AML-EVs to inhibitory receptors. Unlike most solid tumors, AML exists predominantly in the vascular space, the highly fenestrated bone marrow, spleen, and other lymphoid

tissues, which lack the dense encapsulated architecture often present in solid tumors. The systemic release of immunosuppressive EVs into circulation and lymphoid tissue, may oppose the efficacy of not only checkpoint blockade but also other T-cell-based therapies. Many critical questions remain, but we present further evidence demonstrating that EVs contribute to suppressing the immune system in AML. We found that CD8+T-cell suppression occurs in part through EV trafficking of PD-L1, however it is expected that additional immunomodulatory cargos (such as TGF-β, FASL) described by others [139, 253], are also trafficked via EVs compounding the observed effect. Together, EVs and their immunosuppressive molecules may allow myeloid blasts to expand unchecked and to precipitate leukemic relapse. For AML and other cancers alike, EV-mediated immune cell dysfunction is an important signaling paradigm that has only begun to be explored.

Materials and methods

AML culture and PD-L1 expression analysis

Human AML cell lines were obtained from ATCC (VA, USA), and were transduced with myristoylated GFP expression cassette as previously described [21, 265]. TIB-49 cells also obtained from ATCC, and were transduced with palmitoylated-acGFP (rLV.EF1.AcGFP1-Mem-9, Takara, CA, USA). AML cells were cultured in RPMI in 9% vesicle-depleted FBS (Invitrogen, Waltham, Massachusetts, USA), 1% pen-step. Cells were pulsed in IFNγ for 24 hours (10ng/ml human; 20ng/ml mouse; Biolegend, San Diego, California, USA), then washed and pelleted at 400xg twice before adding fresh EV-depleted media. EVs were collected from conditioned media at 24-hour intervals post-washout to prevent transfer of IFNγ to T cell assay. For flow cytometric analysis of surface protein, AML cells were washed in 1x PBS with 2% EV-depleted FBS, then stained with 200ng/ml anti-PD-L1 or isotype control (Biolegend) on ice for 30 minutes prior to washing and adding DAPI as a live/dead marker. Cells were analyzed using a Benton Dickenson Canto II (NJ, USA) and data processed using FlowJo (OR, USA).

Syngenetic Mouse Model

Mice used in this study were C57BL/6J wild-type mice (#000664) purchased from The Jackson Laboratory (ME, USA). These animals were housed and bred in the OHSU animal facility. Sex and age -matched (8-12 weeks old) mice were injected with 1x105 TIB-49 cells (C1498; ATCC) to allow for slow progression of tumors and development of immune response. Mice were euthanized 21-25 days after injection to assess a range of tumor burdens. Mouse studies were conducted in accordance with the National Institutes of Health Guide for the Care and Use of Laboratory animals, and approved by the Institutional Animal Care and Use Committee (IACUC) of Oregon Health & Science University (protocol TR01_IP00000038).

Human AML samples

Human tissues studied in this paper were analyzed in a retrospective and anonymized fashion. Samples were retrieved from the Beat AML database containing 672 tumor samples from 562 patients (www.vizome.org) [258]. Viable peripheral blood mononuclear cell samples were chosen based on RNAseq PD-L1 expression collected at diagnosis from patients with >80 blasts in the peripheral blood. Peripheral blood was collected by venipuncture and mononuclear cells separated by Ficoll gradient and frozen in liquid nitrogen until use. Informed consent was obtained from all patients prior to specimen collection, under the approval of approval and guidance of the institutional review boards at Oregon Health & Science University (OHSU) and other participating institutions.

EV purification and protein analysis

AML-EVs were collected from conditioned media taken from 30 million Molm-14mGFP or U937 cells as previously described [21, 179]. For Density gradients EVs were concentrated by ultracentrifugation into cushion of 20% (2ml) and 50%(0.5ml) cushion of iodixanol (Optiprep; Axis-Shield, Dundee, Scotland). Bulk EVs were then transferred into discontinuous gradient (0%-10%-25%-30%-40%-50% iodixanol), layering the cushion

into the middle of the gradient. Density gradients were then centrifuged at 100k x g for 16-hours. Sedimented gradients were then divided into fraction 20 and transferred into a 96well plate. EV containing fractions were identified using a plate reader to measure relative mGFP intensity. Western Blots were conducted on concentrated EVs as described [294] using anti-PD-L1 (Cell Signaling, MA, USA; BioxCell, NH, USA;) and TSG101 (Abcam, Camb, UK). Immunoblots were performed on nitrocellulose using anti-PD-L1 (Abcam), and detected with horseradish peroxidase with streptavidin amplification (Vector Labs, CA, USA).

Harvesting and culturing CD8+Tcells:

For human cells, PBMCs were separated from whole blood using a ficoll gradient, while mouse cells were isolated directly from spleens or bone marrow by passing through a 40μm cell strainer. CD8+Tcells were isolated from bulk lymphocytes using negative selection with iron-conjugated antibodies and a magnetic column (StemCell Technologies, BC, Canada). Cells were cultured in RPMI in 9% vesicle-depleted FBS (Invitrogen, MA, USA) at 2.5x104 cells per 200ul in a 96 well plate. Human cells then were co-stimulated with 10μl human anti-CD3/CD28 tetrameric antibodies for 1 hour prior to adding 10μl purified AML-EVs (EVs purified from 3 million cells, ~10^8 total EVs/well) or vehicle (complete growth media). Mouse CD8+ T cells were stimulated in 96 well plates coated with 10ug/ml anti-CD3 (BioXcell) for 1 hour prior to adding EVs. For checkpoint inhibition assays, cells were cultured with 5μg/ml blocking antibodies (Full antibody list **Appx Table 4.2.1**).

Intracellular flow cytometry

Human CD8+Tcells were treated with Brefeldin A (Biolegend) 4 hours prior to flow cytometric analysis to inhibit cytokine secretion. Cells were than stained on ice with anti-CD8 and Live/Dead Blue (ThermoFisher, CA, USA), prior to being fixed (4% PFA) and permeablized (0.25% Tween) for 10 minutes respectively at room temperature. CD8+T-cell cytokine production was measured by staining CD8+T cells with 500ng/ml anti-IL2 and anti-IFNγ (Biolegend) for 4 hours at 4°C. Intracellular cytokine levels were

analyzed on BD Canto II Flow Cytometer and data processed using FACS Diva (Benton Dickenson) and FlowJo (OR, USA).

EV binding assay

CD8+T cells were co-stimulated with tetrameric anti-CD3/CD28 antibodies (StemCell Technologies) for 24 hours prior to being exposed to AML-EVs from Molm-14 mGFP cells for 1 hour. Cells were washed and transferred to imaging chambers coated with poly-L lysine (ThermoFisher) in 1xPBS. After incubation, cells were stained with CellMask plasma membrane stain and Hoechst (ThermoFisher), and analyzed in phenol free RPMI using an Olympus/Deltavision CoreDV microscope equipped with a 60X 1.49NA and Nikon Coolpix CCD camera. Representative 3D Z-stacks were acquired using a Zeiss Elyra equipped with an Airyscan super resolution detection array (Zeiss: Oberkocken, Germany).

Immunofluorescence

Immunostaining of cellular PD-L1 localization was conducted in Molm-14mGFP, U937 cells and P2 Blasts. Cells were stained with AF-647 conjugated anti-PD-L1 (Abcam) at 37C for 1 hour, and for non-mGFP expressing patient blasts, cells were stained for 5 minutes in CellMask (ThermoFisher) to label the plasma membrane. Cells were then fixed with 4% PFA with 0.1% glutaraldehyde, then permeabilized briefly in 0.25% tween-20 for 10-minutes on ice. Cells were then stained for another hour in anti-PDL1 to access intracellular epitopes. Cells were washed, stained with Hoechst, embedded in Vectashield (Vector Labs), and imaged using a Zeiss Elyra microscope (described above).

High resolution flow cytometry

Conditioned media from standardized AML cell cultures were centrifuged at 1000xg and 2500xg for 20 minutes each to remove large debris. Remaining supernatant was then passed through a 0.2µm filter. Supernatant was then pipetted in 10µl aliquots into a 96 well plate for antibody staining. Direct conjugated antibodies were diluted to a final concentration of 1-0.2µg/ml, and incubated for 2 hours at room temperature. Volume was

brought up to 250µl with 0.1µm filter, 1XPBS, and samples were transferred to FACS tubes. Unstained supernatant and antibody only controls were included to assess staining quality. Addition of Triton X-100 detergent at a final concentration of 0.1% was used to to demonstrate loss of vesicle-associated signal. Samples were run on a BD FACS Canto II with the blue laser increased to 200mW to increase side scatter sensitivity. Events were recorded over 60 seconds using the lowest flow rate. Flow plots analyzed using FlowJo.

Immunocapture of PD-L1+ EV

EVs were harvested from conditioned media from Molm-14mGFP cells treated with or without IFNγ and 293TmGFP cells via ultracentrifugation. Ibidi plastic imaging chambers were coated with 10µg/ml anti-PD-L1 in 0.1M bicarbonate buffer (pH 9.6) overnight at 4°C, before being washed 3-times in 1xPBS with 2% FBS (EV depleted). EVs were added to wells and incubated overnight at 4°C, before being washed in 1xPBS. Chambers were then stained with 200ng/ml anti-ICAM1, washed and imaged using an Olympus/CoreDV microscope (described above). The total number of GFP+/ICAM1+ foci were counted in 5-fields (105 µm x105µm) in two independent replicates.

Statistical analysis

Unpaired student's t-test were used for direct comparison of among sham and tumor groups for animal studies. Animal data was normalized to mean values for non-engrafted sham (PBS-injected) animals. For *in vitro* studies, one-way ANOVA analysis with Dunnett's T3 multiple comparisons were performed using pairwise comparison to control (C2) values. For Data sets with multiple categorical variables, two-way ANOVA was performed with Tukey multiple comparison against paired control values. Data from *in vitro* assays was normalized to controls as described in respective figure legends. Statistical significance was set at *p <0.05, **p <0.01, and ***p<0.001. Statistics were calculated using Prism Software (GraphPad, CA, USA).

Funding

This study was supported by the National Cancer Institute NRSA program (JTB; F30CA247601), the Friends of Doernbecher (JTB), The Tartar Trust (JTB), and the Hyundai Hope on Wheels Foundation (JTB, BHC, PK).

Chapter 5: Methods of fluorescence-based EV characterization

Abstract

A critical bottleneck to studying exosomes and small microvesicles is their size—one–hundred-fold smaller than a red blood cell—which makes it technically challenging to resolve their composition and cell-specific origins. Over the years, EV-related studies have relied on molecular techniques that fail to resolve differences in EV subpopulations, and particle counters that cannot identify EV-specific markers. Due to their inherent flexibility, more fluorescence-based labeling techniques are needed to advance our understanding of EV-biology. In this chapter, I discuss the technical limitations of analyzing nanoscale EVs using visible light, and offer methods to improve characterization of EV composition and fate. To facilitate the detection of EVs, our group created AML cells that express GFP fused to their internal and peripheral membranes through myristoylation (mGFP). These cells release GFP-tagged membrane-derived EXs and MVs that are detectable in both *in vitro* and *in vivo* experiments, and have aided in the development and optimization of microscopy and flow cytometry techniques to study EVs. Using these techniques, I am able to quantify cell-specific EV concentrations, and incorporate dye and antibody staining to label EV-specific markers. These fluorescence-based methods have facilitated the research described in the previous chapters, and have the potential to further advance our understanding of EV-biology.

Introduction

Better methods to study EV structure, surface markers, internal cargo, and heterogeneity of EV populations are critical to advancing the understanding of EV-biology and cell signaling. It is widely accepted that individual cells, irrespective of tissue origin

or disease state, release diverse populations of EVs, which are formed through multiple distinct pathways [23, 36]. This compositional diversity of EVs has complicated the fundamental understanding of EV-mediated signaling, and has slowed the identification of EV-type specific markers. Due to their nanoscale size, methods of flow cytometry or fluorescence microscopy approaches—with highly flexible labeling strategies—have only recently gained interest for use in studying EVs. Instead, molecular techniques have predominated in the field of EV biology. They rely on crudely separating EVs based solely on size or density, prior to analyzing EV populations by western blot, mass spectrometry or PCR. These techniques are both time- and labor intensive and highly affected by contamination, and most importantly, provide little insight into the composition of surface markers or cargo with respect to their diversity across individual EVs released by any one cell type. This has compounded the slow progress in identifying cancer-specific biomarkers, which for AML, could serve to monitor disease and detect relapse more quickly, in addition to providing necessary insight to the underlying biology of AML pathogenesis.

Imaging-based characterization of extracellular vesicles

The ability to combine multiplexed labeling with structural analysis, makes fluorescence microscopy a promising platform to study EVs. Over the last ten years multiple labeling strategies have been used for detecting EVs by fluorescence microscopy. These include the use lipid dyes to stain the vesicle membrane, or fluorescent proteins that tag EV-incorporated molecules via transgene expression in parent cells [179 2015, 265, 295]. To date, the majority of studies that include imaging-based detection of EVs have focused on demonstrating *in vitro* uptake into cells propagated in the tissue culture environment. Here, I set out to extend the use of fluorescence microscopy to quantify EV concentrations and composition, independent of uptake into recipient cells. I also developed live-cell microscopy-based techniques to quantify binding and uptake of AML-specific EVs that occur *in vivo,* using specialized mouse models, while also improving upon *in vitro* methods to study EV uptake.

Extracellular vesicles and the diffraction-limit

Due to their nanoscale size, detection of EVs by microscopy is challenging as exosomes and small microvesicles fall beneath the limit of resolution for light microscopy (~250nm) [296, 297]. Within any optical system, light waveforms are subject to dispersion as they pass through a spherical lenses and material interfaces, which limit resolution beneath a specific physical distance. For both microscopes and telescopes, this physical distance is known as the diffraction limit. It was first described by Ernst Abbe in 1873 [298], as a distance at least half that of the wavelength of visible light passing through an optical system. Due to this inherent property of optics, the vast majority of light microscopy systems (widefield and confocal) are referred to diffraction-limited systems. Once thought to be unbreakable barrier of optics, major advances in the last twenty years have made it possible to create "super resolution" systems that allow for acquisition approaching 5-10nm resolution [297, 299, 300]. These super resolution methods will likely prove invaluable for the field of EV biology over the next decade, yet their potential applications for studying EVs have only begun to be explored.

For light-based detection of nanoscale EVs, super resolution microscopes are helpful, but are not required. If a fluorescently labeled structure is smaller than limit of resolution, this does not mean the signal emitted from a single EVs cannot be detected. Further defined by Lord Rayleigh in 1903, the limit of resolution denotes the spatial distance at which light emission from two distinct points can be distinguished as separate entities [301]. This means a single exosome is detectable, but if two exosomes are closer than the diffraction-limit, they would be difficult (but not impossible) to resolve as separate. This physical distance, known as the Rayleigh Criterion, is proportional to the wavelength of light passing through the optical system, and inversely proportional to both the numerical aperture (NA; number of angles that can pass through aperture) of the microscope objective and the refraction index of the optical medium (Air =1; water 1.33; Oil=1.52). I have found that both widefield and confocal systems equipped with a high NA oil immersion objective, a sensitive detector, and vibrationally-dampened setup, allows for adequate detection of low density signal emitted from a nanoscale EV. Herein I show that

detection of nanoscale EVs are indeed possible using diffraction-limited systems and validate these finding using reference beads of equivalent size.

Due to the diffraction of light through the optical system, the detected size of the nanoscale EV signal is distorted, causing it to appear larger than the originating structure. In a particular system, a well-labeled exosome with a diameter of 100nm is detected as ~400nm. The difference in detected signal is referred to as point-spread, and masks the ability to identify adjacent structures. Light focused through a spherical lens is detected as an "airy-disk" composed of a central intensity and concentric rarefications, the size of which correspond to the aperture diameter (numerical aperture) and extent of photonic diffraction in the optical system [301, 302]. The point-spread of a given microscopy system and objective can be measured using reference beads of a defined diameter through post-acquisition analysis [303]. The calculated point-spread can be used with image restoration algorithms to enhance micrographs by removing light that falls at the periphery of respective Airy disks. Known as image deconvolution, these methods have been used since 1983 to artificially improve image resolution [304] and are useful for enhancing nanoscale signal. The CoreDV/Olympus microscope system I use frequently throughout *this chapter* operates on this principal and produces high resolution 3-D live-cell images.

For imaging small EVs, minor signal diffraction can actually provide useful information, and be harnessed to improve resolution. Using a widefield microscope with a 100x objective and a with a charged–couple device camera (CCD), the physical distance represented by each pixel within the CCD chip array (pixel-pitch) typically corresponds to 45-90nm of the optical field (depending on objective and camera chip). However, diffraction causes the signal from a single 80nm exosomes to be spread across multiple adjacent pixel sensors. For small structures, the diffraction captured by the detector provides information about origin of light at a sub-pixel level. The pixelated geometry and intensity values captured by the detector corresponds to the true centroid (origin) of the signal, and can be exploited to make "super" resolution imaging possible [305].

Improving resolution and breaking the diffraction-limit

Fluorescence microscopy relies on densely labeling structures with fluorescence reporters. When multiple adjacent points—that are located at a distance smaller than the diffraction limit—emit light simultaneously, their respective waveforms overlap and mask the underlying structure of the labeled points. The simultaneous emission and signal point-spread of these fluorophores, produces out-of-focus light which blends together to greatly reduce resolution. If the light emission from these adjacent points does not occur simultaneously, it is possible to resolve the respective locations of adjacent fluorophores. Optical resolution can be improved by reducing out-of-focus light through the temporal control of fluorophore emission within an optical field. This is achieved with confocal microscopes by rastering a "pin hole"-focused beam across the optical field (laser scanning confocal), or by spinning a disk containing multiple pin holes that limits light collection to defined and distant points of the optical field (spinning disk confocal) [306]. In contrast to confocal, by definition "widefield" microscopes illuminate the entire optical field evenly. In these systems, out-of-focus light can be identified and reduced by post-hoc image deconvolution or by harnessing specialized photoactivatable fluorophores [297, 306].

The development of "photo-blinking" fluorophores that can be cycled between active and dark states through buffer chemistry or addition of UV light, has revolutionized fluorescence imaging, and was recognized for a Nobel Prize in Chemistry 2014. Through stochastic activation and coupled emission of fluorophores within the optical field, the development of single molecule localization microscopy techniques (SMLM) has been made possible. These techniques produce images with a ~10nm resolution, a 20-fold improvement over conventional widefield imaging [297, 307]. Two of the best know SMLM techniques are Photoactivation-Localization Microscopy (PALM) and Stochastic Optical Reconstruction Microscopy (STORM) [299, 300]. Though a huge leap in imaging, these SMLM techniques rely on highly customized modular systems, fluorophores, buffers, software and post-image analysis, and are therefore can be challenging to adapt to certain biological applications.

Other super resolution approaches can be implemented using "turn-key" microscope systems, with commercially available modules and software. Many of these do not reach the same level of resolution as SMLM, yet still provide sub-diffraction level imaging without requiring highly specialized preparation of samples. These include Zeiss's Airyscan technology and Structured illumination microscopy (SIM)—both used herein—achieving x- and y- axis resolutions in the 100nm range [308, 309]. Airyscan is a laser scanning confocal system that replaces the use of a single photomultiplier tube with a detection array that identifies signal localization as the confocal rasters step-wise across the optical field [308]. While Structured Illumination microscopy is a widefield technique that incorporates a rotating diffraction grid in the light path to identify and remove diffracted light that obscures the localization proximal structures [309]. Together with SMLM, these technologies have overcome the diffraction limit, allowing fluorescence microscopes to produce images that approach the resolution of electron microscopes, while retaining the flexibility of multicolor labeling in live-cells and fixed tissues [174, 307, 310]. Together, these techniques are a powerful, yet underutilized tool for studying extracellular vesicles. Herein I describe the diffraction-limited, and "turn-key" super resolution approaches used to study EVs in context of AML in Chapters 2-4 of this thesis. Through additional optimization, these methods could be translated for use with SMLM techniques in the future to further advance our understanding of EV biology.

Solid Capture Imaging

EVs in a fluid medium are subject to Brownian motion, making detection by high resolution microscopy very challenging (**Fig 5.1A**). In order to image single EVs, they need to be fixed in place. This has been accomplished by attaching EVs to an optical surface through antibody binding (**Appx 4.4.1**), charge interactions mediated by substrates like poly-L lysine, or by relying on uptake by recipient cells [142, 263, 311]. I have found that these methods only capture a minority of EVs released from a given cell type, making them less than ideal to characterize diversity within EV population. Additionally, in my experience, surface attachment does not adequately stabilize EVs in order to prevent wobble due to Brownian forces, which are compounded by environmental vibration in most steel reinforced buildings, limiting imaging resolution.

In order to overcome this, I created an imaging approach which relies on capturing EVs directly from cell culture conditioned media, or animal body fluids, into an optically clear 3-dimensional hydrogel (**Fig 5.1B-C**). This allows for EVs to become stably embedded within a molecular matrix that prevents vesicle movement and selection biases created by methods that rely on binding EVs to an optical surface. Using solid capture, EVs remain stationary within an optically clear hydrogel, allowing for focused acquisition, and the detection of fluorescent labels without spectral crosstalk. (**Fig 5.1B-D**). This was accomplished using hydrogels, agarose (low melting point), polyacrylamide and Matrigel (Corning). Of these, Matrigel was the fastest matrix to work with and is described *herein*. The endothermic and exothermic conditions of agarose and polyacrylamide matrix formation respectively, subjected EVs to increased temperatures, and required more nuanced preparation methods to maintain EV integrity. It should be noted though, that agarose and polyacrylamide both maintain low background following fixation with aldehydes, while Matrigel becomes highly autofluorescent. However, fixation is not necessary when labeling the lipid membrane and surface-bound molecules, and can actually be detrimental. I have found that fixation with 4% paraformaldehyde (with or without addition of 0.1% glutaraldehyde) actually diminishes-membrane-associated signal intensity due to inadequate stabilization of the lipid bilayer. Therefore, solid capture imaging experiments using Matrigel were performed without fixation.

Solid capture imaging was performed by diluting body fluids or conditioned media containing mGFP+ EVs, directly into Matrigel on ice (1:5 ratio). To reduce background phenol-free cell culture media and Matrigel were used in these preparations. Since Matrigel is liquid at 4°C and begins to solidifies as it warms above 8-10°C, it is critical that EV samples, tubes for dilution and pipet tips are pre-chilled on ice before beginning, or the Matrigel will prematurely solidify within the pipet tip or dilution tube. Samples were diluted one at a time, then mixed thoroughly by pipetting up a down with a pre-chilled pipet tip for 30 seconds, with care not to introduce air bubbles into the viscous solution. Immediately after sample was adequately mixed, the solution was transferred to a well of an Ibidi imaging chamber (containing 500µm etched grids for focal reference) and spread

evenly across the surface. Imaging chambers were then incubated in the dark at 37°C for 2-hours or 4-hours at room temperature to allow the matrix to solidify before imaging.

Using this method EVs released from cells expressing myristoylated GFP (mGFP) of TdTomato (mTomato) were resolved without fluid movement or cross-talk between fluorescence reporters (**Fig 5.1B, D**). Images were first captured using a CoreDV/Olympus wide-field microscope with 1.49 NA objective, and a high quality Nikon Coolpix CCD camera. Later Airyscan and SIM systems were used to improve the resolution of EV images. Due to the relative sensitivity of solid capture imaging, I set out to use this technique to simultaneously measure EV concentration, size, and composition by incorporating multiple labeling strategies.

Figure 5.1: Solid Capture: Imaging EVs embedded into hydrogel

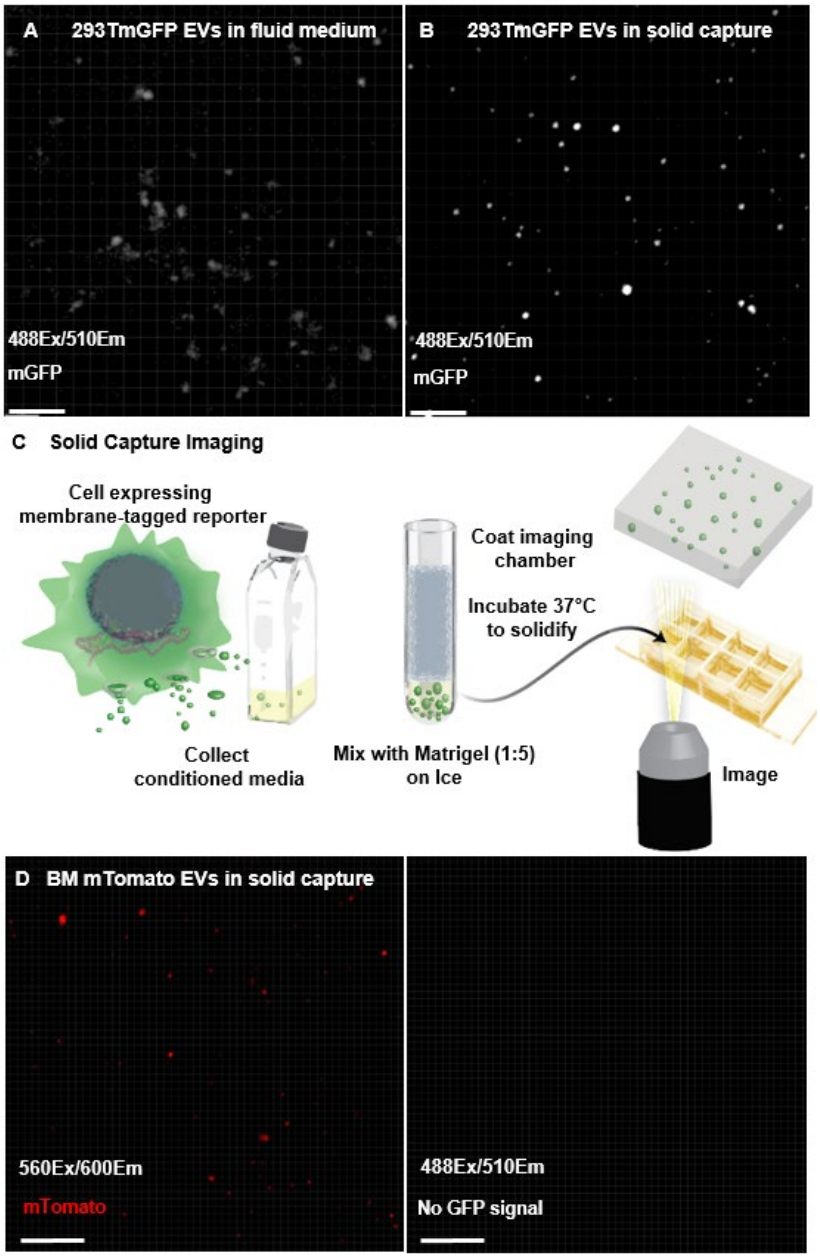

.**A)** mGFP+ EVs in fluid are subject to Brownian forces which disperse signal and prevent focused acquisition. Brightness increased in panel A to display weak signal **B)** Capturing mGFP+ EVs within a solid matrix eliminated Browian motion, increased signal density and allowed vesicle concentration to be analyzed by fluorescence microscopy. **C)** Graphical workflow for solid capture imaging using Matrigel. **D)** Signal specificity is demonstrated with EVs from myristoylated tdTomato expressing bone marrow cells. EVs are detectable with 560/600 excitation and emission but not with 488/510. A-C) Images captured with CoreDV microscope with 100x 1.49 TIRF objective and Nikon Coolpix CCD camera under identical exposures and camera gain. Scale bars =5µm.

Validating nanoscale resolution of solid capture imaging

Since exosomes and small microvesicles fall beneath the diffraction-limit of standard fluorescent microscopy, I employed fluorescent reference beads (36nm, 100nm and 180nm, ThermoFisher) to determine the limit of spatial resolution of our microscopy systems and measure the relative point-spread of the signal emitted from sub-diffraction limit structures. Using a 100X Plan Apo 1.49 TIRF objective, and 60X 1.45NA Plan-Apo, signals from all three beads were detectable with consistent size and intensity without significant aggregation (**Fig 5.2A-B**). Under these experimental conditions, even the 36nm beads were easily detected using both objectives, and some aggregates were distinguished by increased signal density and spherical aberrations. To estimate the diffraction of signal from nanoscale beads, the diameter of the point-spread of the three different beads in the X, Y and Z axis. The measured point-spread (detected signal) was consistently 4-fold larger in the X-Y axis than the true diameter across the respective reference beads (**Fig 5.2 C**), with greater diffraction evident in the Z-axis, as expected. Despite the measured diffraction, the use of reference beads ensured our microscope systems and imaging approach were sensitive enough to not only detect similarly sized EVs, but also use imaging to determine EV concentration.

Measuring EV concentration by solid capture imaging

To validate if vesicle concentration could be measured by solid capture imaging, I created serial dilutions of 100nm reference beads and embedded them Matrigel to determine sensitivity and linearity of measurement. Serial dilutions were captured with 3D Z-stacks of a fixed volume (100µm x 100µm x 10µm = $1x10^{-4}$µl), using 4 replicates per condition to assess precision. Bitplane's Imaris software was used to determine the signal threshold, and individual beads were identified and counted using Imaris's "Surface function". The measured bead count maintained linearity, with a strong correlation (R^2 value= 0.88) across all 5 serial dilutions (range 1:100-1:3200) (**Fig 5.3A-C**).

Figure 5.2: Validating Nanoscale resolution of EVs

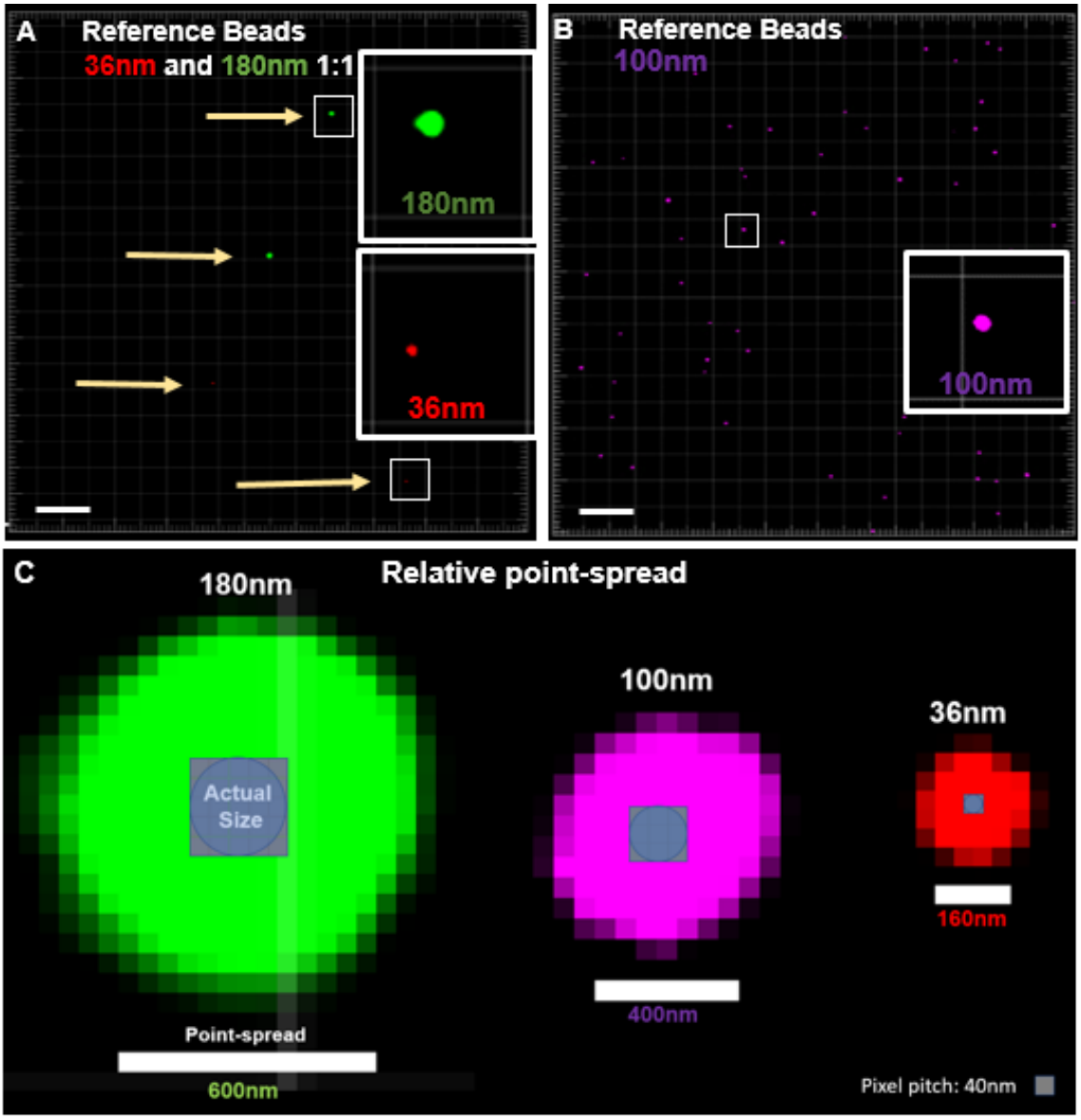

A-B) Fluorescent reference beads, 180nm and 36nm mixed 1:1 (A), and 100nm (B) embedded into Matrigel. (A-B**)** Scale bars = 5µm. **C)** All three sizes of beads (36nm, 100nm, 180nm) are resolved with distinct and reproducible spherical point-spreads in solid capture. Respective beads displayed with maximum digital zoom. Point-spread scale bars = 600nm, 400nm, 160nm, voxel pitch = 40nm. Images captured with CoreDV microscope with 100x 1.49 TIRF objective and Nikon Coolpix CCD camera.

Figure 5.3: Validating imaging-based measurement of EVs using reference beads

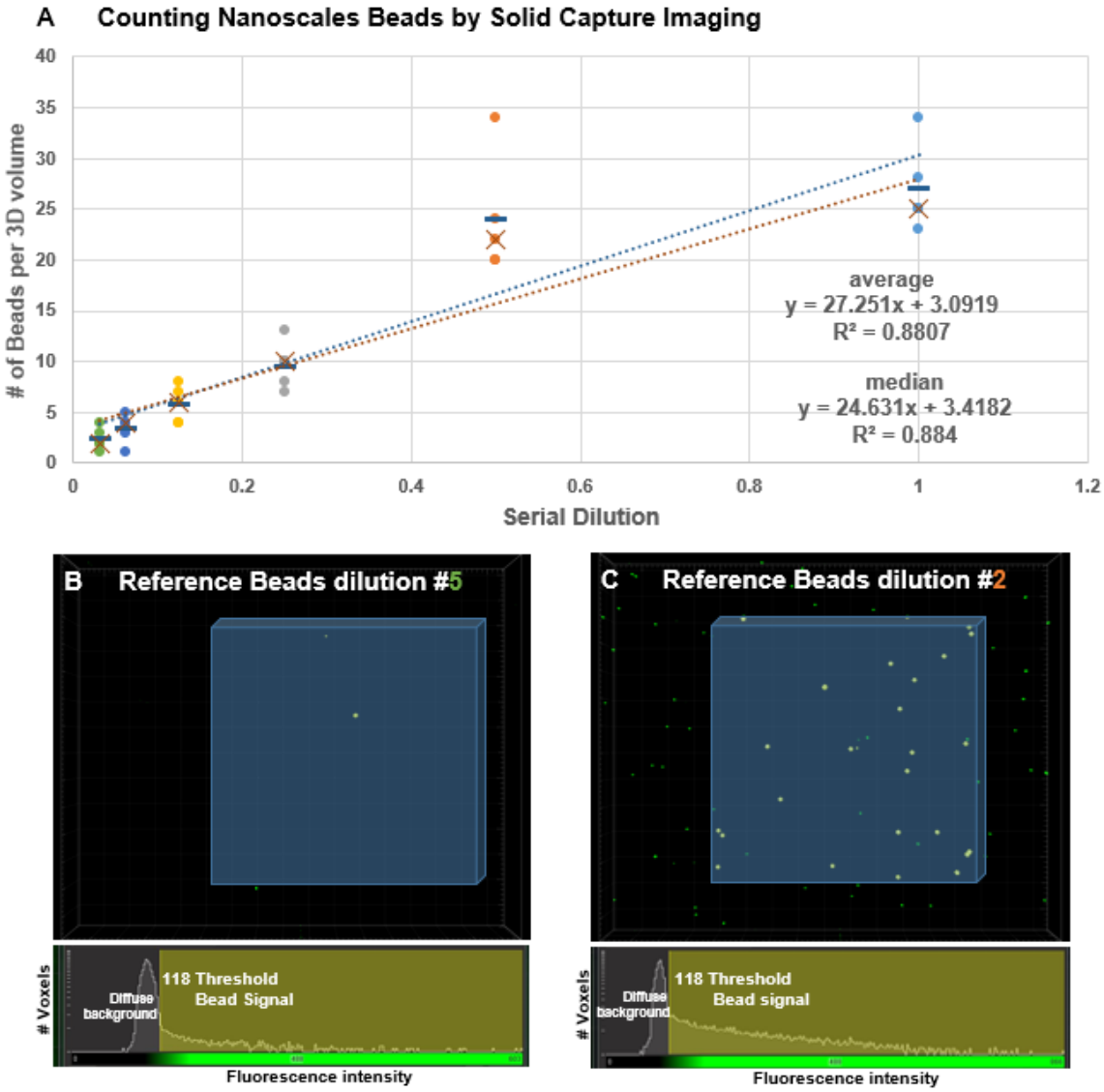

A-C) Measuring reference beads in serial dilution to determine linearity of measurement of solid capture imaging technique. **A)** Solid capture imaging detects 100nm beads embedded into Matrigel with linear correlation across 5 serial dilutions (R2=0.88). Each point represents one-unit volume of $1x10^{-4}$µl., 4 replicates per condition. Starting dilution of beads 1:100. **B-C)** (top) Representative images of bead serial dilutions #5 (B; 1:3200) and #2 (C; 1:200) using Imaris spot function to identify (yellow) and count individual beads within one-unit (100µm x 100µm x 10µm). Foci falling outside of unit-volume (green) are not counted. **B-C)** (bottom) Gray value histograms showing threshold applied to remove diffuse background fluorescence for each respective image.

Prior to the development of solid capture imaging, measuring the concentration of EVs was previously done in our lab using a Nanosight device which performed nanoparticle tracking analysis (NTA) based on capturing dynamic light scattering of particles suspended in a fluid medium of known viscosity [312]. Across the field of EV–related research, this device became the gold standard of measuring EV concentration and relative EV size [23]. This methodology was highly limited by its lack of specificity as it was unable to distinguish the composition of detected particles. The Nanosight was highly vulnerable to interference caused by contamination with plastic particles, cellular debris, particle aggregation, air bubbles, soluble protein concentration, and temperature fluctuations that greatly affected sensitivity and reproducibility of data [312]. Early in the development of the solid capture technique, OHSU's only Nanosight device was broken, and was not replaced. Therefore, I had to rely on solid capture imaging to measure EVs counts for studies described in chapter 2 and 3, and did not have the ability to compare analysis by the two techniques side by side. In chapter 2, I relied on solid capture imaging to measure the relative change in number of EVs released from Molm-14mGFP cells depending on culture condition. I hypothesized that the release of AML-EVs increased proportionally along with ER-stress and the activation of the unfolded protein response pathway (**Chapter 2**). By using solid capture, I found that AML cells exposed to ER-stress inducing agent thapsigargin, significantly increased EV release in dose-dependent manner (**Fig 5.4A**). This data was also consistent with the increase in EV-related protein BMP2 measured in parallel by ELISA (**Fig 5.4B**).

With the ability to detect EV concentration differences with solid capture, I set out to measure the concentration of AML-specific EVs in the peripheral blood of animals engrafted with mGFP expressing Molm-14 cells. To accomplish this, I isolated peripheral blood plasma from 2 cohorts of mice, with 20% and 50% bone marrow tumor burden respectively. Plasma was centrifuged for 25 minutes at 2500xg to remove platelets. Platelet poor plasma was then mixed at a 1:5 v/v ratio with Matrigel on ice, then coated onto an Ibidi imaging chamber (**Figure 5.5**). Following incubation, solid gels containing mGFP-labeled EVs were imaged and analyzed using Imaris Bitplane as described above. Concentrations were again determined by acquiring 3D Z-stacks with a fixed volume

(100µm x 100µm x 10µm = $1x10^{-4}$ µl) using 488 laser excitation. Signal threshold was determined to remove non-specific background, which was calculated by imagining plasma from non-engrafted NSG control animals. The number of circulating AML-EVs was found to stratify according to bone marrow tumor burden (**Fig 5.5B**). 3D Imaging showed that the peripheral blood plasma of animal with 20% bone marrow tumor burden contained an average of 40 EVs per $1x10^{-4}$ µl, while the animals with 50% had 658 EVs per $1x10^{-4}$ µl. To determine a plasma concentration, the average EV count was multiplied by the dilution factor (5), and number of volumes within 1 µl ($1x10^{4}$) (**Fig 5.5C-D**). This showed that animal xenografts with 20% and 50% tumor burden had $2x10^{6}$ and $3.29x10^{7}$ AML-specific EVs per µl in the peripheral blood plasma, respectively.

Figure 5.4: Using solid capture imaging to measure relative EV concentrations

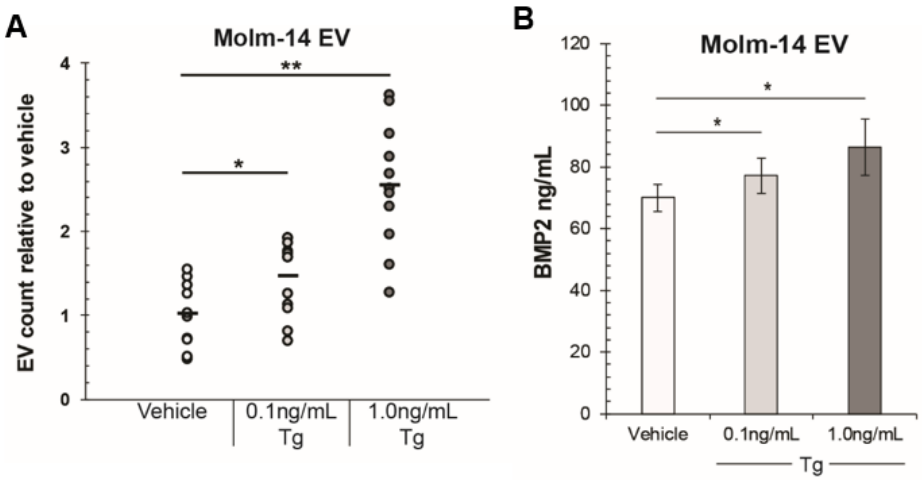

A) Quantification of EV output by Molm-14 cells experiencing UPR stress. Solid capture imaging of EVs harvested from Molm-14 treated with two doses of thapsigargin compared to vehicle-treated cells. Points represent EV count within fixed volumes of $1x10^{-4}$ µl. **B)** Concentration of BMP2 protein in EVs following normalization of EV output. ELISA was used to determine protein concentration. Error bars are standard error of the mean from three separate experiments Significance was determined by ANOVA and Pairwise Student's two-tailed t-test, *P<0.05, **P<0.01.

Figure 5.5: Measuring AML-EVs concentration in Peripheral Blood

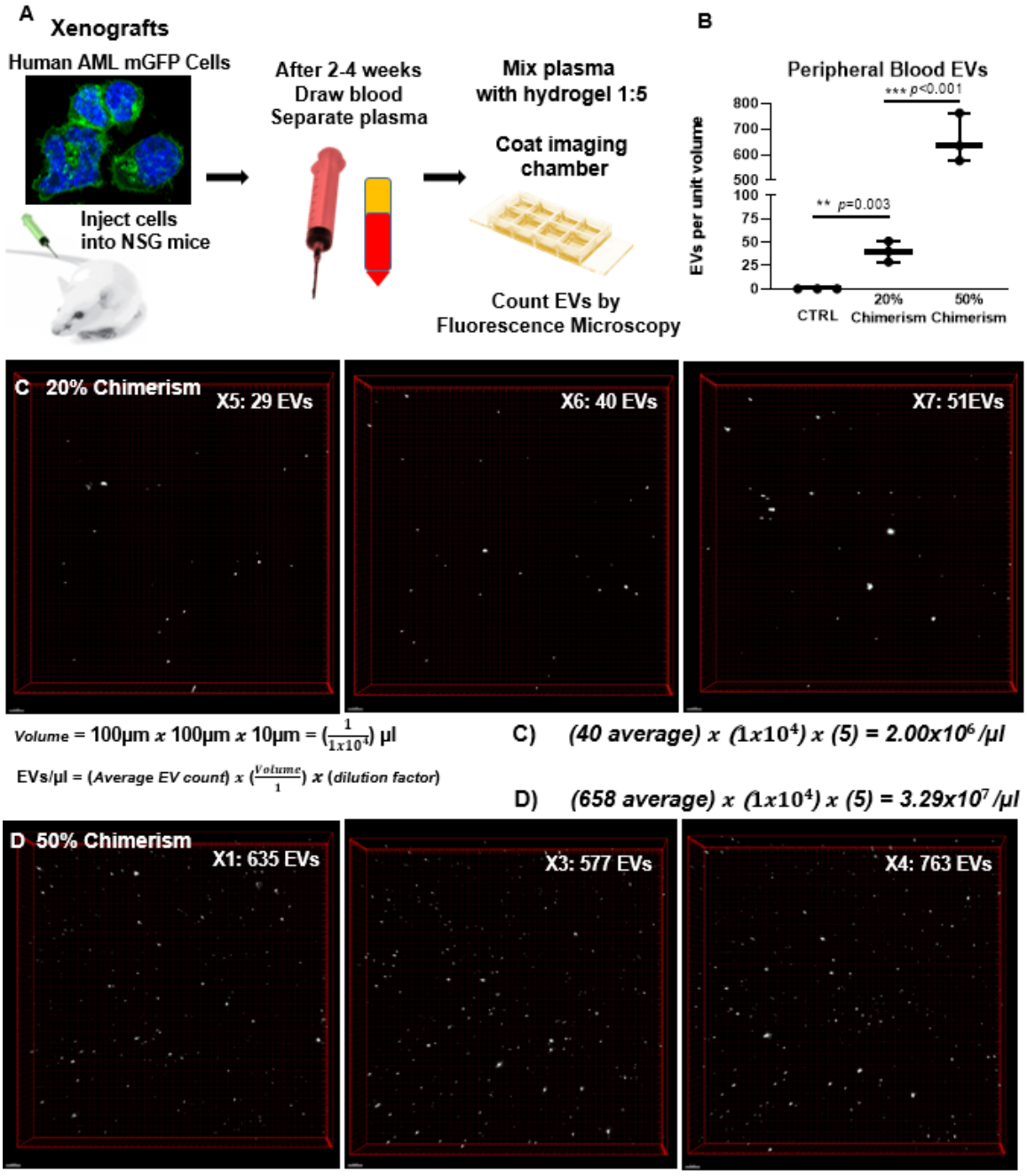

A) Workflow measuring AML-EVs in the peripheral blood of animals xenografted with AML cells expressing a membrane-tagged reporter. **B)** EV counts per unit volume ($1x10^{-4}$µl) correspond to bone marrow tumor burden. Significance determined by Student's two-tailed t-test. ** $p<0.01$, *** $p<0.001$ **C-D)** Representative 3D-images and concentration calculation for 20% (C) and 50% (D) animal cohorts. Images captured with CoreDV epifluorescence microscope with 100x 1.49 TIRF objective and Nikon Coolpix CCD camera. Bounding box represents 100µm x 100µm x10µm volume.

Staining and imaging EVs

Dye Labeling EVs

To expand solid capture imaging technique, I tested multiple lipid dyes for the detection of EVs from cells that do not express EV-specific fluorescent reporters. To minimize background fluorescence, I specifically tested lipid dyes that fluoresce predominantly in lipid-bound states and/or through hydrophobic interaction, and have limited fluorescence in aqueous solution. First I stained 293T cell EVs with DIL-c and DiO, but found that the dyes diffused out of the EVs once embedded into hydrogels, and created high levels of background. I then tested styryl dyes FM-1-43 and FM-4-64, containing a polar head group and hydrophobic tail. In aqueous solution FM-1-43 is non-fluorescent but is switched into an activated sate through hydrophobic interactions that increase quantum yield 40-fold [313]. This dye labeled 293T EVs with a moderate signal intensity, while creating very low levels of background fluorescence in the 488/510 channel (**Fig 6.5A**). This allowed for the addition of dye directly into EV embedded hydrogels. Interestingly however I observed spectral shift of FM-1-43 dye labeled EVs, emitting both red and green fluorescence making it less than ideal for multi-color imaging. The other FM dye 4-64 did not appear to stain 293T EVs, nor produce any appreciable background.

Cellmask is a proprietary lipid dye (CellMask Deep Red Plasma Membrane Stain C10046; Thermofisher, Waltham, MA) that contains a hydrophobic moiety coupled to a hydrophilic membrane anchor that stabilizes signal and prevents diffusion [314]. It is fluorescent in an unbound state; however, signal is disbursed in aqueous solution limiting

signal intensity. CellMask has been used successfully in live-cell imaging experiments to label the plasma membrane and endosomal compartment [314]. Since the dye concentrates within the cell membrane, and becomes incorporated into endocytic vesicles, I tested CellMask for its ability to stain EVs. I found that the dye brightly labels EVs, but unbound dye created high background that interfered with detection. Therefore, cell mask staining was performed prior to embedding EVs in hydrogel and required a washing step **(Fig 5.6B)**.

With the ability to broadly label lipid associated vesicles with CellMask, and differentiate between labels with solid capture imaging, I set out to measure the portion of circulating vesicles that were AML-specific in leukemic animals (**Fig 5.6C-F**). To accomplish this, I collected peripheral blood into EDTA tubes from Molm-14mGFP xenografted mice (20% tumor burden) and non-engrafted controls. Whole blood was centrifuged at 500g for 10 minutes to separate blood cells. Plasma was then drawn off the top and re-centrifuged at 2500g and 10,000g (25 minutes each) to collect platelet-poor plasma and deplete cellular debris, respectively. Supernatant (100µl) from the 10,000g spin was stained with CellMask Deep Red, 0.5ul/ml for 30 minutes at 37°C. Stained supernatant was then diluted to 5 ml and passed through a 0.2µm syringe filter, before collecting EVs by ultracentrifugation at 100,000g for 2 hours at 4°C. Supernatant was decanted, and the EV pellet was resuspended in 100ul PBS with agitation for 4 hours at 4°C. After resuspension, 20ul of purified EVs were embedded into Matrigel 1:5 and imaged as described above.

Solid capture imaging clearly demonstrated a large population of CellMask+ foci, and a smaller population of AML-EVs that co-labeled with both CellMask and GFP (**Fig 5.6C-E**). This dual-labeled EV population was not present in non-AML engrafted control animals, while the CellMask positive foci were present in both animals in similar concentrations (**Fig 5.6B-C**). Distinguishing distinct tissue-specific EV populations within animal plasma is not possible using traditional methods of EV measurement. Particle counters like the qNANO, cannot distinguish particle composition and cannot differentiate membrane-derived vesicles from plastic debris [315]. In contrast, solid capture imaging can

measure distinct EV populations, and demonstrate cell-specific origins of EVs circulating in the peripheral blood and fluids of tumor-bearing animals.

Figure 5.6: Dye Labeling lipid structure

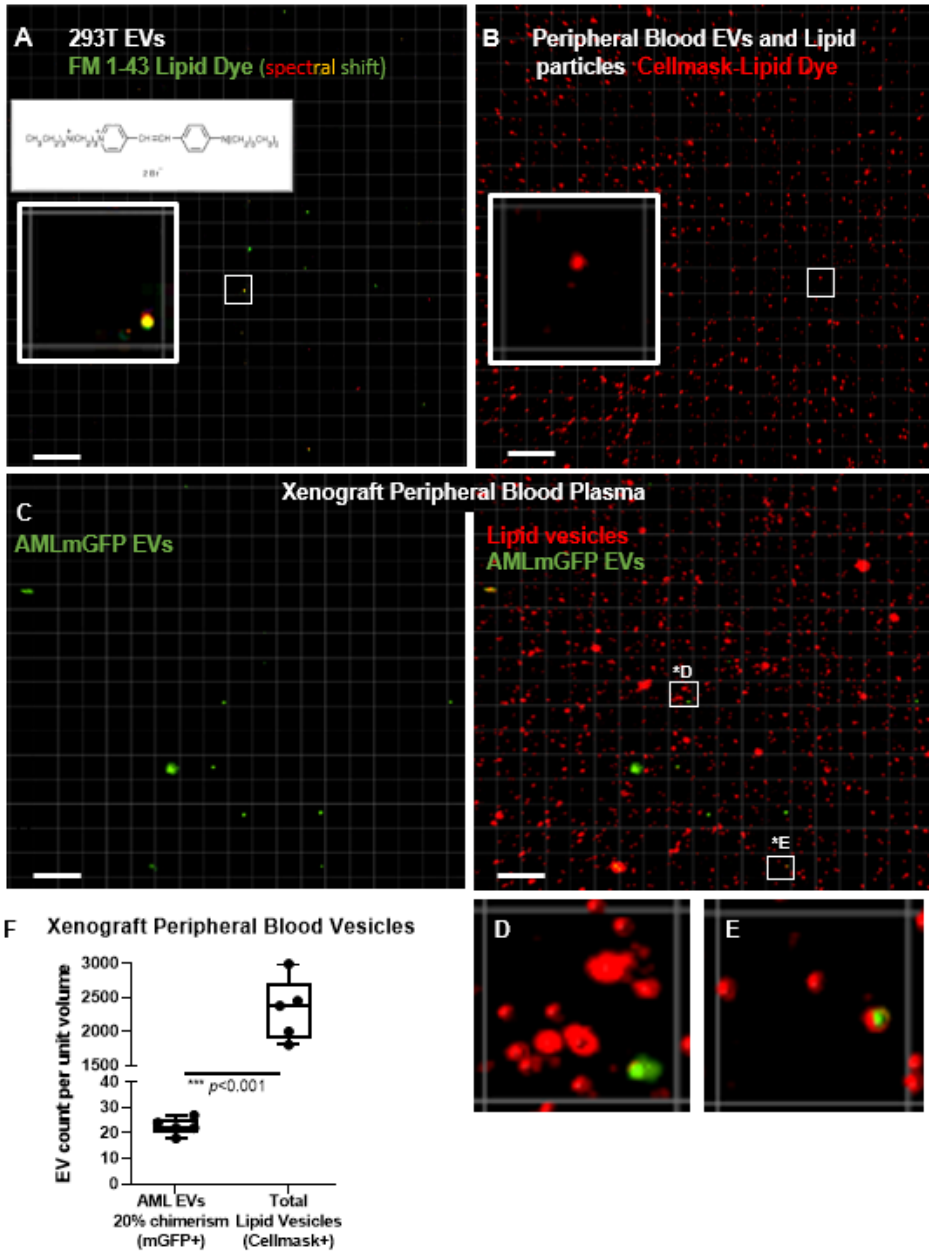

A) Representative image of 293T EVs stained with lipid dye FM-1-43 directly within solid capture. **B)** EVs and lipid particles from peripheral blood plasma of non-engrafted (control) NSG mouse stained with Cellmask lipid dye prior to washing and embedding in Matrigel. **C-D)** Representative images of AML-EVs (green) and total lipid vesicles stained with Cellmask (red) in the peripheral blood of NSG mice xenografted with Molm-14mGFP cells (20% tumor burden). **F)** Quantification of relative AML-EV count in the peripheral blood compared to total lipid vesicles in plasma. Each point represents EV count in one-unit volume ($1x10^{-4}$µl). Significance determined by Student's two-tailed t-test. *** $p<0.001$

Labeling EVs by antibody staining

To expand the characterization AML-EVs by solid capture imaging, I set out to test whether direct and indirect antibody staining can be used to detect surface molecules on small EXs and MVs. I have previously found using transmission electron microscopy that GFP epitopes are accessible on the surface of EVs for binding with gold labeled anti-GFP antibodies (unpublished). For fluorescence microscopy, the ability to stain mGFP+ EVs with red conjugated anti-GFP (Alexa Fluor 555) acted as an ideal positive control, as dual color registration provided a metric of staining efficiency. Additionally, to confirm that mGFP+ foci contain EV-associated tetraspanins (some of which are highly enriched in exosomes), I stained AML-EVs with an antibody against CD63 (Alexa Fluor 647 conjugated; **Fig 5.7A-B**).

For antibody staining, I collected EVs from conditioned media by ultracentrifugation *as previously described* [21, 179, 265]. EV pellets were resuspended in 200ul PBS with 2% FBS for 4 hours with agitation at 4°C, before staining over night at 4°C with rabbit anti-GFP antibody at 500ng/ml. EV samples were diluted in 40ml of 1xPBS and ultracentrifuge for 2 hours at 100,000g. Supernatant was decanted and EV pellets were again resuspended in 200ul PBS and blocked with 2% FBS (vesicle-depleted) for 2 hours with agitation at 4°C. EV pellets were then stained over night at 4°C with direct conjugated anti-CD63 antibody and donkey anti-rabbit Alexa 555 secondary antibody at 500ng/ml in PBS with 2% FBS. Both antibody stocks and dilutions were centrifuged at 15,000g for 20 minutes prior to use to remove any aggregates. After staining, EV samples were diluted again in 40ml of 1xPBS and ultracentrifuge for 2 hours at 100,000g. Supernatant was decanted and EV pellets were again resuspended in 200ul PBS with 2% FBS for 2 hours with agitation at 4°C. To control for non-specific background signal, staining was done in parallel in using EV-depleted media in place of EV pellets. Additionally, unstained controls were also included to assess background fluorescence in 555 and 647nm channels. Following ultracentrifugation, respective samples were embedded *as described previously*.

Solid capture imaging showed that the majority of mGFP+ EVs stained with anti-GFP (red). Similarly, direct staining with CD63 (magenta) stained many GFP+ foci both with and without anti-GFP dual staining (**Fig 5.7A-B**). Control samples that lacked EVs, contained diffuse background similar to EV samples. These controls also contained sparse punctate localizations of CD63 and anti-GFP antibodies, which failed to register with any GFP signal. This indicated that unbound antibodies produced some artifactual signal, but were distinguished by lacking colocalized GFP fluorescence.

In stained EV samples, the registration of CD63 (magenta) and anti-GFP (red) signal relative to GFP (green) was not perfectly aligned. This was expected for multiple reasons: The first is that molecules of IgG are nanoscale structures about 1/10th the diameter of a standard exosomes [316]. Using multiple fluorophore conjugated antibodies to label the EV surface molecules could result in a detectable separation between the EV signal and that of the antibody reporter if resolution is adequate (**Fig 5.7C**). Secondly, light of different wavelengths is subject to differential refraction as it passes through an imaging system. Plan-apochromat objectives used in this experiment contain additional lenses to correct for chromatic aberration, however at high magnification some separation is still apparent, as demonstrated with 4-color 100nm Tetraspeck™ bead (**Fig 5.7D**).

Importantly, in comparing stained EVs to unstained control samples, I found a significant loss of mGFP+ EVs following successive ultracentrifugation. Roughly 50% of mGFP + EVs were lost following each staining, dilution, and re-concentration step. In sum, it is possible to incorporate antibody staining of EVs for analysis by solid capture imaging, however non-ultracentrifugation-based methods need to be explored to separate unbound antibodies. Also, to improve labeling efficiency and close registration of EVs with antibody signal, direct conjugated antibodies should be used. Furthermore, the use of single domain nanobodies, which are a class of antibodies composed of a monomeric variable domain [317], may hold value for imaging-based characterization of EVs (**Fig 5.7**). Since nanobodies are only a fraction of the size of IgG molecules, they may diffuse freely through hydrogels and not require successive ultracentrifugation steps to washout unbound antibody.

Figure 5.7: Antibody staining EVs prior to solid capture imaging

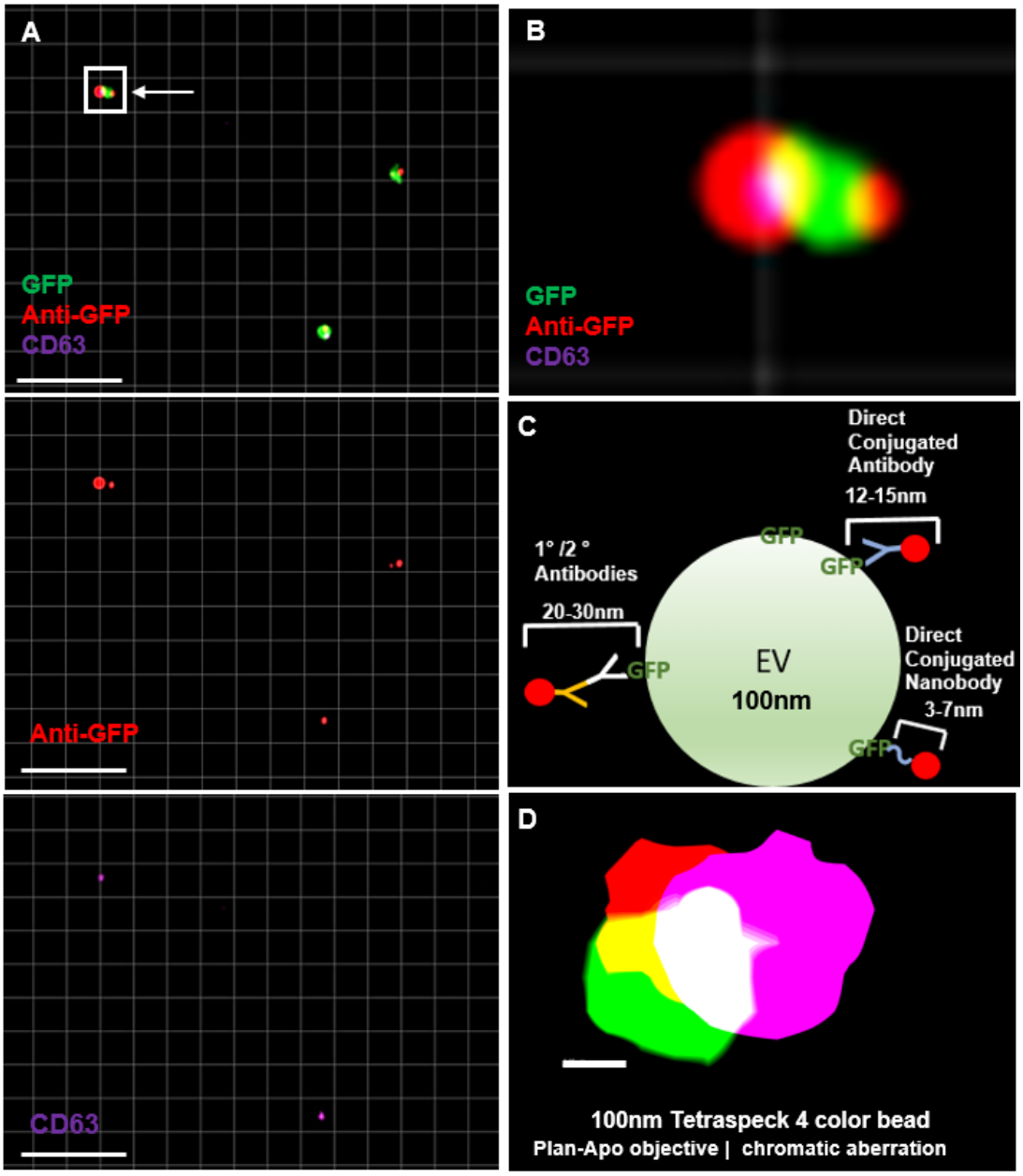

A) Molm-14mGFP EVs (Green) stained with antibodies anti-GFP (red; 1°/2° AF555) and anti-CD63 (magenta; direct conjugated AF647) prior to embedding in Matrigel. Scale bar = 5µm, Grids = 1 µm. **B)** Bounding box contains single EV which demonstrates surface staining of both anti-GFP and anti-CD63 with localization off-center from native GFP signal. Images acquired using a Zeiss Elyra, equipped with 60x 1.45 NA objective and Airyscan detection module. **C)** A graphical illustration depicts the relative sizes of antibody complexes to nanoscale vesicles. **D)** A single 4-color 100nm Tetraspeck bead demonstrates wavelength-dependent chromatic aberration, imaged using 60x Plan-apochromat 1.49NA, displayed using maximum digital zoom and saturated intensity. Scale Bar= 100nm.

Imaging cellular binding and uptake of extracellular vesicles

Imaging *in vivo* binding and uptake of EVs in immunophenotyped tissues

To map the systemic trafficking of AML-EVs, I developed an *ex vivo* imaging assay that couples fluorescence activated cell sorting (FASC) with live cell microscopy to detect the transfer of cell-specific EVs within mouse tissues. By engrafting mice with AML cell lines expressing membrane tagged-GFP [21, 265, 295], I was able to quantify the binding and/or uptake of EVs into recipient cell types using the highly sensitive methods of live-cell microscopy. Through this technique I can perform single cell analysis to identified EVs accumulation with adequate resolution to identify directional transfer of nanoscale EVs into immunophenotyped recipient cells.

To analyze AML-EV association with hematopoietic and stromal cells (**Fig 2.1; 3.1**), I harvested the bone marrow from the long bones of NSG mice xenografted with mGFP expressing AML cell lines. Bone marrow and supportive stroma were flushed using RPMI with 2% FBS and 1% pen strep and collected by centrifugation at 300 *g*. Red blood cells (RBC) were hemolyzed, and cells were filtered through cell strainers (hematopoietic cells 35µm/ stromal cells 70µm) then suspended in PBS with 2% FBS. Freshly harvested cells were then stained with the appropriate antibodies at 4°C for 30 min before flow cytometric sorting using the Influx™ cell sorter (BD Biosciences). In order to prevent spectral cross-talk of antibody-bound fluorophores used in cell sorting from interfering with imaging-based analysis, fluorophores detected in the 488nm-1 channel (i.e. FITC) were avoided. Likewise, fluorophores detected in the adjacent 488nm-2 channel were only used for cell exclusion, as the fluorophore phycoerythrin (PE) interfered with GFP detection by microscopy using a standard 510nm emission filter with a 20nm band pass. The immunophenotypic classification of relevant cell populations, and fluorophores used are listed in **Table 5.1**. Cell populations from non-engrafted wild-type animals were used

to validate the antibody panels and assess background fluorescence in the GFP channel by microscopy.

Table: 5.1: Antibodies for immunophenotyping

Population	Antibody	Fluorophore	Source	Identifier
All	Live/Dead	Aqua	Life Technologies	L34957
Stroma OPC CD31-/CD45-/Sca-1-/CD51+ MSC CD31-/CD45-/Sca-1+/CD51+	CD31	FITC	Biolegend	102406
	CD45	PE	Biolegend	304037
	CD51	AF647	Biolegend	104105
	SCA-1	APC/Cy7	Biolegend	108126
KSL cKit+/Sca-1+/Lineage-	cKIT	APC	Biolegend	105808
	SCA-1	APC/Cy7	Biolegend	108126
SLAM KSL/CD48-/CD150+	CD150	PE/Cy7	Biolegend	115914
	CD48	PerCP/Cy5.5	Biolegend	103422
Lineage+	CD3	APC or PE	Biolegend	100312
	CD4	APC or PE	Biolegend	100412
	CD5	APC or PE	Biolegend	100626
	CD45R (B220)	APC or PE	Biolegend	103212
	CD11b (Mac-1)	APC or PE	Biolegend	101212
	Ly6G/ Ly6C (Gr-1)	APC or PE	Biolegend	108412
	TER-119	APC or PE	Biolegend	116212

For improved sensitivity of detecting internalized mGFP EVs, freshly sorted cells need to be imaged under-live cell conditions soon after harvest. Live-cell conditions are important because fixation increases background, and reduces signal density of membrane-associated fluorescent proteins. Bone Marrow cells typically require an hour of incubation on Matrigel at 37°C to allow for attachment. Since live cells are metabolically active it is also important to not culture cells for expended lengths of time to avoid degradation of internalized mGFP+ EVs, or loss of cell viability due to culture conditions.

To prepare cells for imaging, cell populations were sorted into 2 ml Eppendorf tubes containing 1 ml of media (4°C). Freshly purified cells were centrifuged at 300g for 10 minutes at 4°C and resuspended in fresh phenol-free media, before being replated onto Matrigel (growth factor reduced/phenol free; diluted 1:9) in 35mm live cell culture

chambers with 4 well inserts and #1.5 polymer coverslip bottom (Ibidi, Germany). Cells were then incubated at 37°C 5% CO2 for 45 minutes to allow for attachment to Matrigel coated chamber. Cells were then stained with Hoechst (250ng/ml; ThermoFisher) and Cellmask Deep Red (1ul/ml; ThermoFisher) for 15 minutes at 37°C and gently washed twice with warmed phosphate buffered saline (1X) before adding fresh media. Cells were then imaged using a Deltavision CoreDV/Olympus IX71 microscope, equipped with 60X Plan Apo N 1.49 objective, 7-color solid state LED illumination, motorized stage, Nikon Coolpix HQ CCD camera, and live-cell chamber supplying 37°C/5% CO_2. Three dimensional Z-stacks were acquired using 200nm Z-step through the entire cell volume to maximize capture speed while maintaining adequate axial resolution. Exposure times and laser intensity were held constant between conditions. To identify non-specific background for the 488 channel (GFP), Z-stacks of respective cell populations from non-xenografted NSG mice were captured to determine signal threshold value. Images were deconvolved using SoftworX and analyzed using Imaris Bitplane.

For CD8+ T lymphocyte experiments, cells were harvested from spleens of C57BL/6 mice engrafted with syngenetic palmitoylated-acGFP expressing TIB-49 cells (C1498) (**Fig 4.1**). CD8+ T cells were isolated using ferric-conjugate antibodies and a magnetic column (EasySep Mouse 19853 CD8+ T cell isolation kit, Stem cell, Vancouver, Canada) from both sham injected and TIB-49 engrafted animals. Ferromagnetic antibodies provided no spectral interference in imaging experiments, as CD8+ T cells from sham animals contained only low background level signal in GFP channel. Since CD8+T-cell show limited adherence to Matrigel, cells were plated onto Ibidi™ imaging chambers coated with poly-L-lysine. Cells were added directly to coated plates in PBS without FBS to prevent quenching of positively charge poly-L lysine. Cells were briefly centrifuged at 100g to promote fast adhesion of non-adherent cells. Cells were incubated for 30 minutes at 37°C with 5% CO_2, then 1 volume of RPMI with 20%FBS was gently added before cells were imaged as described above.

Bone marrow resident HSCs, stromal cells and T-cells harvested from mice engrafted with mGFP expressing AML, contained numerous punctate mGFP foci, similar

in size and intensity those seen in solid capture imaging experiments (**Fig 5.8A**). Surprisingly, cells containing associated mGFP EVs were identifiable during FACS sorting (**Fig 5.8B**). This was unexpected due to the relatively small size and intensity of EVs compared to cellular stains, yet am GFP positive cell populations was apparent on flow plots. To confirm this finding, I sorted HSCs (KSL) from Molm-14mGFP xenografted animals into low, mid and high populations based of GFP intensity. I exploited the high sensitivity of live-cell imaging to validate the presence of EVs puncta in sorted populations. By doing so I found that EV foci were present in all three populations, and increased significantly from GFP-low to GFP-high populations (**Fig 5.8C-D**; low vs high $p < 0.012$, and mid vs high $p < 0.011$). This finding demonstrated the relative sensitivity of flow cytometry in detecting nanoscale EVs within recipient cells. Additionally, to confirm that punctate GFP signal seen engrafted mice was not due to non-specific microenvironmental stress (such as hemoglobin degradation and reactive oxygen species) precipitated by leukemia engraftment, I analyzed HSCs from animals xenografted with wild-type Molm-14 cells (non-GFP). HSCs from these animals lacked puncta and contained only diffuse background equivalent to non-engrafted controls (**Fig 5.8D**).

Figure 5.8: FACS sorting and imaging HSCs based on *in vivo* mGFP EV uptake

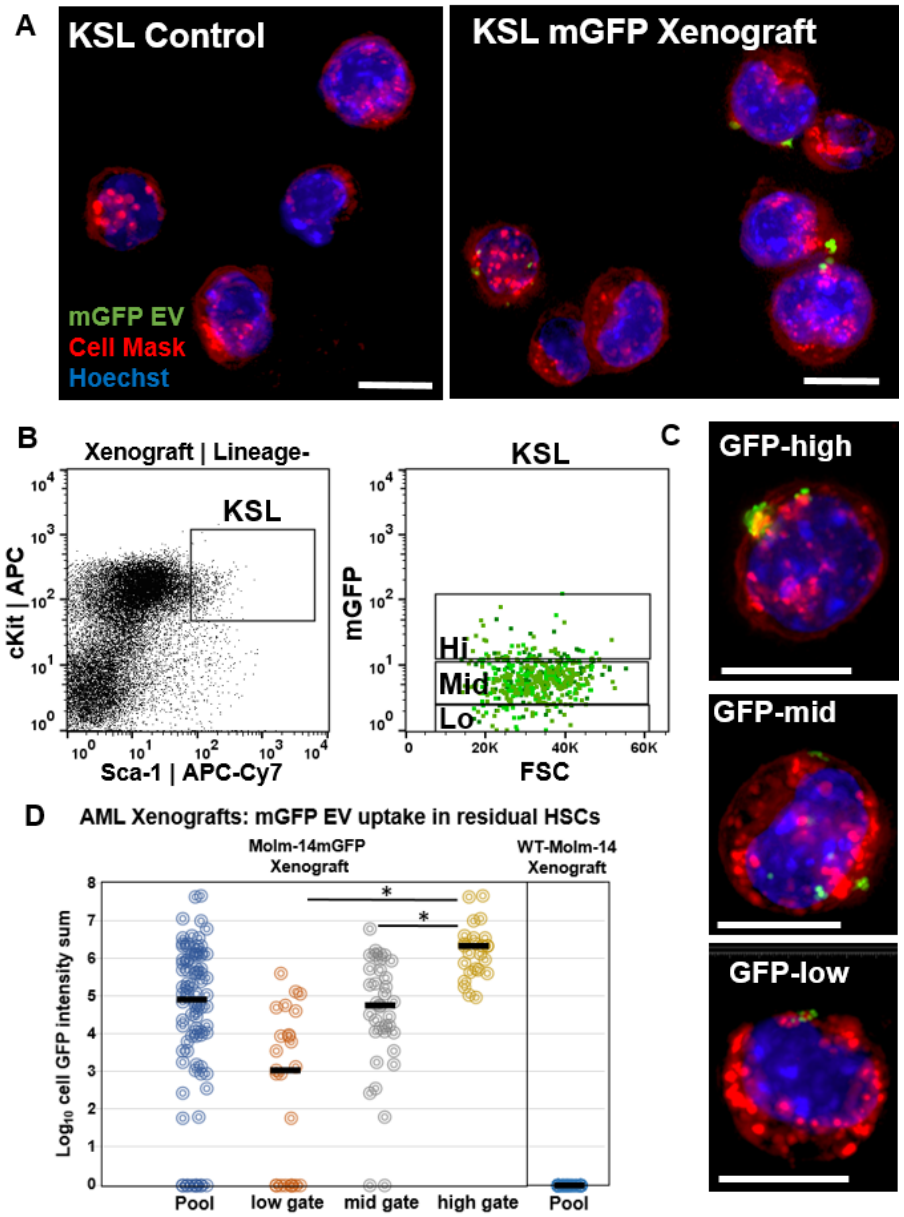

A) Representative images of HSCs (KSL) from control animals and Molm-14mGFP xenografts. **B)** Representative flow plots of KSL from xenografted animals sorted into three populations based on GFP intensity. **C)** Representative live-cell images from each population. Images captured with CoreDV microscope with 60x 1.49 TIRF objective and Nikon Coolpix CCD camera. Scale bars = 5µm. **D)** Image-based analysis of GFP intensity sum of individual cells from low, mid, and high GFP gates normalized to KSL from non-engrafted animals. Gated populations compared to KSL pool from animal xenografted with Molm-14mGFP and wild-type Molm-14 cells. Bars represent median value, significance determined with a one-way ANOVA with Tukey's multiple comparison (* $p<0.05$).

In vitro analysis of EV binding and uptake into recipient cells

With AML-EVs accumulating in recipient cells *in vivo*, I set out to validate if binding and uptake of AML-EVs occurs in these cell types *in vitro,* and determine the relative kinetics of internalization. To analyze the association of EVs with recipient cells, I purified respective cell populations (by FACS or immuno-magnetic separation as previously described) and exposed them to EVs isolated from mGFP/pmGFP expressing AML cells. The methods used for each recipient cell type are summarized *as follows*.

Bone Marrow Stroma

To analyze *in vitro* uptake of AML-EVs into hematopoiesis-supporting stromal cells, we harvested MSCs and OPCs by FACS (as described above in **Table 4.1**) and expanded cells for one week on Matrigel (1:11 dilution) coated Ibidi culture slides (#1.5 coverglass). I have found that Matrigel coating allows the cytoplasm of stromal cells to grow flatter, improving the spatial and temporal resolution of live-cell imaging by reducing the Z-axis height, the number of slices needed for acquisition, as well as interference from out of focus light. MSCs and OPCs were then treated with $1x10^8$ Molm-14 mGFP EVs or vehicle at 0 and again at 24 hours. At hour 36, cells were washed in 37°C phosphate buffered saline. To quantity the intracellular association of EVs with the endoplasmic reticulum, cells were stained with ER-Tracker Red (500nM in Hank's Balanced Salt Solution) for 1 hour. Cells were then washed and stained with Hoechst (250ng/ml; ThermoFisher) and Cellmask Deep Red (1ul/ml; ThermoFisher) for 15 minutes at 37°C. Cells were washed twice with warmed phosphate buffered saline (1X) before adding fresh media. Cells were then imaged under live-cell conditions using a Nikon TiE microscope equipped with Yokogawa CSU-W1 Spinning Disk confocal, 60X Plan Apo 1.45 objective, Nikon CCD camera, and live cell chamber supplying 37C/5% CO2. Z-stacks were acquired at 100nm Z-step using 50nm pinhole through the total volume of the cell with exposure times and laser power held constant across conditions. Images were analyzed using Imaris

Bitplane. Cellmask staining demarcating the plasma membrane was used to determine the outer limit of the cells and determine mGFP foci internal to the plasma membrane, while masking those found external to the cells. To measure mGFP foci and their association with the ER territory, Imaris "Spot" function was used to identify, count and differentially pseudo-color internal mGFP foci based on association with the ER (**Fig 2.1E**).

To confirm that cell-internal mGFP+ foci were intact EVs and not aggregates of GFP protein, mouse C57BL/6 MSCs were cultured in Ibidi™ imaging chambers, exposed to human EVs and stained with human specific anti-CD63. Since intracellular staining requires fixation and permeablization of cells, Matrigel was omitted for fixed-cell imaging, as it acquires autofluoresence through aldehyde fixation. Instead, cells were grown directly on plastic #1.5 imaging chambers (Ibidi™). Following attachment, cells were stained for 10 minutes with CellMask Red™ (1ul/ml) then fixed with 4% paraformaldehyde and 0.1% glutaldehyde for 20 minutes at room temperature, before permeablizing cells in 0.1% Triton X-100 for 10 minutes on ice. Cells were then stained with human anti-CD63 (Abcam) over night at 4°C (**Fig 5.9A**). Images were captured using a Zeiss Elyra equipped with Airyscan module, using a 60X 1.45 NA objective. Z-stacks were acquired at 100nm Z-step using Airyscan acquisition through the total volume of the cell. Images showed that mGFP+ foci co-stained with human CD63, indicating that internalized vesicles were in fact human-derived EVs.

Additionally, using 3D time-lapse microscopy of stromal cells, I captured uptake of AML-EVs beginning within minutes following *in vitro* exposure. After only 4 hours, stromal cells contained tens to hundreds of GFP+ EVs (**Fig 5.9B**), the majority of which resided in and around the ER (ER-associated: green/ non-associated: white). To determine if AML-EVs are internalized into the endosomal pathway, we labeled live stromal cells (MSCs and OPCs) with CellMask Deep Red for 20 minutes before washing cells twice. From previous experiments, we found that cell mask begins to cycle from plasma membrane into the endosomal compartment after 20-30 minutes of culture. Once plasma membranes were stained and the media changed, GFP+ AML-EVs were spiked into the fresh media, and incubated for another 20 minutes prior to live-cell imaging. By taking

time-lapse acquisitions, we found that EVs bind the membrane surface of recipient cells, and become internalized into the cells, surrounded by cell mask labeled plasma membrane. The majority of cell-internal mGFP+ EVs moved through the cells within individual CellMask+ endosomes that were larger in size than the signal emitted from EVs. Endosomes loaded with mGFP+ EVs tracked along peripheral ER filaments (likely on microtubules) and accumulated around the perinuclear ER (**Fig 5.9B-C**); an association previously reported in healthy human fibroblasts [55]. Further time-lapse imaging (**Fig5.10A-C**) demonstrated that EVs remain intact for hours and can move between individual endosomes or can separate from them entirely. Internalized EVs frequently appear to partially fuse with endosomal membrane (**Fig 5.10B**) where they come in contact with other endosomes and sites of the ER. Internalized EVs in the perinuclear region appeared to transiently fuse with the ER membrane (**Fig 5.10C**). Time-lapse images were captured using a Deltavision CoreDV/Olympus IX71 microscope, equipped with 60× Plan Apo N 1.49 objective, Nikon Coolpix HQ CCD camera, and live-cell chamber supplying 37°C with 5% CO2. 3D Z-stacks were acquired in fast acquisition mode with multiple channels using 3-5 Z-planes to maximize capture speed while maintaining axial resolution.

Hematopoietic Stem Cells

To study the kinetics of AML-EV uptake in hematopoietic stem cells (**Figure 3.1F**), we harvested bone marrow from C57BL/6J mice and purified LT-HSCs and KSL cells by FACS (as described above in Table 5.1). Isolated cells were washed and centrifuged before plating onto Matrigel-coated (1:11 dilution) Ibidi culture slides with #1.5 coverslip for 45 min. Cells were imaged to assess background autofluorescence in the 488 channel (time 0) cells to determine signal threshold value. Cells were then exposed to 1×10^8 Molm-14-mGFP EV and were imaged at 30 and 150 min following exposure. Images were captured using a Deltavision CoreDV/Olympus IX71 microscope as described above. 3D Z-stacks were acquired in 2 channels with a 300 nm Z-step through the entire cell volume to maximize capture speed while maintaining adequate axial resolution. Exposure times and laser power were held constant across conditions. Images were analyzed using Imaris software (Bitplane). By capturing live-cell 3D z-stacks at 0, 30 and 150 minutes, we found that both KSL and LT-HSC bind and internalize numerous

$mGFP^+$ EV within 30 minutes of exposure with continued accumulation at 150 minutes (**Fig 3.1F-G**).

CD8+ T Lymphocytes

For Analysis of EV binding to CD8+ T lymphocyte (**Fig 4.3A**), T cells were isolated by negative selection using ferric-conjugate antibodies and a magnetic column (Human 17953 CD8+ T cell isolation kit, Stem cell, Vancouver, Canada) from peripheral blood. CD8+Tcells were co-stimulated with anti-CD3/CD28 tetrameric beads for 24 hours. Cells were washed in PBS w/2%FBS, centrifuged at 300g and incubated in RPMI with 10% FBS, with or without the addition of Molm-14 EVs (collected from a 24-hour cultures of 6 million total cells with or without IFNγ exposure). After 1 hour, CD8+ T cells were washed twice in 10 volumes of cold 1xPBS and centrifuged at 300g before plating cells onto imaging chambers coated with poly-L-lysine. Imaging chambers containing cell suspension were briefly centrifuged at 100g for 2 minutes to facilitate adhesions, then incubated for 45 minutes at 37°C with 5% CO2. Cells were then stained with Hoechst (100ng/ml; ThermoFisher) and Cellmask Deep Red (1ul/ml; ThermoFisher) for 5 minutes at 37°C and gently washed twice with warmed phosphate buffered saline (1X) before adding fresh RPMI (phenol-free) with 10% FBS media. Live cell images were captured using a Zeiss LSM880 equipped with Fast Airy module, using a 60X 1.49NA objective. Z-stacks were acquired at 200nm Z-step using Airyscan acquisition through the total volume of the cell, with exposure times and laser power held constant across conditions. Foci binding was analyzed using Olympus/Deltavision CoreDV Microscope. Cellmask staining demarcating the plasma membrane was used to determine the outer limit of the cells and facilitate the quantification of cell-associated EV foci. After incubation, 48% and 32% of CD8+T-cells contained bound GFP+ foci following treatment of EVs from Molm-14mGFP cells culture with and without IFN, respectively (**Fig 4.3A**). The size and intensity of T-cell-associated EV foci were comparable to that seen in the peripheral blood and spleens of leukemia engrafted animals (**Fig 4.1G**). In vehicle treated control cells only diffuse autofluorescence was detected.

Figure 5.9: Intracellular Fate of Internalized AML-EVs

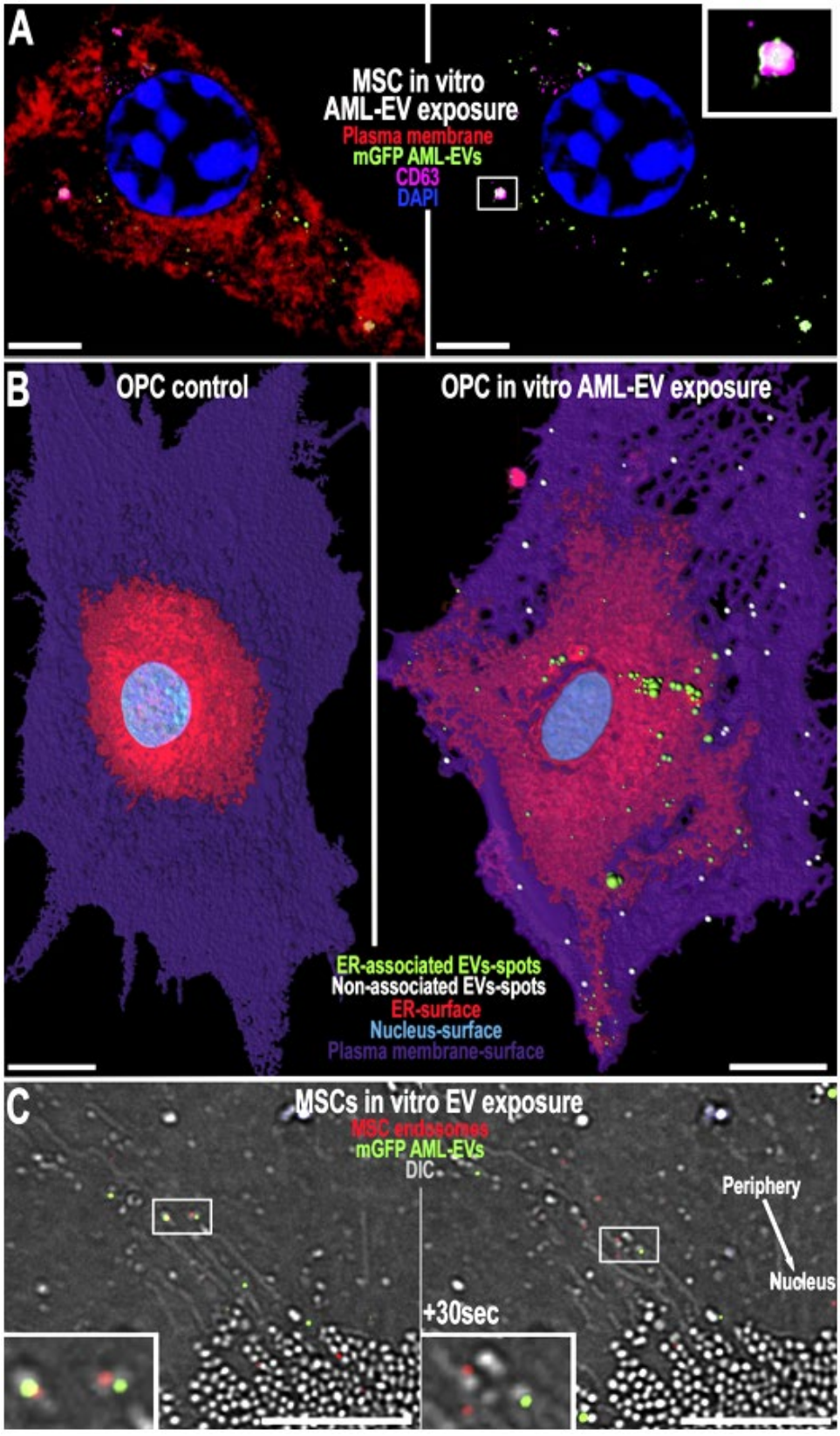

A) Human Molm-14mGFP EVs (green) internalized *in vitro* by mouse MSCs co-stain with human specific CD63. Images acquired using a Zeiss Elyra, equipped with 60x 1.45 NA objective and Airyscan detection module. **B)** AML-EVs accumulate in and around the endoplasmic reticulum (ER) of OPCs *in vitro,* and result in ER-dilation (red) and activation of the unfolded protein response pathway. EVs are differentially pseudocolored based on localization with the ER (ER-associated Green, non-associated white). Images captured with Nikon TiE microscope equipped with Yokogawa CSU-W1 Spinning Disk confocal, 60X Plan Apo TIRF 1.49 objective, Nikon CCD camera, and live cell chamber supplying 37C/5% CO2.**C)** Live-cell time-lapse imaging shows that AML-EVs are internalized into plasma membrane-derived endosomes (CellMask-red) which track along peripheral ER filaments (DIC) to accumulate around the perinuclear ER in MSCs. Boxes show separation of mGFP EV from the endosome at the ER: All scale bars = 5μm. Images captured using a Deltavision CoreDV/Olympus IX71 microscope, equipped with 60× Plan Apo N 1.49 objective, Nikon Coolpix HQ camera, and live-cell chamber supplying 37°C with 5% CO2.

Figure 5.10: AML-EVs are internalized into endosomal compartment and interact with the endoplasmic reticulum

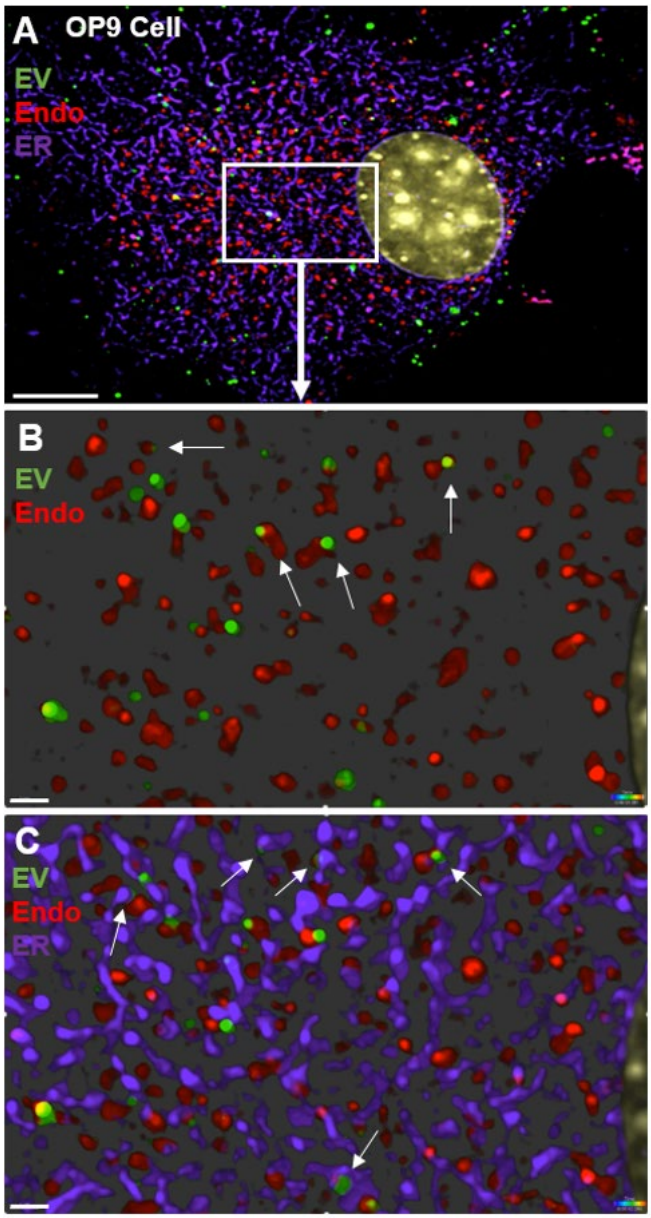

A-C) Representative time-lapse acquisition of EV uptake and fate in a mouse stromal cell. **A)** AML-EVs (green) enter OP9 cells via endocytosis and interact with the ER (purple). (Live-cell 10 minute time-lapse; scale bar =10 μm) **B)** EVs (green) remain localized with endosomes (red) and often appear fused with the periphery of endosomal membrane (as indicated by arrows). **C)** Both endosome-associated and non-associated EVs interact with the ER (purple). ER filaments are observed remodeling around and fusing with AML-EV. Arrows indicate sites of EV-ER colocalization (scale bars = 1μm). Images captured using a Deltavision CoreDV/Olympus IX71 microscope, equipped with 60× Plan Apo N 1.49 objective, Nikon Coolpix HQ camera, and live-cell chamber supplying 37°C with 5% CO2.

Characterizing AML-EVs using High Resolution Flow Cytometry

In the last few years, multiple groups have shown that by modifying flow cytometery parameters, nanoscale EVs can be detected in biofluids, and characterized using antibody labeling to distinguish cell and tissue origins [278, 279]. Referred to as high resolution flow cytometry (HRFC), this method relies on increased laser voltages to detect nanoparticles using side-scatter (SSC), combined with additional laser channels to identify EV-associated fluorescent labels [278, 279]. Using HRFC, I was able to characterize surface markers on AML-EVs, again using mGFP signal as an internal control to compare differences in staining efficiency. Compared to solid capture imaging, the experimental setup and analysis can be performed in a fraction of the time, and allows for greater flexibility in staining. However due to variable flow rates, low signal to noise, and questionable sensitivity, I have found that HRFC is not ideal for quantifying exact EV concentrations. However, despite these limitations, the high throughput nature, and capacity for incorporating numerous labels simultaneously (or in parallel), makes HRFC an ideal platform for screening EV-associated markers.

HFRCs was performed by directly staining microliter volumes of conditioned media from mGFP expressing cells without requiring ultracentrifugation. Conditioned media was collected from 24-hour cultures (5 x 10^5 cells/ml) and centrifuged at 1000xg and 2500xg for 20 minutes respectively to remove cells and large debris. Supernatant was then passed through a 0.2µm filter, and pipetted into 10µl aliquots into a 96 well plate for antibody staining. Direct conjugated antibodies were diluted to a final concentration of 1-0.2µg/ml, and incubated for 2 hours at room temperature. To reduce background noise from the antibody staining, I relied on non-tandem fluorophores, PE, APC or Alexa Fluor 647 to co-stain mGFP+ EVs. After incubation, sample volumes were brought up to 250µl with 0.1µm filter PBS, and samples were transferred to FACS tubes. Samples were run on a BD FACS Canto II with the blue laser increased to 200mW to increase side-scatter sensitivity. Samples events were recorded over 60 seconds using the lowest flow rate.

Figure 5.11: Characterizing AML-EVs by HRFC

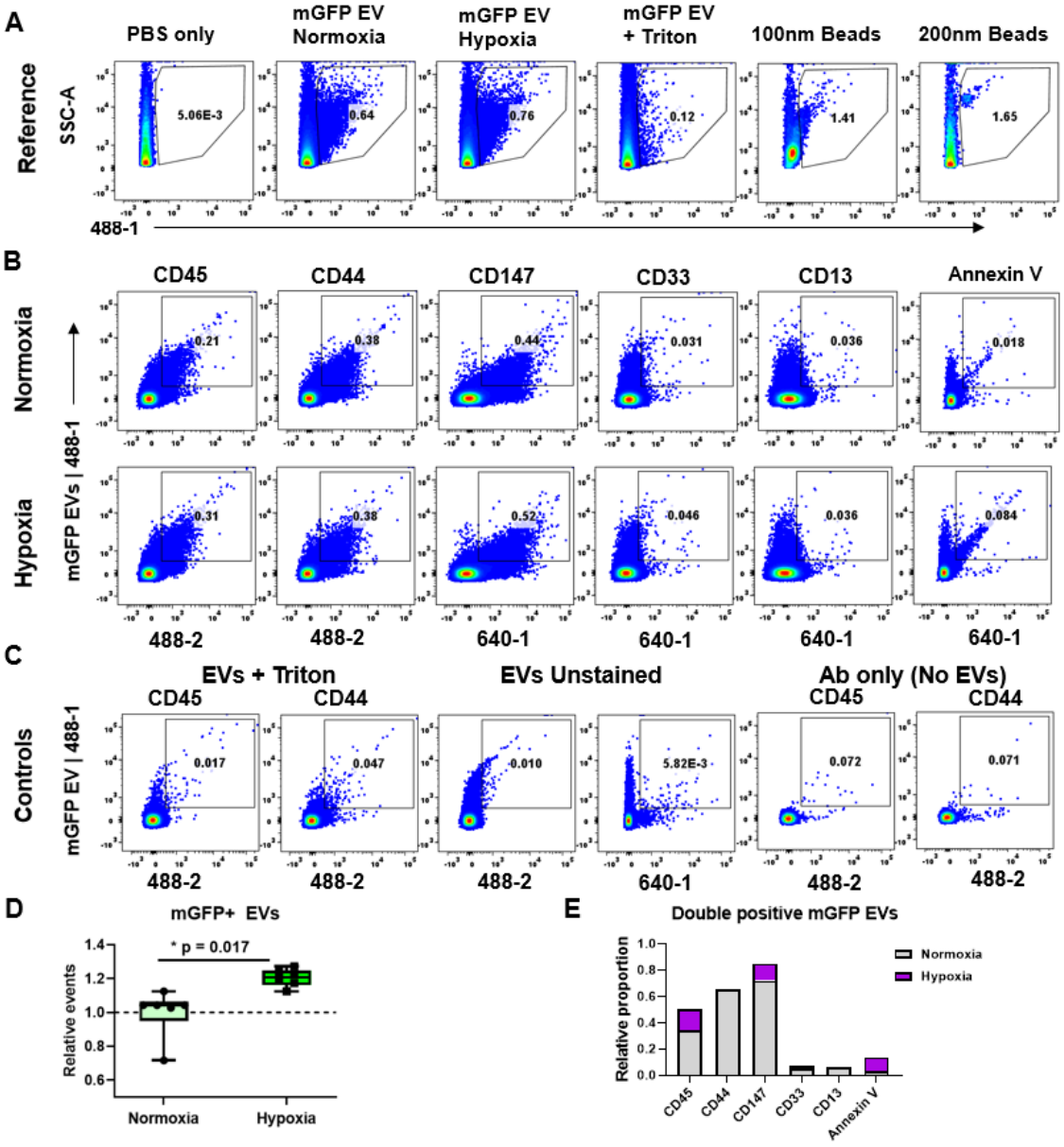

A-C) Representative HRFC flow plots. **A)** (Left) PBS–only sample demonstrates baseline noise detected via side-scatter (SSC). (Middle) Conditioned media from Molm-14mGFP cells contains right-shifted nano-sized GFP+ events, which increase in hypoxic conditions. (Right) Fluorescent reference beads have distinct size-specific SSC profiles. Gates indicate relative proportion of positive events. **B)** EV staining in normoxic (upper) vs hypoxic conditions (lower). Gates indicate dual-positive events. **C)** (Left) Triton causes loss of vesicle associated events. (Middle) Unstained EVs lack fluoresence in respective channels. (Right) Antibodies diluted in PBS produce minimal background. Statistical significance determined by Student's two-tailed t-test. * P =<0.05. **D)** Relative change in double positive mGFP EV counts based on culture conditions. Relative proportion normalized to average mGFP EVs event count under normoxic conditions.

To validate the detection of nanoscale EVs, I included 100nm and 200nm reference beads which were used to set gates for EV-associated signal (**Fig 5.11A**). To assess staining quality, I compared stained EV samples to unstained EVs and antibody only controls. Additionally, to demonstrates the loss of membrane-associated vesicles, I added Triton X-100 detergent at a final concentration of 0.1% after running EV samples, which resulted on the loss of both mGFP+ and co-stained vesicle populations (**Fig 5.11B, C**).

In previous studies, our group has found that culturing AML cells in hypoxic conditions increased the release of EVs [108]. To see if HFRC could resolve relative differences in EV populations, I compared conditioned media from cells grown in normoxic and hypoxic conditions (20% vs 5% O_2). Analysis by HRFC showed a relative 1.2-fold increase in mGFP+ events under hypoxic conditions ($p=0.017$) (**Fig 5.11D**). As expected, mGFP+ EVs co-stained with hematopoietic-associated markers CD45. They also stained with CD44, as well as malignancy-associated marker CD147, which are both highly expressed on the surface of Molm-14 cells (**Fig 5.11B**). Interestingly, EVs did not stain for CD13 or CD33 despite being prominently expressed on the cell surface. To act as a negative staining control, I stained AML-EVs with platelet-specific marker CD41, which as expected, did not label mGFP+ EVs. (**Appx 4.6.1A**). A very minor subset of EVs also stained for annexin V indicating the presence surface phosphatidylserines. Consistent with other reports of exosomes, mGFP+ EVs stained for tetraspannins CD63 and CD9, though the CD9+ population was small compared to CD63 or CD45 populations (**Appx 4.6.1A**).

Based on these experiments, I find HRFC to be an exceptional screening test for EV specific makers. Due to the difficulty of separating baseline noise from true EV signal, it is difficult to determine the full extent of sensitivity achieved with this method. To improve signal to noise, stained EV samples frequently require additional dilution prior to analyzing, often in an iterative manner. Flow rates are also subject to change while running individual samples, laser alignment can change overtime, and contamination within the microfluidic system can cause cross contamination of sample data. Together these can lead to inconsistencies in data collection. Because of these limitations, HRFC is not ideal for

measuring exact concentrations of EVs, however if proper care is given, relative differences in EV populations and associated surface markers can be estimated between conditions. In sum, HRFC is a fast method for screening EV-associated surface markers, and will prove to be a useful tool for advancing the field of EV biology.

Conclusion

In sum, we demonstrate that fluorescence microscopy and HRFC are able to shed light on the release and composition of EVs from distinct cells and tissues. Despite limitations, EVs are readily detectable by diffraction-limited microscopes, and flow cytometers. Together these systems can be harnessed to identify cell-specific release of EVs, and allows for analysis of EV-associated proteins and lipids. In the future, imaging-based methods may be translated to work with SMLM techniques for even greater gains in resolution. From analyzing EV populations, to tracking the uptake and intracellular fate of EVs in recipient cells, fluorescence microscopy and flow cytometry are both powerful techniques that can be exploited to study EV-mediated signaling in both health and disease.

Funding

These studies were supported by a Hyundai Hope on Wheels Grant (PK, JTB), Friends of Doernbecher Grant (JTB), OHSU's Tartar Trust Grant (JTB), and the National Cancer Institute Award Number F30CA247601 (JTB).

Chapter 6: Conclusion and future directions

Conclusion

The development of a self-reinforcing niche in AML has become an important aspect of leukemogenesis, that enables not only the continuous expansion of abnormal blasts, but also precipitates their transformation. Studies have demonstrated that by disrupting Dicer1 and Notch signaling in bone marrow osteoprogenitors alone, induced hematopoietic dysfunction, producing myelodysplasia and eventual leukemic transformation [10, 103]. Thus, dysregulation of the bone marrow microenvironment remains a constitutive aspect of leukemic initiation and clonal evolution that facilitates disease relapse and chemoresistance. EVs have emerged as key mediators of bone marrow dysregulation; their widespread release effectively alters the stromal compartment, residual HSCs and even immune cells in the leukemic niche.

Prior to the work described in this thesis, the functional potential of AML-EVs enacting regulatory changes in bone marrow resident cells and lymphocytes had only begun to be understood. We first set out to study the functional outcomes of EV trafficking to bone marrow stromal cells. With knowledge that cellular composition of hematopoiesis-supporting stroma is altered, we hypothesized that AML effectively reprograms these cells through the paracrine release of EVs. We found that EVs rapidly accumulate within key stromal elements and transmit endoplasmic reticulum stress, enforcing differentiation and apoptosis to modify the cellular composition [6]. Another group had previously demonstrated that the transmission of ER-stress occurs in solid tumors—through an unknown secretory mechanism—leading to activation of the UPR pathway and chemoresistance in multiple solid tumor models [162, 163]. Our study was the first to describe EVs as the vehicle that selectively transmits ER-stress in recipient cell type-specific manner. We found that EVs potently activated the unfolded protein response in stromal cells but not HSCs.

Next, we set out to define the mechanism underlying EV-mediated dysregulation of hematopoietic stem cells. It is well known that AML represses normal hematopoiesis to produce lethal anemias and pancytopenias. Our group previously found that EVs reduce clonogencity of HSPCs by blocking transcription factor c-Myb, while also promoting their displacement from the medullary space. Interestingly, long-term HSC, with the greatest pluripotent capacity, proportionally increased within the leukemic niche as they assumed a quiescent state. We hypothesize that EV-mediated signaling enforces quiescence in LT-HSCs to limit homeostatic proliferation, reducing cellular competition with AML blast for niche occupancy. We found that AML-EVs traffic distinct miRNAs that target the mTOR pathway to suppress protein synthesis in LT-HSCs. This suppressive effect was reversible upon transplant to a non-leukemic niche, however we found evidence of lasting DNA damage following EV exposure. Together these finding provide additional evidence for EV-mediated suppression of hematopoiesis, and indicates that residual HSCs acquire genomic-stress that may increase the risk for secondary transformation and relapse.

With mounting evidence indicating that AML is able to evade destruction by the immune system, I set out to test the immunosuppressive effects of AML-EVs on cytotoxic T lymphocytes. After discovering that AML-EVs carry immunosuppressive ligand, PD-L1, I hypothesized that EVs functionally inhibit effector CD8+T cells, a key component of the immune system's anti-tumor response. I found that AML cells incorporate PD-L1 onto EVs response to T-cell secreted IFNγ, which bind CD8+T-cells in a greater capacity. CD8+ T cells exposed to AML-EVs demonstrate increased apoptosis and reduced activation and expansion in response to TCR-stimulation. Importantly, this effect was largely rescued by blocking PD-1, which improved cytokine expression and proliferation. This study is the first to show the functional effect of EV-associated PD-L1 in AML, and demonstrates that AML-EVs enter systemic circulation to interact with distant lymphocytes. This systemic release of EVs likely contributes to T-cell exhaustion commonly seen at relapse in AML, and may impede response to immunotherapy.

Furthermore, through this work I developed and optimized new methods to improve the study of AML-extracellular vesicles. Using both solid capture imaging and flow

cytometry approaches, I was able to quantify EV concentrations with respect to cellular origin, and characterize surface markers on AML-EVs. To improve the identification of EV trafficking to recipient cells, I developed live-cell imaging techniques to resolve the binding and uptake of EVs *in vitro* and *in vivo* conditions.

Together, the work described in this thesis identifies mechanisms of EV-mediated signaling used by AML to differentially regulate recipient cells. It is clear that AML-EV shape a pro-leukemic niche, and are involved in multiple aspects of leukemogenesis. This work begins to clarify the distinct roles of AML-EVs in driving leukemic initiation, progression, chemoresistance and relapse. However, this work has also identified undefined aspects of AML, and many important questions remain. Additional research will be key to realizing the functional effects of EV-mediated signaling in AML, and to develop better therapies to improve the 5-year survival beyond 25%. Select questions and approaches are summarized as follows:

Future Directions

Understanding recipient cell binding and tissue tropism of AML-EVs

Throughout my studies examining AML, I have identified the widespread release of EVs, and begun to map the fate EV in the bone marrow microenvironment and distant tissues. One thing that is striking is the abundance of AML-EVs that associate with hematopoietic cells, stromal cells and immune cells in leukemic animals. Using *in vitro* studies, I directly observed binding and uptake of AML-EVs within minutes of exposure across multiple cell types, this is particularly striking in stromal cell populations which can contain hundreds of internalized EVs after only an hour. I have yet to find a cell population under *in vitro* conditions which do not adsorb AML-EVs. It remains to be tested whether the ability to gain access to so many cell types is a fundamental property of exosomes and microvesicles, or if this phenomenon is specific to those released by AML blasts, or even differs between AML subtypes or in leukemia initiating cells. It has been suggested that

this is an artifact of *in vitro* conditions, yet analysis of mice engrafted with mGFP expressing AML confirms that EV internalization occurs in these same cell populations *in vivo*, and across multiple subtypes of AML.

Fully characterizing the surface molecules that facilitate binding and/or entry to recipient cells is key to advancing our understanding of EV-mediated signaling in AML. By determining whether AML blasts release distinct subpopulation of EVs that are able to target specific cell types, we can begin to identify potential adhesion molecules, chemokines, and receptor-ligand interactions that facilitate cell binding and internalization. To date multiple studies have shown that EVs rely primarily on endocytosis to gain entry into recipient cells, and suggest roles for heparan sulfate, tetraspanins, and integrins as an binding and entry mechanisms [36, 46, 318, 319]. We have found that entry of AML-EVs is temperature dependent, and occurs through the in-folding of the recipient cell membrane into an endosome-like structure that surrounds the internalized vesicle (**Fig 5.10**). These findings are highly consistent with other reports describing endocytosis as the predominate mechanism of entry [320]. Despite this, no specific receptor-ligand candidate(s) has not been found for AML to date. This may be because the apparatus the confers binding and entry is both recipient cell type-dependent and highly variable across subtypes of AML.

In breast and pancreatic cancer, specific integrins incorporated in the exosomal surface were shown to direct tropism to distinct tissues. Exosomes containing integrins α6β4/ α6β1 were found to target the lung, while αVβ5 distributed to the liver, conditioning these areas as a pre-metastatic niche [29]. For AML, it remains to be determined if integrin-restricted exosomes carry distinct cargos to recipient cells. The finding that AML-EVs transmit ER-stress and activate UPR in stromal cells but not HSCs or T cells, supports the presence of discrete EV-subpopulations. Further characterization of AML-EV surface molecules and internal cargos will allow for identification of distinct subpopulations, and offer insight into tissue tropism and paracrine/endocrine function. This will also inform mechanisms of EV biogenesis, particularly how certain factors are packaged together into a vesicle capable of inducing a functional response in recipient cell.

Identifying EVs surface markers and their role in leukemogenesis

In this thesis, we have begun to examine surface markers and bioactive cargos through the use of solid capture imaging and high resolution flow cytometry. These techniques have identified multiple EV-associated proteins that may facilitate binding, entry and even recipient cell chemotaxis. We have found that AML cells shed EVs that contain surface-bound tetraspanins CD9 and CD63 that are well conserved across exosomes, regardless of cellular origin [36, 319]. AML-EVs are highly enriched for hematopoietic-specific markers CD45 and CD44, as well as the malignancy-associated marker CD147, which are all heavily expressed on the surface of AML blasts.

CD44 is a known receptor for osteolineage/mesenchymal-matrix proteins such as collagens and osteopontin, which may act to target EVs to the bone marrow stromal compartment. Additionally, EV-associated CD44 may also exist in a glycosylated form, called HCELL (hematopoietic E/L-selectin ligand) which is a ligand for both E- and L-selectin [321]. E-selectin expression is restricted to cytokine activated endothelial cells and is involved in cellular homing to the bone marrow, while L-selectin is widely expressed by hematopoietic cells and lymphocytes [321, 322]. Together this makes CD44 an interesting candidate to facilitate AML-EV binding to a range of recipient cell types, both locally in the marrow and in distant lymphoid tissue.

CD147 (basigin), a factor first identified to be involved in the regulation of matrix metalloproteinases [323, 324], is densely packaged onto the surface of AML-EVs. Its relative abundance on EVs may make CD147 a candidate biomarker for monitoring minimal residual disease and identifying relapse by liquid biopsy. It is highly expressed across subtypes of AML blasts compared to normal hematopoietic cells, and its upregulation has been linked to unfavorable prognosis [325, 326]. Additionally, in hepatocellular carcinoma, activation of the unfolded protein response pathway is associated with upregulation of CD147. In this context, it is thought to act as a chaperone during ER stress to shuttle proteins out of the cell to oppose apoptosis, and promote chemoresistance [327].

Interestingly, it is able to bind to itself in *trans* and act as a cell surface receptor for extracellular forms of CD147. One of its well know *cis* binding partners is CD44, which is also abundant on AML-EVs [323]. Together these two glycoproteins were found in other solid tumor models to colocalize into membrane rafts, and mediate nutrient transport, chemoresistance and drug efflux [324].

Recently, a link between unfolded protein response induction and chemotherapy resistance in both hematological and non-hematologic cancers has been demonstrated [162, 194]. Though untested, I hypothesize that that AML blasts respond to chemotoxic and metabolic stresses by transmitting EVs to not only stromal cells, but to other leukemic cells as well. This directional transfer between AML cells may upregulate chemo-protective transcription via the UPR pathway, and confers resistance across distant niches. Future research into this, and the role of CD147 and CD44—and other EV-associated cargos like BMPs—may provide fundamental insight into EV-mediated transmission of ER-stress and acquired drug resistance in AML.

Furthermore, I identified AML-EVs containing surface-bound, lymphocyte associated ligands PD-L1 and ICAM1. These EVs are potently immunosuppressive, and inhibit CD8+T-cell activation through an PD-1 dependent mechanism. Though unproven, it is tempting to speculate that EV-associated ICAM1 mediates binding to LFAs on the surface of antigen-experienced CD8+ T cells and other lymphocytes. Similar to integrins in other cancers, ICAM1 and CD44 could dictate tropism to the spleen and other lymphoid tissues by targeting LFAs and L-selectin. It would be interesting to test if blocking these interaction, rescues CD8+ T cell activation. In addition to PD-L1, it is likely that other immunosuppressive ligands and metabolites are packaged into EVs to collectively inhibit CD8+ T cells through distinct pathways. Much work is still needed to be done to fully understand how the systemic release of EVs impacts effector T cell function, and if it interferes with priming and differentiation of naïve T cells in secondary lymphoid tissues. Currently, it remains to be determined if the AML-EVs that target lymphocytes in the bone marrow and spleen are fundamentally different from those that transmit ER-stress within the bone marrow stroma. Further research into EV-associated molecules and heterogeneity

of subpopulations will be essential to understating the fate and function of EVs in AML, and identify ways to mitigate EV-mediated dysregulation.

EVs as a biomarker of therapeutic response to immunotherapy.

For many solid tumors, check point inhibitor therapies have shown profound improvement in patient survival, but only for a minor subset of patients. The expression of PD-L1 in the tumor microenvironment alone has failed to identify patients who respond to check point inhibitor therapy. For AML, early clinical trials of PD-1/L1 blockade have shown mixed efficacy, and like solid tumor models, will require development of new strategies to optimize enrollment and better identify patients who will benefit from related treatment. In a melanoma-specific study by Chen et al., high pre-treatment levels of circulating PD-L1+ exosomes correlated with poor response to PD-1 blockade [142]. They speculated that high-levels of exosomal PD-L1 represented a state of overt T cell exhaustion that not be rescued by PD-1 blockade. Conversely, they found that an increase in exosomal PD-L1 during PD-1 blockade distinguished clinical responders, and identified a reinvigoration of the T cell response that elicited an upregulation in circulating PD-L1 [142]. It is also possible that high pre-treatment levels of PD-L1+ EVs are able to outcompete therapeutic antibodies for PD-1 binding sites, or sequestering anti-PD-L1 to facilitate resistance. Therefore, circulating exosomal PD-L1 identify resistance to checkpoint inhibitors, and other immune-based strategies for the treatment of AML. Though EVs enforce a pre-leukemic microenvironment, they may be a useful biomarker to improve AML diagnostic by identifying relapse, and predicting response to conventional and novel therapies.

Improving image-based characterization of EVs

In chapter 5, I describe the potential of imaging-based analyses to characterize EVs. Imaging nanoscale EVs without movement artifacts was accomplished by embedded EVs

into hydrogels. This allowed for quantification of vesicle concentration from cell culture supernatant or from the peripheral blood of tumor engrafted animals, with the ability to distinguish cell-specific origins of EVs. We expanded upon this technique by staining EVs with lipid dyes and antibodies such as anti-CD63. Unfortunately—due to Matrigel's proprietary, and complex composition—staining EVs pre-embedded into Matrigel produced high levels of background. Therefore, EV needed to be stained prior to embedding, using time consuming successive ultracentrifugation steps to washout unbound labels, which greatly reduced the yield of EVs. To avoid this, directly staining EV in a more inert hydrogel may allow for unbound labels to be washed out without high background, or the need for damaging ultracentrifugation steps. Polymers like acrylamide or agarose, with well characterized physical properties, may allow small molecules labels to diffuse freely, while EVs are held in place. Polyacrylamide, commonly used for electrophoresis is optically clear and has been used to embed embryos for immunofluorescence (IF) [328]. By changing the concentration of acrylamide or agarose, the pore size of the matrix can be modified to accommodate staining [329]. Additionally, by adding a fixation step to crosslink vesicle-associated proteins to amines in an acrylamide matrix, EV membranes may be permeabilized by saponin-based cholesterol extraction, to gain access to vesicle contents without washing away cargo or destroying the membrane integrity.

Furthermore, translating solid capture and live-cell imaging techniques for use with SMLM techniques such as multispectral super resolution microscopy (MSSRM), should be explored. MSSRM provides 20-40nm spatial resolution, with the flexibility of simultaneously resolving up to 20 different colors through prismatic refraction of spectra [330]. With SMLM techniques, the true underlying ultrastructure of EVs, their cargos, and intracellular fate within recipient cells could be mapped in great detail. These techniques could also be exploited to study EV biogenesis to gain a better understating of how internal cargo and membrane associated molecules are packaged into vesicles. Imaging-based approaches to resolve EV contents and structure, have great promise in advancing EV-biology, and merit further exploration.

Mapping the intracellular fate of EVs in recipient cells

Through live cell analysis I have mapped the internalization and accumulation of EVs in recipient stromal cells, which results in the transmission of ER-stress. In time-lapse imaging, EVs appear to be internalized via endocytosis, and travel within endosomes to the perinuclear endoplasmic reticulum where they may fuse with the ER membrane. This EV-ER interaction was also reported to occur in fibroblasts in a non-AML context [55]. It remains to be determined if ER-stress is induced through a physical interaction between EVs (and their cargo) with the ER, or whether there are indirect intracellular signaling pathways that lead to ER-stress. It is possible that AML-EVs transport abnormal BMPs and/or CD147 directly to the luminal ER which act to destabilize protein folding. However, it is equally possible that cargos activate intracellular signaling pathways by binding receptors at the cell surface during entry. There exist few studies that examine the intracellular fate of EVs. More research is needed to elucidate how EVs and their cargo are unpackaged to regulate recipient cells in AML. Similar to viral entry and uncoating, understating cell-intrinsic processing of internalized EVs may reveal new therapeutic strategies to prevent dysregulation caused by the transfer of EV-related cargo. For AML, such discoveries may identify new ways to prevent AML blasts from establishing a pro-leukemic niche through the systemic release of EVs.

Determining the role of EV-mediated HSC transformation in relapse and refractory disease

Both the functional alteration [151] and mutation accrual in residual HSC have been reported in AML patients in remission [227, 228] yet underlying mechanism facilitating these observations remained unexplained. In our study, we found that AML-EV enforce quiescence on LT-HSCs by transferring miRNAs that inhibit Raptor, a subunit of the mTOR pathway. By inducing quiescence in LT-HSCs, AML blasts are able to prevent competitive displacement from the leukemic niche. Our findings suggest a model of cell-cell crosstalk involving AML-derived EVs that affect residual HSC function by eliciting

reversible quiescence, and accrual of lasting DNA-damage. Following transplantation of residual LT-HSCs into a healthy bone marrow, cells showed enhanced repopulation capacity and persistence of DNA damage. In other studies, acquired mutation in residual HSC have been described to promote clonal expansion, malignant transformation, and overt relapse in AML [227, 228, 249]. In patients, once blasts are cleared from medullary space with induction chemotherapy, it is tempting to speculate that both EV-enforced DNA damage and a remodeled stem cell niche cooperate to transform residual LT-HSCs into malignant cells. In a similar capacity, AML-EVs may contribute to relapse by enforcing quiescence in founding clones of dysplastic, yet pre-leukemic HSCs, conferring protection from chemo-induced elimination. Furthermore, the ability to induce DNA damage suggests that EVs may have a role in driving clonal evolution in dysplastic HSCs, or perhaps even blasts themselves. Many critical questions remain. Additional studies will be key to fully realizing the role EV trafficking plays in promoting AML relapse and refractory disease.

Throughout this thesis, I have shown that AML-EVs successively remodel the bone marrow and immune landscape to create a pro-leukemic microenvironment. Current therapies used for the treatment of AML, rely on chemotherapies and small molecule drugs that solely target dividing blasts. Yet, leukemia has been long understood to be a disease of dysfunctional and self-reinforcing niche. Induction chemotherapy is capable of producing remission in 80% of patients, yet more than half eventually relapse, and often with gains in therapeutic resistance. Alterations to both residual HSC, the hematopoiesis-supporting stromal cells, and immune function remain following the clearance of AML blasts with induction chemotherapy, leaving an environment poised for relapse. Through multiple studies, I have shown that EVs deliver tumor-derived regulatory cargos to resident bone marrow cells, and distant immune cells to enforce functional modifications. I believe that a better understanding of the molecular constituents that facilitate recipient cell binding and EV-mediated signaling, will greatly inform the mechanisms promoting AML relapse and drug resistance. From these studies and continued research, strategies to mitigate EV-enforced dysregulation of hematopoiesis and immune function will become evident. This work could form the basis of new therapeutic options that target the leukemic microenvironment, in order to disrupt self-reinforcing modifications that lead to resistance

and relapse. Together with conventional chemotherapies, these new approaches may improve the survival of patients suffering from AML.

Appendix

Appendix Figure:3.2.1: AML-EV induce a p53-dependent quiescence in hematopoietic cells with no evidence of apoptosis

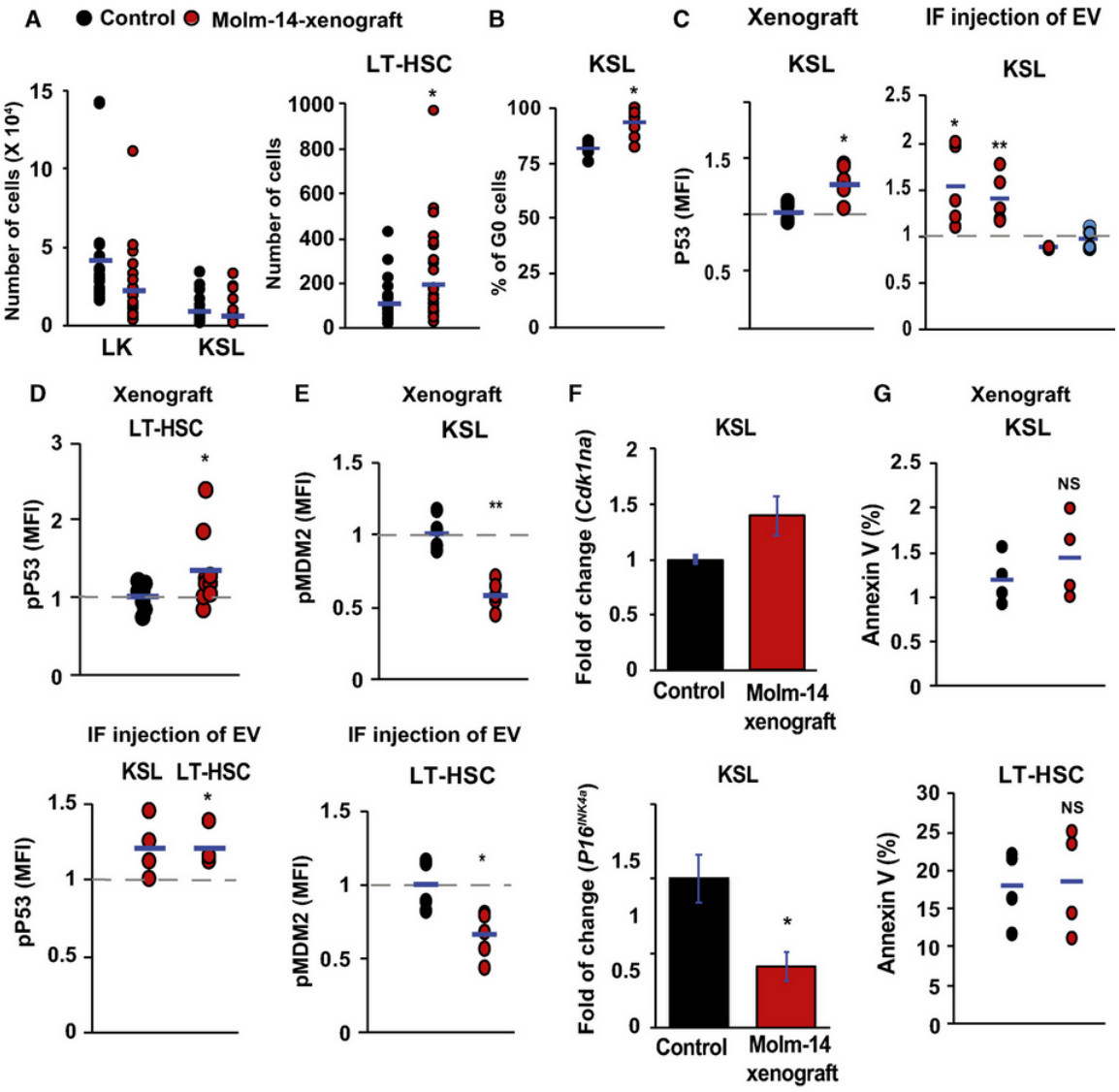

A) Flow cytometric analysis showing the absolute cell number of LK and KSL cells in lineage-negative cells (left panel) and LT-HSC (right panel) in Molm-14 xenograft (red, n = 10) versus control (black, n = 10). Statistics: Student's t-test (*P < 0.05). **B)** Flow cytometric analysis of KSL percentage in G0 phase from Molm-14 xenografts (red, n = 7) versus control (black, n = 9). Statistics: Student's t-test (*P < 0.05). **C)** Flow cytometric analysis of P53 MFI in KSL in: (left panel) Molm-14 xenograft (red, n = 6) versus control (black, n = 4), or (right panel) IF injection of EV from Molm-14, U-937, HL-60 (red, n = 5,5,3), or CD34 cells (blue, n = 6) normalized to vehicle-injected femurs. Statistics: Student's t-test (*P < 0.05, **P < 0.01) **D)** Flow cytometric analysis of pP53ser15 MFI of LT-HSC in: (upper panel) Molm-14 xenografts, n = 9 red versus control, n = 7 black, or (lower panel) LT-HSC and KSL after IF injection of Molm-14 EV (red, n = 4) normalized to vehicle-injected contralateral femurs. Data are presented after subtracting the background fluorescence. Statistics: Student's t-test (*P < 0.05). **E)** Flow cytometric analysis of the pMDM2 MFI in KSL (upper panel) and LT-HSC (lower panel) in Molm-14 xenografts (red, n = 5) versus control (black, n = 4). Statistics: Student's t-test (*P < 0.05, **P < 0.01). **F)** qRT–PCR showing the fold change of Cdkn1a (upper panel) and P16INK4a (lower panel) in KSL from Molm-14 xenografts relative to control mice and normalized to Gapdh endogenous control. Data are mean ± SEM from at least three independent experiments with technical replicates. Statistics: one-way ANOVA with Bonferroni post hoc correction (*P < 0.05). **G)** Annexin V+ analysis of KSL (upper panel) and LT-HSC (lower panel), in Molm-14 xenograft (red, n = 4) versus control (black, n = 4). Statistics: Student's t-test (NS = not significant)

Appendix Figure 3.3.1: AML do not suppress protein synthesis in other hematopoietic populations

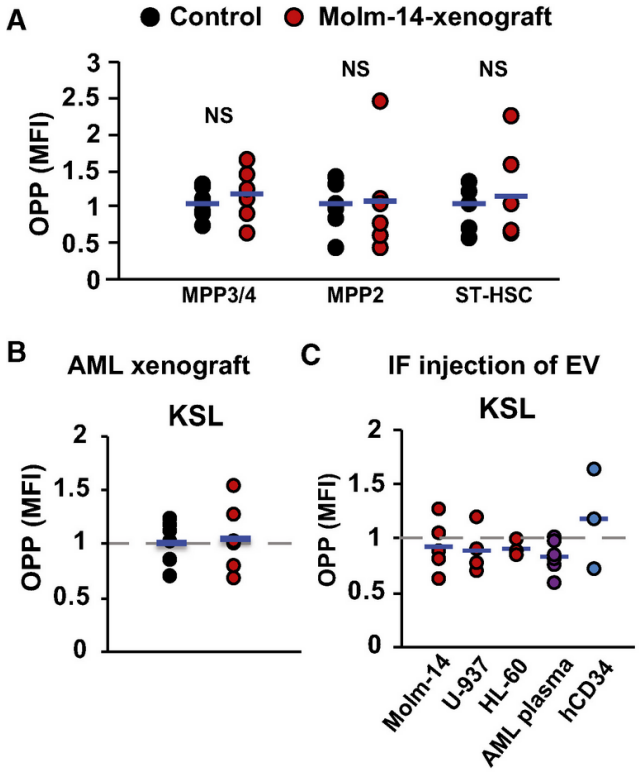

A) Flow cytometric analysis showing MFI of OPP incorporation in MPP3/4, MPP2, and ST-HSC in the Molm-14 xenografts (red, n = 6) versus non-engrafted mice (black, n = 6). Statistics: Student's t-test (not significant "NS"). **B-C)** OPP flow cytometric analysis of KSL in: (B) Molm-14 xenografts (red, n = 6) versus non-engrafted mice (black, n = 6), or (C) IF injection of EV from Molm-14, U-937, HL-60 (red, n = 5,4,3), AML patient plasma (orange, n = 6), or CD34+ cells (blue, n = 3) normalized to contralateral femurs after subtracting background fluorescence.

Appendix Figure 3.4.1: AML-EV suppress mTOR pathway, but not cMyc, in hematopoietic cells

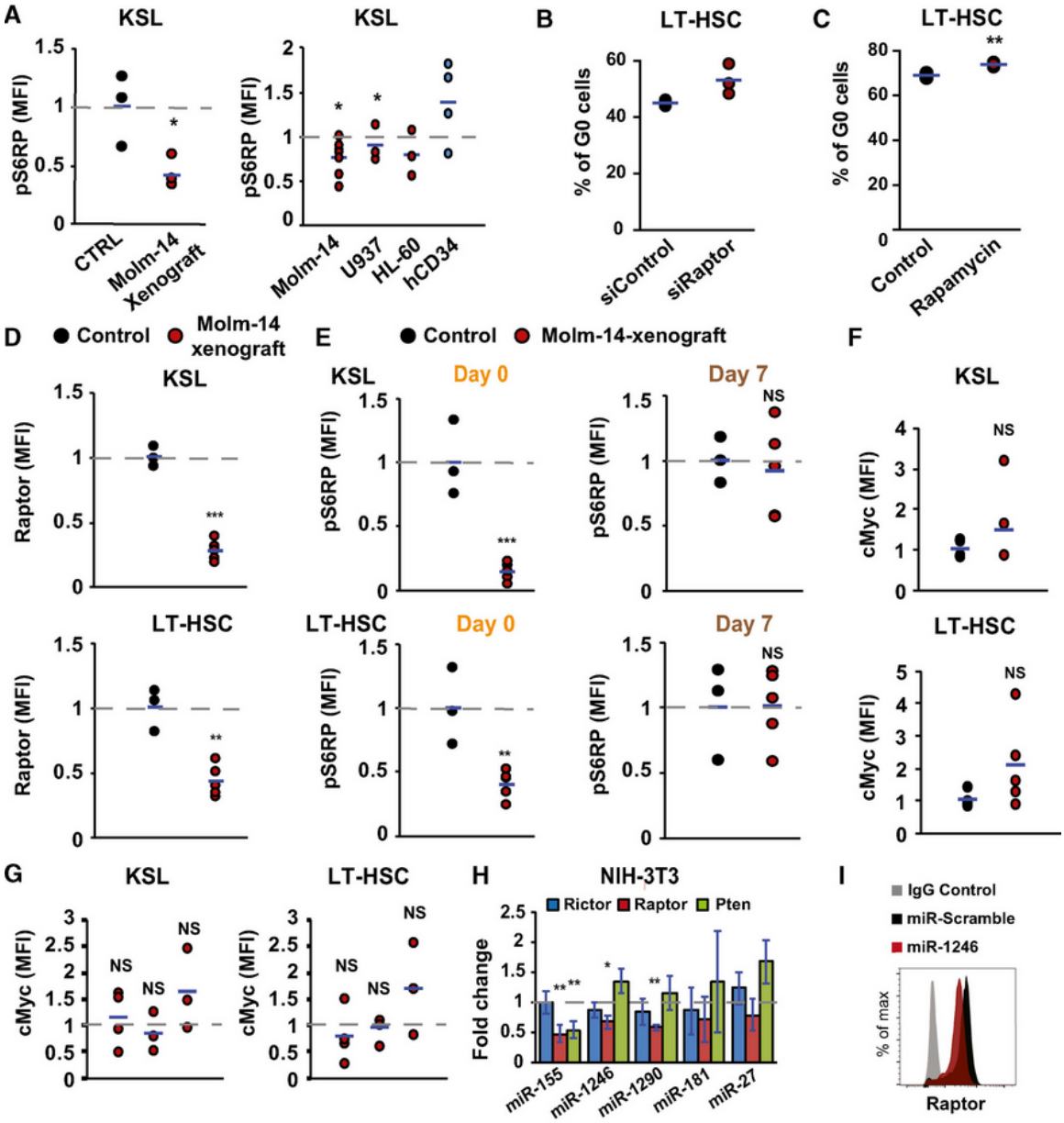

A) Flow cytometric analysis of pS6KRP MFI in KSL in: (left panel) Molm-14 xenografts, red, n = 4 versus control mice, black, n = 3; or (right panel) IF injection of EV from Molm-14, U-937, HL-60 (red, n = 7,3,3), or CD34 cells (blue, n = 4) normalized to vehicle-injected contralateral femurs. The background fluorescence was subtracted. Statistics: Student's t-test (*P < 0.05). **B-C)**. Cell-cycle flow cytometric analysis using Ki67/Hoechst-33342 staining of the percentage of LT-HSC in the G0 phase after (B) nucleofection of cKit+ cells with siControl or siRaptor for 72 h using the Amaxa™ P3 Primary Cell 4D-Nucleofector Kit. (C) Treatment of ex vivo-cultured cKit+ cells with vehicle or rapamycin (100 nM) for 72 h. Statistics: Student's t-test (**P < 0.01). **D)** Flow cytometric analysis of intracellular Raptor MFI levels in KSL (upper panel) and LT-HSC (lower panel) derived from Molm-14 xenografts (red, n = 5) versus control (black, n = 3). Statistics: Student's t-test (**P < 0.01, ***P < 0.001). **E)** Flow cytometric analysis of pS6RP MFI in KSL (upper panel) and LT-HSC (lower panel) obtained from Molm-14 xenografts (red, n = 5) versus non-engrafted mice (black, n = 3) at Day 0 (freshly isolated HSPC cells) or Day 7 (after 7 days of ex vivo culture in RPMI with 50 ng/ml IL-3/SCF and 10% FBS at 37°C, 5% CO2). Statistics: Student's t-test (not significant “NS”, **P < 0.01 and ***P < 0.001). **F-G)** Flow cytometric analysis of cMyc MFI in KSL (left panel) and LT-HSC (right panel) in: (F) Molm-14 xenografts (red, n = 3 and 5) versus control (black, n = 3 and 3), or (G) IF injection of EV from Molm-14, U-937, and HL-60 (n = 4,3, and 3). Statistics: Student's t-test (not significant “NS”). **H)** qRT–PCR gene expression showing the fold change of Raptor, Rictor, or Pten genes in NIH-3T3 transfected with the indicated miRNA mimics for 48 h. The fold change was calculated relative to miR-scramble after normalizing to Gapdh endogenous control. Data are mean ± SEM from at least three independent experiments, performed in technical replicates. Statistics: one-way ANOVA with Bonferroni post hoc correction (*P < 0.05 and **P < 0.01). **I)** Flow cytometric analysis showing the histograms of Raptor in NIH-3T3 cells 72 h after transfection with miR-scramble or miR-1246 mimics.

Appendix Figure 3.5.1: AML and short-term HSC repopulation

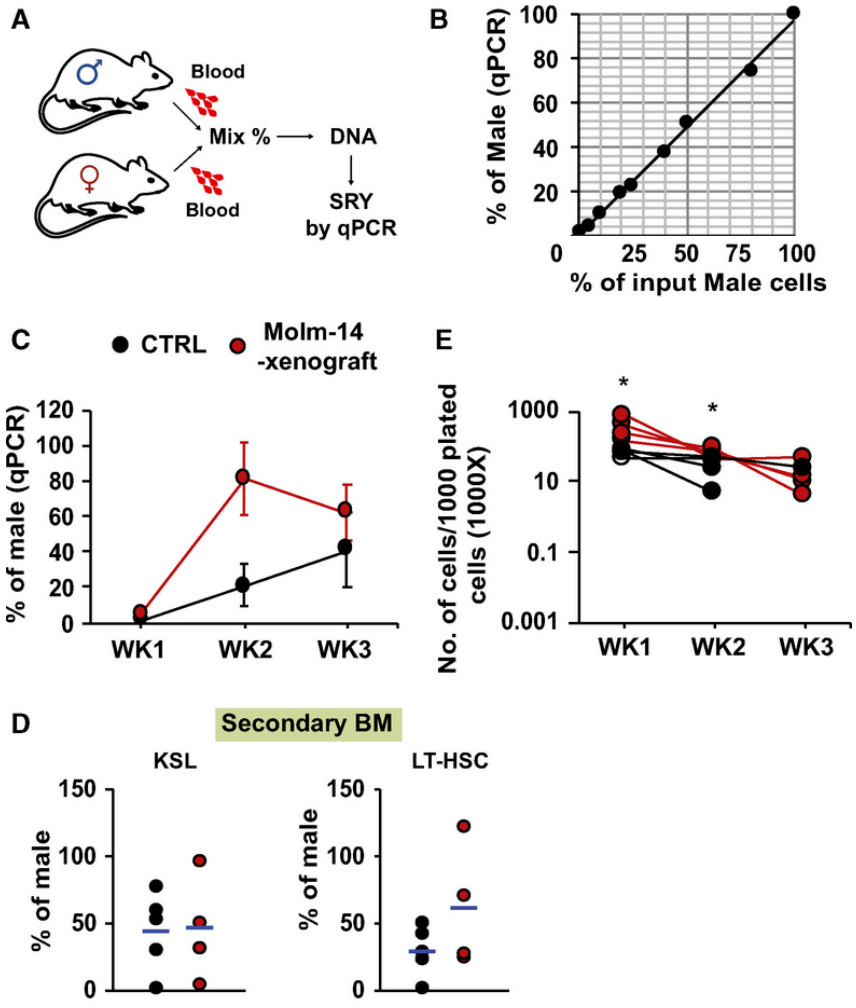

A) Schematic diagram of the workflow. PB samples were collected from male and female mice. Blood leukocytes were counted and mixed at different proportions. DNA from the mixtures was extracted, and SRY was quantified by qRT–PCR and normalized to Gapdh. **B)** Correlation between measured male DNA determined by qPCR on the Y-axis and the corresponding input male cells on the X-axis (n = 1, R2 = 0.9965). **C)** qRT–PCR of the PB donor male DNA from Molm-14 xenografts (red, n = 4), or controls (black, n = 4) transplanted into secondary female recipients for 3 weeks. Data were normalized to Gapdh and are presented as mean ± SEM **D)** qRT–PCR of male chimerism in: (left panel) KSL or (right panel) LT-HSC, from mice transplanted by either Molm-14 xenografts (red, n = 4) or controls (black, n = 4) for 16 weeks. **E)** Total number of cells per 1,000 input cells, serially replated into methylcellulose media for three successive weeks. Cells derived from Molm-14 xenografts and control mice were represented in red and black, respectively. Data were performed in technical triplicates. Statistics: Student's t-test (*P < 0.05).

Appendix Figure 4.2.1: Flow cytometry gating strategy

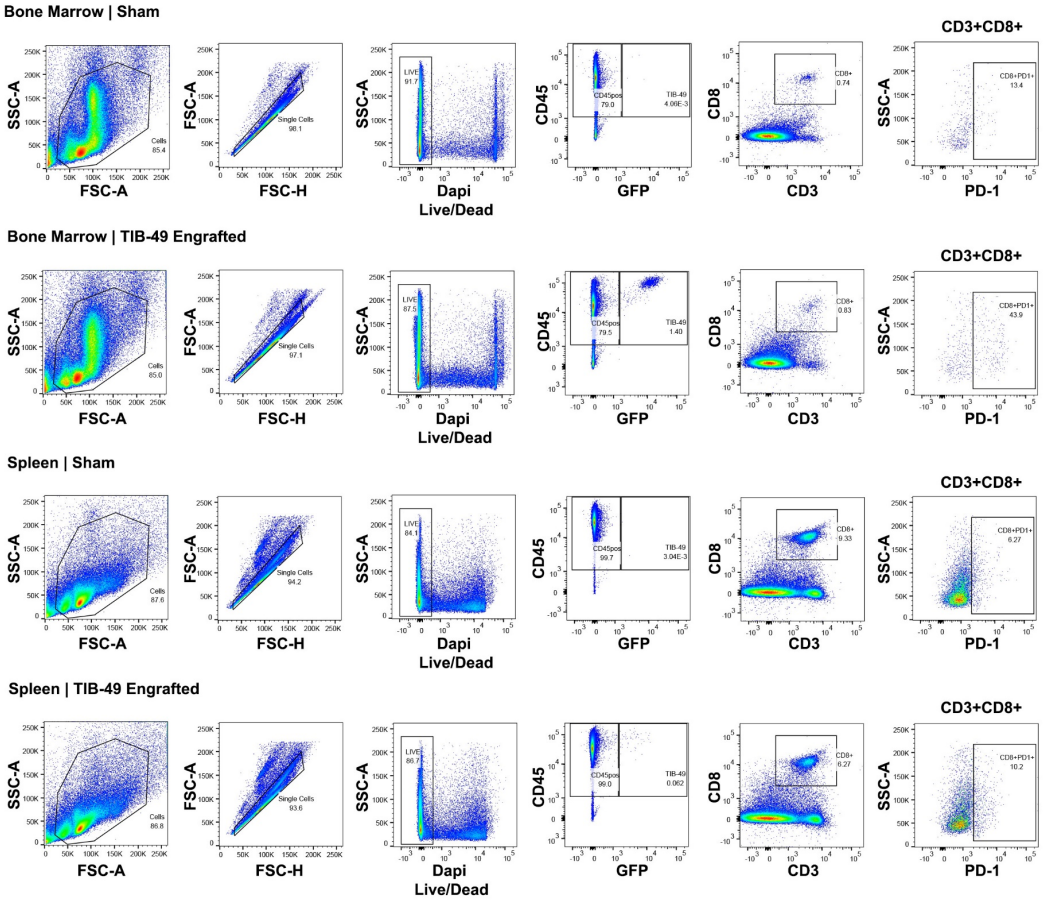

Representative flow plots and gates for TIB-49 cell and CD8+T-cell analysis from the bone marrow and spleens of tumor and sham injected animals

Appendix Figure 4.2.1: CD8+T cell dysfunction from the spleen and bone marrow of syngenetic TIB-49 engrafted C57BL/6 mice

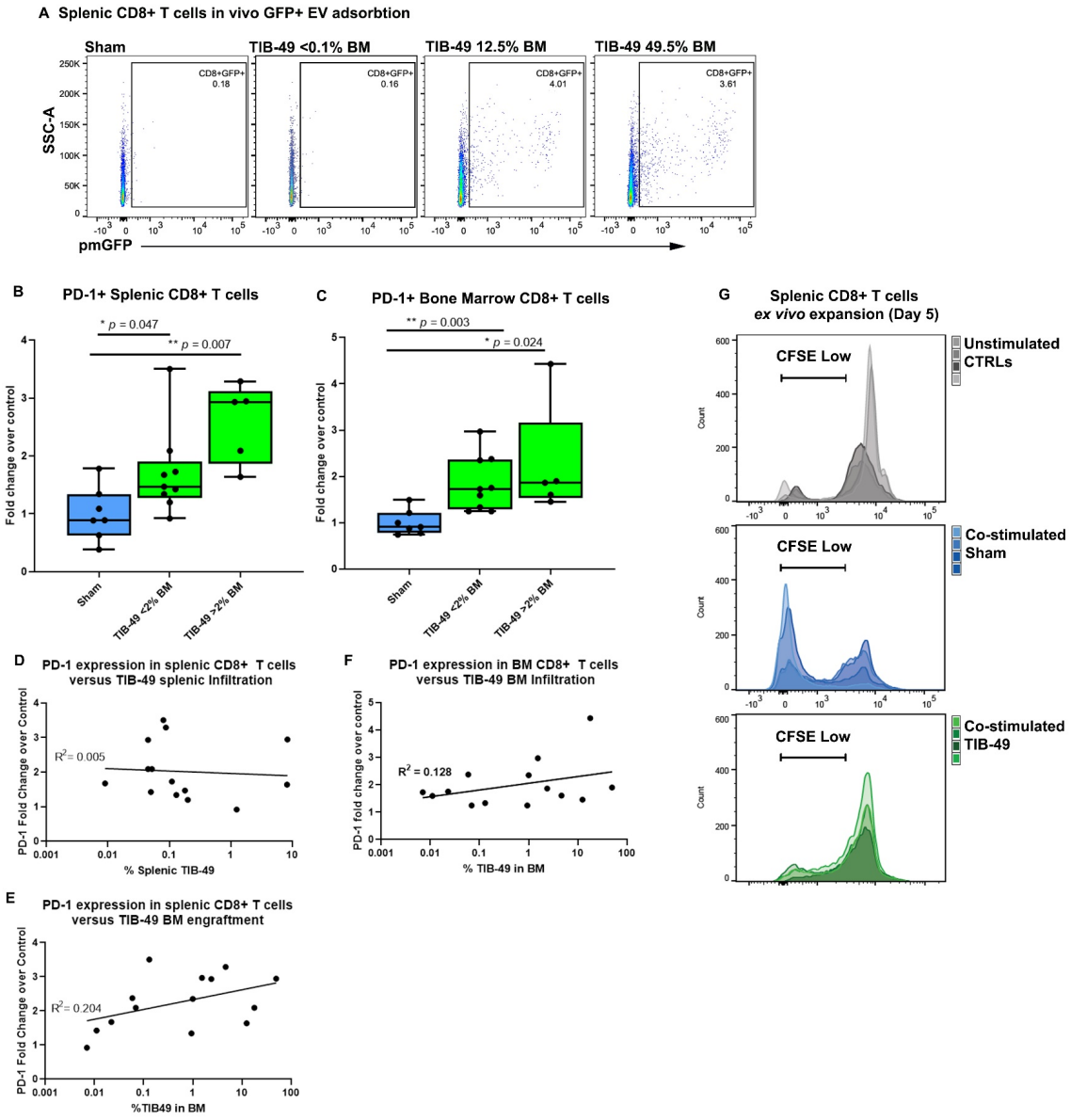

A) Splenic CD8+T-cells from tumor animals contain GFP+ EVs at the time of harvest as detected by flow cytometry. **B-C)** PD-1 expression on splenic (B) and bone marrow (C) CD8+T cells increases with bone marrow tumor burden. PD-1 expression normalized to sham animals, points represent individual animals. **D-F)** Splenic PD-1 expression does not correlate with TIB-49 cell infiltration into the spleen of tumor animals, yet does increase with bone marrow tumor burden. Points represent individual animals (n =14) **G)** *Ex vivo* expansion of co-stimulated splenic CD8+T cells from sham (Blue) and TIB-49 engrafted animals (green) compared to non-stimulated controls from both animals (Grey). Dividing population determined by flow cytometry by gating on CFSE low staining 5-days after harvest +/- co-stimulation. Overlaid histograms represent 4 animals per condition.

Appendix Figure 4.3.1: Human CD8+T-cell gating strategy and GFP EV binding

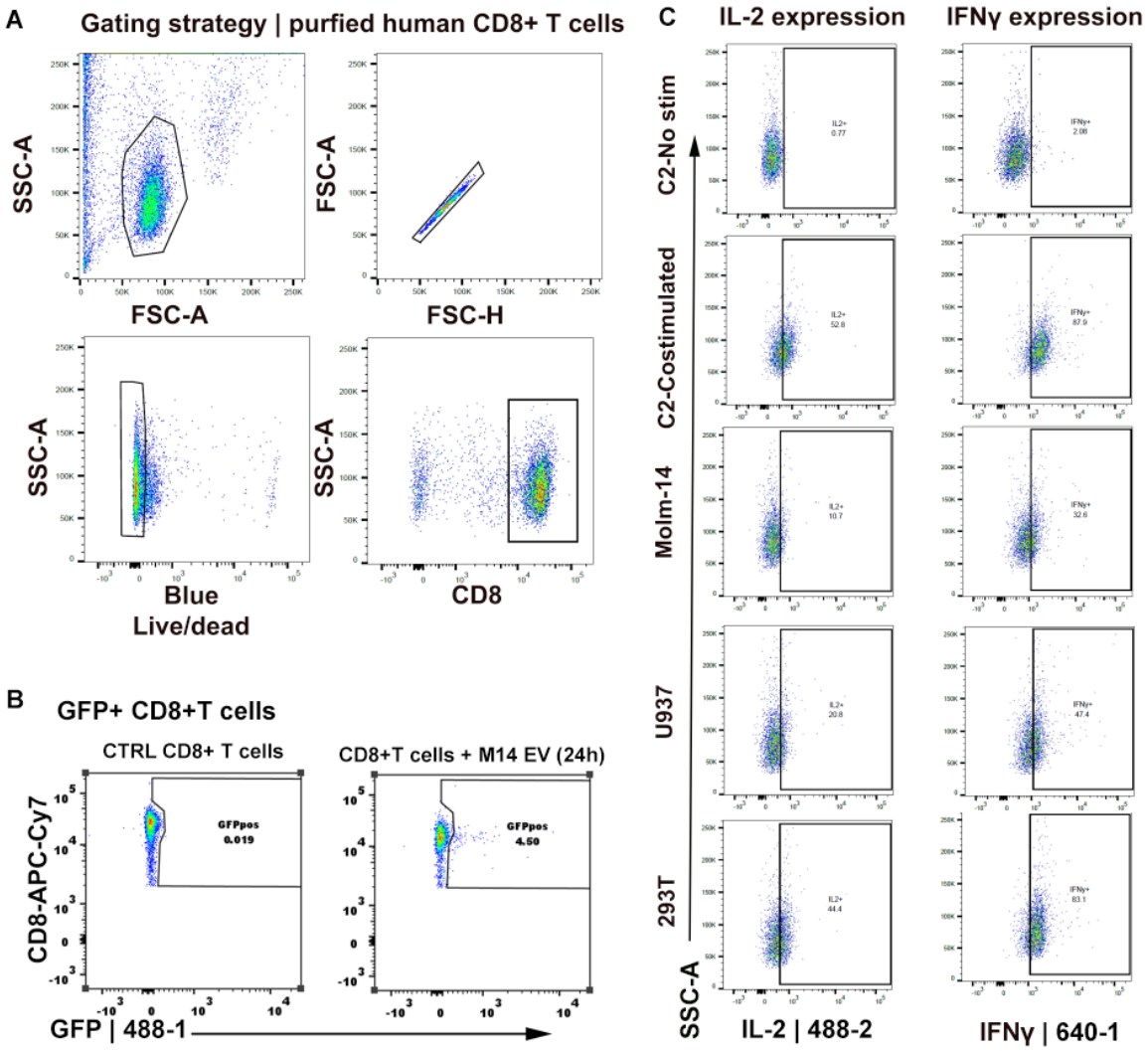

A) Flow cytometry gating strategy for column purified peripheral blood CD8+T cells. **B)** Human CD8+T-cells adsorb GFP+ EVs during *in vitro* exposure, signal detected 24 hours after exposure. **C)** Representative flow plots of intracellular staining of IL-2 and IFNγ in human CD8+T-cells following co-stimulation and exposure to cell line-derived EVs.

Appendix Figure 4.4.1: AML cell PD-L1 expression and modulation with IFN γ

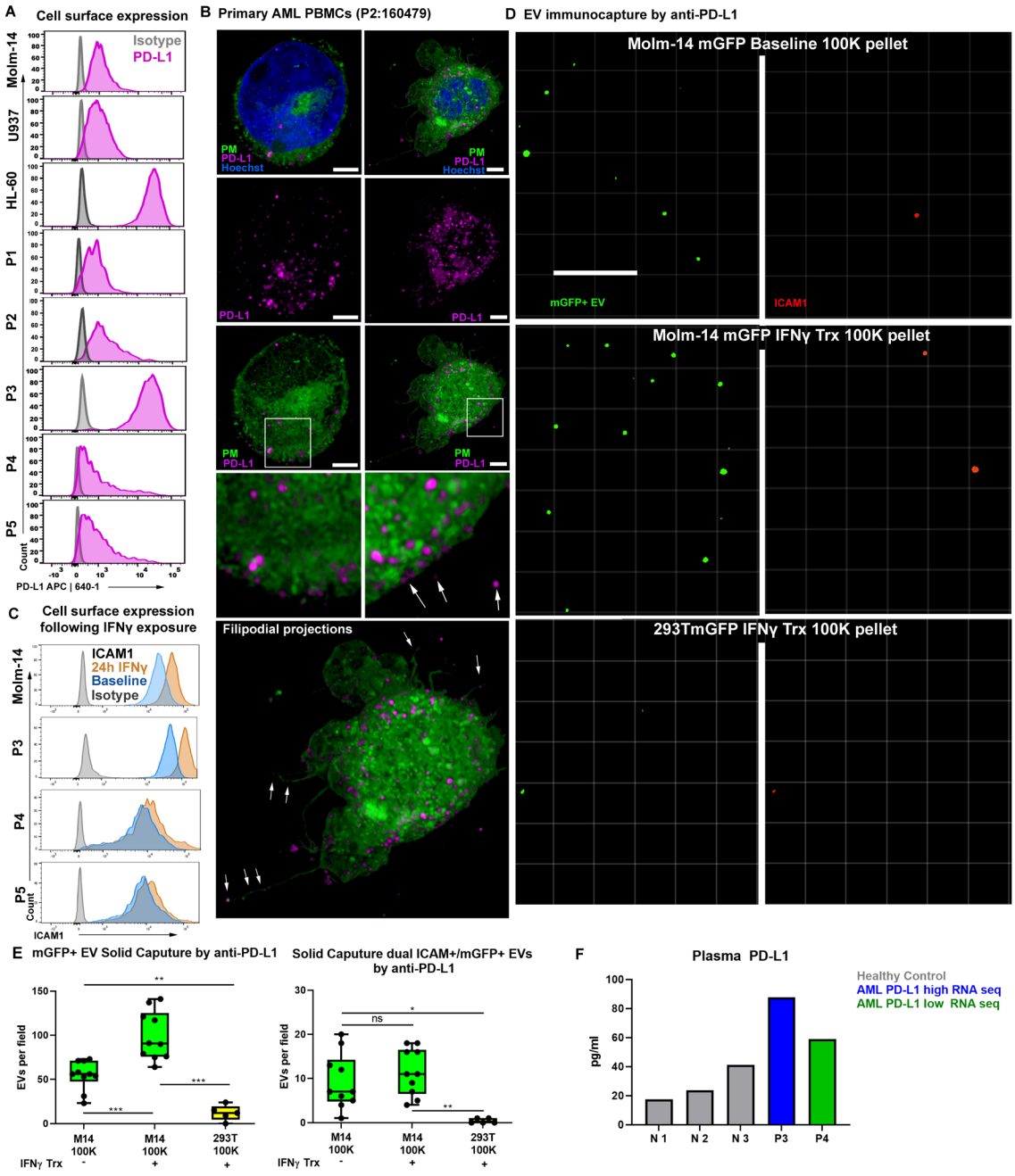

A) Histograms showing cell surface expression of PD-L1 (magenta) on AML cell lines and patient samples, compared to isotype control (grey) Biolegend antibody 29E.2A3. **B)** Primary patient blast (P2 160479) showing two distinct morphologies with differential expression of PD-L1. Cells stained with PD-L1 (magenta), CellMask plasma membrane stain (*PM*, green) and Hoechst (DNA, blue). Top panels shows typical blast morphology with low to moderate PD-L1 expression. Bottom panel shows a PD-L1 high expressing blast with filopodial projections. Bottom right panels show a cluster of PD-L1 (magenta) residing in a membrane invagination with proximal EV-like foci in the extracellular space. Arrows indicate PD-L1 foci on filipodial projections. All images are Airyscan Super resolution 3D Z-stacks displayed as maximum projections. All scale bars = 5µm**. C)** Cell surface expression of ICAM-1 (Blue) also increases following with IFNy exposure (orange) in AML cell lines and patient samples. **D)** Represented images of mGFP+(green) Molm-14 EVs immunocaptured by anti-PD-L1 coated imaging chambers, and stained for ICAM1(red). Scale bar = 10 µm **E)** Analysis of EV count per field from 100k pellets of Molm-14 cells cultured with and without IFNγ compared to non-hematopoietic 293TmGFP cells**.** Each point represents EV count per 105µm x 105µm area captured in two independent experiments. Significance determined with one-way ANOVA with Tukey's multiple comparisons. *$p<0.05$; **$p<0.01$; ***$p<0.001$. F) Concentrations of extracellular PD-L1 in the plasma of 2 AML-patient (P3-P4) and 3 healthy controls (N1-3) determined by ELISA.

Appendix Figure 4.5.1: AML-EV density gradient analysis and western blots

A

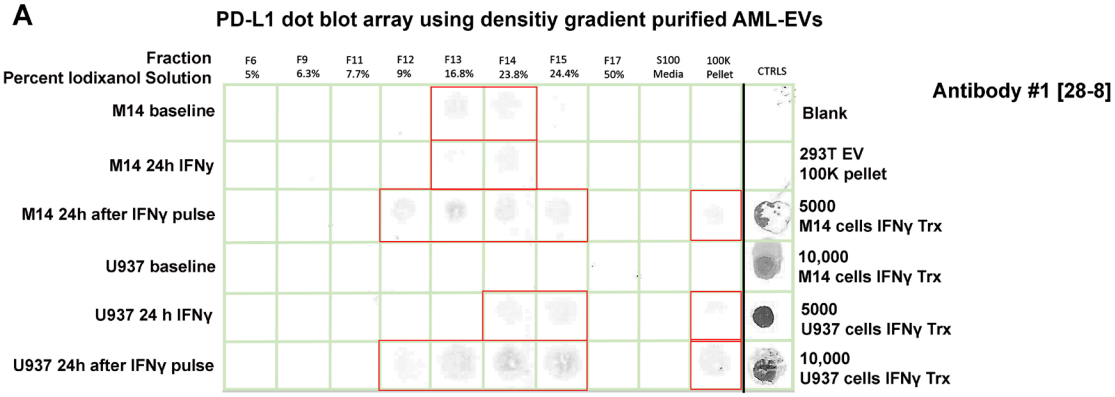

B

mGFP+ Denisty gradient fractions

Fraction	1	2	3	4	5	6	7	8	9	10	11	12	13	14	15	16	17	18	19	20
M14 baseline	-34	2	-11	-4	10	8	8	13	12	4	28	30	212	168	-17	-86	-55	46	52	35
M14 24h IFNγ	26	49	32	33	32	36	52	34	42	64	72	86	232	323	226	-9	-70	1	22	19
M14 24h after IFNγ pulse	-36	-32	-23	-20	-9	17	9	18	29	60	125	359	469	468	313	233	92	-4	41	-16

RFI >100 = GFP positive

C

AML-EV western blots (Licor)

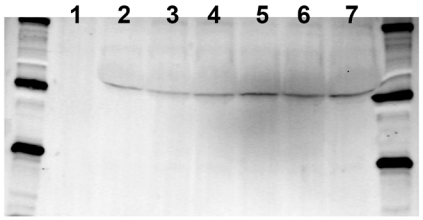

1: Rec PD-L1-FC chimeric protein (pos CTRL)
2: Molm-14 baseline
3: Molm-14 24h 10ng/ml IFNγ
4 Molm-14 24h after IFNγ pulse
5: U937 baseline
6: U937 24h 10ng/ml IFNγ
7: U937 24h after IFNγ pulse

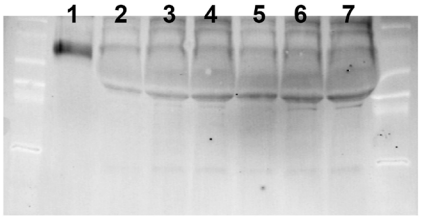

Antibody #2 [29E.2A3]

D

(Chemiluminescence)

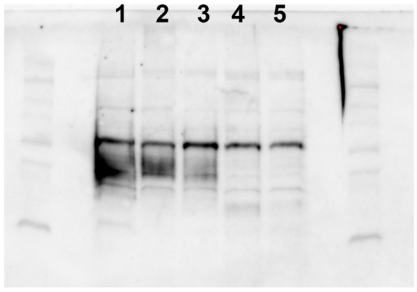

1: Molm-14 24h after IFNγ pulse
2: U937 24h after IFNγ pulse
3: HL-60 24h after IFNγ pulse
4: Molm-14 PD-L1 het KO clone 5
5: Molm-14 PD-L1 het KO clone 2

Antibody #3 [E1J2J]
Chen et al., 2018

A) Dot blot array of anti-PD-L1 (HRP) stained density gradient fractions from conditioned media of AML cell lines treated with or without IFNγ. **B)** Membrane associated mGFP signal is found in density gradient fractions that correspond with positive anti-PD-L1 staining. Treatment with IFNγ increase total GFP+ signal and associated PD-L1 staining. Relative fluorescence intensity >100 used as a threshold value for positive signal in the 488ex/510em channel. **C)** Licor fluoresence imaging-based westerns using PD-L1 FC chimeric protein as a positive control (1), and TSG101 as a loading control. **D)** Chemiluminescence-HRP based western blot of AML cell lines using validated PD-L1 antibody.

Appendix Figure 4.6.1: AML-EV characterization by HRFC

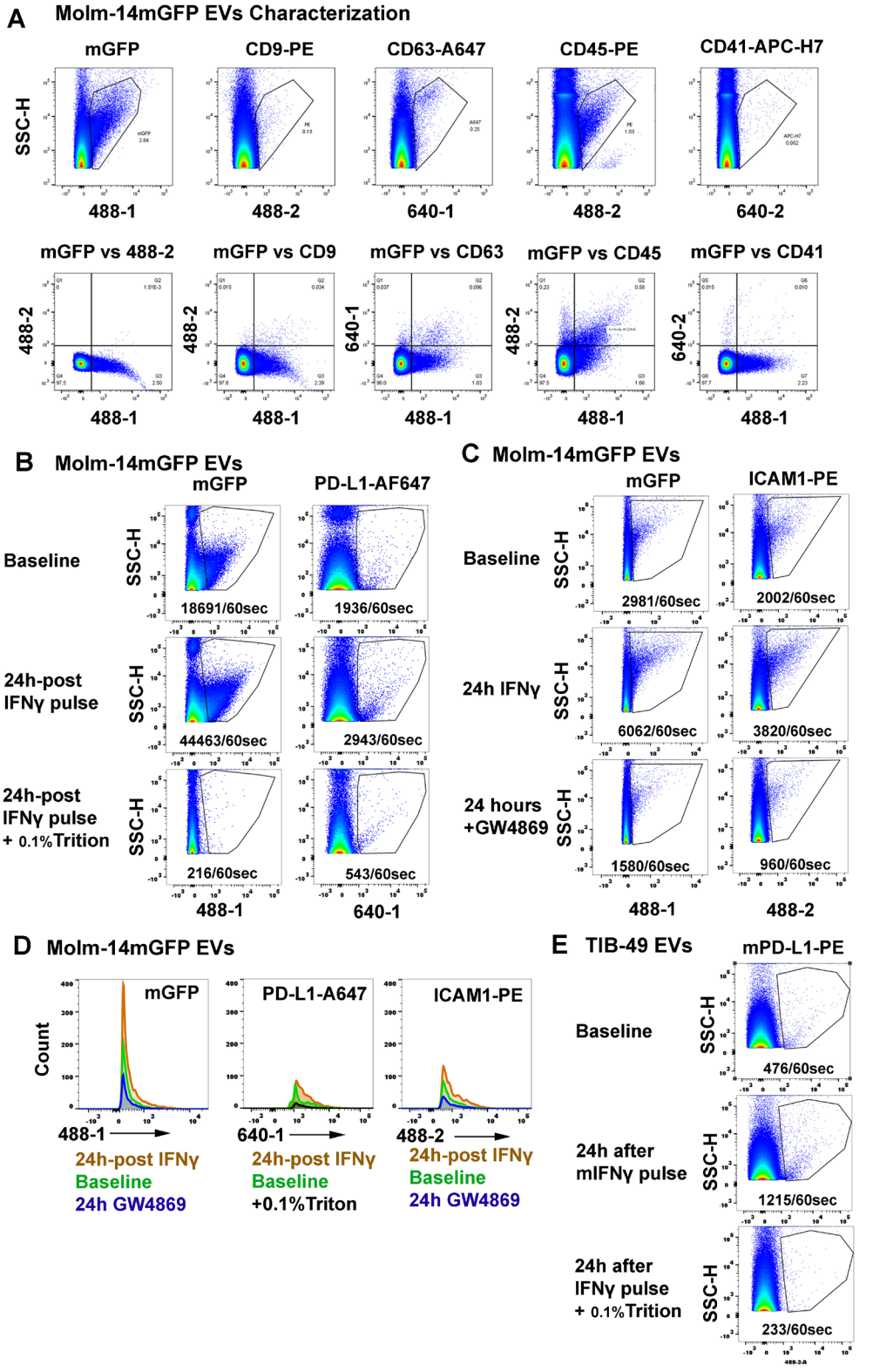

A) High resolution flow cytometry (HRFC) characterization of EVs from the conditioned media of Molm-14mGFP cells. GFP+ EVs co stain with EV-specific tetraspanins (CD9, CD63), hematopoietic marker (CD45). Top panel represent total events per 120second capture, with sample dilution maintained across conditions. Bottom panel show multiplexed detection of GFP and other markers. **B-D)** Representative flow plots showing mGFP+, PD-L1+ and ICAM-1+ EVs at baseline, 24-hours post IFNγ exposure, or after 24-hours of GW4869 treatment. Addition of Triton X-100 added demonstrates loss of membrane associated signal. Each gate shows number of positive events per 60sec capture. Cell number, 24-hour culture time, and sample dilution maintained across conditions. **D)** Histograms showing relative change in mGFP+, PD-L1+ and ICAM-1+ EVs at baseline, 24-hours post IFNγ exposure, or after 24-hours of GW4869 treatment. Each peak represents number of positive events per 60sec capture. Cell number, 24-hour culture time, and sample dilution maintained across conditions. **E)** Similar to human AML cell lines, conditioned media from TIB-49 cells contains very low number of detectable PD-L1+ EVs at baseline, but increase following exposure to mouse IFNγ. Each gate shows number of positive events per 60sec capture. Cell number and sample dilution maintained across conditions.

Appendix Figure 4.7.1: Checkpoint inhibitors rescue EV-mediated T-cell suppression from patient samples

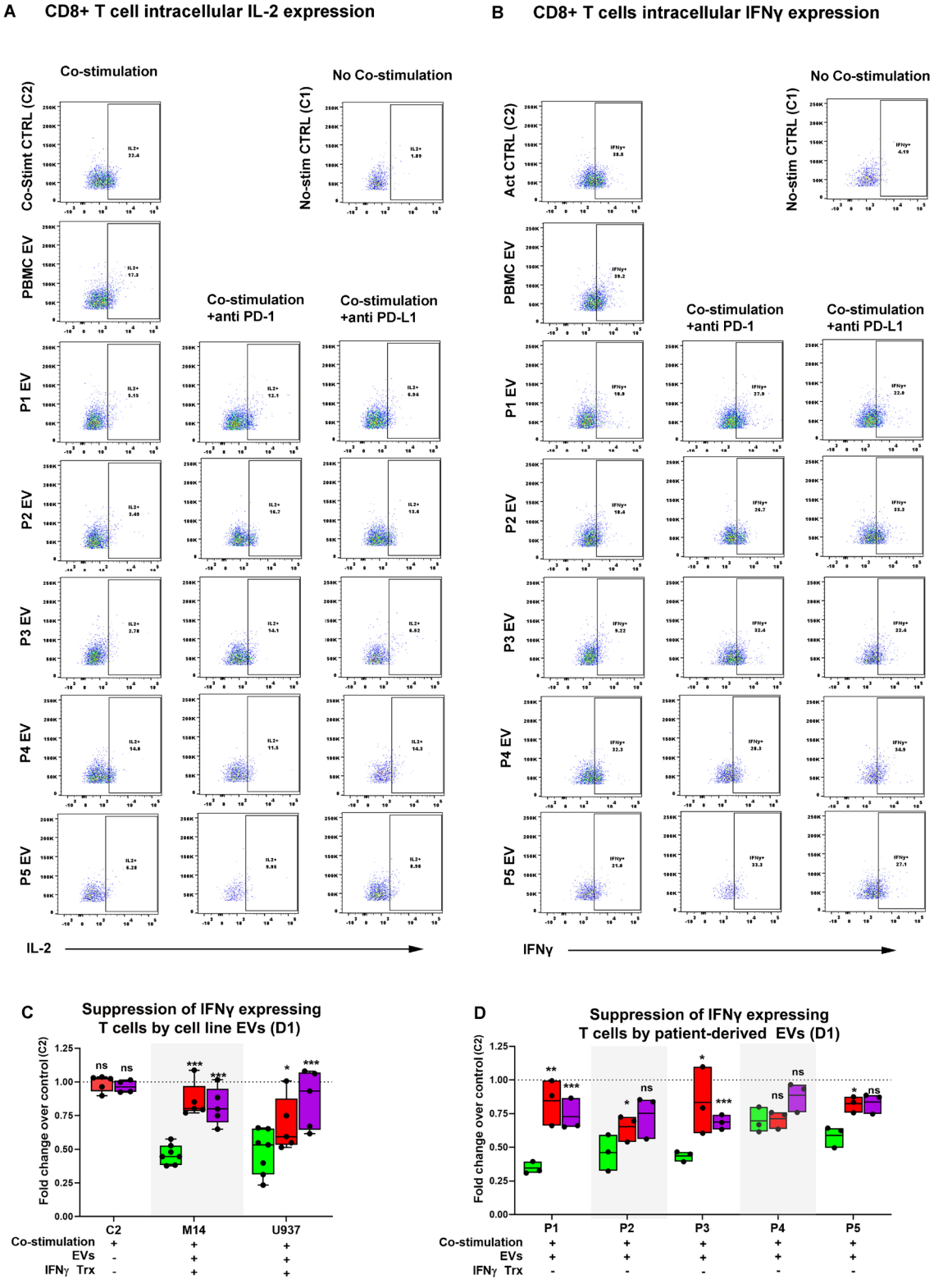

A-B) Representative flow plots of IL-2 **(A)** and IFNγ **(B)** intracellular staining following patient-derived EV exposure with or without the addition of PD-1/PD-L1 checkpoint blockade. **C)** CD8+Tcell production of IL-2 following exposure to cell line AML-EVs alone, or with the addition of blocking antibodies (PD-L1, red; PD-1, Purple). Total cytokine expressing cells in each condition compared to non-EV exposed controls that were co-stimulated (C2) with blocking antibodies, and normalized to co-stimulated controls without blockade. Graphs represent two biological replicates with 2-4 technical replicates per condition. **D)** CD8+Tcell production of IL-2 following exposure to patient-derived PBMC EVs alone, or with the addition of blocking antibodies (PD-L1, red; PD-1, Purple). Total cytokine expressing cells in each condition normalized to co-stimulated controls without blockade. Due to limited sample, graph represents a standalone experiment with three technical replicates. Statistics: **C-D)** Significance determined by two-way ANOVA with Tukey's multiple comparison test to respective EV exposed conditions without antibody blockade. (* $p<0.05$, ** $p<0.01$, *** $p<0.001$, n.s.= not significant).

Appendix Table 4.2.1: Antibody List

Mouse				
Application	**Target**	**Modification**	**Source**	**Product #**
CD8+T-cell isolation	Isolation cocktail	Immunomagnentic negative selection	StemCell	19853
Surface staining flow cytometry	CD45	PE/Cy5	Biolegend	103110
	CD3	APC	Biolegend	100236
	CD8a	APC/Cy7	Biolegend	100714
	CD4	PE	Biolegend	100408
	PD-1	PE/Cy7	Biolegend	135216
	PD-L1	PE	Biolegend	124308
T cell activation	CD3e	Unlabeled	BioXCell	BE0001-1
	CD28	Unlabeled	BioXCell	BE0015-1
Mouse blockade	PD-1	Unlabeled	BioXCell	BE0033-2
Human				
Application	**Target**	**Modification**	**Source**	**Product #**
Surface staining flow cytometry	CD45	PE	Biolegend	368510
	CD3	PerCP/Cy5.5	Biolegend	344814
	CD8	APC/Cy7	Biolegend	344714
	PD-1	PE/Cy7	Biolegend	621616
	PD-L1	AlexaFluor	Abcam	ab209960
	PD-L1	APC	Biolegend	329708
CD8+T-cell isolation	Isolation cocktail	Immunomagnentic negative selection	StemCell	17953
Dot blot array	PD-L1	Unlabeled	Abcam	ab205921
Western blot	PD-L1	Unlabeled	BioXCell	BE0285
	PD-L1	Unlabeled	Cell Signaling	13684S
	TSG-101	Unlabeled	Abcam	ab30871
Blockade	PD-1	Unlabeled	BioXCell	BE0193
	PD-L1	Unlabeled	BioXCell	BE0285
T cell activation	ImmunoCult CD3/CD28	Tetrameric Activator	StemCell	10971
Intracellular staining	IL2	PE	Biolegend	500307
	IFNy	APC	BIolegend	502512

Bibliography

1. Morrison, S.J. and D.T. Scadden, *The bone marrow niche for haematopoietic stem cells.* Nature, 2014. **505**(7483): p. 327-34. *PMC4514480*.
2. Sun, D., M. Luo, M. Jeong, B. Rodriguez, Z. Xia, R. Hannah, . . . M.A. Goodell, *Epigenomic profiling of young and aged HSCs reveals concerted changes during aging that reinforce self-renewal.* Cell Stem Cell, 2014. **14**(5): p. 673-88. *PMC4070311*.
3. Sawai, C.M., S. Babovic, S. Upadhaya, D. Knapp, Y. Lavin, C.M. Lau, . . . B. Reizis, *Hematopoietic Stem Cells Are the Major Source of Multilineage Hematopoiesis in Adult Animals.* Immunity, 2016. **45**(3): p. 597-609. *PMC5054720*.
4. Chitteti, B.R., Y.H. Cheng, B. Poteat, S. Rodriguez-Rodriguez, W.S. Goebel, N. Carlesso, . . . E.F. Srour, *Impact of interactions of cellular components of the bone marrow microenvironment on hematopoietic stem and progenitor cell function.* Blood, 2010. **115**(16): p. 3239-48. *PMC2858485*.
5. Doron, B., M. Handu, and P. Kurre, *Concise Review: Adaptation of the Bone Marrow Stroma in Hematopoietic Malignancies: Current Concepts and Models.* Stem Cells, 2018. **36**(3): p. 304-312. *PMID29235199*.
6. Doron, B., S. Abdelhamed, J.T. Butler, S.K. Hashmi, T.M. Horton, and P. Kurre, *Transmissible ER stress reconfigures the AML bone marrow compartment.* Leukemia, 2019. **33**(4): p. 918-930. *PMC6411460*.
7. Brenner, A.K., I. Nepstad, and O. Bruserud, *Mesenchymal Stem Cells Support Survival and Proliferation of Primary Human Acute Myeloid Leukemia Cells through Heterogeneous Molecular Mechanisms.* Front Immunol, 2017. **8**: p. 106. *PMC5299032*.
8. Schepers, K., T.B. Campbell, and E. Passegue, *Normal and leukemic stem cell niches: insights and therapeutic opportunities.* Cell Stem Cell, 2015. **16**(3): p. 254-67. *PMC4391962*.
9. Schepers, K., E.M. Pietras, D. Reynaud, J. Flach, M. Binnewies, T. Garg, . . . E. Passegue, *Myeloproliferative neoplasia remodels the endosteal bone marrow niche into a self-reinforcing leukemic niche.* Cell Stem Cell, 2013. **13**(3): p. 285-99. *PMC3769504*.
10. Raaijmakers, M.H., S. Mukherjee, S. Guo, S. Zhang, T. Kobayashi, J.A. Schoonmaker, . . . D.T. Scadden, *Bone progenitor dysfunction induces myelodysplasia and secondary leukaemia.* Nature, 2010. **464**(7290): p. 852-7. *PMC3422863*.
11. Almosailleakh, M. and J. Schwaller, *Murine Models of Acute Myeloid Leukaemia.* Int J Mol Sci, 2019. **20**(2). *PMC6358780*.
12. Pietras, E.M., M.R. Warr, and E. Passegué, *Cell cycle regulation in hematopoietic stem cells.* The Journal of cell biology, 2011. **195**(5): p. 709-720.

13. Blank, U. and S. Karlsson, *TGF-β signaling in the control of hematopoietic stem cells.* Blood, 2015. **125**(23): p. 3542-3550.
14. Fleming, H.E., V. Janzen, C. Lo Celso, J. Guo, K.M. Leahy, H.M. Kronenberg, and D.T. Scadden, *Wnt signaling in the niche enforces hematopoietic stem cell quiescence and is necessary to preserve self-renewal in vivo.* Cell stem cell, 2008. **2**(3): p. 274-283.
15. Yilmaz, O.H. and S.J. Morrison, *The PI-3kinase pathway in hematopoietic stem cells and leukemia-initiating cells: a mechanistic difference between normal and cancer stem cells.* Blood cells, molecules & diseases, 2008. **41**(1): p. 73-76.
16. Colmone, A., M. Amorim, A.L. Pontier, S. Wang, E. Jablonski, and D.A. Sipkins, *Leukemic cells create bone marrow niches that disrupt the behavior of normal hematopoietic progenitor cells.* Science, 2008. **322**(5909): p. 1861-5. *PMID19095944*.
17. Johnstone, R.M., *Exosomes biological significance: A concise review.* Blood Cells, Molecules, and Diseases, 2006. **36**(2): p. 315-321.
18. Thomou, T., M.A. Mori, J.M. Dreyfuss, M. Konishi, M. Sakaguchi, C. Wolfrum, . . . C.R. Kahn, *Adipose-derived circulating miRNAs regulate gene expression in other tissues.* Nature, 2017. **542**(7642): p. 450-455.
19. Mittelbrunn, M., C. Gutiérrez-Vázquez, C. Villarroya-Beltri, S. González, F. Sánchez-Cabo, M.Á. González, . . . F. Sánchez-Madrid, *Unidirectional transfer of microRNA-loaded exosomes from T cells to antigen-presenting cells.* Nature communications, 2011. **2**: p. 282-282.
20. Yanez-Mo, M., P.R. Siljander, Z. Andreu, A.B. Zavec, F.E. Borras, E.I. Buzas, . . . O. De Wever, *Biological properties of extracellular vesicles and their physiological functions.* J Extracell Vesicles, 2015. **4**: p. 27066. *PMC4433489*.
21. Hornick, N.I., B. Doron, S. Abdelhamed, J. Huan, C.A. Harrington, R. Shen, . . . P. Kurre, *AML suppresses hematopoiesis by releasing exosomes that contain microRNAs targeting c-MYB.* Sci Signal, 2016. **9**(444): p. ra88. *PMID27601730*.
22. Kumar, B., M. Garcia, L. Weng, X. Jung, J.L. Murakami, X. Hu, . . . C.C. Chen, *Acute myeloid leukemia transforms the bone marrow niche into a leukemia-permissive microenvironment through exosome secretion.* Leukemia, 2017.
23. Butler, J.T., S. Abdelhamed, and P. Kurre, *Extracellular vesicles in the hematopoietic microenvironment.* Haematologica, 2018. **103**(3): p. 382-394. *PMC5830368*.
24. Wolf, P., *The Nature and Significance of Platelet Products in Human Plasma.* British Journal of Haematology, 1967. **13**(3): p. 269-288.
25. Pan, B.-T. and R.M. Johnstone, *Fate of the transferrin receptor during maturation of sheep reticulocytes in vitro: Selective externalization of the receptor.* Cell, 1983. **33**(3): p. 967-978.
26. Goloviznina, N.A., S.C. Verghese, Y.M. Yoon, O. Taratula, D.L. Marks, and P. Kurre, *Mesenchymal Stromal Cell-derived Extracellular Vesicles Promote Myeloid-biased Multipotent Hematopoietic Progenitor Expansion via Toll-Like Receptor Engagement.* The Journal of biological chemistry, 2016. **291**(47): p. 24607-24617.
27. Geddings, J.E., Y. Hisada, Y. Boulaftali, T.M. Getz, M. Whelihan, R. Fuentes, . . . N. Mackman, *Tissue factor-positive tumor microvesicles activate platelets and*

enhance thrombosis in mice. Journal of thrombosis and haemostasis : JTH, 2016. **14**(1): p. 153-166.

28. Al-Nedawi, K., B. Meehan, R.S. Kerbel, A.C. Allison, and J. Rak, *Endothelial expression of autocrine VEGF upon the uptake of tumor-derived microvesicles containing oncogenic EGFR.* Proceedings of the National Academy of Sciences of the United States of America, 2009. **106**(10): p. 3794-3799.
29. Hoshino, A., B. Costa-Silva, T.L. Shen, G. Rodrigues, A. Hashimoto, M. Tesic Mark, . . . D. Lyden, *Tumour exosome integrins determine organotropic metastasis.* Nature, 2015. **527**(7578): p. 329-35. *PMC4788391*.
30. Roccaro, A.M., A. Sacco, P. Maiso, A.K. Azab, Y.-T. Tai, M. Reagan, . . . I.M. Ghobrial, *BM mesenchymal stromal cell-derived exosomes facilitate multiple myeloma progression.* The Journal of clinical investigation, 2013. **123**(4): p. 1542-1555.
31. Kowal, J., G. Arras, M. Colombo, M. Jouve, J.P. Morath, B. Primdal-Bengtson, . . . C. Thery, *Proteomic comparison defines novel markers to characterize heterogeneous populations of extracellular vesicle subtypes.* Proc Natl Acad Sci U S A, 2016. **113**(8): p. E968-77. *PMC4776515*.
32. Willms, E., H.J. Johansson, I. Mager, Y. Lee, K.E. Blomberg, M. Sadik, . . . P. Vader, *Cells release subpopulations of exosomes with distinct molecular and biological properties.* Sci Rep, 2016. **6**: p. 22519. *PMC4773763*.
33. Gu, H., C. Chen, X. Hao, C. Wang, X. Zhang, Z. Li, . . . J. Zheng, *Sorting protein VPS33B regulates exosomal autocrine signaling to mediate hematopoiesis and leukemogenesis.* The Journal of clinical investigation, 2016. **126**(12): p. 4537-4553.
34. Ostrowski, M., N.B. Carmo, S. Krumeich, I. Fanget, G. Raposo, A. Savina, . . . C. Thery, *Rab27a and Rab27b control different steps of the exosome secretion pathway.* Nature Cell Biology, 2009. **12**(1): p. 19-30.
35. Smith, Z.J., C. Lee, T. Rojalin, R.P. Carney, S. Hazari, A. Knudson, . . . S. Wachsmann-Hogiu, *Single exosome study reveals subpopulations distributed among cell lines with variability related to membrane content.* J Extracell Vesicles, 2015. **4**: p. 28533. *PMC4673914*.
36. Raposo, G. and W. Stoorvogel, *Extracellular vesicles: exosomes, microvesicles, and friends.* J Cell Biol, 2013. **200**(4): p. 373-83. *PMC3575529*.
37. Timár, C.I., A.M. Lorincz, R. Csépányi-Kömi, A. Vályi-Nagy, G. Nagy, E.I. Buzás, . . . E. Ligeti, *Antibacterial effect of microvesicles released from human neutrophilic granulocytes.* Blood, 2013. **121**(3): p. 510-518.
38. Johnson, S.M., C. Dempsey, C. Parker, A. Mironov, H. Bradley, and V. Saha, *Acute lymphoblastic leukaemia cells produce large extracellular vesicles containing organelles and an active cytoskeleton.* Journal of extracellular vesicles, 2017. **6**(1): p. 1294339-1294339.
39. Di Vizio, D., M. Morello, A.C. Dudley, P.W. Schow, R.M. Adam, S. Morley, . . . M.R. Freeman, *Large oncosomes in human prostate cancer tissues and in the circulation of mice with metastatic disease.* The American journal of pathology, 2012. **181**(5): p. 1573-1584.
40. Taylor, R.C., S.P. Cullen, and S.J. Martin, *Apoptosis: controlled demolition at the cellular level.* Nature Reviews Molecular Cell Biology, 2008. **9**(3): p. 231-241.

41. Holmgren, L., A. Szeles, E. Rajnavölgyi, J. Folkman, G. Klein, I. Ernberg, and K.I. Falk, *Horizontal Transfer of DNA by the Uptake of Apoptotic Bodies.* Blood, 1999. **93**(11): p. 3956-3963.
42. Hakulinen, J., L. Sankkila, N. Sugiyama, K. Lehti, and J. Keski-Oja, *Secretion of active membrane type 1 matrix metalloproteinase (MMP-14) into extracellular space in microvesicular exosomes.* Journal of Cellular Biochemistry, 2008. **105**(5): p. 1211-1218.
43. Becker, A., B.K. Thakur, J.M. Weiss, H.S. Kim, H. Peinado, and D. Lyden, *Extracellular Vesicles in Cancer: Cell-to-Cell Mediators of Metastasis.* Cancer Cell, 2016. **30**(6): p. 836-848. *PMC5157696*.
44. Takahashi, Y., M. Nishikawa, H. Shinotsuka, Y. Matsui, S. Ohara, T. Imai, and Y. Takakura, *Visualization and in vivo tracking of the exosomes of murine melanoma B16-BL6 cells in mice after intravenous injection.* Journal of Biotechnology, 2013. **165**(2): p. 77-84.
45. Mulcahy, L.A., R.C. Pink, and D.R. Carter, *Routes and mechanisms of extracellular vesicle uptake.* J Extracell Vesicles, 2014. **3**. *PMC4122821*.
46. Christianson, H.C., K.J. Svensson, T.H. van Kuppevelt, J.P. Li, and M. Belting, *Cancer cell exosomes depend on cell-surface heparan sulfate proteoglycans for their internalization and functional activity.* Proc Natl Acad Sci U S A, 2013. **110**(43): p. 17380-5. *PMC3808637*.
47. Escrevente, C., S. Keller, P. Altevogt, and J. Costa, *Interaction and uptake of exosomes by ovarian cancer cells.* BMC cancer, 2011. **11**: p. 108-108.
48. Svensson, K.J., H.C. Christianson, A. Wittrup, E. Bourseau-Guilmain, E. Lindqvist, L.M. Svensson, . . . M. Belting, *Exosome uptake depends on ERK1/2-heat shock protein 27 signaling and lipid Raft-mediated endocytosis negatively regulated by caveolin-1.* The Journal of biological chemistry, 2013. **288**(24): p. 17713-17724.
49. Barrès, C., L. Blanc, P. Bette-Bobillo, S. André, R. Mamoun, H.-J. Gabius, and M. Vidal, *Galectin-5 is bound onto the surface of rat reticulocyte exosomes and modulates vesicle uptake by macrophages.* Blood, 2010. **115**(3): p. 696-705.
50. Zoller, M., *Tetraspanins: push and pull in suppressing and promoting metastasis.* Nat Rev Cancer, 2009. **9**(1): p. 40-55. *PMID19078974*.
51. Yáñez-Mó, M., O. Barreiro, M. Gordon-Alonso, M. Sala-Valdés, and F. Sánchez-Madrid, *Tetraspanin-enriched microdomains: a functional unit in cell plasma membranes.* Trends in Cell Biology, 2009. **19**(9): p. 434-446.
52. Hemler, M.E., *Tetraspanin functions and associated microdomains.* Nature Reviews Molecular Cell Biology, 2005. **6**(10): p. 801-811.
53. Anzai, N., Y. Lee, B.-S. Youn, S. Fukuda, Y.-J. Kim, C. Mantel, . . . H.E. Broxmeyer, *c-kit associated with the transmembrane 4 superfamily proteins constitutes a functionally distinct subunit in human hematopoietic progenitors.* Blood, 2002. **99**(12): p. 4413-4421.
54. Beckwith, K.A., J.C. Byrd, and N. Muthusamy, *Tetraspanins as therapeutic targets in hematological malignancy: a concise review.* Front Physiol, 2015. **6**: p. 91. *PMC4369647*.
55. Heusermann, W., J. Hean, D. Trojer, E. Steib, S. von Bueren, A. Graff-Meyer, . . . N.C. Meisner-Kober, *Exosomes surf on filopodia to enter cells at endocytic hot*

spots, traffic within endosomes, and are targeted to the ER. J Cell Biol, 2016. **213**(2): p. 173-84. *PMC5084269*.

56. Kucharzewska, P., H.C. Christianson, J.E. Welch, K.J. Svensson, E. Fredlund, M. Ringnér, . . . M. Belting, *Exosomes reflect the hypoxic status of glioma cells and mediate hypoxia-dependent activation of vascular cells during tumor development.* Proceedings of the National Academy of Sciences of the United States of America, 2013. **110**(18): p. 7312-7317.
57. Wen, S., M. Dooner, Y. Cheng, E. Papa, M. Del Tatto, M. Pereira, . . . P. Quesenberry, *Mesenchymal stromal cell-derived extracellular vesicles rescue radiation damage to murine marrow hematopoietic cells.* Leukemia, 2016. **30**(11): p. 2221-2231.
58. Gutiérrez-Vázquez, C., C. Villarroya-Beltri, M. Mittelbrunn, and F. Sánchez-Madrid, *Transfer of extracellular vesicles during immune cell-cell interactions.* Immunological reviews, 2013. **251**(1): p. 125-142.
59. Tadokoro, H., T. Umezu, K. Ohyashiki, T. Hirano, and J.H. Ohyashiki, *Exosomes derived from hypoxic leukemia cells enhance tube formation in endothelial cells.* The Journal of biological chemistry, 2013. **288**(48): p. 34343-34351.
60. Huan, J., N.I. Hornick, N.A. Goloviznina, A.N. Kamimae-Lanning, L.L. David, P.A. Wilmarth, . . . P. Kurre, *Coordinate regulation of residual bone marrow function by paracrine trafficking of AML exosomes.* Leukemia, 2015. **29**(12): p. 2285-2295.
61. Salvucci, O., K. Jiang, P. Gasperini, D. Maric, J. Zhu, S. Sakakibara, . . . G. Tosato, *MicroRNA126 contributes to granulocyte colony-stimulating factor-induced hematopoietic progenitor cell mobilization by reducing the expression of vascular cell adhesion molecule 1.* Haematologica, 2012. **97**(6): p. 818-826.
62. Mathiyalagan, P., Y. Liang, D. Kim, S. Misener, T. Thorne, C.E. Kamide, . . . S. Sahoo, *Angiogenic Mechanisms of Human CD34(+) Stem Cell Exosomes in the Repair of Ischemic Hindlimb.* Circulation research, 2017. **120**(9): p. 1466-1476.
63. Lombardo, G., P. Dentelli, G. Togliatto, A. Rosso, M. Gili, S. Gallo, . . . M.F. Brizzi, *Activated Stat5 trafficking Via Endothelial Cell-derived Extracellular Vesicles Controls IL-3 Pro-angiogenic Paracrine Action.* Scientific reports, 2016. **6**: p. 25689-25689.
64. Weilner, S., E. Schraml, M. Wieser, P. Messner, K. Schneider, K. Wassermann, . . . J. Grillari, *Secreted microvesicular miR-31 inhibits osteogenic differentiation of mesenchymal stem cells.* Aging cell, 2016. **15**(4): p. 744-754.
65. Hromada, C., S. Mühleder, J. Grillari, H. Redl, and W. Holnthoner, *Endothelial Extracellular Vesicles-Promises and Challenges.* Frontiers in physiology, 2017. **8**: p. 275-275.
66. Gong, M., B. Yu, J. Wang, Y. Wang, M. Liu, C. Paul, . . . M. Xu, *Mesenchymal stem cells release exosomes that transfer miRNAs to endothelial cells and promote angiogenesis.* Oncotarget, 2017. **8**(28): p. 45200-45212.
67. Record, M., K. Carayon, M. Poirot, and S. Silvente-Poirot, *Exosomes as new vesicular lipid transporters involved in cell–cell communication and various pathophysiologies.* Biochimica et Biophysica Acta (BBA) - Molecular and Cell Biology of Lipids, 2014. **1841**(1): p. 108-120.

68. Hoggatt, J., P. Singh, J. Sampath, and L.M. Pelus, *Prostaglandin E2 enhances hematopoietic stem cell homing, survival, and proliferation.* Blood, 2009. **113**(22): p. 5444-5455.
69. Madrigal, M., K.S. Rao, and N.H. Riordan, *A review of therapeutic effects of mesenchymal stem cell secretions and induction of secretory modification by different culture methods.* Journal of translational medicine, 2014. **12**: p. 260-260.
70. Jiang, J., C.-Y. Kao, and E.T. Papoutsakis, *How do megakaryocytic microparticles target and deliver cargo to alter the fate of hematopoietic stem cells?* Journal of controlled release : official journal of the Controlled Release Society, 2017. **247**: p. 1-18.
71. O'Connell, R.M., A.A. Chaudhuri, D.S. Rao, W.S.J. Gibson, A.B. Balazs, and D. Baltimore, *MicroRNAs enriched in hematopoietic stem cells differentially regulate long-term hematopoietic output.* Proceedings of the National Academy of Sciences of the United States of America, 2010. **107**(32): p. 14235-14240.
72. Shi, X.-F., H. Wang, F.-X. Kong, Q.-Q. Xu, F.-J. Xiao, Y.-F. Yang, . . . L.-S. Wang, *Exosomal miR-486 regulates hypoxia-induced erythroid differentiation of erythroleukemia cells through targeting Sirt1.* Experimental Cell Research, 2017. **351**(1): p. 74-81.
73. Wang, N., D. Guo, Y.Y. Zhao, C.Y. Dong, X.Y. Liu, B.X. Yang, . . . X.T. Ma, *TWIST-1 promotes cell growth, drug resistance and progenitor clonogenic capacities in myeloid leukemia and is a novel poor prognostic factor in acute myeloid leukemia.* Oncotarget, 2015. **6**(25): p. 20977-92. *PMC4673244*.
74. Davis, C., A. Dukes, M. Drewry, I. Helwa, M.H. Johnson, C.M. Isales, . . . M.W. Hamrick, *MicroRNA-183-5p Increases with Age in Bone-Derived Extracellular Vesicles, Suppresses Bone Marrow Stromal (Stem) Cell Proliferation, and Induces Stem Cell Senescence.* Tissue engineering. Part A, 2017. **23**(21-22): p. 1231-1240.
75. Ratajczak, J., K. Miekus, M. Kucia, J. Zhang, R. Reca, P. Dvorak, and M.Z. Ratajczak, *Embryonic stem cell-derived microvesicles reprogram hematopoietic progenitors: evidence for horizontal transfer of mRNA and protein delivery.* Leukemia, 2006. **20**(5): p. 847-856.
76. De Kouchkovsky, I. and M. Abdul-Hay, *'Acute myeloid leukemia: a comprehensive review and 2016 update'.* Blood Cancer J, 2016. **6**(7): p. e441. *PMC5030376*.
77. Piller, G., *Leukaemia - a brief historical review from ancient times to 1950.* Br J Haematol, 2001. **112**(2): p. 282-92.
78. Estey, E.H., *Acute myeloid leukemia: 2019 update on risk-stratification and management.* Am J Hematol, 2018. **93**(10): p. 1267-1291.
79. Dohner, H., E. Estey, D. Grimwade, S. Amadori, F.R. Appelbaum, T. Buchner, . . . C.D. Bloomfield, *Diagnosis and management of AML in adults: 2017 ELN recommendations from an international expert panel.* Blood, 2017. **129**(4): p. 424-447. *PMC5291965*.
80. Sasine, J.P. and G.J. Schiller, *Acute Myeloid Leukemia: How Do We Measure Success?* Curr Hematol Malig Rep, 2016. **11**(6): p. 528-536.
81. Arber, D.A., A. Orazi, R. Hasserjian, J. Thiele, M.J. Borowitz, M.M. Le Beau, . . . J.W. Vardiman, *The 2016 revision to the World Health Organization classification of myeloid neoplasms and acute leukemia.* Blood, 2016. **127**(20): p. 2391-405.

82. Pourrajab, F., M.R. Zare-Khormizi, A.S. Hashemi, and S. Hekmatimoghaddam, *Genetic Characterization and Risk Stratification of Acute Myeloid Leukemia.* Cancer Manag Res, 2020. **12**: p. 2231-2253. *PMC7104087*.
83. Estey, E. and H. Dohner, *Acute myeloid leukaemia.* Lancet, 2006. **368**(9550): p. 1894-907.
84. Prada-Arismendy, J., J.C. Arroyave, and S. Rothlisberger, *Molecular biomarkers in acute myeloid leukemia.* Blood Rev, 2017. **31**(1): p. 63-76.
85. DiNardo, C.D. and J.E. Cortes, *Mutations in AML: prognostic and therapeutic implications.* Hematology Am Soc Hematol Educ Program, 2016. **2016**(1): p. 348-355. *PMC6142505*.
86. Daver, N., R.F. Schlenk, N.H. Russell, and M.J. Levis, *Targeting FLT3 mutations in AML: review of current knowledge and evidence.* Leukemia, 2019. **33**(2): p. 299-312. *PMC6365380*.
87. Moarii, M. and E. Papaemmanuil, *Classification and risk assessment in AML: integrating cytogenetics and molecular profiling.* Hematology Am Soc Hematol Educ Program, 2017. **2017**(1): p. 37-44. *PMC6142605 interest.*
88. Bose, P., P. Vachhani, and J.E. Cortes, *Treatment of Relapsed/Refractory Acute Myeloid Leukemia.* Curr Treat Options Oncol, 2017. **18**(3): p. 17.
89. Luskin, M.R. and D.J. DeAngelo, *Midostaurin/PKC412 for the treatment of newly diagnosed FLT3 mutation-positive acute myeloid leukemia.* Expert Rev Hematol, 2017. **10**(12): p. 1033-1045.
90. Tsirigotis, P., M. Byrne, C. Schmid, F. Baron, F. Ciceri, J. Esteve, . . . A. Nagler, *Relapse of AML after hematopoietic stem cell transplantation: methods of monitoring and preventive strategies. A review from the ALWP of the EBMT.* Bone Marrow Transplant, 2016. **51**(11): p. 1431-1438.
91. Ramos, N.R., C.C. Mo, J.E. Karp, and C.S. Hourigan, *Current Approaches in the Treatment of Relapsed and Refractory Acute Myeloid Leukemia.* J Clin Med, 2015. **4**(4): p. 665-95. *PMC4412468*.
92. Alfred, L.J., A. Wojdani, M. Nieto, R. Perez, and G. Yoshida, *A chemical carcinogen, 3-methylcholanthrene, alters T-cell function and induces T-suppressor cells in a mouse model system.* Immunology, 1983. **50**(2): p. 207-13. *PMC1454341*.
93. Law, L.W., V. Taormina, and P.J. Boyle, *Response of acute lymphocytic leukemias to the purine antagonist 6-mercaptopurine.* Ann N Y Acad Sci, 1954. **60**(2): p. 244-50.
94. Early, E., M.A. Moore, A. Kakizuka, K. Nason-Burchenal, P. Martin, R.M. Evans, and E. Dmitrovsky, *Transgenic expression of PML/RARalpha impairs myelopoiesis.* Proc Natl Acad Sci U S A, 1996. **93**(15): p. 7900-4. *PMC38846*.
95. Stavropoulou, V., S. Kaspar, L. Brault, M.A. Sanders, S. Juge, S. Morettini, . . . J. Schwaller, *MLL-AF9 Expression in Hematopoietic Stem Cells Drives a Highly Invasive AML Expressing EMT-Related Genes Linked to Poor Outcome.* Cancer Cell, 2016. **30**(1): p. 43-58.
96. Chen, W., A.R. Kumar, W.A. Hudson, Q. Li, B. Wu, R.A. Staggs, . . . J.H. Kersey, *Malignant transformation initiated by Mll-AF9: gene dosage and critical target cells.* Cancer Cell, 2008. **13**(5): p. 432-40. *PMC2430522*.

97. Gelebart, P., M. Popa, and E. McCormack, *Xenograft Models of Primary Acute Myeloid Leukemia for the Development of Imaging Strategies and Evaluation of Novel Targeted Therapies.* Curr Pharm Biotechnol, 2016. **17**(1): p. 42-51.
98. Ailles, L.E., B. Gerhard, H. Kawagoe, and D.E. Hogge, *Growth characteristics of acute myelogenous leukemia progenitors that initiate malignant hematopoiesis in nonobese diabetic/severe combined immunodeficient mice.* Blood, 1999. **94**(5): p. 1761-72.
99. Vadakekolathu, J., M.D. Minden, T. Hood, S.E. Church, S. Reeder, H. Altmann, . . . S. Rutella, *Immune landscapes predict chemotherapy resistance and immunotherapy response in acute myeloid leukemia.* Sci Transl Med, 2020. **12**(546).
100. Mopin, A., V. Driss, and C. Brinster, *A Detailed Protocol for Characterizing the Murine C1498 Cell Line and its Associated Leukemia Mouse Model.* J Vis Exp, 2016(116). *PMC5092196*.
101. Zhang, L., T.F. Gajewski, and J. Kline, *PD-1/PD-L1 interactions inhibit antitumor immune responses in a murine acute myeloid leukemia model.* Blood, 2009. **114**(8): p. 1545-52. *PMC2731636*.
102. Moshofsky, K.B., H.J. Cho, G. Wu, K.A. Romine, M.T. Newman, Y. Kosaka, . . . E.F. Lind, *Acute myeloid leukemia-induced T-cell suppression can be reversed by inhibition of the MAPK pathway.* Blood Adv, 2019. **3**(20): p. 3038-3051. *PMC6849941*.
103. Evans, A.G. and L.M. Calvi, *Notch signaling in the malignant bone marrow microenvironment: implications for a niche-based model of oncogenesis.* Ann N Y Acad Sci, 2015. **1335**: p. 63-77. *PMC4289406*.
104. Ishikawa, F., S. Yoshida, Y. Saito, A. Hijikata, H. Kitamura, S. Tanaka, . . . L.D. Shultz, *Chemotherapy-resistant human AML stem cells home to and engraft within the bone-marrow endosteal region.* Nat Biotechnol, 2007. **25**(11): p. 1315-21.
105. Yang, X., A. Sexauer, and M. Levis, *Bone marrow stroma-mediated resistance to FLT3 inhibitors in FLT3-ITD AML is mediated by persistent activation of extracellular regulated kinase.* Br J Haematol, 2014. **164**(1): p. 61-72. *PMC4076672*.
106. Viola, S., E. Traer, J. Huan, N.I. Hornick, J.W. Tyner, A. Agarwal, . . . P. Kurre, *Alterations in acute myeloid leukaemia bone marrow stromal cell exosome content coincide with gains in tyrosine kinase inhibitor resistance.* Br J Haematol, 2016. **172**(6): p. 983-6. *PMC4755922*.
107. Wojtuszkiewicz, A., G.J. Schuurhuis, F.L. Kessler, S.R. Piersma, J.C. Knol, T.V. Pham, . . . C.R. Jimenez, *Exosomes Secreted by Apoptosis-Resistant Acute Myeloid Leukemia (AML) Blasts Harbor Regulatory Network Proteins Potentially Involved in Antagonism of Apoptosis.* Mol Cell Proteomics, 2016. **15**(4): p. 1281-98. *PMC4824855*.
108. Huan, J., N.I. Hornick, N.A. Goloviznina, A.N. Kamimae-Lanning, L.L. David, P.A. Wilmarth, . . . P. Kurre, *Coordinate regulation of residual bone marrow function by paracrine trafficking of AML exosomes.* Leukemia, 2015. **29**(12): p. 2285-95. *PMC4834971*.

109. Razmkhah, F., M. Soleimani, D. Mehrabani, M.H. Karimi, S. Amini Kafi-abad, M. Ramzi, . . . J. Kakoui, *Leukemia microvesicles affect healthy hematopoietic stem cells.* Tumor Biology, 2017. **39**(2): p. 101042831769223.
110. Szczepanski, M.J., M. Szajnik, A. Welsh, T.L. Whiteside, and M. Boyiadzis, *Blast-derived microvesicles in sera from patients with acute myeloid leukemia suppress natural killer cell function via membrane-associated transforming growth factor-beta1.* Haematologica, 2011. **96**(9): p. 1302-9. *PMC3166100*.
111. Horiguchi, H., M. Kobune, S. Kikuchi, M. Yoshida, M. Murata, K. Murase, . . . J. Kato, *Extracellular vesicle miR-7977 is involved in hematopoietic dysfunction of mesenchymal stromal cells via poly(rC) binding protein 1 reduction in myeloid neoplasms.* Haematologica, 2016. **101**(4): p. 437-447.
112. Muntión, S., T.L. Ramos, M. Diez-Campelo, B. Rosón, L.I. Sánchez-Abarca, I. Misiewicz-Krzeminska, . . . M.-C. Del Cañizo, *Microvesicles from Mesenchymal Stromal Cells Are Involved in HPC-Microenvironment Crosstalk in Myelodysplastic Patients.* PloS one, 2016. **11**(2): p. e0146722-e0146722.
113. Corrado, C., L. Saieva, S. Raimondo, A. Santoro, G. De Leo, and R. Alessandro, *Chronic myelogenous leukaemia exosomes modulate bone marrow microenvironment through activation of epidermal growth factor receptor.* Journal of cellular and molecular medicine, 2016. **20**(10): p. 1829-1839.
114. Peinado, H., M. Aleckovic, S. Lavotshkin, I. Matei, B. Costa-Silva, G. Moreno-Bueno, . . . D. Lyden, *Melanoma exosomes educate bone marrow progenitor cells toward a pro-metastatic phenotype through MET.* Nat Med, 2012. **18**(6): p. 883-91. *PMC3645291*.
115. Ding, L., T.J. Ley, D.E. Larson, C.A. Miller, D.C. Koboldt, J.S. Welch, . . . J.F. DiPersio, *Clonal evolution in relapsed acute myeloid leukaemia revealed by whole-genome sequencing.* Nature, 2012. **481**(7382): p. 506-10. *PMC3267864*.
116. Ghiaur, G., M. Wroblewski, and S. Loges, *Acute Myelogenous Leukemia and its Microenvironment: A Molecular Conversation.* Semin Hematol, 2015. **52**(3): p. 200-6.
117. Zhang, J., X. Hu, J. Wang, A.D. Sahu, D. Cohen, L. Song, . . . X.S. Liu, *Immune receptor repertoires in pediatric and adult acute myeloid leukemia.* Genome Med, 2019. **11**(1): p. 73. *PMC6880565*.
118. Whiteside, T.L., *The effect of tumor-derived exosomes on immune regulation and cancer immunotherapy.* Future Oncol, 2017. **13**(28): p. 2583-2592. *PMC5827821*.
119. Barrett, A.J., *Acute myeloid leukaemia and the immune system: implications for immunotherapy.* Br J Haematol, 2020. **188**(1): p. 147-158.
120. Zhang, J., Y. Gu, and B. Chen, *Mechanisms of drug resistance in acute myeloid leukemia.* Onco Targets Ther, 2019. **12**: p. 1937-1945. *PMC6417008*.
121. Bouvy, C., A. Wannez, J. Laloy, C. Chatelain, and J.M. Dogne, *Transfer of multidrug resistance among acute myeloid leukemia cells via extracellular vesicles and their microRNA cargo.* Leuk Res, 2017. **62**: p. 70-76.
122. Menck, K., C. Sonmezer, T.S. Worst, M. Schulz, G.H. Dihazi, F. Streit, . . . J.C. Gross, *Neutral sphingomyelinases control extracellular vesicles budding from the plasma membrane.* J Extracell Vesicles, 2017. **6**(1): p. 1378056. *PMC5699186*.

123. Nehrbas, J., J.T. Butler, D.W. Chen, and P. Kurre, *Extracellular Vesicles and Chemotherapy Resistance in the AML Microenvironment.* Front Oncol, 2020. **10**: p. 90. *PMC7033644*.
124. Lamble, A.J. and E.F. Lind, *Targeting the Immune Microenvironment in Acute Myeloid Leukemia: A Focus on T Cell Immunity.* Front Oncol, 2018. **8**: p. 213. *PMC6008423*.
125. Le Dieu, R., D.C. Taussig, A.G. Ramsay, R. Mitter, F. Miraki-Moud, R. Fatah, . . . J.G. Gribben, *Peripheral blood T cells in acute myeloid leukemia (AML) patients at diagnosis have abnormal phenotype and genotype and form defective immune synapses with AML blasts.* Blood, 2009. **114**(18): p. 3909-16. *PMC2773481*.
126. Teague, R.M. and J. Kline, *Immune evasion in acute myeloid leukemia: current concepts and future directions.* J Immunother Cancer, 2013. **1**(13). *PMC3864190*.
127. Chen, X., D.E. Kline, and J. Kline, *Peripheral T-cell tolerance in hosts with acute myeloid leukemia.* Oncoimmunology, 2013. **2**(8): p. e25445. *PMC3812197*.
128. Toffalori, C., L. Zito, V. Gambacorta, M. Riba, G. Oliveira, G. Bucci, . . . L. Vago, *Immune signature drives leukemia escape and relapse after hematopoietic cell transplantation.* Nat Med, 2019. **25**(4): p. 603-611.
129. Zhang, N. and M.J. Bevan, *CD8(+) T cells: foot soldiers of the immune system.* Immunity, 2011. **35**(2): p. 161-8. *PMC3303224*.
130. Kumar, B.V., T.J. Connors, and D.L. Farber, *Human T Cell Development, Localization, and Function throughout Life.* Immunity, 2018. **48**(2): p. 202-213. *PMC5826622*.
131. Keir, M.E., L.M. Francisco, and A.H. Sharpe, *PD-1 and its ligands in T-cell immunity.* Curr Opin Immunol, 2007. **19**(3): p. 309-14.
132. Chen, L. and D.B. Flies, *Molecular mechanisms of T cell co-stimulation and co-inhibition.* Nat Rev Immunol, 2013. **13**(4): p. 227-42. *PMC3786574*.
133. Schreiber, R.D., L.J. Old, and M.J. Smyth, *Cancer immunoediting: integrating immunity's roles in cancer suppression and promotion.* Science, 2011. **331**(6024): p. 1565-70.
134. Liao, D., M. Wang, Y. Liao, J. Li, and T. Niu, *A Review of Efficacy and Safety of Checkpoint Inhibitor for the Treatment of Acute Myeloid Leukemia.* Front Pharmacol, 2019. **10**: p. 609. *PMC6562221*.
135. Giannopoulos, K., *Targeting Immune Signaling Checkpoints in Acute Myeloid Leukemia.* J Clin Med, 2019. **8**(2). *PMC6406869*.
136. Sehgal, A., T.L. Whiteside, and M. Boyiadzis, *Programmed death-1 checkpoint blockade in acute myeloid leukemia.* Expert Opin Biol Ther, 2015. **15**(8): p. 1191-203. *PMC4778424*.
137. Zamora, A.E., J.C. Crawford, E.K. Allen, X.J. Guo, J. Bakke, R.A. Carter, . . . P.G. Thomas, *Pediatric patients with acute lymphoblastic leukemia generate abundant and functional neoantigen-specific CD8(+) T cell responses.* Sci Transl Med, 2019. **11**(498).
138. Gale, R.P. and G. Opelz, *Commentary: does immune suppression increase risk of developing acute myeloid leukemia?* Leukemia, 2012. **26**(3): p. 422-3.
139. Hong, C.S., P. Sharma, S.S. Yerneni, P. Simms, E.K. Jackson, T.L. Whiteside, and M. Boyiadzis, *Circulating exosomes carrying an immunosuppressive cargo*

interfere with cellular immunotherapy in acute myeloid leukemia. Sci Rep, 2017. **7**(1): p. 14684. *PMC5666018*.

140. Zhou, Q., M.E. Munger, S.L. Highfill, J. Tolar, B.J. Weigel, M. Riddle, . . . B.R. Blazar, *Program death-1 signaling and regulatory T cells collaborate to resist the function of adoptively transferred cytotoxic T lymphocytes in advanced acute myeloid leukemia.* Blood, 2010. **116**(14): p. 2484-93. *PMC2953885*.
141. Boddu, P., H. Kantarjian, G. Garcia-Manero, J. Allison, P. Sharma, and N. Daver, *The emerging role of immune checkpoint based approaches in AML and MDS.* Leuk Lymphoma, 2018. **59**(4): p. 790-802. *PMC5872841*.
142. Chen, G., A.C. Huang, W. Zhang, G. Zhang, M. Wu, W. Xu, . . . W. Guo, *Exosomal PD-L1 contributes to immunosuppression and is associated with anti-PD-1 response.* Nature, 2018. **560**(7718): p. 382-386. *PMC6095740*.
143. Poggio, M., T. Hu, C.C. Pai, B. Chu, C.D. Belair, A. Chang, . . . R. Blelloch, *Suppression of Exosomal PD-L1 Induces Systemic Anti-tumor Immunity and Memory.* Cell, 2019. **177**(2): p. 414-427 e13. *PMC6499401*.
144. Paggetti, J., F. Haderk, M. Seiffert, B. Janji, U. Distler, W. Ammerlaan, . . . E. Moussay, *Exosomes released by chronic lymphocytic leukemia cells induce the transition of stromal cells into cancer-associated fibroblasts.* Blood, 2015. **126**(9): p. 1106-17. *PMC4560344*.
145. Mendez-Ferrer, S., T.V. Michurina, F. Ferraro, A.R. Mazloom, B.D. Macarthur, S.A. Lira, . . . P.S. Frenette, *Mesenchymal and haematopoietic stem cells form a unique bone marrow niche.* Nature, 2010. **466**(7308): p. 829-34. *PMC3146551*.
146. Jung, Y., J. Song, Y. Shiozawa, J. Wang, Z. Wang, B. Williams, . . . R.S. Taichman, *Hematopoietic stem cells regulate mesenchymal stromal cell induction into osteoblasts thereby participating in the formation of the stem cell niche.* Stem Cells, 2008. **26**(8): p. 2042-51. *PMC3513687*.
147. El-Badri, N.S., B.Y. Wang, Cherry, and R.A. Good, *Osteoblasts promote engraftment of allogeneic hematopoietic stem cells.* Exp Hematol, 1998. **26**(2): p. 110-6.
148. Mendez-Ferrer, S., A. Chow, M. Merad, and P.S. Frenette, *Circadian rhythms influence hematopoietic stem cells.* Curr Opin Hematol, 2009. **16**(4): p. 235-42. *PMC4117204*.
149. Boyd, A.L., J.C. Reid, K.R. Salci, L. Aslostovar, Y.D. Benoit, Z. Shapovalova, . . . M. Bhatia, *Acute myeloid leukaemia disrupts endogenous myelo-erythropoiesis by compromising the adipocyte bone marrow niche.* Nat Cell Biol, 2017. **19**(11): p. 1336-1347.
150. Kumar, B., M. Garcia, L. Weng, X. Jung, J.L. Murakami, X. Hu, . . . C.C. Chen, *Acute myeloid leukemia transforms the bone marrow niche into a leukemia-permissive microenvironment through exosome secretion.* Leukemia, 2018. **32**(3): p. 575-587. *PMC5843902*.
151. Miraki-Moud, F., F. Anjos-Afonso, K.A. Hodby, E. Griessinger, G. Rosignoli, D. Lillington, . . . D.C. Taussig, *Acute myeloid leukemia does not deplete normal hematopoietic stem cells but induces cytopenias by impeding their differentiation.* Proc Natl Acad Sci U S A, 2013. **110**(33): p. 13576-81. *PMC3746910*.

152. Zhang, B., Y.W. Ho, Q. Huang, T. Maeda, A. Lin, S.U. Lee, . . . R. Bhatia, *Altered microenvironmental regulation of leukemic and normal stem cells in chronic myelogenous leukemia.* Cancer Cell, 2012. **21**(4): p. 577-92. *PMC3332001*.
153. Duan, C.W., J. Shi, J. Chen, B. Wang, Y.H. Yu, X. Qin, . . . D.L. Hong, *Leukemia propagating cells rebuild an evolving niche in response to therapy.* Cancer Cell, 2014. **25**(6): p. 778-93.
154. Chandran, P., Y. Le, Y. Li, M. Sabloff, J. Mehic, M. Rosu-Myles, and D.S. Allan, *Mesenchymal stromal cells from patients with acute myeloid leukemia have altered capacity to expand differentiated hematopoietic progenitors.* Leuk Res, 2015. **39**(4): p. 486-93.
155. Reikvam, H., A.K. Brenner, K.M. Hagen, K. Liseth, S. Skrede, K.J. Hatfield, and O. Bruserud, *The cytokine-mediated crosstalk between primary human acute myeloid cells and mesenchymal stem cells alters the local cytokine network and the global gene expression profile of the mesenchymal cells.* Stem Cell Res, 2015. **15**(3): p. 530-41.
156. Huang, J.C., S.K. Basu, X. Zhao, S. Chien, M. Fang, V.G. Oehler, . . . P.S. Becker, *Mesenchymal stromal cells derived from acute myeloid leukemia bone marrow exhibit aberrant cytogenetics and cytokine elaboration.* Blood Cancer J, 2015. **5**: p. e302. *PMC4450324*.
157. Passaro, D., A. Di Tullio, A. Abarrategi, K. Rouault-Pierre, K. Foster, L. Ariza-McNaughton, . . . D. Bonnet, *Increased Vascular Permeability in the Bone Marrow Microenvironment Contributes to Disease Progression and Drug Response in Acute Myeloid Leukemia.* Cancer Cell, 2017.
158. Frisch, B.J., J.M. Ashton, L. Xing, M.W. Becker, C.T. Jordan, and L.M. Calvi, *Functional inhibition of osteoblastic cells in an in vivo mouse model of myeloid leukemia.* Blood, 2012. **119**(2): p. 540-50. *PMC3384480*.
159. Battula, V.L., P.M. Le, J.C. Sun, K. Nguyen, B. Yuan, X. Zhou, . . . M. Andreeff, *AML-induced osteogenic differentiation in mesenchymal stromal cells supports leukemia growth.* JCI Insight, 2017. **2**(13). *PMC5499365*.
160. Lim, M., Y. Pang, S. Ma, S. Hao, H. Shi, Y. Zheng, . . . T. Cheng, *Altered mesenchymal niche cells impede generation of normal hematopoietic progenitor cells in leukemic bone marrow.* Leukemia, 2016. **30**(1): p. 154-62.
161. Mirantes, C., E. Passegue, and E.M. Pietras, *Pro-inflammatory cytokines: emerging players regulating HSC function in normal and diseased hematopoiesis.* Exp Cell Res, 2014. **329**(2): p. 248-54. *PMC4250307*.
162. Rodvold, J.J., K.T. Chiu, N. Hiramatsu, J.K. Nussbacher, V. Galimberti, N.R. Mahadevan, . . . M. Zanetti, *Intercellular transmission of the unfolded protein response promotes survival and drug resistance in cancer cells.* Sci Signal, 2017. **10**(482).
163. Rodvold, J.J., N.R. Mahadevan, and M. Zanetti, *Immune modulation by ER stress and inflammation in the tumor microenvironment.* Cancer Lett, 2016. **380**(1): p. 227-36.
164. Tohmonda, T., Y. Miyauchi, R. Ghosh, M. Yoda, S. Uchikawa, J. Takito, . . . K. Horiuchi, *The IRE1alpha-XBP1 pathway is essential for osteoblast differentiation through promoting transcription of Osterix.* EMBO Rep, 2011. **12**(5): p. 451-7. *PMC3090012*.

165. Horiuchi, K., T. Tohmonda, and H. Morioka, *The unfolded protein response in skeletal development and homeostasis.* Cell Mol Life Sci, 2016. **73**(15): p. 2851-69.
166. Moore, K.A. and J. Hollien, *The unfolded protein response in secretory cell function.* Annu Rev Genet, 2012. **46**: p. 165-83.
167. Su, X., M. Yu, G. Qiu, Y. Zheng, Y. Chen, R. Wen, . . . D. Wang, *Evaluation of nestin or osterix promoter-driven cre/loxp system in studying the biological functions of murine osteoblastic cells.* Am J Transl Res, 2016. **8**(3): p. 1447-59. *PMC4859630*.
168. Hornick, N.I., J. Huan, B. Doron, N.A. Goloviznina, J. Lapidus, B.H. Chang, and P. Kurre, *Serum Exosome MicroRNA as a Minimally-Invasive Early Biomarker of AML.* Sci Rep, 2015. **5**: p. 11295. *PMC4650871*.
169. Hawkins, E.D., D. Duarte, O. Akinduro, R.A. Khorshed, D. Passaro, M. Nowicka, . . . C. Lo Celso, *T-cell acute leukaemia exhibits dynamic interactions with bone marrow microenvironments.* Nature, 2016. **538**(7626): p. 518-522. *PMC5164929*.
170. Boot-Handford, R.P. and M.D. Briggs, *The unfolded protein response and its relevance to connective tissue diseases.* Cell Tissue Res, 2010. **339**(1): p. 197-211. *PMC2784867*.
171. Hamamura, K., Y. Liu, and H. Yokota, *Microarray analysis of thapsigargin-induced stress to the endoplasmic reticulum of mouse osteoblasts.* J Bone Miner Metab, 2008. **26**(3): p. 231-40.
172. Riggs, A.C., E. Bernal-Mizrachi, M. Ohsugi, J. Wasson, S. Fatrai, C. Welling, . . . M.A. Permutt, *Mice conditionally lacking the Wolfram gene in pancreatic islet beta cells exhibit diabetes as a result of enhanced endoplasmic reticulum stress and apoptosis.* Diabetologia, 2005. **48**(11): p. 2313-21.
173. Oslowski, C.M. and F. Urano, *Measuring ER stress and the unfolded protein response using mammalian tissue culture system.* Methods Enzymol, 2011. **490**: p. 71-92. *PMC3701721*.
174. Shim, S.H., C. Xia, G. Zhong, H.P. Babcock, J.C. Vaughan, B. Huang, . . . X. Zhuang, *Super-resolution fluorescence imaging of organelles in live cells with photoswitchable membrane probes.* Proc Natl Acad Sci U S A, 2012. **109**(35): p. 13978-83. *PMC3435176*.
175. Zanetti, M., J.J. Rodvold, and N.R. Mahadevan, *The evolving paradigm of cell-nonautonomous UPR-based regulation of immunity by cancer cells.* Oncogene, 2016. **35**(3): p. 269-78.
176. Kanemoto, S., R. Nitani, T. Murakami, M. Kaneko, R. Asada, K. Matsuhisa, . . . K. Imaizumi, *Multivesicular body formation enhancement and exosome release during endoplasmic reticulum stress.* Biochem Biophys Res Commun, 2016. **480**(2): p. 166-172.
177. Hara, Y., G. Yamato, N. Shiba, K. Ohki, M.-J. Park, D. Tomizawa, . . . Y. Hayashi, *High BMP2 Expression Is a Poor Prognostic Factor and a Good Candidate to Identify CBFA2T3-GLIS2-like High-Risk Subgroup in Pediatric Acute Myeloid Leukemia.* Blood, 2015. **126**(23): p. 2583-2583.
178. Krause, D.S. and D.T. Scadden, *A hostel for the hostile: the bone marrow niche in hematologic neoplasms.* Haematologica, 2015. **100**(11): p. 1376-87. *PMC4825315*.

179. Huan, J., N.I. Hornick, M.J. Shurtleff, A.M. Skinner, N.A. Goloviznina, C.T. Roberts, Jr., and P. Kurre, *RNA trafficking by acute myelogenous leukemia exosomes.* Cancer Res, 2013. **73**(2): p. 918-29.
180. Valadi, H., K. Ekstrom, A. Bossios, M. Sjostrand, J.J. Lee, and J.O. Lotvall, *Exosome-mediated transfer of mRNAs and microRNAs is a novel mechanism of genetic exchange between cells.* Nat Cell Biol, 2007. **9**(6): p. 654-9.
181. Duarte, D., E.D. Hawkins, O. Akinduro, H. Ang, K. De Filippo, I.Y. Kong, . . . C. Lo Celso, *Inhibition of Endosteal Vascular Niche Remodeling Rescues Hematopoietic Stem Cell Loss in AML.* Cell Stem Cell, 2018. **22**(1): p. 64-77 e6. *PMC5766835*.
182. Yadav, R.K., S.W. Chae, H.R. Kim, and H.J. Chae, *Endoplasmic reticulum stress and cancer.* J Cancer Prev, 2014. **19**(2): p. 75-88. *PMC4204165*.
183. Schardt, J.A., B.U. Mueller, and T. Pabst, *Activation of the unfolded protein response in human acute myeloid leukemia.* Methods Enzymol, 2011. **489**: p. 227-43.
184. Sun, H., D.C. Lin, X. Guo, B. Kharabi Masouleh, S. Gery, Q. Cao, . . . H.P. Koeffler, *Inhibition of IRE1alpha-driven pro-survival pathways is a promising therapeutic application in acute myeloid leukemia.* Oncotarget, 2016. **7**(14): p. 18736-49. *PMC4951325*.
185. Wey, S., B. Luo, C.C. Tseng, M. Ni, H. Zhou, Y. Fu, . . . A.S. Lee, *Inducible knockout of GRP78/BiP in the hematopoietic system suppresses Pten-null leukemogenesis and AKT oncogenic signaling.* Blood, 2012. **119**(3): p. 817-25. *PMC3265205*.
186. Murakami, T., A. Saito, S. Hino, S. Kondo, S. Kanemoto, K. Chihara, . . . K. Imaizumi, *Signalling mediated by the endoplasmic reticulum stress transducer OASIS is involved in bone formation.* Nat Cell Biol, 2009. **11**(10): p. 1205-11.
187. Montgomery, T.A. and G. Ruvkun, *MicroRNAs visit the ER.* Cell, 2013. **153**(3): p. 511-2.
188. Stalder, L., W. Heusermann, L. Sokol, D. Trojer, J. Wirz, J. Hean, . . . N.C. Meisner-Kober, *The rough endoplasmatic reticulum is a central nucleation site of siRNA-mediated RNA silencing.* EMBO J, 2013. **32**(8): p. 1115-27. *PMC3630355*.
189. Zylbersztejn, F., M. Flores-Violante, T. Voeltzel, F.E. Nicolini, S. Lefort, and V. Maguer-Satta, *The BMP pathway: A unique tool to decode the origin and progression of leukemia.* Exp Hematol, 2018. **61**: p. 36-44.
190. Geyh, S., M. Rodriguez-Paredes, P. Jager, C. Khandanpour, R.P. Cadeddu, J. Gutekunst, . . . T. Schroeder, *Functional inhibition of mesenchymal stromal cells in acute myeloid leukemia.* Leukemia, 2016. **30**(3): p. 683-91.
191. Krause, D.S., K. Fulzele, A. Catic, C.C. Sun, D. Dombkowski, M.P. Hurley, . . . D.T. Scadden, *Differential regulation of myeloid leukemias by the bone marrow microenvironment.* Nat Med, 2013. **19**(11): p. 1513-7. *PMC3827980*.
192. Raaijmakers, M.H., *Niche contributions to oncogenesis: emerging concepts and implications for the hematopoietic system.* Haematologica, 2011. **96**(7): p. 1041-8. *PMC3128224*.
193. Creutzig, U., M. Zimmermann, M.N. Dworzak, B. Gibson, R. Tamminga, J. Abrahamsson, . . . G.L. Kaspers, *The prognostic significance of early treatment response in pediatric relapsed acute myeloid leukemia: results of the international*

study Relapsed AML 2001/01. Haematologica, 2014. **99**(9): p. 1472-8. *PMC4562536*.

194. Madden, E., S.E. Logue, S.J. Healy, S. Manie, and A. Samali, *The role of the unfolded protein response in cancer progression: From oncogenesis to chemoresistance.* Biol Cell, 2019. **111**(1): p. 1-17.
195. Bi, M., C. Naczki, M. Koritzinsky, D. Fels, J. Blais, N. Hu, . . . C. Koumenis, *ER stress-regulated translation increases tolerance to extreme hypoxia and promotes tumor growth.* EMBO J, 2005. **24**(19): p. 3470-81. *PMC1276162*.
196. Cubillos-Ruiz, J.R., S.E. Bettigole, and L.H. Glimcher, *Tumorigenic and Immunosuppressive Effects of Endoplasmic Reticulum Stress in Cancer.* Cell, 2017. **168**(4): p. 692-706. *PMC5333759*.
197. Guo, F.J., R. Jiang, Z. Xiong, F. Xia, M. Li, L. Chen, and C.J. Liu, *IRE1a constitutes a negative feedback loop with BMP2 and acts as a novel mediator in modulating osteogenic differentiation.* Cell Death Dis, 2014. **5**: p. e1239. *PMC4047903*.
198. Bahar, E., J.Y. Kim, and H. Yoon, *Chemotherapy Resistance Explained through Endoplasmic Reticulum Stress-Dependent Signaling.* Cancers (Basel), 2019. **11**(3). *PMC6468910*.
199. Pession, A., R. Masetti, C. Rizzari, M.C. Putti, F. Casale, F. Fagioli, . . . A.A.S. Group, *Results of the AIEOP AML 2002/01 multicenter prospective trial for the treatment of children with acute myeloid leukemia.* Blood, 2013. **122**(2): p. 170-8.
200. Kantarjian, H., S. O'Brien, J. Cortes, F. Giles, S. Faderl, E. Jabbour, . . . E. Estey, *Results of intensive chemotherapy in 998 patients age 65 years or older with acute myeloid leukemia or high-risk myelodysplastic syndrome: predictive prognostic models for outcome.* Cancer, 2006. **106**(5): p. 1090-8.
201. Kim, J.A., J.S. Shim, G.Y. Lee, H.W. Yim, T.M. Kim, M. Kim, . . . I.H. Oh, *Microenvironmental remodeling as a parameter and prognostic factor of heterogeneous leukemogenesis in acute myelogenous leukemia.* Cancer Res, 2015. **75**(11): p. 2222-31.
202. Hanoun, M., D. Zhang, T. Mizoguchi, S. Pinho, H. Pierce, Y. Kunisaki, . . . P.S. Frenette, *Acute myelogenous leukemia-induced sympathetic neuropathy promotes malignancy in an altered hematopoietic stem cell niche.* Cell Stem Cell, 2014. **15**(3): p. 365-375. *PMC4156919*.
203. Sun, J., A. Ramos, B. Chapman, J.B. Johnnidis, L. Le, Y.J. Ho, . . . F.D. Camargo, *Clonal dynamics of native haematopoiesis.* Nature, 2014. **514**(7522): p. 322-7. *PMC4408613*.
204. Akinduro, O., T.S. Weber, H. Ang, M.L.R. Haltalli, N. Ruivo, D. Duarte, . . . C. Lo Celso, *Proliferation dynamics of acute myeloid leukaemia and haematopoietic progenitors competing for bone marrow space.* Nat Commun, 2018. **9**(1): p. 519. *PMC5802720*.
205. Cheng, H., S. Hao, Y. Liu, Y. Pang, S. Ma, F. Dong, . . . T. Cheng, *Leukemic marrow infiltration reveals a novel role for Egr3 as a potent inhibitor of normal hematopoietic stem cell proliferation.* Blood, 2015. **126**(11): p. 1302-13. *PMC4574014*.

206. Kahlert, C. and R. Kalluri, *Exosomes in tumor microenvironment influence cancer progression and metastasis.* J Mol Med (Berl), 2013. **91**(4): p. 431-7. *PMC4073669*.
207. Tkach, M. and C. Thery, *Communication by Extracellular Vesicles: Where We Are and Where We Need to Go.* Cell, 2016. **164**(6): p. 1226-1232.
208. Sakamoto, H., N. Takeda, F. Arai, K. Hosokawa, P. Garcia, T. Suda, . . . M. Ogawa, *Determining c-Myb protein levels can isolate functional hematopoietic stem cell subtypes.* Stem Cells, 2015. **33**(2): p. 479-90.
209. Liu, Y., S.E. Elf, Y. Miyata, G. Sashida, Y. Liu, G. Huang, . . . S.D. Nimer, *p53 regulates hematopoietic stem cell quiescence.* Cell Stem Cell, 2009. **4**(1): p. 37-48. *PMC2839936*.
210. Robinson, M.D., D.J. McCarthy, and G.K. Smyth, *edgeR: a Bioconductor package for differential expression analysis of digital gene expression data.* Bioinformatics, 2010. **26**(1): p. 139-40. *PMC2796818*.
211. He, X., Y. Li, M.S. Dai, and X.X. Sun, *Ribosomal protein L4 is a novel regulator of the MDM2-p53 loop.* Oncotarget, 2016. **7**(13): p. 16217-26. *PMC4941309*.
212. Signer, R.A., J.A. Magee, A. Salic, and S.J. Morrison, *Haematopoietic stem cells require a highly regulated protein synthesis rate.* Nature, 2014. **509**(7498): p. 49-54. *PMC4015626*.
213. Gan, B. and R.A. DePinho, *mTORC1 signaling governs hematopoietic stem cell quiescence.* Cell Cycle, 2009. **8**(7): p. 1003-6. *PMC2743144*.
214. Wullschleger, S., R. Loewith, and M.N. Hall, *TOR signaling in growth and metabolism.* Cell, 2006. **124**(3): p. 471-84.
215. Jastrzebski, K., K.M. Hannan, E.B. Tchoubrieva, R.D. Hannan, and R.B. Pearson, *Coordinate regulation of ribosome biogenesis and function by the ribosomal protein S6 kinase, a key mediator of mTOR function.* Growth Factors, 2007. **25**(4): p. 209-26.
216. Signer, R.A., L. Qi, Z. Zhao, D. Thompson, A.A. Sigova, Z.P. Fan, . . . S.J. Morrison, *The rate of protein synthesis in hematopoietic stem cells is limited partly by 4E-BPs.* Genes Dev, 2016. **30**(15): p. 1698-703. *PMC5002975*.
217. Jarzebowski, L., M. Le Bouteiller, S. Coqueran, A. Raveux, S. Vandormael-Pournin, A. David, . . . M. Cohen-Tannoudji, *Mouse adult hematopoietic stem cells actively synthesize ribosomal RNA.* RNA, 2018. **24**(12): p. 1803-1812. *PMC6239186*.
218. Zhi, F., X. Cao, X. Xie, B. Wang, W. Dong, W. Gu, . . . Y. Liu, *Identification of circulating microRNAs as potential biomarkers for detecting acute myeloid leukemia.* PloS one, 2013. **8**(2): p. e56718-e56718.
219. Guo, Q., J. Luan, N. Li, Z. Zhang, X. Zhu, L. Zhao, . . . X. Li, *MicroRNA-181 as a prognostic biomarker for survival in acute myeloid leukemia: a meta-analysis.* Oncotarget, 2017. **8**(51): p. 89130-89141. *PMC5687675*.
220. de Leeuw, D.C., W. van den Ancker, F. Denkers, R.X. de Menezes, T.M. Westers, G.J. Ossenkoppele, . . . L. Smit, *MicroRNA profiling can classify acute leukemias of ambiguous lineage as either acute myeloid leukemia or acute lymphoid leukemia.* Clin Cancer Res, 2013. **19**(8): p. 2187-96.

221. Tanoue, A., T. Nakamura, F. Endo, S. Nishiyama, H. Sakiyama, and I. Matsuda, *Sex-determining region Y (SRY) in a patient with 46,XX true hermaphroditism.* Jpn J Hum Genet, 1992. **37**(4): p. 311-20.
222. Beerman, I., J. Seita, M.A. Inlay, I.L. Weissman, and D.J. Rossi, *Quiescent hematopoietic stem cells accumulate DNA damage during aging that is repaired upon entry into cell cycle.* Cell Stem Cell, 2014. **15**(1): p. 37-50. *PMC4082747*.
223. Flach, J., S.T. Bakker, M. Mohrin, P.C. Conroy, E.M. Pietras, D. Reynaud, . . . E. Passegue, *Replication stress is a potent driver of functional decline in ageing haematopoietic stem cells.* Nature, 2014. **512**(7513): p. 198-202. *PMC4456040*.
224. Ogawa, L.M. and S.J. Baserga, *Crosstalk between the nucleolus and the DNA damage response.* Mol Biosyst, 2017. **13**(3): p. 443-455. *PMC5340083*.
225. Jacamo, R., Y. Chen, Z. Wang, W. Ma, M. Zhang, E.L. Spaeth, . . . M. Andreeff, *Reciprocal leukemia-stroma VCAM-1/VLA-4-dependent activation of NF-kappaB mediates chemoresistance.* Blood, 2014. **123**(17): p. 2691-702. *PMC3999754*.
226. Boyd, A.L., C.J.V. Campbell, C.I. Hopkins, A. Fiebig-Comyn, J. Russell, J. Ulemek, . . . M. Bhatia, *Niche displacement of human leukemic stem cells uniquely allows their competitive replacement with healthy HSPCs.* The Journal of experimental medicine, 2014. **211**(10): p. 1925-1935.
227. Shlush, L.I., S. Zandi, A. Mitchell, W.C. Chen, J.M. Brandwein, V. Gupta, . . . J.E. Dick, *Identification of pre-leukaemic haematopoietic stem cells in acute leukaemia.* Nature, 2014. **506**(7488): p. 328-33. *PMC4991939*.
228. Corces-Zimmerman, M.R., W.J. Hong, I.L. Weissman, B.C. Medeiros, and R. Majeti, *Preleukemic mutations in human acute myeloid leukemia affect epigenetic regulators and persist in remission.* Proc Natl Acad Sci U S A, 2014. **111**(7): p. 2548-53. *PMC3932921*.
229. Boyiadzis, M. and T.L. Whiteside, *Exosomes in acute myeloid leukemia inhibit hematopoiesis.* Curr Opin Hematol, 2018. **25**(4): p. 279-284.
230. Lai, C.P., E.Y. Kim, C.E. Badr, R. Weissleder, T.R. Mempel, B.A. Tannous, and X.O. Breakefield, *Visualization and tracking of tumour extracellular vesicle delivery and RNA translation using multiplexed reporters.* Nat Commun, 2015. **6**: p. 7029. *PMC4435621*.
231. Fumagalli, S. and G. Thomas, *The role of p53 in ribosomopathies.* Semin Hematol, 2011. **48**(2): p. 97-105.
232. Galili, N., S.A. Qasim, and A. Raza, *Defective ribosome biogenesis in myelodysplastic syndromes.* Haematologica, 2009. **94**(10): p. 1336-8. *PMC2754946*.
233. Cmejla, R., J. Cmejlova, H. Handrkova, J. Petrak, and D. Pospisilova, *Ribosomal protein S17 gene (RPS17) is mutated in Diamond-Blackfan anemia.* Hum Mutat, 2007. **28**(12): p. 1178-82.
234. Gazda, H.T., M.R. Sheen, A. Vlachos, V. Choesmel, M.F. O'Donohue, H. Schneider, . . . A.H. Beggs, *Ribosomal protein L5 and L11 mutations are associated with cleft palate and abnormal thumbs in Diamond-Blackfan anemia patients.* Am J Hum Genet, 2008. **83**(6): p. 769-80. *PMC2668101*.
235. Hirao, A. and T. Hoshii, *Mechanistic / mammalian target protein of rapamycin signaling in hematopoietic stem cells and leukemia.* Cancer Sci, 2013. **104**(8): p. 977-82.

236. Huang, J., M. Nguyen-McCarty, E.O. Hexner, G. Danet-Desnoyers, and P.S. Klein, *Maintenance of hematopoietic stem cells through regulation of Wnt and mTOR pathways.* Nat Med, 2012. **18**(12): p. 1778-85. *PMC3518679*.
237. Kalaitzidis, D., S.M. Sykes, Z. Wang, N. Punt, Y. Tang, C. Ragu, . . . S.A. Armstrong, *mTOR complex 1 plays critical roles in hematopoiesis and Pten-loss-evoked leukemogenesis.* Cell Stem Cell, 2012. **11**(3): p. 429-39. *PMC3743253*.
238. Fabian, M.R., N. Sonenberg, and W. Filipowicz, *Regulation of mRNA translation and stability by microRNAs.* Annu Rev Biochem, 2010. **79**: p. 351-79.
239. Selbach, M., B. Schwanhausser, N. Thierfelder, Z. Fang, R. Khanin, and N. Rajewsky, *Widespread changes in protein synthesis induced by microRNAs.* Nature, 2008. **455**(7209): p. 58-63.
240. Pillai, R.S., S.N. Bhattacharyya, and W. Filipowicz, *Repression of protein synthesis by miRNAs: how many mechanisms?* Trends Cell Biol, 2007. **17**(3): p. 118-26.
241. Lechman, E.R., B. Gentner, S.W. Ng, E.M. Schoof, P. van Galen, J.A. Kennedy, . . . J.E. Dick, *miR-126 Regulates Distinct Self-Renewal Outcomes in Normal and Malignant Hematopoietic Stem Cells.* Cancer Cell, 2016. **29**(2): p. 214-28. *PMC4749543*.
242. Qian, P., X.C. He, A. Paulson, Z. Li, F. Tao, J.M. Perry, . . . L. Li, *The Dlk1-Gtl2 Locus Preserves LT-HSC Function by Inhibiting the PI3K-mTOR Pathway to Restrict Mitochondrial Metabolism.* Cell Stem Cell, 2016. **18**(2): p. 214-28. *PMC5545934*.
243. Bianchi, N., A. Finotti, M. Ferracin, I. Lampronti, C. Zuccato, G. Breveglieri, . . . R. Gambari, *Increase of microRNA-210, decrease of raptor gene expression and alteration of mammalian target of rapamycin regulated proteins following mithramycin treatment of human erythroid cells.* PLoS One, 2015. **10**(4): p. e0121567. *PMC4388523*.
244. Kim, G., H.J. An, M.J. Lee, J.Y. Song, J.Y. Jeong, J.H. Lee, and H.C. Jeong, *Hsa-miR-1246 and hsa-miR-1290 are associated with stemness and invasiveness of non-small cell lung cancer.* Lung Cancer, 2016. **91**: p. 15-22.
245. Li, X.J., Z.J. Ren, J.H. Tang, and Q. Yu, *Exosomal MicroRNA MiR-1246 Promotes Cell Proliferation, Invasion and Drug Resistance by Targeting CCNG2 in Breast Cancer.* Cell Physiol Biochem, 2017. **44**(5): p. 1741-1748.
246. Moshiri, F., A. Salvi, L. Gramantieri, A. Sangiovanni, P. Guerriero, G. De Petro, . . . M. Negrini, *Circulating miR-106b-3p, miR-101-3p and miR-1246 as diagnostic biomarkers of hepatocellular carcinoma.* Oncotarget, 2018. **9**(20): p. 15350-15364. *PMC5880609*.
247. Mohrin, M., E. Bourke, D. Alexander, M.R. Warr, K. Barry-Holson, M.M. Le Beau, . . . E. Passegue, *Hematopoietic stem cell quiescence promotes error-prone DNA repair and mutagenesis.* Cell Stem Cell, 2010. **7**(2): p. 174-85. *PMC2924905*.
248. Yahata, T., T. Takanashi, Y. Muguruma, A.A. Ibrahim, H. Matsuzawa, T. Uno, . . . K. Ando, *Accumulation of oxidative DNA damage restricts the self-renewal capacity of human hematopoietic stem cells.* Blood, 2011. **118**(11): p. 2941-50.
249. Jan, M., T.M. Snyder, M.R. Corces-Zimmerman, P. Vyas, I.L. Weissman, S.R. Quake, and R. Majeti, *Clonal evolution of preleukemic hematopoietic stem cells precedes human acute myeloid leukemia.* Sci Transl Med, 2012. **4**(149): p. 149ra118. *PMC4045621*.

250. Oguro, H., L. Ding, and S.J. Morrison, *SLAM family markers resolve functionally distinct subpopulations of hematopoietic stem cells and multipotent progenitors.* Cell Stem Cell, 2013. **13**(1): p. 102-16. *PMC3736853*.
251. Latchman, Y., C.R. Wood, T. Chernova, D. Chaudhary, M. Borde, I. Chernova, . . . G.J. Freeman, *PD-L2 is a second ligand for PD-1 and inhibits T cell activation.* Nat Immunol, 2001. **2**(3): p. 261-8.
252. Greiner, J., H. Dohner, and M. Schmitt, *Cancer vaccines for patients with acute myeloid leukemia--definition of leukemia-associated antigens and current clinical protocols targeting these antigens.* Haematologica, 2006. **91**(12): p. 1653-61.
253. Hong, C.S., G. Danet-Desnoyers, X. Shan, P. Sharma, T.L. Whiteside, and M. Boyiadzis, *Human acute myeloid leukemia blast-derived exosomes in patient-derived xenograft mice mediate immune suppression.* Exp Hematol, 2019. **76**: p. 60-66 e2.
254. Zhou, Q., M.E. Munger, R.G. Veenstra, B.J. Weigel, M. Hirashima, D.H. Munn, . . . B.R. Blazar, *Coexpression of Tim-3 and PD-1 identifies a CD8+ T-cell exhaustion phenotype in mice with disseminated acute myelogenous leukemia.* Blood, 2011. **117**(17): p. 4501-10. *PMC3099570*.
255. Annibali, O., A. Crescenzi, V. Tomarchio, A. Pagano, A. Bianchi, A. Grifoni, and G. Avvisati, *PD-1 /PD-L1 checkpoint in hematological malignancies.* Leuk Res, 2018. **67**: p. 45-55.
256. Wang, X., J. Li, K. Dong, F. Lin, M. Long, Y. Ouyang, . . . H. Zhang, *Tumor suppressor miR-34a targets PD-L1 and functions as a potential immunotherapeutic target in acute myeloid leukemia.* Cell Signal, 2015. **27**(3): p. 443-52.
257. Zajac, M., J. Zaleska, A. Dolnik, L. Bullinger, and K. Giannopoulos, *Expression of CD274 (PD-L1) is associated with unfavourable recurrent mutations in AML.* Br J Haematol, 2017.
258. Tyner, J.W., C.E. Tognon, D. Bottomly, B. Wilmot, S.E. Kurtz, S.L. Savage, . . . B.J. Druker, *Functional genomic landscape of acute myeloid leukaemia.* Nature, 2018. **562**(7728): p. 526-531. *PMC6280667*.
259. Lamble, A.J., Y. Kosaka, T. Laderas, A. Maffit, A. Kaempf, L.K. Brady, . . . E.F. Lind, *Reversible suppression of T cell function in the bone marrow microenvironment of acute myeloid leukemia.* Proc Natl Acad Sci U S A, 2020.
260. Kronig, H., L. Kremmler, B. Haller, C. Englert, C. Peschel, R. Andreesen, and C.U. Blank, *Interferon-induced programmed death-ligand 1 (PD-L1/B7-H1) expression increases on human acute myeloid leukemia blast cells during treatment.* Eur J Haematol, 2014. **92**(3): p. 195-203.
261. Kondo, A., T. Yamashita, H. Tamura, W. Zhao, T. Tsuji, M. Shimizu, . . . K. Ogata, *Interferon-gamma and tumor necrosis factor-alpha induce an immunoinhibitory molecule, B7-H1, via nuclear factor-kappaB activation in blasts in myelodysplastic syndromes.* Blood, 2010. **116**(7): p. 1124-31. *PMC3375140*.
262. Krupka, C., P. Kufer, R. Kischel, G. Zugmaier, F.S. Lichtenegger, T. Kohnke, . . . M. Subklewe, *Blockade of the PD-1/PD-L1 axis augments lysis of AML cells by the CD33/CD3 BiTE antibody construct AMG 330: reversing a T-cell-induced immune escape mechanism.* Leukemia, 2016. **30**(2): p. 484-91.
263. Ricklefs, F.L., Q. Alayo, H. Krenzlin, A.B. Mahmoud, M.C. Speranza, H. Nakashima, . . . E.A. Chiocca, *Immune evasion mediated by PD-L1 on*

glioblastoma-derived extracellular vesicles. Sci Adv, 2018. **4**(3): p. eaar2766. *PMC5842038*.

264. Daassi, D., K.M. Mahoney, and G.J. Freeman, *The importance of exosomal PDL1 in tumour immune evasion.* Nat Rev Immunol, 2020.
265. Abdelhamed, S., J.T. Butler, B. Doron, A. Halse, E. Nemecek, P.A. Wilmarth, . . . P. Kurre, *Extracellular vesicles impose quiescence on residual hematopoietic stem cells in the leukemic niche.* EMBO Rep, 2019. **20**(7): p. e47546.
266. Kong, Y., J. Zhang, D.F. Claxton, W.C. Ehmann, W.B. Rybka, L. Zhu, . . . H. Zheng, *PD-1(hi)TIM-3(+) T cells associate with and predict leukemia relapse in AML patients post allogeneic stem cell transplantation.* Blood Cancer J, 2015. **5**: p. e330. *PMC4526784*.
267. Williams, P., S. Basu, G. Garcia-Manero, C.S. Hourigan, K.A. Oetjen, J.E. Cortes, . . . N.G. Daver, *The distribution of T-cell subsets and the expression of immune checkpoint receptors and ligands in patients with newly diagnosed and relapsed acute myeloid leukemia.* Cancer, 2019. **125**(9): p. 1470-1481. *PMC6467779*.
268. Berger, R., R. Rotem-Yehudar, G. Slama, S. Landes, A. Kneller, M. Leiba, . . . A. Nagler, *Phase I safety and pharmacokinetic study of CT-011, a humanized antibody interacting with PD-1, in patients with advanced hematologic malignancies.* Clin Cancer Res, 2008. **14**(10): p. 3044-51.
269. Taylor, O.A.-W.J., *The Potential Utility of Immunotherapy for AML.* Blood, 2017. **14**(5).
270. Haroun, F., S.A. Solola, S. Nassereddine, and I. Tabbara, *PD-1 signaling and inhibition in AML and MDS.* Ann Hematol, 2017. **96**(9): p. 1441-1448.
271. Nahas, M.R., D. Stroopinsky, J. Rosenblatt, L. Cole, A.R. Pyzer, E. Anastasiadou, . . . D. Avigan, *Hypomethylating agent alters the immune microenvironment in acute myeloid leukaemia (AML) and enhances the immunogenicity of a dendritic cell/AML vaccine.* Br J Haematol, 2019. **185**(4): p. 679-690. *PMC6590084*.
272. Zhou, Q., C. Bucher, M.E. Munger, S.L. Highfill, J. Tolar, D.H. Munn, . . . B.R. Blazar, *Depletion of endogenous tumor-associated regulatory T cells improves the efficacy of adoptive cytotoxic T-cell immunotherapy in murine acute myeloid leukemia.* Blood, 2009. **114**(18): p. 3793-802. *PMC2773484*.
273. Kline, D.E., B.W. MacNabb, X. Chen, W.C. Chan, D. Fosco, and J. Kline, *CD8alpha(+) Dendritic Cells Dictate Leukemia-Specific CD8(+) T Cell Fates.* J Immunol, 2018. **201**(12): p. 3759-3769. *PMC6444187*.
274. Berthon, C., V. Driss, J. Liu, K. Kuranda, X. Leleu, N. Jouy, . . . B. Quesnel, *In acute myeloid leukemia, B7-H1 (PD-L1) protection of blasts from cytotoxic T cells is induced by TLR ligands and interferon-gamma and can be reversed using MEK inhibitors.* Cancer Immunol Immunother, 2010. **59**(12): p. 1839-49. *PMC2945474*.
275. Winterrowd, G.E. and J.E. Chin, *Flow cytometric detection of antigen-specific cytokine responses in lung T cells in a murine model of pulmonary inflammation.* J Immunol Methods, 1999. **226**(1-2): p. 105-18.
276. Duong, P., A. Chung, L. Bouchareychas, and R.L. Raffai, *Cushioned-Density Gradient Ultracentrifugation (C-DGUC) improves the isolation efficiency of extracellular vesicles.* PLoS One, 2019. **14**(4): p. e0215324. *PMC6459479*.
277. Raiborg, C. and H. Stenmark, *The ESCRT machinery in endosomal sorting of ubiquitylated membrane proteins.* Nature, 2009. **458**(7237): p. 445-52.

278. Morgan, T.K., *Cell- and size-specific analysis of placental extracellular vesicles in maternal plasma and pre-eclampsia.* Transl Res, 2018. **201**: p. 40-48.
279. Morales-Kastresana, A., B. Telford, T.A. Musich, K. McKinnon, C. Clayborne, Z. Braig, . . . J.C. Jones, *Labeling Extracellular Vesicles for Nanoscale Flow Cytometry.* Sci Rep, 2017. **7**(1): p. 1878. *PMC5431945*.
280. Boyiadzis, M. and T.L. Whiteside, *The emerging roles of tumor-derived exosomes in hematological malignancies.* Leukemia, 2017. **31**(6): p. 1259-1268.
281. Szajnik, M., M. Czystowska, M.J. Szczepanski, M. Mandapathil, and T.L. Whiteside, *Tumor-derived microvesicles induce, expand and up-regulate biological activities of human regulatory T cells (Treg).* PLoS One, 2010. **5**(7): p. e11469. *PMC2908536*.
282. Benci, J.L., B. Xu, Y. Qiu, T.J. Wu, H. Dada, C. Twyman-Saint Victor, . . . A.J. Minn, *Tumor Interferon Signaling Regulates a Multigenic Resistance Program to Immune Checkpoint Blockade.* Cell, 2016. **167**(6): p. 1540-1554 e12. *PMC5385895*.
283. Segura, E., C. Nicco, B. Lombard, P. Veron, G. Raposo, F. Batteux, . . . C. Thery, *ICAM-1 on exosomes from mature dendritic cells is critical for efficient naive T-cell priming.* Blood, 2005. **106**(1): p. 216-23.
284. Chapuis, A.G., D.N. Egan, M. Bar, T.M. Schmitt, M.S. McAfee, K.G. Paulson, . . . P.D. Greenberg, *T cell receptor gene therapy targeting WT1 prevents acute myeloid leukemia relapse post-transplant.* Nat Med, 2019. **25**(7): p. 1064-1072. *PMC6982533*.
285. Noviello, M., F. Manfredi, E. Ruggiero, T. Perini, G. Oliveira, F. Cortesi, . . . C. Bonini, *Bone marrow central memory and memory stem T-cell exhaustion in AML patients relapsing after HSCT.* Nat Commun, 2019. **10**(1): p. 1065. *PMC6434052*.
286. Schnorfeil, F.M., F.S. Lichtenegger, K. Emmerig, M. Schlueter, J.S. Neitz, R. Draenert, . . . M. Subklewe, *T cells are functionally not impaired in AML: increased PD-1 expression is only seen at time of relapse and correlates with a shift towards the memory T cell compartment.* J Hematol Oncol, 2015. **8**: p. 93. *PMC4518596*.
287. Wang, M., J. Bu, M. Zhou, J. Sido, Y. Lin, G. Liu, . . . E. Shen, *CD8(+)T cells expressing both PD-1 and TIGIT but not CD226 are dysfunctional in acute myeloid leukemia (AML) patients.* Clin Immunol, 2018. **190**: p. 64-73.
288. Dama, P., M. Tang, N. Fulton, J. Kline, and H. Liu, *Gal9/Tim-3 expression level is higher in AML patients who fail chemotherapy.* J Immunother Cancer, 2019. **7**(1): p. 175. *PMC6621946*.
289. Brodska, B., P. Otevrelova, C. Salek, O. Fuchs, Z. Gasova, and K. Kuzelova, *High PD-L1 Expression Predicts for Worse Outcome of Leukemia Patients with Concomitant NPM1 and FLT3 Mutations.* Int J Mol Sci, 2019. **20**(11). *PMC6600137*.
290. Boyiadzis, M. and T.L. Whiteside, *Plasma-derived exosomes in acute myeloid leukemia for detection of minimal residual disease: are we ready?* Expert Rev Mol Diagn, 2016. **16**(6): p. 623-9. *PMC5400097*.
291. Hong, C.S., S. Funk, L. Muller, M. Boyiadzis, and T.L. Whiteside, *Isolation of biologically active and morphologically intact exosomes from plasma of patients with cancer.* J Extracell Vesicles, 2016. **5**: p. 29289. *PMC4808740*.

292. Bisset, L.R., T.L. Lung, M. Kaelin, E. Ludwig, and R.W. Dubs, *Reference values for peripheral blood lymphocyte phenotypes applicable to the healthy adult population in Switzerland.* Eur J Haematol, 2004. **72**(3): p. 203-12.
293. Ahn, E., K. Araki, M. Hashimoto, W. Li, J.L. Riley, J. Cheung, . . . R. Ahmed, *Role of PD-1 during effector CD8 T cell differentiation.* Proc Natl Acad Sci U S A, 2018. **115**(18): p. 4749-4754. *PMC5939075*.
294. Kowal, E.J.K., D. Ter-Ovanesyan, A. Regev, and G.M. Church, *Extracellular Vesicle Isolation and Analysis by Western Blotting.* Methods Mol Biol, 2017. **1660**: p. 143-152.
295. Doron, B., S. Abdelhamed, J.T. Butler, S.K. Hashmi, T.M. Horton, and P. Kurre, *Transmissible ER stress reconfigures the AML bone marrow compartment.* Leukemia, 2018.
296. Weiss, S., *Shattering the diffraction limit of light: A revolution in fluorescence microscopy?* Proceedings of the National Academy of Sciences, 2000. **97**(16): p. 8747-8749.
297. Huang, B., H. Babcock, and X. Zhuang, *Breaking the diffraction barrier: super-resolution imaging of cells.* Cell, 2010. **143**(7): p. 1047-58. *PMC3272504*.
298. Abbe, E., *Beiträge zur Theorie des Mikroskops und der mikroskopischen Wahrnehmung.* Archiv für Mikroskopische Anatomie, 1873. **9**(1): p. 413-468.
299. Betzig, E., G.H. Patterson, R. Sougrat, O.W. Lindwasser, S. Olenych, J.S. Bonifacino, . . . H.F. Hess, *Imaging intracellular fluorescent proteins at nanometer resolution.* Science, 2006. **313**(5793): p. 1642-5.
300. Rust, M.J., M. Bates, and X. Zhuang, *Sub-diffraction-limit imaging by stochastic optical reconstruction microscopy (STORM).* Nat Methods, 2006. **3**(10): p. 793-5. *PMC2700296*.
301. Rayleigh, L., *On the Theory of Optical Images, with special reference to the Microscope.* Journal of the Royal Microscopical Society, 1903. **23**(4): p. 474-482.
302. Airy, G.B., *On the Diffraction of an Object-glass with Circular Aperture: From the Transactions of the Cambridge Philosophical Society, Vol. V, Part III*. 1835: Printed at the Pitt Press by John Smith.
303. Cole, R.W., T. Jinadasa, and C.M. Brown, *Measuring and interpreting point spread functions to determine confocal microscope resolution and ensure quality control.* Nature Protocols, 2011. **6**(12): p. 1929-1941.
304. Sibarita, J.B., *Deconvolution microscopy.* Adv Biochem Eng Biotechnol, 2005. **95**: p. 201-43.
305. Henriques, R. and M.M. Mhlanga, *PALM and STORM: What hides beyond the Rayleigh limit?* Biotechnology Journal, 2009. **4**(6): p. 846-857.
306. Combs, C.A., *Fluorescence microscopy: a concise guide to current imaging methods.* Curr Protoc Neurosci, 2010. **Chapter 2**: p. Unit2 1. *PMC3805368*.
307. Huang, B., M. Bates, and X. Zhuang, *Super-resolution fluorescence microscopy.* Annu Rev Biochem, 2009. **78**: p. 993-1016. *PMC2835776*.
308. Huff, J., *The Airyscan detector from ZEISS: confocal imaging with improved signal-to-noise ratio and super-resolution.* Nature Methods, 2015. **12**: p. 1205.
309. Ostrowski, A., D. Nordmeyer, A. Boreham, C. Holzhausen, L. Mundhenk, C. Graf, . . . A.D. Gruber, *Overview about the localization of nanoparticles in tissue and*

cellular context by different imaging techniques. Beilstein J Nanotechnol, 2015. **6**: p. 263-80. *PMC4311646*.

310. Godin, A.G., B. Lounis, and L. Cognet, *Super-resolution microscopy approaches for live cell imaging.* Biophys J, 2014. **107**(8): p. 1777-84. *PMC4213717*.
311. Higginbotham, J.N., M. Demory Beckler, J.D. Gephart, J.L. Franklin, G. Bogatcheva, G.J. Kremers, . . . R.J. Coffey, *Amphiregulin exosomes increase cancer cell invasion.* Curr Biol, 2011. **21**(9): p. 779-86. *PMC3417320*.
312. Bai, K., G.V. Barnett, S.R. Kar, and T.K. Das, *Interference from Proteins and Surfactants on Particle Size Distributions Measured by Nanoparticle Tracking Analysis (NTA).* Pharm Res, 2017. **34**(4): p. 800-808.
313. Cochilla, A.J., J.K. Angleson, and W.J. Betz, *Monitoring secretory membrane with FM1-43 fluorescence.* Annu Rev Neurosci, 1999. **22**: p. 1-10.
314. Monkemoller, V., M. Schuttpelz, P. McCourt, K. Sorensen, B. Smedsrod, and T. Huser, *Imaging fenestrations in liver sinusoidal endothelial cells by optical localization microscopy.* Phys Chem Chem Phys, 2014. **16**(24): p. 12576-81.
315. Maas, S.L., J. De Vrij, and M.L. Broekman, *Quantification and size-profiling of extracellular vesicles using tunable resistive pulse sensing.* J Vis Exp, 2014(92): p. e51623. *PMC4335984*.
316. Tan, Y.H., M. Liu, B. Nolting, J.G. Go, J. Gervay-Hague, and G.Y. Liu, *A nanoengineering approach for investigation and regulation of protein immobilization.* ACS Nano, 2008. **2**(11): p. 2374-84. *PMC4512660*.
317. Harmsen, M.M. and H.J. De Haard, *Properties, production, and applications of camelid single-domain antibody fragments.* Appl Microbiol Biotechnol, 2007. **77**(1): p. 13-22. *PMC2039825*.
318. Morelli, A.E., A.T. Larregina, W.J. Shufesky, M.L. Sullivan, D.B. Stolz, G.D. Papworth, . . . A.W. Thomson, *Endocytosis, intracellular sorting, and processing of exosomes by dendritic cells.* Blood, 2004. **104**(10): p. 3257-66.
319. Rana, S., S. Yue, D. Stadel, and M. Zoller, *Toward tailored exosomes: the exosomal tetraspanin web contributes to target cell selection.* Int J Biochem Cell Biol, 2012. **44**(9): p. 1574-84.
320. Joshi, B.S., M.A. de Beer, B.N.G. Giepmans, and I.S. Zuhorn, *Endocytosis of Extracellular Vesicles and Release of Their Cargo from Endosomes.* ACS Nano, 2020. **14**(4): p. 4444-4455. *PMC7199215*.
321. Dimitroff, C.J., J.Y. Lee, S. Rafii, R.C. Fuhlbrigge, and R. Sackstein, *CD44 is a major E-selectin ligand on human hematopoietic progenitor cells.* J Cell Biol, 2001. **153**(6): p. 1277-86. *PMC2192031*.
322. Kohn, L.A., Q.L. Hao, R. Sasidharan, C. Parekh, S. Ge, Y. Zhu, . . . G.M. Crooks, *Lymphoid priming in human bone marrow begins before expression of CD10 with upregulation of L-selectin.* Nat Immunol, 2012. **13**(10): p. 963-71. *PMC3448017*.
323. Grass, G.D. and B.P. Toole, *How, with whom and when: an overview of CD147-mediated regulatory networks influencing matrix metalloproteinase activity.* Biosci Rep, 2015. **36**(1): p. e00283. *PMC4718507*.
324. Grass, G.D., L. Dai, Z. Qin, C. Parsons, and B.P. Toole, *CD147: regulator of hyaluronan signaling in invasiveness and chemoresistance.* Adv Cancer Res, 2014. **123**: p. 351-73.

325. Spinello, I., E. Saulle, M.T. Quaranta, L. Pasquini, E. Pelosi, G. Castelli, . . . C. Labbaye, *The small-molecule compound AC-73 targeting CD147 inhibits leukemic cell proliferation, induces autophagy and increases the chemotherapeutic sensitivity of acute myeloid leukemia cells.* Haematologica, 2019. **104**(5): p. 973-985. *PMC6518905*.
326. Fu, J., J. Fu, X. Chen, Y. Zhang, H. Gu, and Y. Bai, *CD147 and VEGF co-expression predicts prognosis in patients with acute myeloid leukemia.* Jpn J Clin Oncol, 2010. **40**(11): p. 1046-52.
327. Tang, J., Y.S. Guo, Y. Zhang, X.L. Yu, L. Li, W. Huang, . . . Z.N. Chen, *CD147 induces UPR to inhibit apoptosis and chemosensitivity by increasing the transcription of Bip in hepatocellular carcinoma.* Cell Death Differ, 2012. **19**(11): p. 1779-90. *PMC3469060*.
328. Germroth, P.G., R.G. Gourdie, and R.P. Thompson, *Confocal microscopy of thick sections from acrylamide gel embedded embryos.* Microsc Res Tech, 1995. **30**(6): p. 513-20.
329. Holmes, D.L. and N.C. Stellwagen, *Estimation of polyacrylamide gel pore size from Ferguson plots of linear DNA fragments. II. Comparison of gels with different crosslinker concentrations, added agarose and added linear polyacrylamide.* Electrophoresis, 1991. **12**(9): p. 612-9.
330. Huang, T., C. Phelps, J. Wang, L.J. Lin, A. Bittel, Z. Scott, . . . X. Nan, *Simultaneous Multicolor Single-Molecule Tracking with Single-Laser Excitation via Spectral Imaging.* Biophys J, 2018. **114**(2): p. 301-310. *PMC5984991*.